Influence of Deformation Path on Microstructure and Damage Evolution during the Open Die Forging of High Strength Steels: Experiments and FE Analysis

by

Prashant DHONDAPURE

MANUSCRIPT-BASED THESIS PRESENTED TO ÉCOLE DE TECHNOLOGIE SUPÉRIEURE IN PARTIAL FULFILLMENT FOR THE DEGREE OF DOCTOR OF PHILOSOPHY
Ph.D.

MONTREAL, SEPTEMBER 3RD, 2025

ÉCOLE DE TECHNOLOGIE SUPÉRIEURE
UNIVERSITÉ DU QUÉBEC

BOARD OF EXAMINERS (THESIS PH.D.)

THIS THESIS HAS BEEN EVALUATED

BY THE FOLLOWING BOARD OF EXAMINERS

Mr. Mohammad Jahazi, Thesis Supervisor
Department of Mechanical Engineering, École de technologie supérieure

Ms. Tasseda Boukherroub, President of the Board of Examiners
Department of Systems Engineering, École de technologie supérieure

Mr. Bouzid Hakim A., Member of the jury
Department of Mechanical Engineering, École de technologie supérieure

Mr. Bruce Williams, External Evaluator
Natural Resources Canada-CanMet

THIS THESIS WAS PRESENTED AND DEFENDED

IN THE PRESENCE OF A BOARD OF EXAMINERS AND PUBLIC

SEPTEMBER 3RD, 2025

AT ÉCOLE DE TECHNOLOGIE SUPÉRIEURE

ACKNOWLEDGMENT

As I reach the conclusion of my PhD journey, I am sincerely thankful to those who played a vital role in this accomplishment. I am especially grateful to my supervisor, Prof. Mohammad Jahazi, for his unwavering support, encouragement, and insightful guidance throughout this work. His mentorship has been instrumental in shaping both my research and academic growth. I also extend my appreciation to Prof. Henri Champliaud for his valuable input and support, particularly in the area of numerical simulations. This thesis would not have been possible without their expertise and dedication.

I am also deeply appreciative of the Jury members for their thoughtful feedback and constructive criticism, which have played a crucial role in elevating my work to new levels. Your expertise and dedication to your field have been a great source of inspiration.

I will always remember the support and kindness extended to me by Mr. Radu Romanica, whose technical guidance, training, and willingness to assist during my experimental work were invaluable. I greatly admire his passion for his work. My sincere thanks also go to Dr. Mohammad Saadati for his help with the SEM and LEXT machines, as well as for his guidance throughout my program.

I am truly grateful to my colleagues and the entire CM2P group for their continuous support, advice, and encouragement throughout my PhD journey. Special thanks to my friend Dr. Soumyaranjan Nayak for his assistance in reviewing papers and drafts of my thesis, as well as for his valuable guidance.

I am deeply grateful to our industrial collaborator, Finkl Steel, especially the teams in R&D, metallurgy, and engineering, for their invaluable support in supplying materials and enabling hands-on experience with large-scale manufacturing operations. Their active involvement

throughout the project was instrumental to its success. I would like to express my sincere thanks to Mr. Jean-Benoit and Dr. Simin Dourandish for their thoughtful feedback and expert guidance.

I also acknowledge the financial assistance provided by MITACS, which partially funded this research through Grant IT164670. My appreciation extends to Nicolas Poulin and John Swanson from Transvalor for their technical support and advice on using the Forge NxT simulation software for modeling the forging processes carried out at Finkl Steel.

Finally, I must acknowledge the unwavering support of my family, who have been my greatest source of love and strength throughout this journey. Your belief in me and the sacrifices you've made to help me succeed have meant everything. I am especially grateful to my mother, Surekha Dhondapure, my father, Nagnath Dhondapure, my brother, Pramod, my sister, Priyanka, my aunties, Surekha and Chandrakala, and my uncles, Balaji and Vijayakumar, and my cousins, for always believing in me. A special thank you to my wife, Diksha Dhondapure, for walking with me through this journey and making personal sacrifices along the way. I also appreciate the support and help from my in-laws, Savita and Omprakash Nila.

This thesis is a testament to the support, encouragement, and guidance I have received from all of you. I will be forever grateful for everything you've done to help me reach this milestone.

I would like to dedicate this thesis to the memory of my late grandmother, Subhidrabai Dhondapure, and my late grandfather, Bhagwan Dhondapure. Their love, wisdom, and unwavering support have shaped me in ways I can never fully express. Their legacy of strength, kindness, and resilience continues to inspire me every day. This work is a reflection of the values they instilled in me, and it is with deep respect and gratitude that I honor their memory through this achievement.

Influence du chemin de déformation sur la microstructure et l'évolution de l'endommagement pendant le forgeage à matrice ouverte des aciers à haute résistance: Études expérimentales et analyse par éléments finis

Prashant DHONDAPURE

RESUME

Les grands blocs forgés en aciers à outils à teneur moyenne en carbone et à haute résistance sont largement utilisés dans les industries de formage pour fabriquer des matrices destinées à des applications telles que le moulage par injection de plastique, la déformation à chaud et l'extrusion. La production de ces composants implique une séquence d'opérations de moulage, de forgeage, de trempe et de revenu. L'objectif principal du processus de forgeage est d'éliminer les défauts de coulée qui peuvent survenir pendant la solidification, tels que la ségrégation, le retrait, la porosité, et la rupture de la structure de la pièce coulée pour la convertir en un matériau plus homogène et isotrope, la microstructure de corroyage. Il est essentiel d'atténuer autant que possible les défauts de coulée au cours de la phase de forgeage. Toutefois, lorsque les défauts sont importants, il devient difficile de les éliminer complètement et de traiter l'hétérogénéité par le seul traitement thermique.

Les paramètres clés présents au cours du processus de forgeage sont la vitesse de déformation, la température et la déformation, qui affectent de manière significative l'efficacité du processus et la qualité du produit final. Outre ces paramètres, des facteurs tels que la géométrie de la matrice et du lingot, le rapport entre la largeur de la matrice et la capacité de la presse influencent l'écoulement du matériau et l'évolution de la microstructure pendant le forgeage. Cette recherche étudie spécifiquement l'impact de la géométrie de la matrice en modifiant sa conception pour créer différents chemins de déformation. L'objectif principal de cette thèse est d'examiner les effets de ces trajectoires de déformation sur l'évolution de la microstructure et le développement des dommages pendant le forgeage à matrice ouverte des aciers à haute résistance.

La première étape de cette étude a consisté à développer un modèle d'éléments finis basé sur la microstructure afin d'examiner l'impact du chemin de déformation sur l'évolution de la microstructure pendant le processus de refoulement des lingots te grande dimension d'acier à haute résistance, moyennement carboné et faiblement allié. Pour ce faire, des essais de compression à chaud ont été réalisés à l'aide du simulateur thermomécanique Gleeble 3800. Les données de contrainte d'écoulement obtenues à partir de ces essais ont été corrigées et utilisées pour établir un modèle de matériau et un modèle de microstructure. Ces modèles ont ensuite été intégrés dans le logiciel de simulation par éléments finis Forge® NxT 3.2 à l'aide

d'une routine utilisateur. Les prévisions des éléments finis ont été validées en les comparant aux résultats expérimentaux des essais de compression à chaud, ce qui a permis d'obtenir des prévisions précises de la contrainte d'écoulement et de la taille des grains recristallisés à la fin de la déformation à chaud. Après validation, le modèle d'éléments finis a été mis à l'échelle pour simuler le processus industriel de refoulement, ce qui a permis d'étudier les effets de la trajectoire de déformation sur l'inhomogénéité de la déformation et l'évolution de la microstructure dans les grands lingots forgés. Une analyse de quatre géométries de matrice a été réalisée afin d'identifier la forme optimale de la filière pour minimiser l'inhomogénéité de la déformation et de la taille des grains dans le lingot. L'étude a montré que la matrice convexe provoquait la déformation la plus faible, tandis que la matrice concave induisait les valeurs de déformation les plus élevées au centre du lingot. En utilisant le coefficient de variation comme mesure de l'hétérogénéité, il a été conclu que la matrice en V et la matrice concave produisaient une distribution plus uniforme de la taille des grains que les matrices plates et convexes.

La deuxième partie de l'étude s'est concentrée sur l'influence du chemin de déformation, illustré par la géométrie de la matrice, sur l'évolution des dommages pendant le cogging de l'acier AISI H13 difficile à forger, à teneur moyenne en carbone et à alliage élevé et à haute résistance. Des essais de compression et de traction à chaud ont été réalisés à l'aide du simulateur thermomécanique Gleeble 3800 pour développer le modèle de matériau optimal qui a ensuite été implémenté dans le code d'éléments finis Forge® NxT 3.2 à l'aide d'un sous-programme développé par l'utilisateur. Le critère d'endommagement normalisé de Cockcroft et Latham et la théorie de la rupture par contrainte de cisaillement maximale (Tresca) ont été utilisés pour prédire l'endommagement et la rupture dans l'axe central de l'arbre au moyen d'une analyse par éléments finis avec trois formes de matrice différentes : concave, plate et convexe. Une étude comparative entre les trois géométries de matrice a été menée pour quantifier les effets de chacune d'entre elles sur la sensibilité à l'endommagement de l'éclatement central. Le modèle d'éléments finis a été validé à l'aide de données industrielles. Les valeurs d'endommagement les plus faibles et les plus élevées ont été trouvées dans le cas d'un cogging avec une matrice concave et une filière plate, respectivement. Le coefficient de variation (CoV) a été utilisé comme mesure de l'hétérogénéité et il a été constaté que la matrice concave fournissait une déformation plus uniforme et les résultats les plus favorables pour le cogging par rapport aux matrices plates et convexes. La nouvelle approche, l'application de la matrice concave, a été mise en œuvre avec succès à l'échelle industrielle.

La troisième et dernière partie de cette étude se concentre sur les simulations physiques et numériques d'un processus de déformation en plusieurs étapes afin d'étudier comment le chemin de déformation influence l'évolution de la microstructure et la distribution des propriétés mécaniques. Des expériences de déformation en plusieurs étapes ont été menées sur des échantillons d'acier à haute résistance à l'aide du simulateur thermomécanique Gleeble 3800, équipé de l'accessoire MaxStrain®. Tous les essais ont été réalisés à une vitesse de déformation de 0,01 s^{-1} et à une température de 1150°C, avec deux trajectoires de déformation différentes. Une déformation réelle totale de 0,84 a été obtenue en quatre étapes, avec une déformation d'environ 0,21 appliquée à chaque étape. Les résultats ont été analysés pour examiner l'effet des différentes trajectoires de déformation sur l'évolution de la microstructure et la distribution de la dureté. Un modèle d'éléments finis a été créé à l'aide du code Forge®

NxT 3.2 pour simuler le processus de déformation en plusieurs étapes. Ce modèle d'éléments finis a été validé par rapport à la taille moyenne des grains mesurée et à la distribution de la dureté à la suite des expériences de déformation en plusieurs étapes. Une fois validé, le modèle FE a permis de prédire la distribution des déformations, la fraction volumique de la recristallisation dynamique (DRX) et l'évolution de la taille des grains au cours du processus. Une analyse comparative des résultats des deux voies de déformation a été réalisée afin d'identifier la voie optimale pour obtenir une déformation uniforme et une distribution de la taille des grains. Le coefficient de variation (CoV) a été utilisé pour évaluer l'hétérogénéité de la distribution de la dureté. Les résultats indiquent que les enclumes concaves favorisent une distribution plus élevée et plus uniforme de la déformation, ce qui se traduit par une distribution plus homogène de la taille des grains et de la dureté.

Mots-clés: Modèle FE basé sur la microstructure, chemins de déformation, évolution de la microstructure, lingot de grande taille, forgeage, acier à moyenne teneur en carbone, cogging, formation d'éclats centraux, AISI H13, géométrie de la matrice, évolution des dommages, Gleeble 3800 Maxstrain®, déformation en plusieurs étapes, analyse FE, propriétés mécaniques

Influence of deformation path on microstructure and damage evolution during the open die forging of high strength steels: Experiments and FE analysis

Prashant DHONDAPURE

ABSTRACT

Large forged blocks of medium carbon, high strength tool steels are widely used in the forming industries to manufacture dies for applications such as plastic injection molding, hot deformation, and extrusion. The production of these components involves a sequence of casting, forging, quenching, and tempering operations. The primary goal of the forging process is to eliminate casting defects that may arise during solidification, such as segregation, shrinkage, porosity and break the as cast structure and convert it to a more homogeneous and isotropic material, wrought microstructure. It is essential to mitigate as many casting defects as possible during the forging stage. However, when the defects are large, it is not possible to fully eliminate them before or after forging through heat treatment alone, making it challenging to address material heterogeneity using heat treatment.

Key parameters present during the forging process are strain rate, temperature, and strain significantly affecting both process efficiency and the quality of the final product. In addition to these parameters, factors like die and ingot geometry, die width ratio, and press capacity influence material flow and microstructure evolution during forging. This research specifically investigates the impact of die geometry by altering its design to create different deformation paths. The main objective of this thesis is to examine the effects of these deformation paths on microstructure evolution and damage development during the open die forging of high strength steels.

The first step of this study was to develop a microstructure-based finite element (FE) model to examine the impact of deformation path on microstructure evolution, DRX fraction and DRX grain size, during the upsetting process of large medium carbon low alloy high strength steel ingot. To achieve this, hot compression tests were performed using the Gleeble 3800 thermomechanical simulator. The flow stress data obtained from these tests were corrected and used to establish both a material model and a microstructure model. These models were then integrated into the Forge® NxT 3.2 finite element simulation software using user routine. The FE predictions were validated by comparing them with experimental results from hot compression test, ensuring accurate predictions of flow stress and recrystallized grain size at the end of hot deformation. After validation, the FE model was scaled up to simulate the industrial upsetting process, enabling an investigation into the effects of deformation path on strain inhomogeneity and microstructure evolution in large forged ingots. An analysis of four die geometries was conducted to identify the optimal die shape for minimizing strain and grain

size inhomogeneity across the ingot. The study found that the convex die caused the least deformation, while the concave die induced the highest deformation values at the ingot's center. Using the coefficient of variation, as a measure of heterogeneity, it was concluded that the v-die and concave die produced a more uniform grain size distribution compared to the flat and convex dies.

The second part of study focused on investigation of the influence of deformation path, illustrated by die geometry, on damage evolution during the cogging of difficult to forge, medium carbon high alloy- high strength AISI H13 steel. Hot compression and tensile tests were performed using Gleeble 3800 thermomechanical simulator to develop the optimum material model which was then implemented in the finite element (FE) code Forge® NxT 3.2 using a developed user subroutine. Normalized Cockcroft and Latham damage criterion and maximum shear stress (Tresca's) theory of failure were used to predict the damage and failure in the center axis of the shaft through FE analysis with three different die shapes: concave, flat, and convex. A comparative study between the three die geometries was conducted to quantify the effects of each of them on the sensitivity to central burst damage. FE model was validated using industrial data. The lowest and highest damage values were found to occur in the case of cogging with concave and flat die, respectively. The coefficient of variation (CoV) was employed as a measure of heterogeneity and it was found that the concave die provided more uniform deformation and most favorable results for the cogging compared to the flat and convex dies. The novel approach, application of concave die was successfully implemented at the industrial scale cogging.

The third and last part of this study focuses on physical and numerical simulations of a multi-step deformation process to investigate how deformation path influences microstructure evolution and the distribution of mechanical properties. Multi-step deformation experiments were conducted on high strength steel specimens using the Gleeble 3800 thermomechanical simulator, equipped with the MaxStrain® attachment. All tests were performed at a strain rate of 0.01 s^{-1} and a temperature of 1150°C, with two different deformation paths considered. A total true strain of 0.84 was achieved over four steps, with approximately 0.21 strain applied in each step. The results were analyzed to examine the effect of varying deformation paths on microstructure evolution and hardness distribution. A finite element (FE) model was created using the Forge® NxT 3.2 FE code to simulate the multi-step deformation process. This FE model was validated against the measured average grain size and hardness distribution following the multi-step deformation experiments. Once validated, the FE model was able to predict strain distribution, dynamic recrystallization (DRX) volume fraction, and grain size evolution during the process. A comparative analysis of results from the two deformation paths was performed to identify the optimal path for achieving a uniform strain and grain size distribution. The Coefficient of Variation (CoV) was used to evaluate the heterogeneity of the hardness distribution. The findings indicated that concave anvils promoted a higher and more uniform strain distribution, which resulted in a more homogeneous grain size and hardness distribution.

Keywords: Microstructure-based FE model, Deformation paths, Microstructure evolution, Large size ingot, Forging, Medium carbon steel, Cogging, Center burst formation, AISI H13, die geometry, Damage evolution, Gleeble 3800 Maxstrain®, Multi-step deformation, FE analysis, Mechanical properties

TABLE OF CONTENTS

Page

LIST OF TABLES

Page

LIST OF FIGURES

Page

LIST OF ABREVIATIONS AND ACRONYMS

3D	Three Dimensions
AISI	American Iron and Steel Institute
ARRE	Average Absolute Relative Error
CAD	Computer-Aided Design
DRV	Dynamic Recovery
DRX	Dynamic Recrystallization
FEM	Finite Element Modelling
FM	Free from Mannesmann Effect
GB	Grain Boundary
HAGB	High Angle Grain Boundary
HS	Hansel-Spittle
JC	Johnson-Cook Hardening Model
JMAK	Johnson-Mehl-Avrami-Kolmogorov
LAGB	Low Angle Grain Boundary
ZA	Zerilli-Armstrong Model
OLS	Optical Laser Scanning Microscope
R	Correlation Coefficient
SFE	Stacking Fault Energy
TC	Thermocouple
WH	Work Hardening

LIST OF SYMBOLS AND UNITS OF MEASURMENT (INTERNATIONAL SYSTEM)

A, A_1, A_2, n, α, n_1, n_2,	Arrhenius equation material constants
B_0-B_6/ C_0-C_6/ D_0-D_6/ E_0-E_6	Constants
A, m_1, m_2 m_3 m_4 m_5 m_6 m_7 m_8 m_9	Parameters of the Hansel-Spittel equation
C_p	Specific heat (J/kg/°K)
D	Grain size (μm)
d_0	Initial grain size (μm)
D_{DRX}	Dynamic recrystallization grain size (μm)
d_g	Growth grain size (μm)
Q	Deformation activation energy (KJ/mol)
t	Time (s)
T_m	Melting point (°C)
T_r	Reference temperature (°C)
T	Temperature (°C)
T_t	Transition temperature (°C)
w	Die width (m)
X_{DRX}	Dynamic recrystallization fraction (%)
Z	Zener-Hollomon parameter
ΔT	Change in temperature (°C)
ε	Strain
ε_f	Strain at fracture
ε_c	Critical strain
$\dot{\varepsilon}$	Strain rate (s^{-1})
$\bar{\varepsilon}$	Equivalent strain
μ	Friction coefficient
ρ	Density (g/m^3)
σ_{max}	Maximum principal stress
$\bar{\sigma}$	Equivalent/Effective stress (MPa)
σ_{wc}	Uncorrected stress (MPa)
σ_c	Critical stress (MPa)
σ_E	Experimental flow stress (MPa)
σ	Flow stress (MPa)
σ_f	Corrected stress (MPa)
$\bar{\sigma}_p$	Average values of predicted flow stress (MPa)
$\int \sigma d\varepsilon$	Area under the uncorrected stress-strain curve

INTRODUCTION

High strength tool steels are essential in the molding and forming industries for manufacturing tools used to shape materials. These steels play a critical role in the production of specialized dies, molds, and rollers, forming a crucial component of the manufacturing industry (Banaszek et al., 2023; Harris, 2016; Tamura & Tajima, 2003). Tool steels are valued for their unique properties, including high wear resistance, high hardness, toughness, durability, and the ability to produce components with high precision. Molding and forming dies, in particular, are designed to withstand high forming loads without failure, while also offering high resistance to thermal softening at higher temperature. This allows them to maintain their shape over extended use, even when in contact with other materials during processes like plastic injection molding and hot deformation (Chadha 2018;Ji et al. 2020). AISI P20 and AISI H13 are two commonly used tool steels, employed in plastic injection molding dies and hot working application dies, respectively. Although these steels have different chemical compositions and applications, they share the fundamental characteristics of tool steels and can be heat treated to enhance their mechanical properties. After the hot deformation specific heat treatments are essential for achieving the hardness and toughness required for their respective applications.
AISI P20, a medium-carbon, low-alloy, high-strength steel, is widely used in manufacturing plastic injection and extrusion molds. This high-strength steel is crucial for mold and die production. The increasing demand for structural components in the automotive industry, such as dashboards, bumpers, and external body parts, has driven a corresponding rise in the need for plastic injection molds and dies (Mha, Dhondapure, Jahazi, & Tongne, 2023). Therefore, it is essential to study the hot deformation behavior of high strength steel.

AISI H13, another medium-carbon, high-alloy steel, is commonly used in hot working dies for processes like hot rolling, extrusion, and forging. Its high wear resistance, toughness, and heat resistance at elevated temperatures make H13 steel ideal for high-temperature applications and environments with significant mechanical stress (Yahui Han, Li, Ren, Qiu, Li, et al., 2021b; Marashi, Yakushina, Xirouchakis, Zante, & Foster, 2017). The balanced properties of

toughness, wear resistance, and machinability contribute to its popularity in the hot working tool industry. The production of these steels begins with melting scrap material in an electric arc furnace, followed by refining and degassing to precisely control the alloy composition. After melting, the process includes ingot casting, solidification, forging, and a final heat treatment to achieve the desired mechanical properties according to client specifications (Dhondapure et al., 2023; Ebacher, Jahazi, Morin, & Ritchey, 2022).

The demand for the components manufactured using the plastic injection molding and heavy forgings has been increasing in heavy industries such as automobile, mining, aerospace etc. results in high demand of plastic injection moldings and hot deformation dies. The manufacturing of large size preform for plastic injection molds and hot deformation dies, begins with steel making followed by ingot casting. The solidification of large size ingots is slow and leads to the formation of casting defects like inhomogeneous microstructure, macro segregation, cavities, voids, inclusions etc. (Ghodrati et al., 2022; C. Zhang, Shahriari, Loucif, Melkonyan, & Jahazi, 2018; Chunping Zhang, Loucif, Tremblay, & Jahazi, 2019). These defects significantly affect the mechanical properties of the final products. These casting defects present must be ideally eliminated or at least reduced to a permissible limit during the subsequent forging and heat treatment process. Forging is one of the most critical process which eliminates casting defects and produce wrought microstructure. The primary aim of forging is to obtain the required shape with the desired microstructural attributes. Some of the crucial thermomechanical parameters include the forging temperature, holding time in the furnace, deformation percentage, deformation rate in each step (Jonšta, Kurka, Vindyš, & Kander, 2021; Wang, Xue, & Zhao, 2018a). These parameters must be controlled to obtain a suitable microstructure and homogeneous mechanical properties through the thickness of the forged component. For the higher productivity and efficiency of forging process, forged products need to be produced with excellent and homogenous mechanical properties through the thickness of the large size forged components. In addition, it should have higher wear resistance and toughness for longer durability. However, the manufacturing of heavy and large size forged products with excellent and homogenous mechanical properties is challenging due to many factors plays a crucial role on it, such as deformation gradient, temperature gradient,

strain rate gradient present during the forging and these gradient values increases as the size of ingot increases. Therefore, it is very important to improve or eliminate these gradients to the possible extent to produce large size forging with homogenous mechanical properties (Dhondapure, Rajakrishnan, Nayak, & Champliaud, 2024; Dourandish, Champliaud, Morin, & Jahazi, 2024).

In addition to the thermomechanical parameter machine characteristics such as, press capacity, ingot geometry, die geometry affects the forging quality of large ingots. In this project die geometry considered for the study and different deformation paths were achieved by varying the die curvatures. The deformation path is an important factor, that mainly depends on equipment specification like dies geometry (flat, V-shape, concave, convex). The deformation path impacts material flow, deformation distribution, microstructure evolution and ultimately the final mechanical properties of the alloy. It is needed to study in detail, the influence of deformation path on microstructure and damage evolution during the open die forging (Upsetting and cogging) of large size ingot. A critical step in designing optimum open die forging processes for industry requires a good understanding of the interaction between process and geometrical parameters and their impact on microstructure and damage evolution (Christiansen, Hattel, Bay, & Martins, 2014; Dudra & Im, 1990; Marcin Kukuryk, 2020, 2021; X. Zhang, Ma, Ma, & Li, 2012). In this study different deformation paths were selected for the study illustrated by different die geometry: Flat, V-shape, Concave and Convex die. Therefore, in this research die geometry considered for comprehensive analysis of microstructure and damage evolution during the open die forging using finite element analysis and experimental approach.

During the forging of metals, as cast structure breaks in to the wrought structure, which has predefined orientated microstructure and homogenous mechanical properties compared to the as cast structure. During the hot forging of steels, hardening and softening phenomena occurs these are known as work hardening (WH) and dynamic softening. Dynamic softening process mainly dominated by dynamic recovery (DRV) and dynamic recrystallization (DRX) (K. Chadha, Shahriari, Tremblay, Bhattacharjee, & Jahazi, 2017). These phenomena play a main

role in the microstructure evolution such as grain refinement, formation of new grains and grain growth. The important factors effects on WH, DRV and DRX are the temperature, strain, strain rate and deformation path. In recent years, many studies have been reported on the development of physical and empirical models to predict the material behavior and microstructure evolution of different alloys during the hot deformation (Cojocaru et al., 2021; W. Li, Liang, & Zhang, 2022; Wang, Xue, & Zhao, 2018b). In most of the reported study using different die geometries were on void closure and most of the authors ignored the effect of different die geometry or deformation path on microstructure and damage evolution during the hot deformation of the metallic materials (Ahmadi, Dehghan, & Ranjbar, 2025; Christiansen, Hattel, et al., 2014; Dudra & Im, 1990; Marcin Kukuryk, 2019, 2024; X. X. Zhang, Cui, Chen, & Li, 2009). This study focuses on generating comprehensive data on the effect of deformation path on microstructure and damage evolution during the open die forging of tool steels by application of FE analysis and physical simulations. The most efficient method to improve the productivity and quality of the final forged products can be achieved through the Finite Element (FE) modeling and numerical simulation of hot deformation process which predicts the microstructure, damage evolution and material behavior during the process. Constitutive and microstructure modeling has been used to predict the material behavior and microstructure evolution during the hot deformation.

There are very limited studies available on the influence of deformation path on microstructure and damage evolution during the forging of industrial size ingot of high strength steel. This study focuses on development of optimum material model and microstructure model to predict the grain size evolution during the open die forging of modified AISI P20 steel. Developed models were integrated in to the Forge® NxT 3.2 FE analysis code and simulated the open die forging process for large size ingot employing different deformation paths, illustrated by four die geometries. In addition, present research which focuses on development of optimum material model and calculation of critical damage value for the forging temperature range for AISI H13 steel. Implementation of selected optimum material model into the finite element (FE) code to simulate the industrial open die forging process to study effect of different deformation paths. FE analysis of industrial cogging process was done to study the influence

of different deformation paths on damage evolution and stress states present during the cogging process. Due to the importance of open die forging in the manufacturing of the heavy components, this project begins with FE analysis large size ingot upsetting and cogging process using different die geometry. In the last step of this study, physical simulation of multi-step deformation process was done and finding reported from the FE analysis was confirmed with measured grain size and mechanical properties. To determine the optimal deformation paths, a heterogeneity study was conducted using the Coefficient of Variation (CoV) as a heterogeneity index on both experimental and simulation results. The CoV, calculated using standard deviation and mean values, allows for the comparison of two different parameters with a single numerical value (Johnson, Richard A., Irwin Miller, 2018; Nayak, Kumar Singh, Gokhale, Prasad, & Narasimhan, 2023). This Ph.D. thesis outlines the context and discusses the gaps identified in the publicly available literature on this subject. In addition, the optimal deformation path obtained in this study will be implemented at the industrial scale for forging large-size ingots. The work is described in the following five chapters.

Chapter 1 provides a comprehensive literature review on the impact of various thermomechanical process parameters on microstructure and damage evolution during conventional forging. The softening mechanisms that occur during hot deformation are explained in detail. This chapter also covers constitutive equations used to predict material behavior at high temperatures, along with related microstructure evolution models. Furthermore, it discusses the numerical implementation of these models and provides an overview of research in the field of high-temperature forging process simulations. Subsequently, the chapter examines the influence of deformation path on void closure during open die forging of large ingots. Finally, the gaps identified in the open literature are presented in the last section of this chapter. Based on these gaps, the objectives of the present research are proposed.

Chapter 2 outlines the experimental and finite element (FE) analysis methodology used in this project. It provides a detailed, step-by-step description of the industrial and experimental measurement procedures. The equipment and software used for the experimental tests are

thoroughly described. The final section of this chapter describes the finite element tool used and the boundary conditions applied in the simulations.

Chapter 3 focuses on the development of material and microstructure models to predict the flow stress and grain size of modified AISI P20 steel under various deformation conditions. The material and microstructure models developed in this study were validated against the experimental measurements. Both models were then implemented into the FE analysis tool via user subroutines to investigate the influence of deformation paths on microstructure evolution during the upsetting of a large ingot. A comparative analysis of four die geometries was conducted to determine the optimal die shape and deformation path for the industrial upsetting process. Finally, a heterogeneity analysis of equivalent strain and average grain size was performed to verify the effectiveness of the identified optimal deformation paths.

Chapter 4 details the development and selection of an optimal material model, as well as the calculation of critical damage values for AISI H13 steel across the forging temperature range. An FE model was developed and validated using industrial data to simulate the industrial cogging process. This validated FE model was then used to study the influence of deformation paths on damage and stress state evolution during the cogging of AISI H13 steel. A comparative analysis of three die geometries: flat, concave, and convex was conducted to propose the optimal die geometry for the industrial cogging process of AISI H13 steel.

Chapter 5 presents the physical and numerical simulation of a multi-step hot deformation process, examining the effect of deformation paths on microstructure evolution and the mechanical properties of the deformed material. This analysis considered two die geometries: flat and concave. Detailed microstructure characterization and heterogeneity study on hardness values revealed that the concave die is superior to the flat die for multi-step deformation. These findings are consistent with the results presented in Chapters 3 and 4.

Conclusions are presented at the end of the thesis. From this work, two journal papers were published in The International Journal of Advanced Manufacturing Technology and the

Journal of Materials Research and Technology, while a third has been submitted to the Journal of Manufacturing Processes. This work was also presented at two international conferences organized by the Forging Industry Association (FIA). The results of this research were implemented at an industrial scale, contributing to improved forge quality by eliminating central burst formation during the forging of sensitive materials such as AISI H13. Additionally, it enhanced the overall efficiency of the manufacturing process.

CHAPTER 1

LITERATURE REVIEW

1.1 Metal forming

Metal forming refers to a broad category of manufacturing processes in which a workpiece or preform is reshaped into a desired final product through the application of force. This transformation occurs without altering the material's mass or composition and often results in improved mechanical properties. Metal forming processes are widely used to produce products ranging from small components to large structures. The field encompasses a variety of processes, each tailored to specific materials, shapes, and production volumes. These processes are typically classified into two main categories: bulk forming, which includes methods such as forging, rolling, and extrusion, and sheet forming, which includes techniques such as stamping and bending (Altan & Ngaile, 2005; Christiansen, Hattel, Bay, & Martins, 2013; Dieter, Kuhn, & Semiatin, 2003; S.-I. Oh, Walters, & Wu, 2018).

1.2 Bulk metal forming

Bulk metal forming processes involve the plastic deformation of a material into a permanent shape by applying compressive forces, it is generally used to create large solid parts. These processes are categorized based on the temperature at which they are performed. Metal forming processes can be classified into three types: cold forming, warm forming, and hot forming. Cold forming refers to processes conducted at room temperature and temperature at which no microstructural evolution occurs. Warm forming is carried out at temperatures between room temperature and the material’s recrystallization temperature, while hot forming takes place at temperatures above the recrystallization temperature. The majority of bulk metal forming processes are carried out at elevated temperatures, commonly referred to as hot working (Dieter et al., 2003). As the temperature of the material increases, its workability improves.

Bulk metal forming processes are typically characterized by significant deformation, which leads to substantial changes in both the shape and mechanical properties of the product. These processes also offer high material utilization efficiency, with minimal material loss from oxide layer and scale formation during operation. Common examples of bulk metal forming processes include forging, rolling, extrusion, and drawing (Altan & Ngaile, 2005). Forging process is important manufacturing process, which produces components with improved mechanical properties due to the microstructure refinements and by eliminating defects. This process widely used in the growing industries like defense, automotive and aerospace, where consistency and strengths are important factors.

1.2.1 Forging

Forging is one of the oldest known metalworking processes, since last thousands of years still it is used as fundamental forming technique in modern manufacturing industries. Forging is the most used metal forming process in today's industries to produce the complex shape products with good mechanical properties. During the forging process, material is shaped by the application of compressive force using mechanical or hydraulic press die, the process changes the material shape and improves the mechanical properties making it stronger and more durable. Forging is classified in to different types depending on the temperature and method of deformation. Depending on the temperature forging process is divided in to the three types: cold, warm and hot forging. In forging process material is shaped above the recrystallization temperature and above the recrystallization temperature material is more ductile and softer, so during hot forging material can be easily shaped into the required shape with improved mechanical properties with minimal risk of cracking. Hot forging is used in the automobile, aerospace, energy and structural industry to produce the complex parts. There are several advantages of hot forging including increasing ductility, less energy required to work with material, eliminate the casting defects such as segregation, porosity and voids (Uddagiri, Spee, Hubig, & Steinbach, 2020). Initial setup cost for the hot forging line is higher than the cold forging because heat treatment required before and after the forging process. Figure 1.1 shows the effect of deformation temperature on the workability of as-cast and wrought metals,

the melting point is denoted as MPc (as-cast metals) and MPw (wrought metals). Absolute temperature refers to the temperature measured in Kelvin scale (K). Forging of as cast material is performed at 75% of its melting temperature to increase the workability and reduce the forging load. As represented in Figure 1.1 workability of as cast material in higher during the hot working process compared to the cold and warm working. Forging is primarily classified into two types based on the deformation method: open die forging and closed die forging. In open die forging, the workpiece is compressed between the upper and lower dies, allowing the material to flow freely in the radial direction. In contrast, closed die forging involves compressing the material within the dies, restricting its flow and forcing it to conform to the shape of the die cavity. Open die forging is an important production process in the large scale industries due to the its capability to produce complex, large size parts and high strength products.

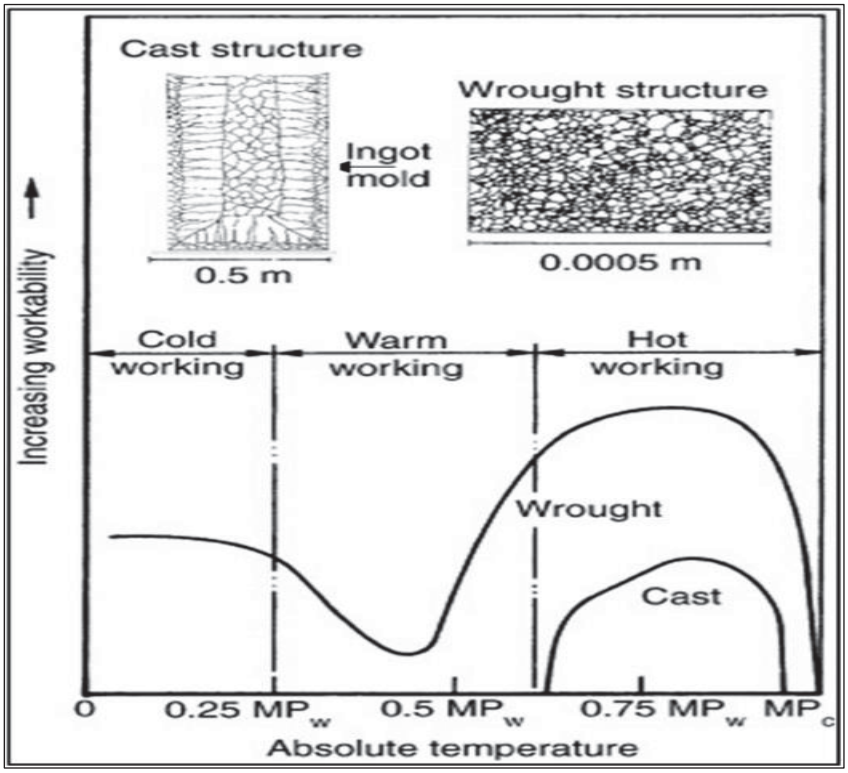

Figure 1.1 Schematic of increasing workability of as cast and wrought material with the increasing the absolute temperature (K) Taken from Dieter et al. (2003)

1.2.2 Open die forging

During the open die forging, the high temperature ingot is squeezed between the upper and lower dies. The aims of the open die forging process are to break the as cast structure in to the wrought microstructure, eliminate the casting defect as possible extent, and reshape the ingot to required approximate dimensions. The open die forging generally used to produce or manufacture the simple products with large size and heavy weight such as simple shafts, stepped shafts, cylindrical blocks, rectangular slabs and preform for the different process etc. This process also called as the ingot breakdown process and this process usually performed at higher temperature in stable austenite phase (Dieter et al., 2003). Before the ingot breakdown process, ingot is heated to the 1200-1260 °C in the forging furnace and held around 24hrs at

this temperature before transferring the ingot to the forging press. Afterwards ingot is transferred to the forging press to perform the upsetting and cogging process with incremental deformation to achieve the final required dimension and shape (Harris, Shahriari, & Jahazi, 2017). During the open die forging process, various microstructural phenomena occur such as Work Hardening (WH), Dynamic Recovery (DRV), Dynamic Recrystallization (DRX). To achieve the final shape ingot is deformed in multiple steps with help of manipulators. Figure 1.2 shows the schematic of open die forging with the upper and lower die, workpiece is supported by the manipulator arm.

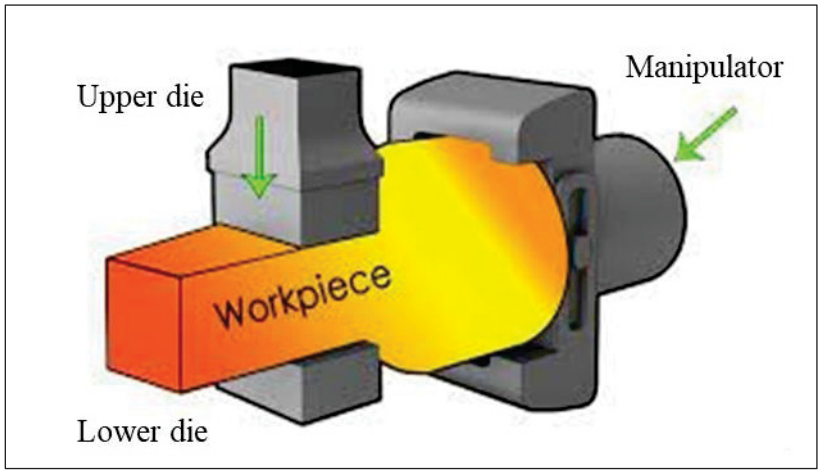

Figure 1.2 Schematic of open die forging process
Taken from Alloys International, INC (2024)

1.2.3 Closed die (Impression die) forging

Figure 1.3 shows the schematic of the closed die forging process. During this process hot metal or preform is placed in between the upper and lower dies, as shown in Figure 1.3a, afterward both dies move forward and hot metal takes shape or impression of the cavity between two dies, as shown in Figure 1.3b. Closed die forging used to manufacture the components with more precision compared to the open die forging (Altan & Ngaile, 2005). Therefore, this process is used to manufacture the automobile and aerospace part, gears etc.

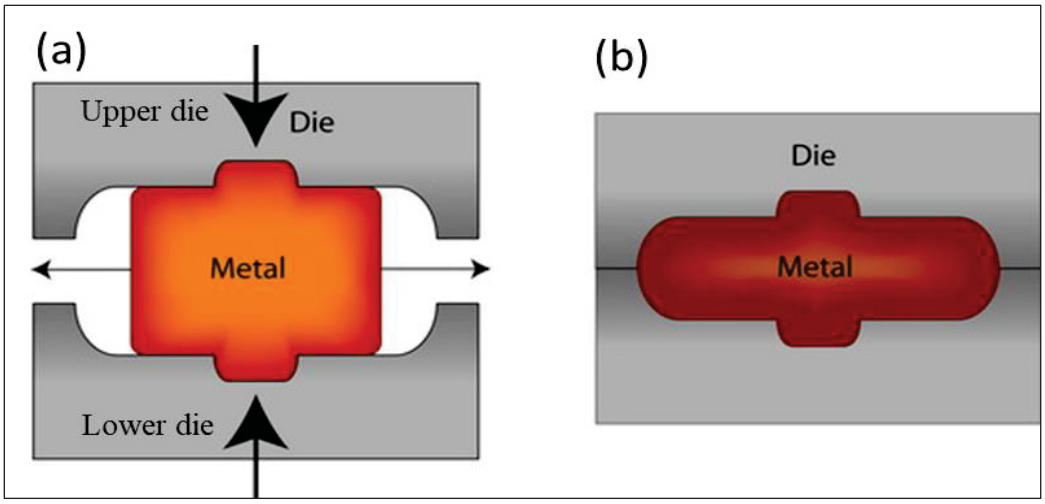

Figure 1.3 Schematic of closed die forging (a) Beginning and
(b) End of closed die forging
Taken from University of Cambridge (2004)

1.2.4 Challenges during the open die forging process

Some challenges present during the open die forging process include:

Deformation gradient: In open die forging, a deformation gradient exists within the ingot, varying from both ends to the center and from the surface to the core. This gradient, which develops during hot deformation, is primarily attributed to the friction between the ingot's surface and the upper and lower dies. Deformation is most pronounced at the center of the ingot, gradually decreasing towards the surface and the top and bottom regions. This significant variation in deformation influences microstructure evolution and, subsequently, the mechanical properties of the forged ingot. Therefore, minimizing or reducing the deformation gradient is essential to improve the quality of the final forged product (Dourandish, Champliaud, Morin, & Jahazi, 2022; B. Tang, Cheng, Kou, & Li, 2015).

Unacceptable grain size: As mentioned above, during the open die forging process deformation gradient influence and which impacts the microstructure evolution, leading to an inhomogeneous grain size distribution from the center to the surface of the forged component.

At the center of the forged ingot, large size grains, in the range of 400 to 500 μm, can be present at the completion of the forging process. This grain size is unacceptable and results in the rejection of these ingots during quality control procedures, consequently reducing the productivity and efficiency of the forging process. Therefore, it is crucial to minimize deformation gradient to the greatest extent possible to enhance overall process efficiency and the quality of the final product (Chamanfar, Chentouf, Jahazi, & Lapierre-Boire, 2020a).

During the hot deformation process, three key microstructural phenomena occur: Work Hardening (WH), Dynamic Recovery (DRV), and Dynamic Recrystallization (DRX). DRV and DRX are considered softening processes. These phenomena are influenced by thermomechanical parameters such as temperature, strain rate, initial grain size and deformation conditions. Therefore, it is essential to examine these phenomena and the factors affecting them. The following section provides a detailed explanation of each phenomenon.

1.3 Phenomena occurs during hot deformation

During hot deformation, both hardening and softening phenomena occur. The hardening process is referred to as work hardening, while the softening processes are known as dynamic recovery and dynamic recrystallization. The flow curves obtained from hot deformation experiments can help distinguish between these phenomena, as illustrated in Figure 1.4. Work hardening typically occurs at the initial stages of the hot deformation process, before reaching peak stress, and is most prominent at lower temperatures and higher strain rates, where the material does not have enough time or energy for dislocation annihilation. In conditions where both WH and DRV are active, the flow curve stabilizes as strain increases, indicating a balance between dislocation generation and recovery. DRX, in contrast, is characterized by softening and the eventual stabilization of the flow curve as strain increases. This happens at higher temperatures and lower strain rates, where there is enough time for dislocation annihilation, nucleation, and grain growth (John J. Jonas, Quelennec, Jiang, & Martin, 2009; Yan, Yu, & Zhao, 2013).

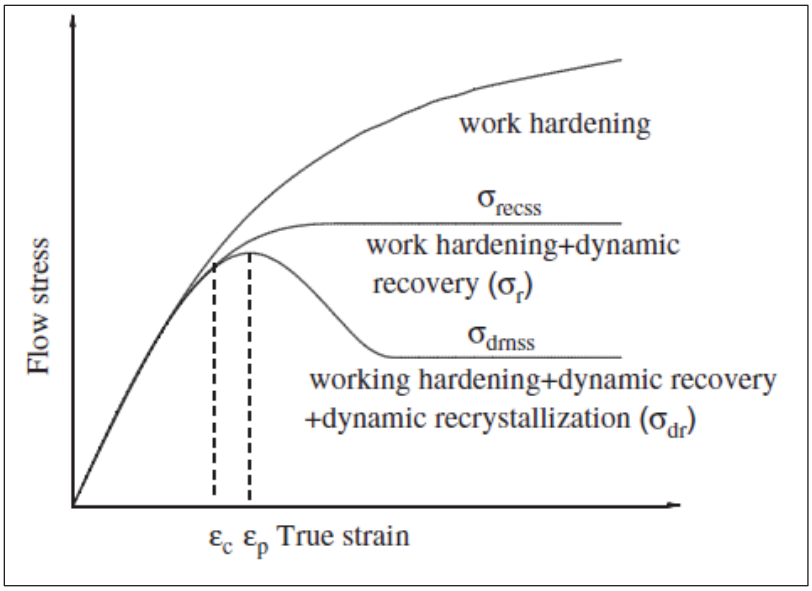

Figure 1.4 Typical flow stress curves during the hot deformation shows three metallurgical phenomena
Taken from Yan, Yu, & Zhao (2013)

1.3.1 Work Hardening (WH)

This phenomenon, also known as strain hardening, is related to an increase in the hardness and strength of a material during plastic deformation due to the accumulation of dislocations. When the material is subjected to an externally applied force, dislocations form and accumulate. Work hardening occurs during the initial stage of the hot deformation process, as shown in Figure 1.4. During hot deformation, plastic deformation is accommodated by the movement of dislocations. As the material is strained, dislocations multiply and interact with one another, leading to dislocation tangling, pinning, and pile-up, which impede further dislocation motion. This increased resistance to dislocation movement results in material hardening. Work hardening increases the resistance to material flow, meaning that more force is required to continue the deformation, thereby increasing the material strength and hardness. At lower temperatures, dislocation mobility is reduced, leading to a greater accumulation of dislocations and more pronounced work hardening. Similarly, at higher strain rates, the deformation occurs more rapidly, limiting the time available for dislocation annihilation via recovery mechanisms.

Therefore, at lower temperatures and higher strain rates, the material experiences significant work hardening (El-Danaf, Kalidindi, & Doherty, 2001; Humphreys & Matherly, 2004; Petryk, Stupkiewicz, & Kuziak, 2008).

1.3.2 Dynamic Recovery (DRV)

This is softening phenomena present during the hot deformation. During plastic deformation, the processes of dislocation formation and annihilation occur simultaneously called as DRV. Recovery, a phenomenon observed in plastically deformed materials, partially restores properties lost during deformation. The stages of recovery are illustrated in Figure 1.5. Recovery primarily results from the rearrangement of dislocations, which leads to the formation of dislocation tangles, as shown in Figure 1.5a. These dislocation tangles then evolve into dislocation cells, as depicted in Figure 1.5b. In materials with high stacking fault energy, these processes can occur concurrently. During recovery, dislocations within the cells are annihilated, leading to the formation of new subgrains. In the later stages, these subgrains continue to grow, resulting in a decrease in internal energy Figure 1.5c-e (Humphreys & Matherly, 2004; Pinheiro, Monteiro, Barbosa, & Cetlin, 2004).

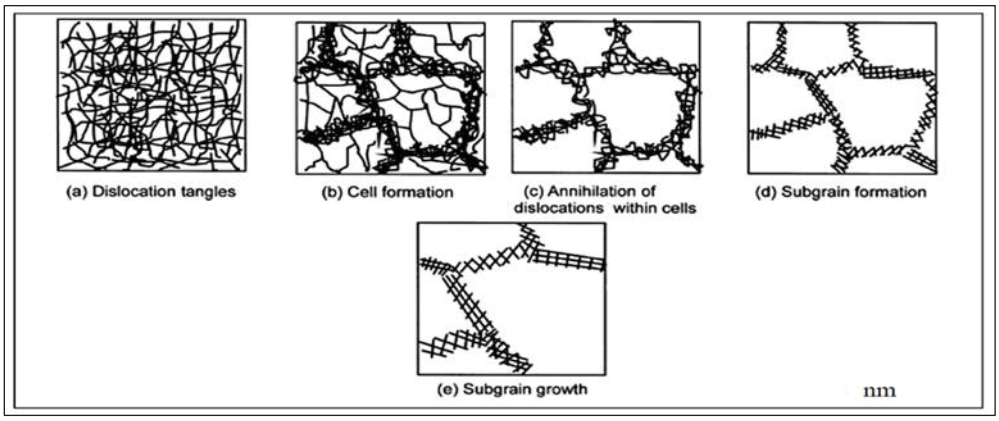

Figure 1.5 Schematic shows the stages present during dynamic recovery of plastically deformed material
Taken from Humphreys & Matherly (2004)

1.3.3 Dynamic Recrystallisation (DRX)

This is a softening phenomenon present during the hot deformation of low staking fault energy materials. DRX starts at high angle grain boundaries and grain boundary bulging is the first step of DRX initiation. During DRX, strain-free new grains nucleate and grow, consuming the plastically deformed matrix. DRX initiates at prior grain boundaries and within the grain interior along dislocation bands, as shown in Figure 1.6. During the hot deformation of the steel prior austenite grain size plays important role on DRX initiation and final microstructure of the steel. As the prior austenite grain size increases its delay in the DRX initiation because of the low fraction of grain boundary area available which act as a nucleation site for DRX and vice versa. Therefore, it increases peak strain and peak stress at given deformation temperature and strain rate. The effect of prior austenite grain size, large and small, on the DRX with the same deformation conditions was studied. It observed in case of initial large grain size DRX process delay compared to the small grain size as shown in Figure 1.7. And, with large size grain, higher strain and temperature requires to initiate the DRX process and grain size effect was observed on the flow stress as shown in Figure 1.8 (El Wahabi, Gavard, Montheillet, Cabrera, & Prado, 2005). DRX classified into two types: continuous DRX and discontinuous DRX. In continuous DRX, homogeneous growth of deformed subgrains occurs, which is promoted by an initial small grain size and a high degree of deformation. In contrast, discontinuous DRX involves inhomogeneous growth of deformed subgrains, typically occurring with an initial coarse grain size and lower degrees of deformation (Humphreys, Frederick John, 2012; Humphreys & Hatherly, 2004; Humphreys & Matherly, 2004).

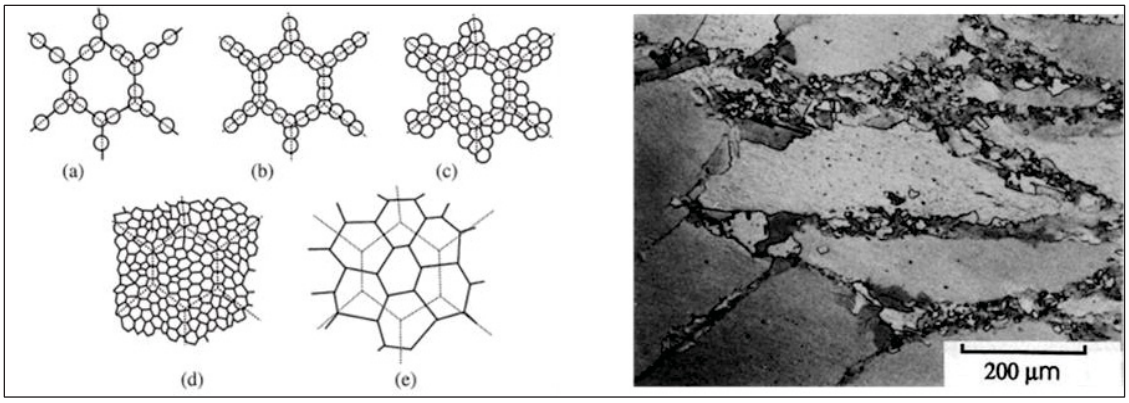

Figure 1.6 Schematic shows the steps present during the dynamic recrystallisation and micrograph shows DRX initiation at prior grain boundaries
Taken from Humphreys & Matherly (2004)

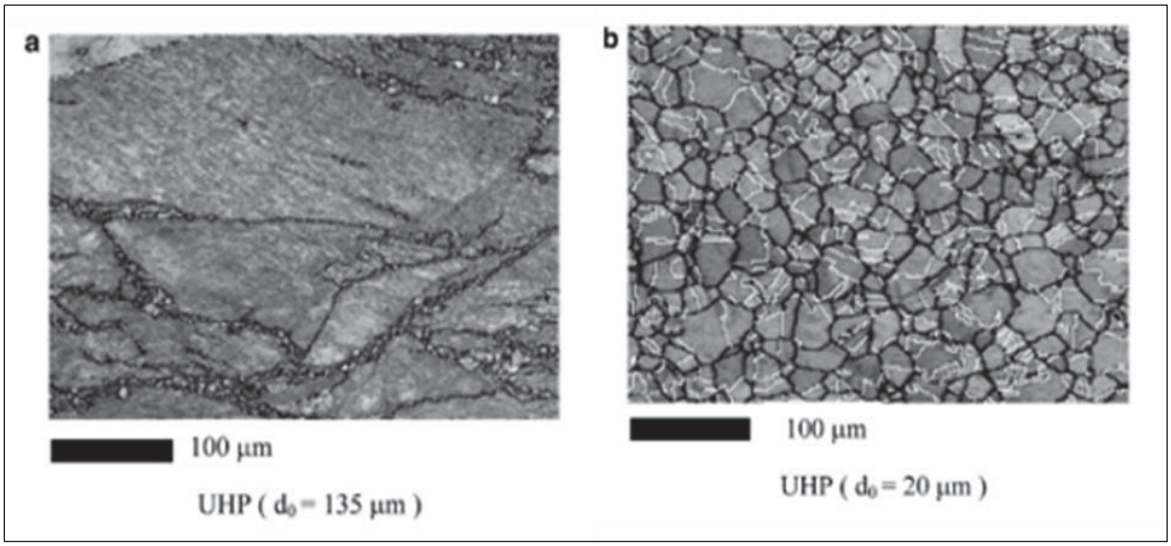

Figure 1.7 Effect of austenite initial grain size at 1% deformation strain, temperature 850ºC, strain rate $0.001s^{-1}$ (a) large grain size (b) small grain size
Taken from Wahabi et al. (2005)

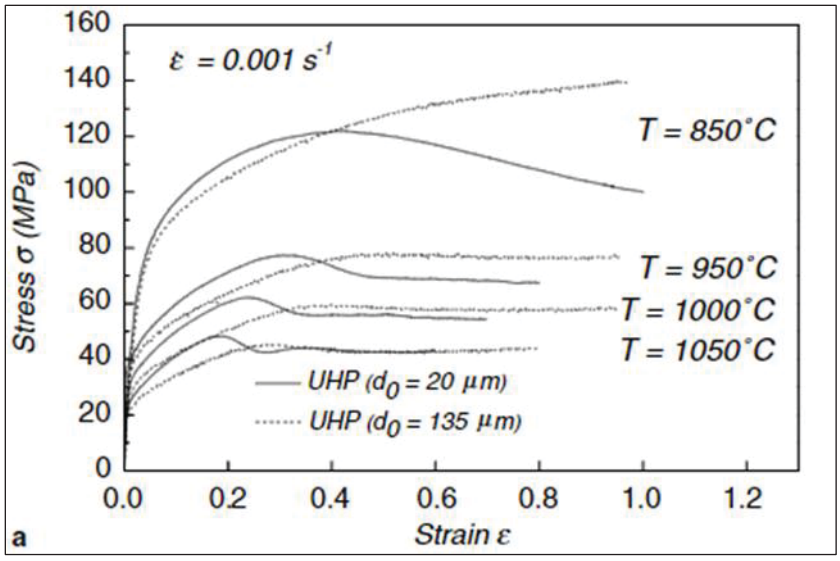

Figure 1.8 Flow curve for austenite stainless steel with two different initials grain size
Taken from Wahabi et al. (2005)

In addition to the initial grain size, thermomechanical parameters play crucial role during DRX phenomena. Therefore, it is important to discuss effect of strain rate, temperature and strain on the DRX. Effect of these parameters was discussed in the following section.

1.4 Effect of Thermomechanical Parameters on DRX

During the hot deformation temperature, strain rate, strain and Prior Austenite Grain Sizes (PAGS) are the key parameters, which affects the material behavior at high temperature. Therefore, temperature and strain rate are considered in the development of constitutive equations for complex problems (Altan & Ngaile, 2005). The combined effect of strain rate and temperature is considered using the Zener–Hollomon parameter using Equation 1.1. The flow stress as a function of the Zener–Hollomon parameter and strain is given in Equation 1.2.

$$Z = \dot{\varepsilon} \exp(Q/RT) \quad (1.1)$$

Where Z is the Zener-Hollomon parameter, $\dot{\varepsilon}$ is strain rate, T is deformation temperature, Q_{def} is the activation energy of hot deformation and R universal gas constant (8.318 J/mole. K).

$$\text{Flow stress} = f(Z, \varepsilon) \tag{1.2}$$

1.4.1 Effect of strain rate

During high temperature deformation, flow curves are highly sensitive to strain rate and selection of appropriate strain rate and temperature is crucial. Figure 1.9 illustrates the flow curve behavior at different strain rates at a constant temperature of 1050°C for a medium carbon steel (Saadatkia, Mirzadeh, & Cabrera, 2015). Authors studied the behavior of the flow curve at low, high and intermediate strain rates, revealing multiple peaks, single peaks, and cyclic phenomena respectively. At a low strain rate of 0.001 s^{-1}, the flow curve exhibits multiple peaks and a plateau (cyclic behavior) before reaching a steady state. This behavior is attributed to the simultaneous occurrence of several independent cycles of DRX, also known as discontinuous DRX. At a higher strain rate of 0.1 s^{-1}, continuous recrystallization leads to softening and a steady-state flow curve, even at the same temperature of 1050°C. At a moderate strain rate of 0.003 s^{-1}, the flow curve transitions between single and cyclic behaviors, a phenomenon referred to as the Multiple Transient Steady State (MTSS). Similar phenomena have also been observed in stainless steel and are reported in the literature (Mirzadeh & Najafizadeh, 2013; Mirzadeh, Najafizadeh, & Moazeny, 2009).

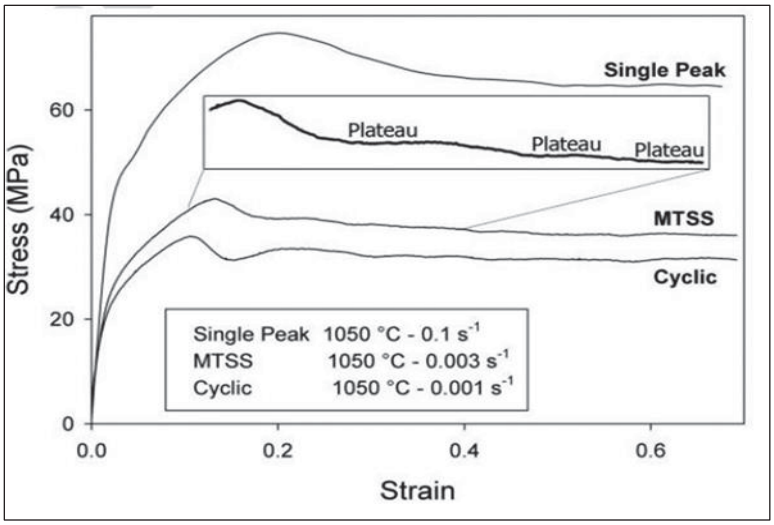

Figure 1.9 Flow curve behavior at different strain rates at a constant temperature for medium carbon steel
Taken from Saadatkia et al. (2015)

1.4.2 Effect of deformation temperature

Figure 1.10 illustrates the dependence of flow curve behavior on temperature at constant strain rates. At a deformation temperature of 900°C, higher peak strains and peak stresses are observed compared to 1200°C, irrespective of strain rates. As strain rate increases at a constant temperature, both peak strain and peak stress also increase. At higher strain rates, the time available for dislocation mobility and annihilation decreases, which delays the initiation of DRX. Conversely, as temperature increases, both peak strain and peak stress decrease. At higher temperatures, dislocation annihilation and movement are enhanced, promoting earlier DRX initiation at lower strains (Ying Han et al., 2015).

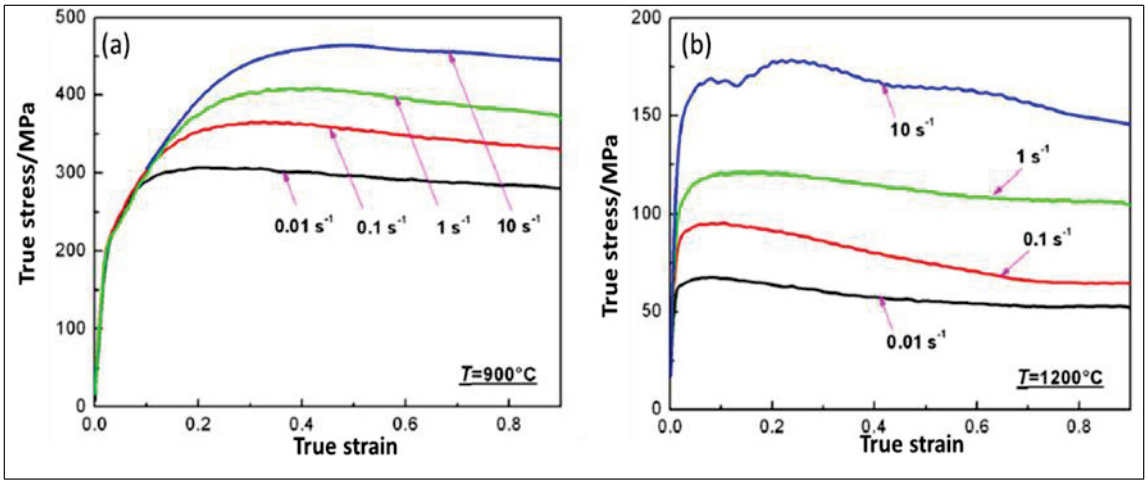

Figure 1.10 Flow curves variation with different temperature (a) 900 °C (b) 1200 °C
Taken from Han et al. (2015)

1.4.3 Effect of strain

Figure 1.11 illustrates the effect of strain level on DRX in as-cast austenitic steel, analyzed using a metallographic approach (Ying Han, Liu, Zou, Liu, & Qiao, 2013). At a lower strain of 0.16, new grains are nucleated at the boundaries of deformed grains, with some dislocation bands observed inside the grains, as indicated by small arrows in Figure 1.11b. As the strain increases to 0.36, a significant amount of DRX grains appear at the initial grain boundaries, forming a necklace structure as shown in Figure 1.11c. Additionally, the dislocation density increases along the previous grain boundaries. With further increasing deformation to the maximum strain of 0.8, the DRX volume increases progressively. A large number of new grains are observed at the previous grain boundaries and within the grains, nucleating along the dislocation bands formed at lower strains as shown in Figure 1.11d. This suggests that additional strain is required to achieve complete DRX under these conditions. In hot deformation at a constant temperature and strain rate, sufficient strain is necessary to obtain a fully recrystallized structure.

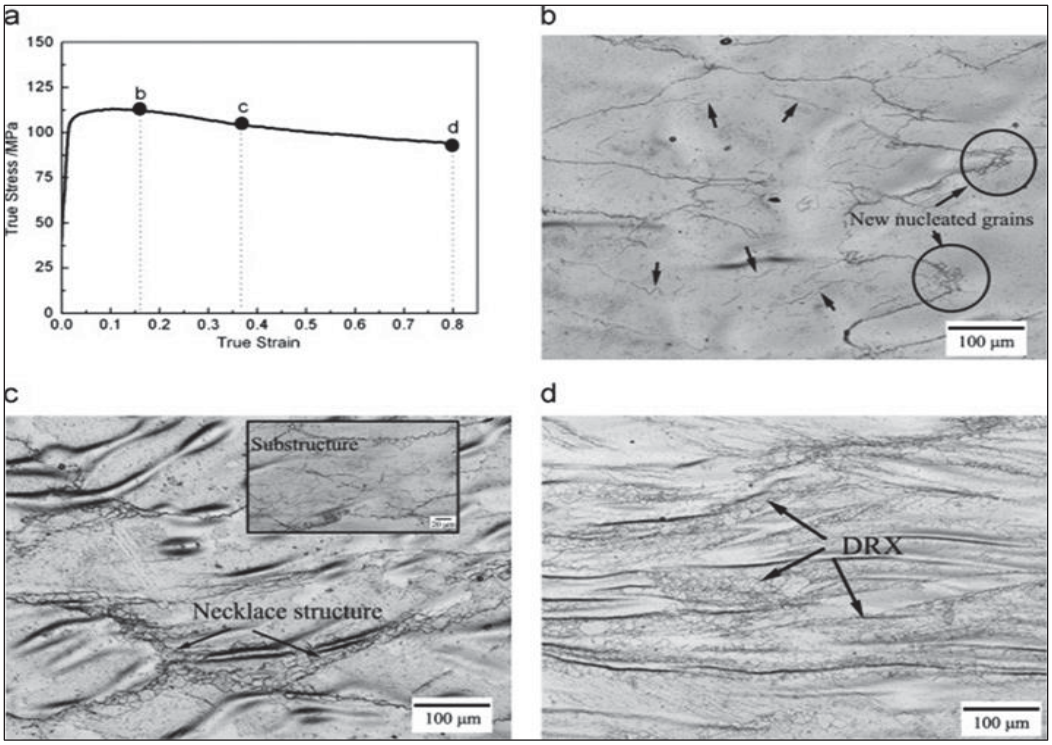

Figure 1.11 Dependence of DRX on deformation degree, (a) flow cure obtained at 1100 °C, $0.1s^{-1}$ and microstructure at different strain level (b) 0.16 (c) 0.36 and (d) 0.8 Taken from Han et al. (2013)

1.4.4 Effect of Initial Grain size

DRX behavior of medium carbon steel is not only sensitive to temperature, strain rate, and strain but also to the initial austenite grain size. The effect of initial austenite grain size on the kinetics of DRX has been studied using 42CrMo steel (M. S. Chen, Lin, & Ma, 2012). Different heating and cooling cycles were employed to produce varying initial grain sizes. The study was divided into two groups, Group 1 and Group 2, as shown in Figure 1.12. In Group 1, the specimens were directly heated to the respective deformation temperatures and held for 5 minutes to ensure uniform temperature and homogenous austenite grain size. In Group 2, the specimens were heated to 1200 °C, held for 5 minutes, and then cooled to the respective deformation temperatures. As the austenitization temperature increases, the initial austenite grain size also increases. The measured average grain sizes were reported as 155, 104, 54, 31.8,

and 15.5 micrometers for specimens heated to temperatures of 1200 °C, 1150 °C, 1050 °C, 950 °C, and 850 °C, respectively.

It was observed that peak strain is sensitive to initial grain size, temperature, and strain rate. The peak strain decreases as the initial austenite grain size decreases. With finer austenitic grain sizes, DRX occurs at an earlier stage compared to coarser grain sizes. In the case of finer grains, there is a greater amount of grain boundary area, which promotes dislocation movement and provides more nucleation sites for DRX.

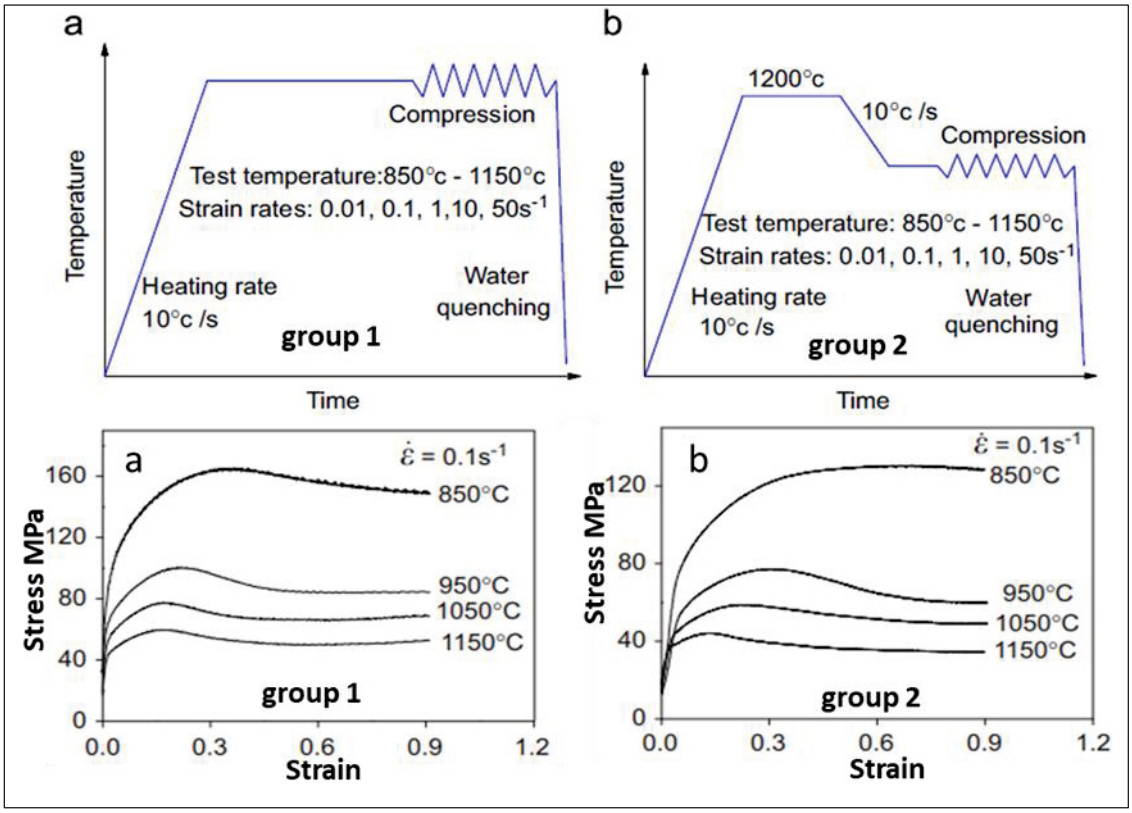

Figure 1.12 Effect of a different initial grain size on hot deformation at constant strain rate (a) group1 (b) group 2
Taken from Chen et al. (2012)

The following section presents a literature review on constitutive and microstructure modeling, damage evolution, and the influence of deformation paths on material flow and void closure

during hot deformation. In the final part of the chapter, gaps in the existing literature are identified and discussed. To address these gaps, the objectives of this thesis are proposed.

1.5 Constitutive and microstructure modeling for hot deformation

1.5.1 Constitutive equations

During hot deformation, materials exhibit varying flow stress behaviors, influenced by factors such as strain, strain rate, and deformation temperature. These factors significantly affect both hardening and softening mechanisms. In addition to thermomechanical parameters, flow stress is also dependent on physical parameters. During hot deformation, phenomena such as WH, DRV, and DRX occur. Therefore, a comprehensive understanding of material flow behavior, along with the associated metallurgical phenomena like DRV and DRX, is essential for optimizing hot deformation processes. A constitutive equation is a mathematical expression that defines the relationship between thermomechanical parameters and physical quantities, typically used to describe the plastic flow behavior of materials. These equations can be implemented as material models through user subroutines in analysis software, such as Abaqus, Deform, and Forge, to simulate material behavior during hot deformation processes. The primary goal is to develop a reliable constitutive equation that accurately predicts material flow behavior. Figure 1.13 displays the typical flow stress curves for the medium carbon steel under the different deformation conditions, temperatures 1050-1250°C and strain rates 0.001-1s^{-1}. It observed that flow curves are strain rate and temperature dependent. Therefore, it is important to develop the precise material model which predict complex flow stress behavior during the hot deformation such as WH, DRV and DRX (Ebrahimi, Momeni, Kazemi, & Alinejad, 2017; Mha et al., 2023; Wei, Liu, Xiao, & Zhang, 2013). Different constitutive models are discussed in the following section:

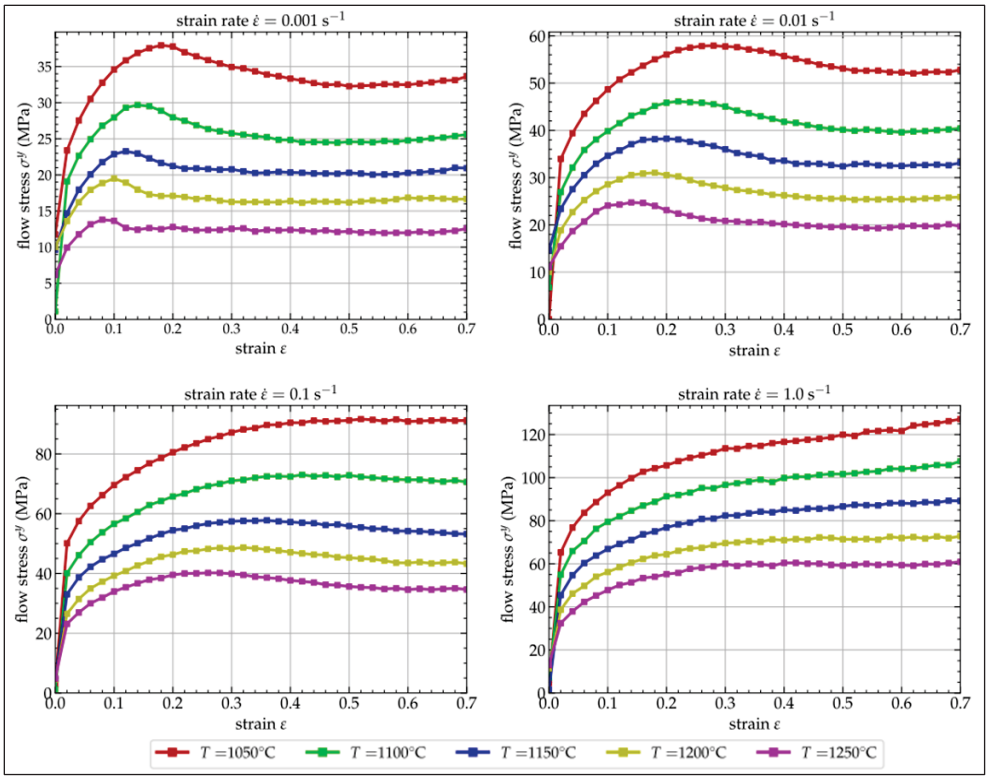

Figure 1.13 Flow stress curves for the medium carbon steel under the different temperature and strain rate conditions
Taken from Mha et al. (2023)

1.5.2 Arrhenius Constitutive model

The Arrhenius model, also known as the hyperbolic sine equation, is a constitutive model that establishes the relationship between strain rate, temperature, and flow stress using the hyperbolic law. The following expressions describe the relationship between material constants and flow stress under varying deformation conditions (Ahmed et al., 2020; Dourandish et al., 2022; Mha et al., 2023; Mochugovskiy, Kaplanskaya, Mosleh, Palacheva, & Mikhaylovskaya, 2023).

$$\dot{\varepsilon} = A_1 + \sigma^{n_1} \exp\left(\frac{Q}{RT}\right), \qquad \alpha\sigma < 0.8 \tag{1.3}$$

$$\dot{\varepsilon} = A_2 \exp(n_2\sigma) \exp\left(\frac{Q}{RT}\right), \quad \alpha\sigma > 1.2 \tag{1.4}$$

$$\dot{\varepsilon} = A[\sinh(\alpha\sigma)]^n \exp\left(\frac{Q}{RT}\right), \quad \text{for all } \alpha\sigma \tag{1.5}$$

Where, σ is the flow stress of a material, Q represent the activation energy of the hot deformation, $\dot{\varepsilon}$ is the applied strain rate, A, n, α are the material constants. R represents the universal gas constant. In this model to introduce the combined effect of strain rate and temperature during the hot deformation of material Zener-Hollomon (Z) parameter or constant introduced (Du, Chen, Song, & Li, 2017; Ying Han et al., 2013):

$$Z = \dot{\varepsilon} \exp\left(\frac{Q}{RT}\right) = A[\sinh(\alpha\sigma)]^n \tag{1.6}$$

In this model, the effect of strain on deformation and flow stress is not considered. As shown in Figure 1.13, as the strain value increases, the flow stress behavior transitions through work hardening (WH), peak stress, softening, and steady state phenomena. Therefore, it is crucial to account for the effect of strain. To address this, a strain-compensated model was introduced, utilizing polynomial equations with a power of n. Using following Equations 1.7-1.10 strain compensated approach was presented in this model (Dourandish et al., 2022; Mha et al., 2023).

$$n = B_0 + B_1\varepsilon + B_2\varepsilon^2 + B_3\varepsilon^3 + B_4\varepsilon^4 + B_5\varepsilon^5 + B_6\varepsilon^6 \tag{1.7}$$

$$\alpha = C_0 + C_1\varepsilon + C_2\varepsilon^2 + C_3\varepsilon^3 + C_4\varepsilon^4 + C_5\varepsilon^5 + C_6\varepsilon^6 \tag{1.8}$$

$$Q = D_0 + D_1\varepsilon + D_2\varepsilon^2 + D_3\varepsilon^3 + D_4\varepsilon^4 + D_5\varepsilon^5 + D_6\varepsilon^6 \tag{1.9}$$

$$\ln A = E_0 + E_1\varepsilon + E_2\varepsilon^2 + E_3\varepsilon^3 + E_4\varepsilon^4 + E_5\varepsilon^5 + E_6\varepsilon^6 \tag{1.10}$$

Equation 1.11 gives the final express of the flow stress considering the Zener-Hollomon parameter and strain compensated constants.

$$\sigma = \frac{1}{\alpha}\ln\left\{\left(\frac{Z}{A}\right)^{\frac{1}{n}} + \sqrt{\left(\frac{Z}{A}\right)^{\frac{2}{n}} + 1}\right\} \tag{1.11}$$

Figure 1.14 shows the comparison of Arrhenius model prediction and measured flow stress under the different deformation conditions.

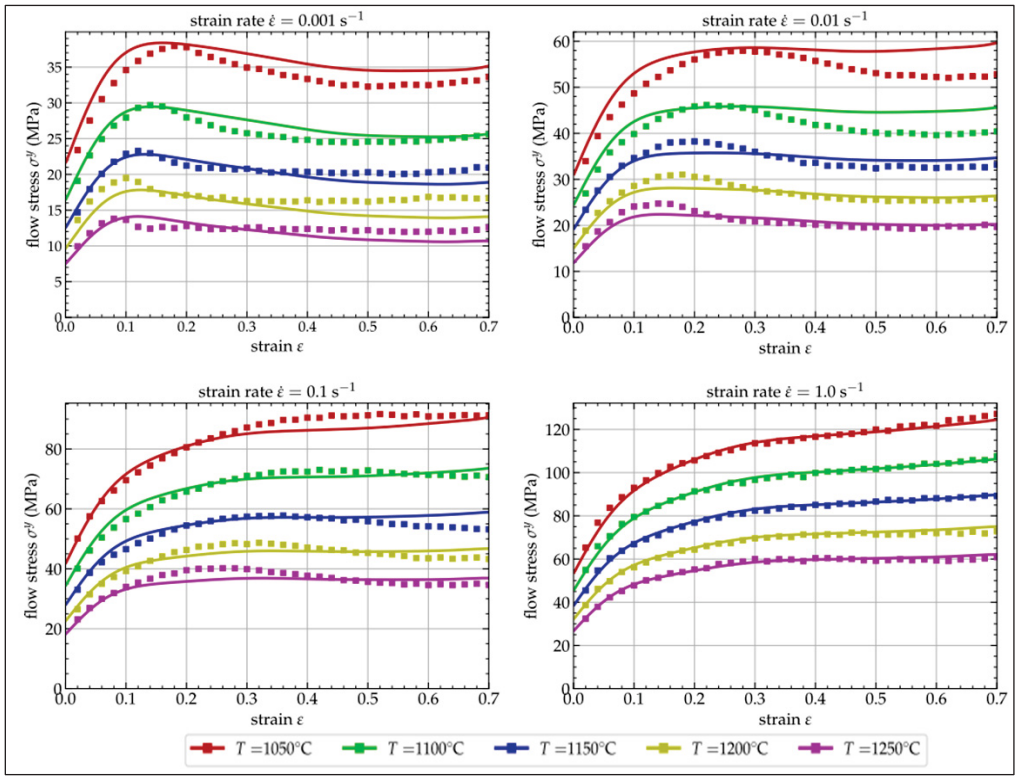

Figure 1.14 Comparison of Arrhenius model prediction (line) with measured (dots) flow stress for medium carbon steel
Taken from Mha et al. (2023)

1.5.3 Hansel-Spittle Model

The Hansel-Spittel model is another phenomenological material model used to predict material behavior under elevated temperature deformation conditions. This model considers the influence of temperature, strain, and strain rate variations (Mha et al., 2023; Niu et al., 2022).

It accounts for both material strengthening and softening mechanisms that occur during hot deformation. Equation 1.12 presents the mathematical expression for the Hansel-Spittel model, which illustrates the relationship between flow stress and the essential material parameters (Gao et al., 2022).

$$\sigma = A_o e^{m_1 T} \varepsilon^{m_2} \dot{\varepsilon}^{m_3} e^{\frac{m_4}{\varepsilon}} (1+\varepsilon)^{m_5 T} e^{m_6 \varepsilon} \dot{\varepsilon}^{m_7} T^{m_8} \quad (1.12)$$

Where, A_o is the material temperature parameter which represent the temperature uniformity during the deformation at given temperature, m_1 to m_8 material parameters which gives the material sensitivity to the temperature, strain rate and strain. These above equation variables were calculated for give material to predict flow stress value at given deformation conditions. The material parameters response is varying material to material, so it required to calculated parameters for every material will be investigated. Material model accuracy calculated by comparing the predicted flow stress data with experimental data. The model which predicts the precisely hardening and softening behavior of material during the hot deformation, will be integrated in to the FE software to simulate the hot deformation process of given material. Figure 1.15 shows the comparison between of predicted flow stress using Hansel-Spittel model and experimental flow stresses at different deformation conditions.

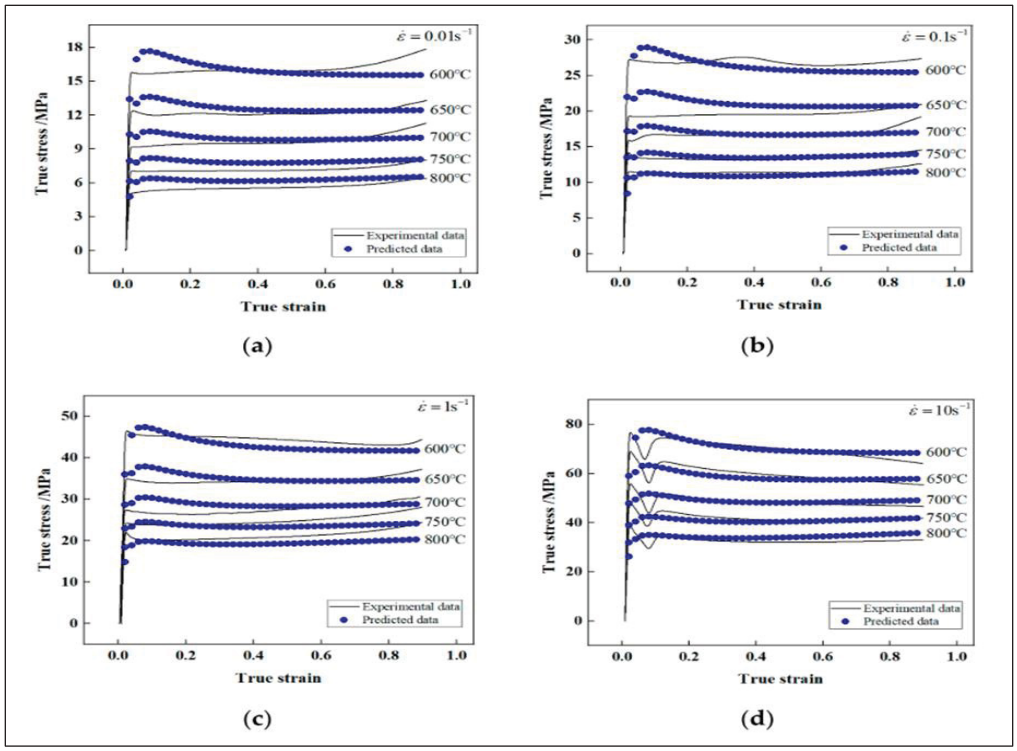

Figure 1.15 Comparison of Hansel-Spittel model prediction (dots)
with experimental (lines) flow stress
Taken from Liang et al. (2020)

1.5.4 Johnson-Cook Model

The Johnson-Cook model is most widely used for the prediction flow stress under different combination of strain, strain rate and deformation temperature. This model does not consider the combine effect of strain, strain rate and temperature. Therefore, it is necessary to consider individual parameter separately as an individual factor in the expression and hence this model will not able to predicts the softening behavior of the material due to the deformation temperature. Below expression give the flow stress Equation 1.13 for the JC model (Johnson & Cook, 1983).

$$\sigma = (A + B\varepsilon^{n})\left(1 + C ln\left(\frac{\dot{\varepsilon}}{\dot{\varepsilon}_0}\right)\right)\left[1 - \left(\frac{T - T_r}{T_m - T_r}\right)^{m}\right] \tag{1.13}$$

Where, σ represents the flow stress, $\dot{\varepsilon}$, $\dot{\varepsilon}_0$ and ε are the strain rate, reference strain rate and plastic strain respectively. T_m, T_r and T are the melting point, reference temperature and the deformation temperature respectively. A is the yield stress at the reference strain rate and reference temperature. B and C are the coefficient of the strain and strain rate hardening, m and n are the thermal softening and strain hardening exponent respectively. Figure 1.16 shows the comparison between predicted flow stress using J-C model and experimental flow stress (Shokry, Gowid, Kharmanda, & Mahdi, 2019).

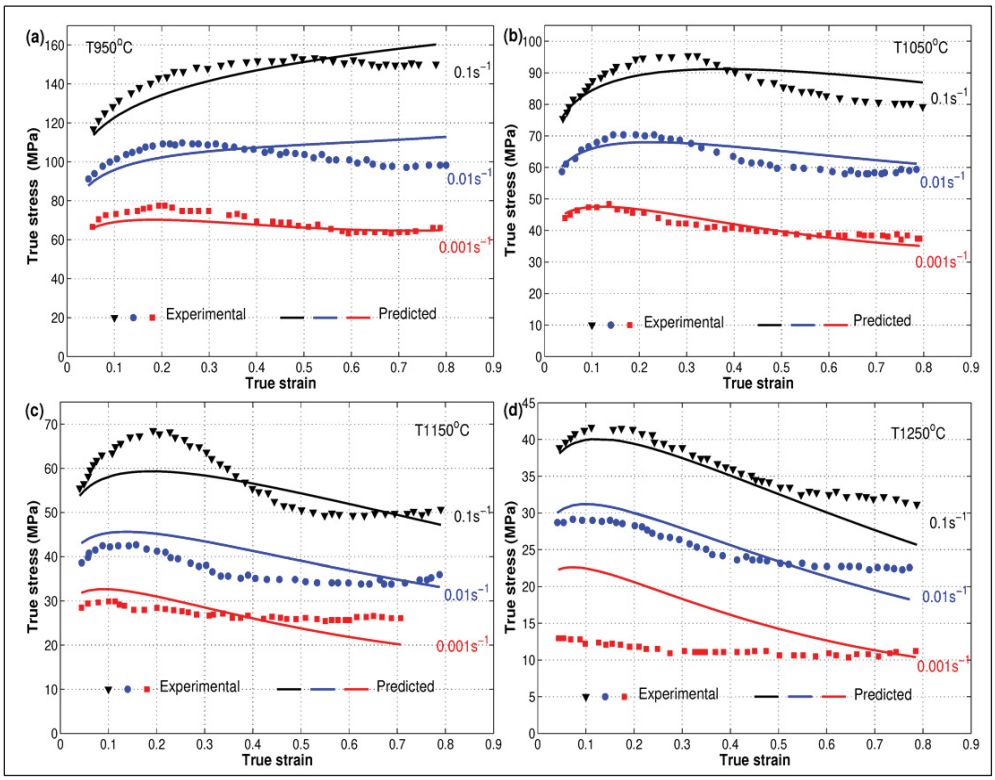

Figure 1.16 Comparison of JC model predicted (lines) flow stress
with experimental (dots) one
Taken from Shokry et al. (2019)

1.5.5 Zerilli-Armstrong (ZA) Model

The ZA model is like JC model and widely used in the FE code. The difference between the ZA and JC model is related to the consideration of all deformation parameters. In the JC model parameters were considered separately, while in the ZA model all deformation parameters were considered simultaneously (Mha et al., 2023; Rudra, Das, & Dasgupta, 2019; Samantaray, Mandal, Borah, Bhaduri, & Sivaprasad, 2009). The flow stress behavior can be predicted using ZA model using the following expression, Equation 1.14 (Murugesan & Jung, 2019; Rudra et al., 2019; Samantaray, Mandal, & Bhaduri, 2009; Samantaray, Mandal, Bhaduri, Venugopal, & Sivaprasad, 2011):

$$\sigma = (C_1 + C_2\varepsilon^n)\exp\{-(C_3 + C_4\varepsilon)T^* + (C_5 + C_6T^*)\, ln\dot{\varepsilon}^*\} \quad (1.14)$$

Where, σ is the flow stress, ε is the true plastic strain, $\dot{\varepsilon}$ is the strain rate, C_1 to C_6, n are the material constants. Figure 1.17 provides the comparison between predicted and experimental flow stress at different temperatures and strain rates.

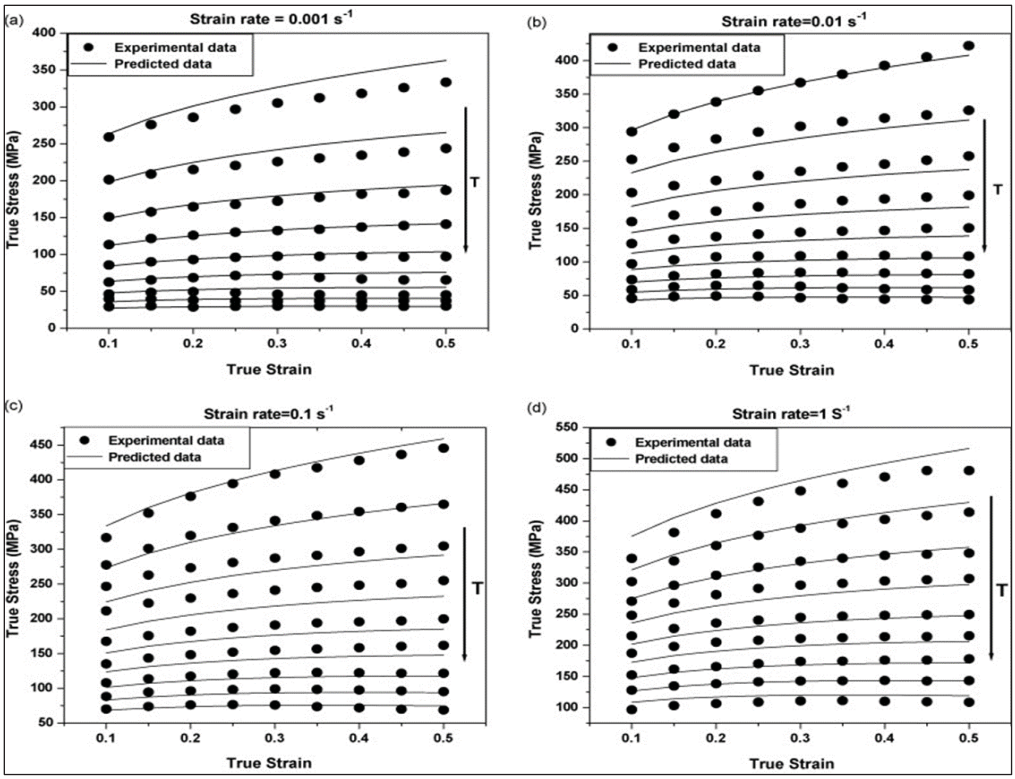

Figure 1.17 Comparison between predicted and experimental flow stress in the range of temperature (1073K-1473K) in 50K steps
Taken from Samantaray et al. (2009)

The accuracy of constitutive model predictions for flow stress and material behavior at high temperature deformation was evaluated based on the average absolute relative error (AARE), R-squared value, and correlation coefficient (R). The AARE quantifies the relative error between predicted and experimental values. The correlation coefficient indicates the linear relationship between predicted and experimental values. The AARE and R values were calculated using the following expressions, Equations 1.15 and 1.16 respectively (Mha et al., 2023; Nayak, Dhondapure, Singh, Prasad, & Narasimhan, 2020; Rudra et al., 2019).

$$AARE = \frac{1}{N}\sum_{i=1}^{N}\left|\frac{\sigma_E - \sigma_p}{\sigma_E}\right| \tag{1.15}$$

$$R = \frac{\sum_{i=1}^{N}\left(\sigma_E^i - \overline{\sigma}_E\right)\left(\sigma_P^i - \overline{\sigma}_P\right)}{\sqrt{\sum_{i=1}^{N}\left(\sigma_E^i - \overline{\sigma}_E\right)^2 \sum_{i=1}^{N}\left(\sigma_P^i - \overline{\sigma}_P\right)^2}} \quad (1.16)$$

1

Where σ_E and σ_P measured/experimental and predicted values of the constitutive model respectively. $\overline{\sigma}_P$ and $\overline{\sigma}_E$ are the mean values of σ_P and σ_E, respectively and N is the number of data points.

Despite the fact significant research has focused on material modeling and the application of various constitutive equations to predict the flow stress of different steel grades, the development of microstructure-based models has received comparatively less attention. Specifically, for tool steels, most studies have concentrated on characterizing hot deformation behavior using constitutive equations, with fewer exploring the relationship between processing parameters and microstructure evolution (Dourandish et al., 2024; Hamad, Chung, & Ko, 2014; L. Tang, Jiang, Teng, Fu, & Zhang, 2019; R. Zhang, Wang, & Yuan, 2017). Microstructure model has been discussed in the detail in the following section.

1.5.6 Microstructure model

As discussed in the above section, during the hot deformation of material, microstructural changes present due to the DRV and DRX phenomena, in this process grain refinement happens. DRX depends on the many factors such as heating rate to target temperature, holding time and amount of deformation applied during the deformation process. DRX phenomena is the primary softening mechanism present in the low staking fault energy material like steels. It is initiated upon reaching the amount of deformation to the critical level called as critical strain ε_c and critical strain value varies with deformation condition such as temperature and rate of deformation. Predication of microstructure and grain size evolution is very important during the hot deformation, which significantly impacts on the final mechanical properties of the forged products. Therefore, it is important and needed to understand the softening mechanism present during the hot deformation and it impact on microstructure and grain size evolution. Several constitutive models have been developed and proposed for the prediction of

microstructure evolution during the hot deformation process. In the literature for the prediction of microstructure evolution most widely used model is JMAK (Johnson-Mehl-Avrami-Kolmogorov), with this model DRX and grain growth phenomena can be predicted more precisely (Chamanfar, Chentouf, Jahazi, & Lapierre-Boire, 2020b; Fanfoni & Tomellini, 1998; Yahui Han, Li, Ren, Qiu, Chen, et al., 2021; Ji et al., 2020; Tize Mha, Dhondapure, Jahazi, Tongne, & Pantalé, 2023). The overall kinetics of the recrystallization process can be described using the semi-empirical JMAK model, as has been demonstrated for over a decade. The model expresses the recrystallized grain fraction, X(t), as a function of time (t). Equation 1.17 give expression for the JMAK model (Melvin Avrami, 1940; Mélvin Avrami, 1939; John J. Jonas et al., 2009).

$$\mathrm{X}(t) = 1 - e^{-b.t^n} \tag{1.17}$$

Where, b is the Avrami coefficient and it is highly sensitive to change in temperature and n is the Avrami exponent and it is related to phase change of material for an instance.

The integration of microstructure models and study microstructure evolution during hot deformation is particularly rare, especially for tool steels. Moreover, there is a notable lack of research on, influence of deformation path on microstructure evolution in large scale industrial applications, which is crucial for the process design of heavy forgings.

1.5.7 Damage and failure criterion

During open die forging, tensile stresses and strain localization present at surface and center of the ingot. These factors can adversely affect the final quality of forged products (Bitterlin et al., 2016). For instance, cracking can occur in regions of high tensile stress or strain concentration. To predict the damage and possible region for cracking during hot deformation, various fracture models have been developed. By employing damage model an optimum hot deformation process can be designed to produce defect free products. During hot deformation, damage or fracture occurs due to ductile failure. In the available literature, ductile damage or failure criteria were used to predict damage during hot forming process. Several damage

criteria have been proposed, including Cockcroft-Latham, Oyane, Brozzo, and Tresca failure criteria (G., 1968; Kvačkaj et al., 2014; Stebunov, Vlasov, & Biba, 2018; Terhorst, Feuerhack, Trauth, & Klocke, 2016). These models involve a critical or threshold value for a material under specific conditions (hot or cold deformation). When the damage value exceeds critical value during the forging process, the material enters a risk zone where crack initiation is imminent. The Oyane criterion was originally proposed for cold forming applications, while the Brozzo and Cockcroft-Latham models are widely used for hot forming processes (Myint, Hagihara, Tanaka, Taketomi, & Tadano, 2017; Shang, Cui, & Fu, 2018; Yu Zhang et al., 2021). Among these criteria, the Cockcroft-Latham normalized criterion damage and Tresca failure criterion are the most widely used for damage prediction during hot deformation expression given in Table 1.1.

Table 1.1 Damage models
Taken from Brozzo (1972), Freudenthal (1950),
Cockcroft & Latham (1968) Oyane et al., (1980)

Damage model and failure theory	Cockcroft & Latham	Tresca theory
	$C = \int_0^{\bar{\varepsilon}_f} \frac{\sigma_{max}}{\bar{\sigma}}\, d\bar{\varepsilon}$	$\tau_{max} = \frac{\sigma_1 - \sigma_3}{2} \geq \frac{S_y}{2}$

Where, σ_{max} and $\bar{\sigma}$ represent the maximum principal and effective stress, σ_1 and σ_3 principal stresses, S_y is a yield strength of material.

Ghazani et al. (Ghazani & Eghbali, 2018) employed the Cockcroft-Latham ductile damage criterion to predict regions of maximum damage during numerical simulation of hot compression testing of AISI 321 austenitic stainless steel. This model predicts ductile fracture initiation when tensile strain energy surpasses a critical threshold. Figure 1.18 illustrates the distribution of Cockcroft-Latham damage values after hot deformation at 800°C and a strain rate of 0.01 s^{-1}. The non-uniform distribution of the damage factor indicates that points A and B are prone to ductile fracture initiation.

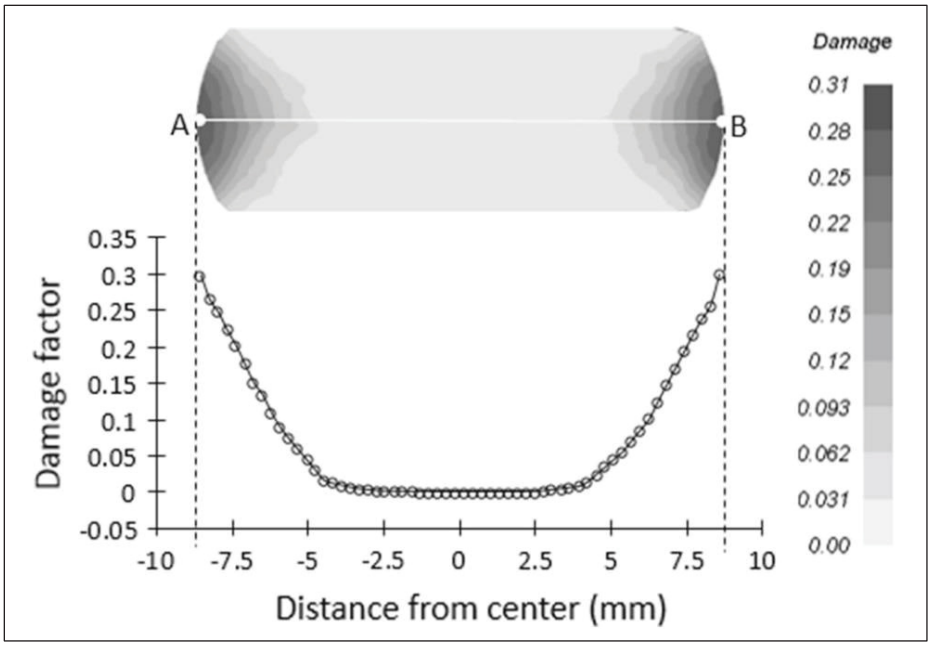

Figure 1.18 Distribution of Cockcroft-Latham damage
inside deformed sample
Taken from Ghazani & Eghbali (2018)

Kukuryk (Marcin Kukuryk, 2021) studied the effect of die geometries on stress states and fracture during the cogging of a shaft with a concave cross-section in V-shaped anvils was investigated. Three damage criteria, namely Cockcroft and Latham, Oyane, and Brozzo, were employed for damage prediction. This study compared these three criteria for fracture prediction during the cogging process after four passes, using parameters, anvil angle (α_c) = 150°, reduction ration (ε_c) = 0.356, and a forging ratio of 4.2. The results, shown in the Figure 1.19, revealed that when using the normalized Cockcroft and Latham criterion as a baseline, the Oyane criterion reduced the crack formation factor in the forging's axial region by 37.6%. Conversely, the Brozzo criterion predicted an increase in the crack formation factor in the same region, with a difference of 17.5%. Based on these findings, the authors concluded that the Cockcroft and Latham criterion is more suitable for ductile damage prediction compared to the other two criteria. Additionally, they examined the effect of varying convex angles (α_c) from 135° to 165° and found that higher convex angles resulted in higher strain and compressive stress at the center of workpiece. The study also explored the interaction between damage and geometric parameters.

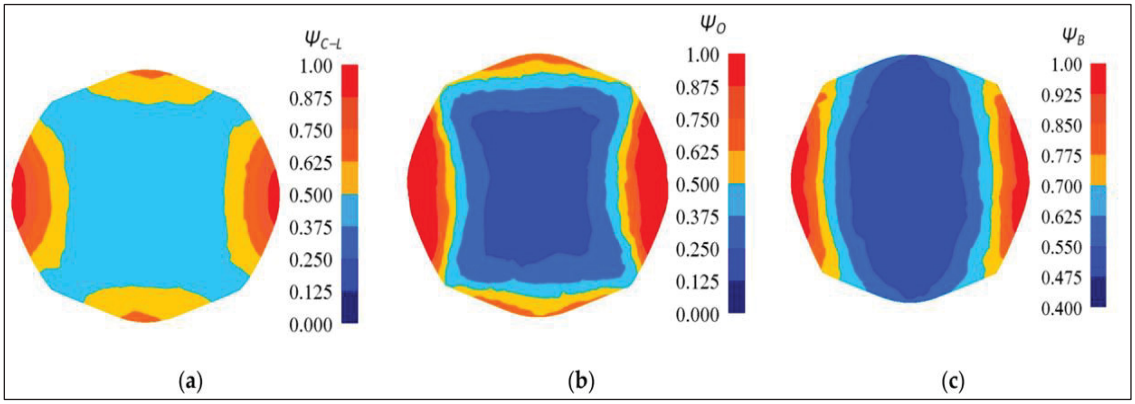

Figure 1.19 Shows the distribution of damage value with (a) Cockroft and Latham (b) Oyane and (c) Brozzo (α_c = 150°, ε_c = 0.356, forging ratio 4.2) Taken from Kukuryk (2021)

Various ductile damage criteria were studied by Yansham et al. (Lou, 2013) for evaluating damage and stress states during metal forming processes, based on both coupled and uncoupled approaches. A comparative study was conducted among the Cockcroft–Latham, Brozzo, Oyane–Sato, Ko–Huh, Clift, MMC, and a proposed was criterion for the Al2021-T351 aluminum alloy. In this study, stress triaxiality and load parameters were considered for damage prediction using both experimental and analytical methods. All the criteria incorporated tensile stress and fracture strain, except the Clift model, which makes it unsuitable for damage prediction when stress triaxiality varies significantly. From the comparative analysis of the damage cut-off values, it was reported that the Cockcroft–Latham, Oh, Ko–Huh, and Brozzo criteria provide satisfactory results for predicting damage during metal forming processes and compression tests.

Based on the findings reported in the literature, it has been observed that the five most widely used damage models for predicting damage evolution during bulk metal forming processes are those proposed by Oyane, Brozzo, Oh, Ko-Huh, and Cockcroft & Latham. Among these, the Cockcroft & Latham model is particularly suitable for predicting damage during forging processes such as forging and extrusion. However, most available studies in the literature focus on damage and fracture in materials subjected to hot deformation at the laboratory scale or on

sub-sized specimens. Consequently, there remains a significant gap in scientific research on damage and stress state analysis in large-size ingots during the forging process. (Arikawa, Yamabe, & Kakimoto, 2014; Dourandish et al., 2024; Kakimoto & Arikawa, 2014).

1.6 Finite Element Analysis (FEA) of hot deformation process

FEA is a powerful tool used to simulate different metal forming processes and predict the material behavior under the different deformation condition at high temperature, which represent the various forging process such as rolling, extrusion, and forging. FE simulation predict results for the distribution of important parameters, stress, strain, temperature, damage, and DRX grain size evolution during hot deformation. In the open literature many studied available on FEA to study effect of thermomechanical parameters such as temperature, strain rate, and strain hot deformation process. In addition, few studies available of effect of tool geometry (die and ingot) on void closure, their impact on material response and flow during the hot deformation process. Furthermore, FEA of hot deformation processes play a crucial role in process design prior to the execution of actual physical trials. FEA also enables the prediction of temperature and deformation gradients, and its effect on microstructure evolution during the hot deformation. Consequently, FEA contributes to the efficient design of processes under various boundary conditions.

The integration of accurate material and microstructure models into a FEA software, helps improve efficiency of the FE analysis. FEA of actual industrial process helps optimiz actual industrial process without performing any physical trail of actual process. In the market range of commercial FEA software packages are available, including Forge NxT, Simufact, DEFORM, QFORM etc. These FE packages are used for the predicting material behavior and microstructure evolution during high temperature metal forming processes (Ren, Chen, & Chen, 2014). Jang et al. (Jang, Ko, & Kim, 2000) numerical simulation was used to predict material behavior and microstructure evolution during the hot deformation of a carbon steel cylinder with dimensions of 85 mm × 42 mm. This prediction was achieved by implementing a developed material and microstructure model into a 3D finite element software package. The

simulation results revealed the effect of inhomogeneous deformation distribution on microstructure evolution. The central region of the forged product exhibited a significant concentration of DRX. This observation is consistent with findings from similar studies where material and microstructure modeling have been utilized to simulate hot deformation processes and analyze the impact of various thermomechanical parameters (Gao et al., 2022; Jin, Li, Wu, & Dong, 2015; R. H. Krishna & Jena, 2019; Ren et al., 2014; Rudra et al., 2019).

Jin et al. (Jin et al., 2015) investigated the influence of non-uniform deformation distribution on grain size evolution following a 6.3 mm reduction in height. Figure 1.20 illustrates the variation in equivalent strain across different height reductions in as-extruded Q325 samples. The results showed that the strain level at the center of the samples increased with greater height reduction, while a lower strain level was consistently observed at the interface between the sample and the dies, due to the friction at the interface between the workpiece and anvils. This variation in equivalent strain distribution significantly affects microstructure evolution.

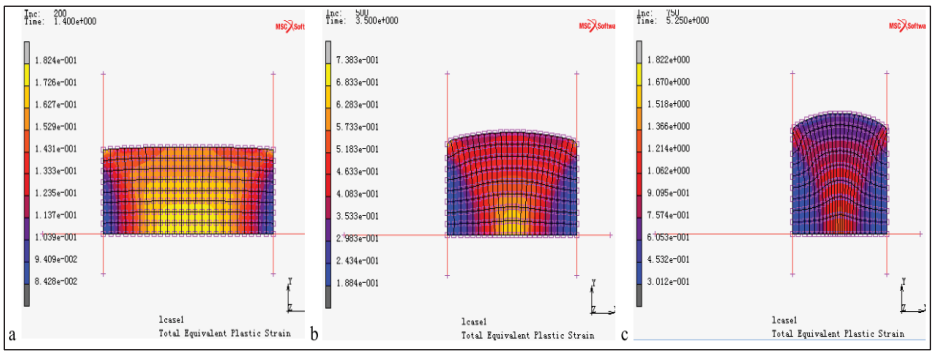

Figure 1.20 Shows the variation of equivalent strain with different level of height reduction (a) 2.1mm, (b) 4.2mm and, (c) 6.3mm
Taken from Jin et al. (2015)

Figure 1.20 compares the predicted and experimental grain size evolution after a 6.3mm height reduction. Due to higher equivalent strain at the center, fine grains were observed at location C, and conversely, larger grains at location A. The grain size at location D falls between that of the center and the upper surface of the sample. The authors concluded that deformation heterogeneity affects the uniformity of microstructure evolution during hot deformation.

Therefore, it is important to minimize the deformation gradient during hot deformation as much as possible.

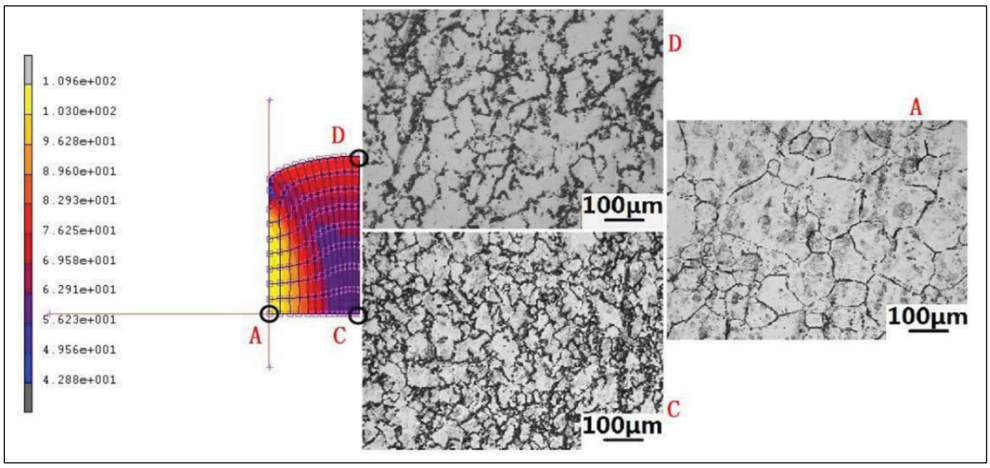

Figure 1.21 Represents the comparison of grain size evolution during numerical simulation and experimental studies after 6.3mm of height reduction
Taken from Jin et al. (2015)

In the following section, literature review presented on influence of different die geometries on material flow to study the strain distribution, material flow and its effect on defect closure, such as void and porosity. Numerical and physical simulation techniques used for the analysis.

1.6.1 Influence of deformation paths on material flow and void closure

Forging is a highly complex process influenced by several factors, including thermomechanical, geometrical (both die and ingot), and process parameters. This section provides a comprehensive literature review on the impact of die geometry on material flow during open die forging. Various die geometries, such as flat, V-shaped, convex, concave, and cymbal-shaped, have been used during the hot deformation. These different geometries result in distinct deformation paths, which affect material flow, microstructure, and damage evolution during the hot deformation process. Therefore, understanding the interaction between thermomechanical and geometrical parameters is crucial.

Ahmadi et al. (Ahmadi et al. 2025) investigated the effect of four die geometries on void and porosity closure during the upsetting of industrial size 100CrMo7-3 steel ingots. Figure 1.22 presents the FE model for upsetting with four combination of die and shows distribution of equivalent strain distribution at 50% and 70% of deformation. The investigation used criteria based on effective strain, with a local threshold of 0.7 for void closure and defect elimination. A comparison between four die geometry combinations (A to D) was performed based on the effective strain distribution from the bottom to the top of the ingot. At both 50% and 70% deformation, the dead metal zone (DMZ) near the upper die was eliminated for die geometries C and D. Additionally, the strain level at the ingot's center was higher compared to A and B. Convex and cymbal-shaped die surface curvatures facilitated the elimination of the DMZ and the closure of voids in critical regions.

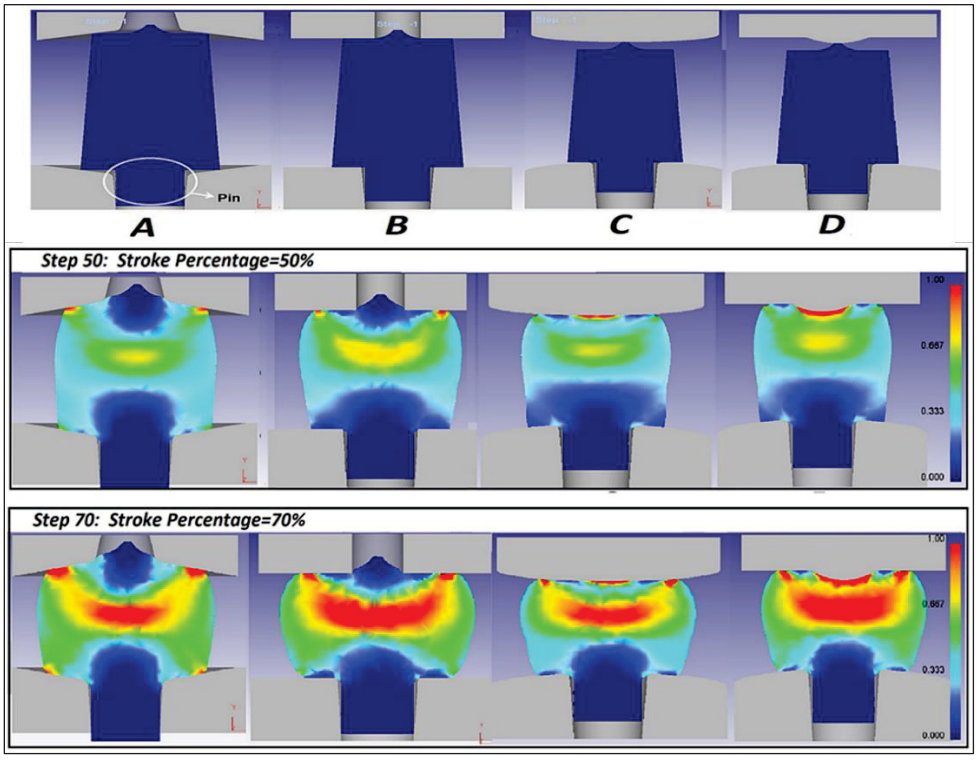

Figure 1.22 Shows FE model setup and effective strain distribution at 50% and 70% of deformation, with combination of different lower and upper die,
A- Pierced Concave-Pierced Concave, B- Pierced Flat-Pierced Flat,
C- Pierced Convex-Convex, D- Pierced Convex-Cymbaled-shaped respectively
Taken from Ahmadi et al. (2025)

Kukuryk, (2024) studied the effects of flat, angled, and three-radius dies on void closure during the cogging process of cylindrical 55NiCrMoV7 steel samples were investigated using both experimental methods and finite element (FE) analysis. The results revealed that, compared to the flat die, the angled and three-radius dies required less reduction and fewer passes to achieve void closure. As shown in the Figure 1.23, the reduction required to close voids along the central axis was 0.7 for the angled die, 1.05 for the three-radius die, and 1.4 for the flat die. This study concludes that, altering the surface curvature of dies, material flow can be altered and which help in the closing of central defects, voids and porosity.

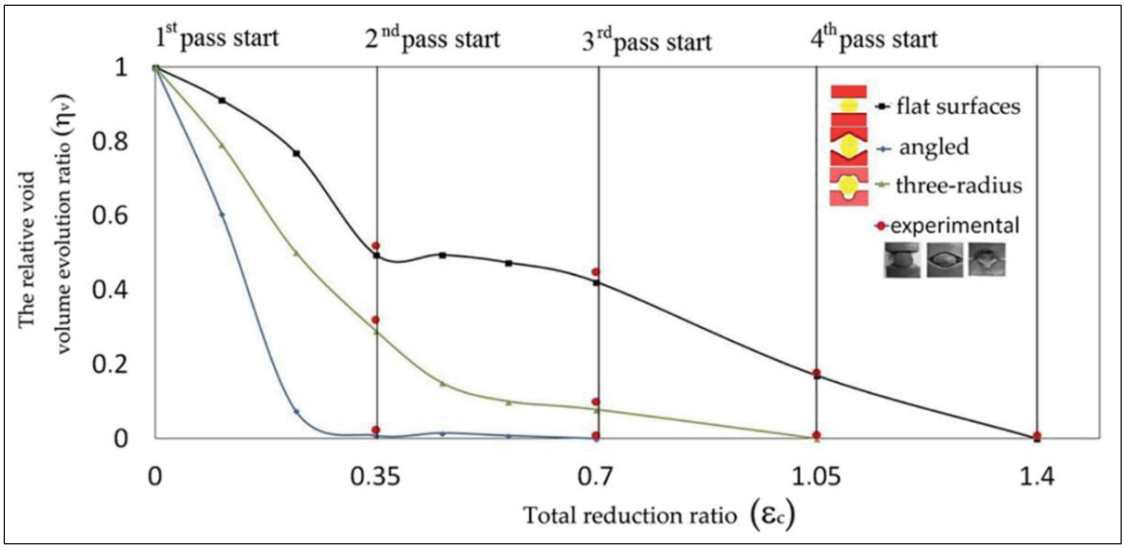

Figure 1.23 Shows the relation between the relative void volume evolution ration and total reduction during the cogging process with different shape of anvils
Taken from Kukuryk (2024)

Kukuryk et al. (Marcin Kukuryk & Winczek, 2018) studied the effect of convex trapezoid, asymmetrical combined with different angles (75° and 60°) and V die with 135° angle on grain size after the DRX during the cogging of waspasaloy alloy. Investigation results shows that V die provides maximum effective strain with relatively more homogenous distribution of the within the forge volume, which influences the grain shape and size. During cogging with V dies results in higher plastic deformation at the center of workpiece, which helps in producing

50% smaller grain sizes compared to the other two anvils. Figure 1.24 shows the comparison of DRX fraction and average grain size after the cogging process. As changing the die geometry, it effects on material flow as well as microstructure evolution, finally it will help in modifying the mechanical properties of final forged products.

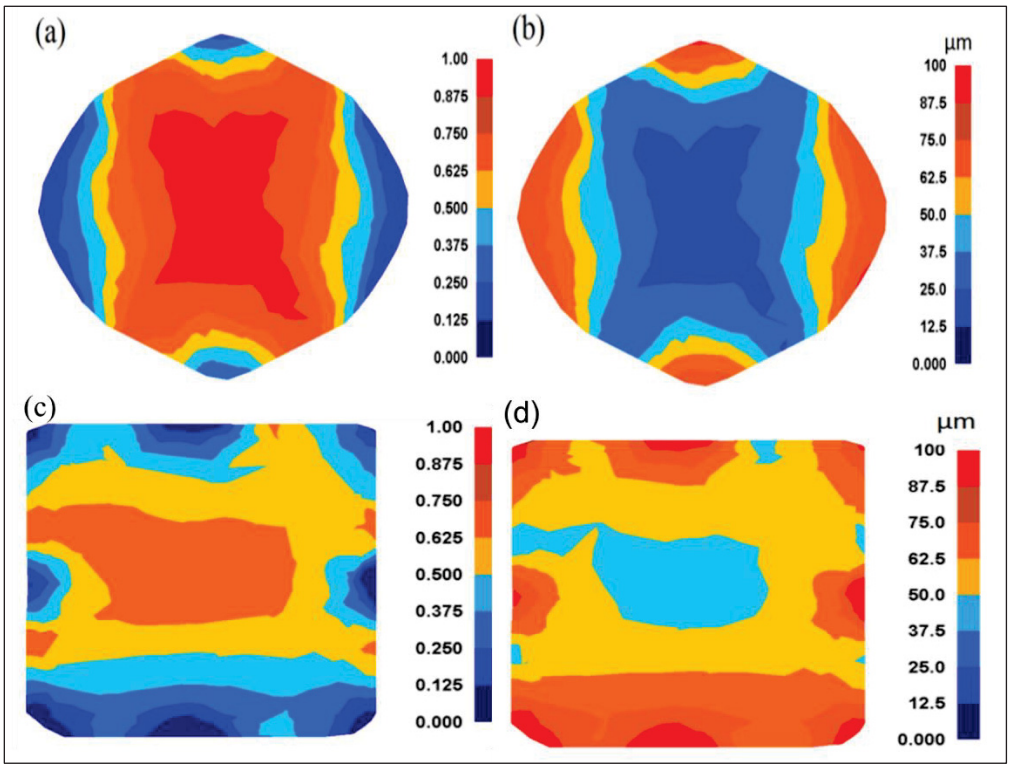

Figure 1.24 Distribution of the DRX fraction (a-c) and average grain size (b-d), after cogging process using V die (a-b) and convex-trapezoid anvils (c-d) Taken from Kukuryk & Winczek (2018)

Christiansen et al. (Christiansen et al. 2014) investigated the effect of a lower V-die on centerline porosity closure by varying the V-die angle (60° to 180°) using a physical modeling and numerical approach. The die and a schematic of the open die forging setup are shown in Figure 1.25a-b, respectively. The experiment was conducted on a small scale lead ingot with a centerline hole to simulate porosity, using an upper flat die and a lower V-die with angles ranging from 60° to 180°. The results indicated that a V-die angle of 120° produced better

deformation and achieved optimal closure of the centerline porosity without requiring higher press loads, as shown in Figure 1.26.

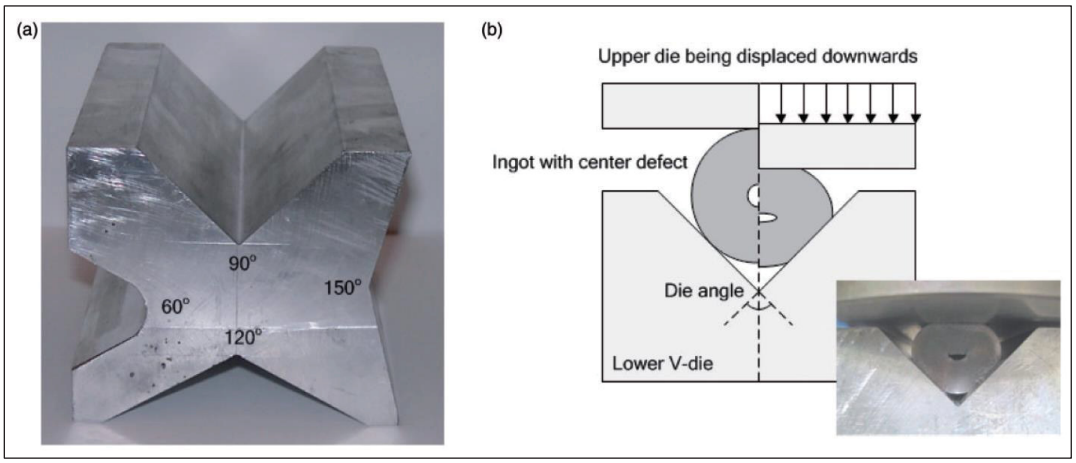

Figure 1.25 (a) Shows V-die with different angles (b) Schematic of open die forging set up and photo after compression with lower die angle 90º
Taken from Christiansen P. et al. (2014)

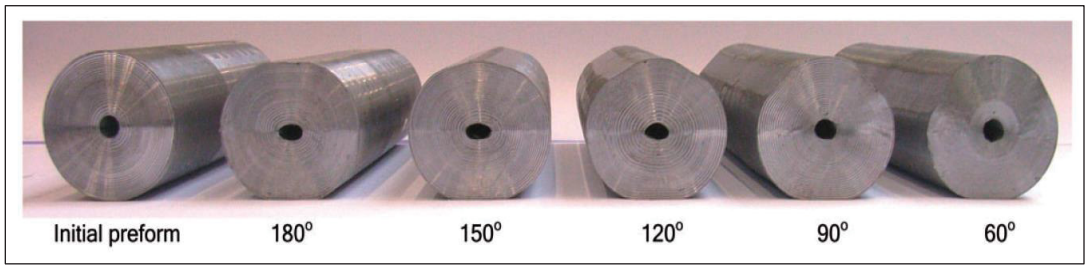

Figure 1.26 Initial preform and specimen after 3mm deformation with V die at different angle
Taken from Christiansen P. et al. (2014)

Dudra et al. (STEVE P. DUDRA and YONG-TAEK IM, 1990) examined the impact of flat and V-dies on porosity removal during the hot forging of a large ingot. They employed a combination of flat dies and Double V dies (with a 135° die angle) in a FEM simulation model, as shown in Figure 1.27. To evaluate the influence of die geometry on porosity removal, they compared the effective strain and hydrostatic stress at the center of the ingot. Higher levels of

effective strain and hydrostatic stress were found to enhance porosity removal both at the center and throughout the thickness of the ingot.

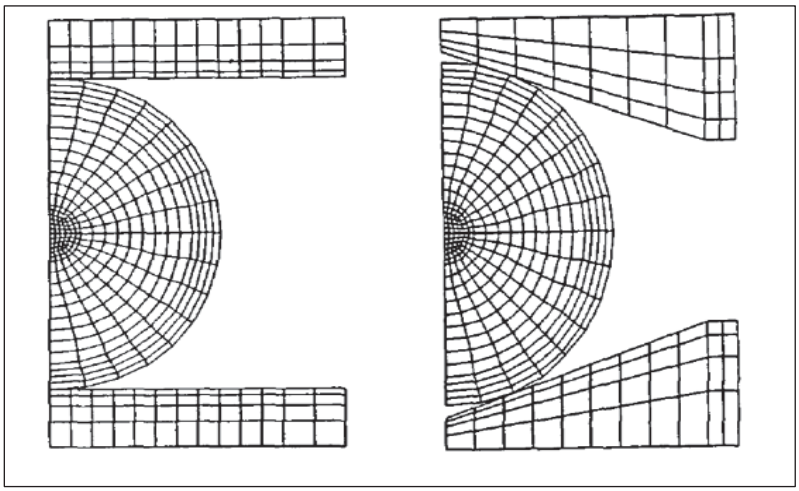

Figure 1.27 Axisymmetric upset (plain strain side pressing)
model for (a) Flat dies and (b) V-shaped dies
Taken from Dudra et al. (1990)

Using axisymmetric upset forging simulation, the predicted results for effective strain and hydrostatic stress at the center of the ingot for both flat and double V-dies are shown in Figure 1.28. The V-die generates a higher amount of effective strain and hydrostatic stress at the center of the ingot compared to the flat die. However, the V-shaped die requires a higher press load than the flat die, as the contact area between the die surface and the ingot is larger with the V-die, resulting in greater contact friction. The study concludes that altering die geometry helps modify material flow and facilitates porosity elimination at the center of the billet.

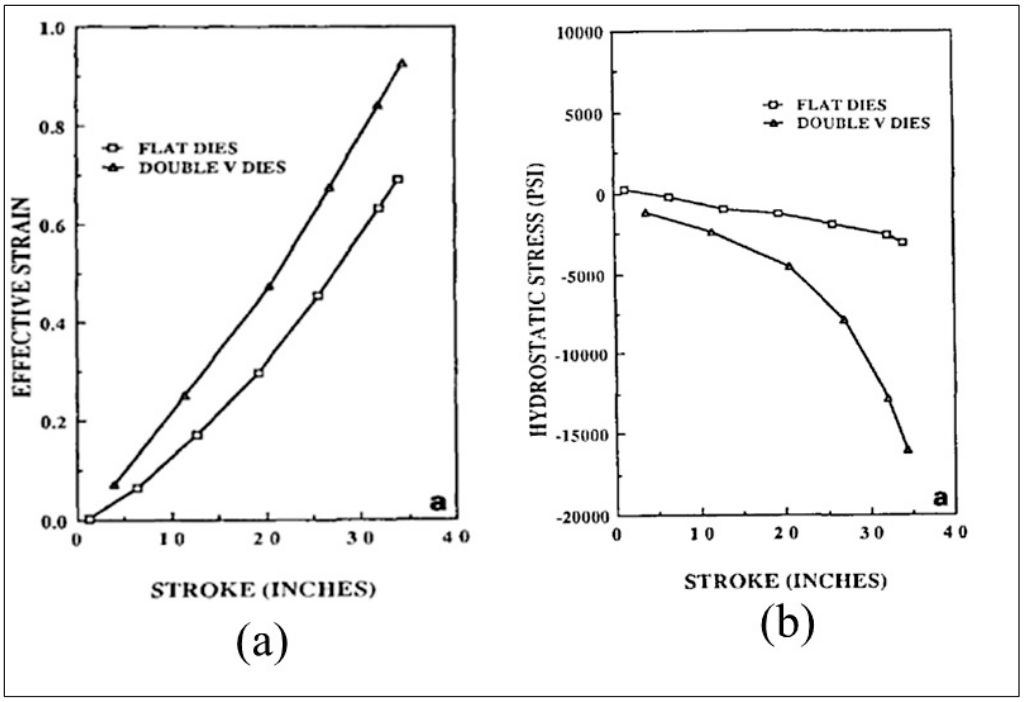

Figure 1.28 Predicted values of stress and strain at the center of the ingot
(a) effective strain (b) hydrostatic stress after side pressing
with flat and double V dies
Taken from Dudra et al. (1990)

Zhang et al. (X. Zhang et al., 2012) investigated void closure during hot forging of large size ingots using a simulation approach with the commercially available software DEFORM. Initially, a model for void closure was developed, programmed, and integrated into the FEM software. The simulation model for upsetting with various die geometries is shown in Figure 1.29. By applying 36% deformation, a result map displaying the distribution and variation of relative void volume for different die geometries is presented in Figure 1.30. The relative void volume (Rv) is defined as the ratio of the final void volume to the initial void volume, where an Rv value approaching zero indicates complete void closure, and an Rv value approaching one indicates that the void has not closed. The results showed that different die geometries produce varying levels of deformation at the ingot's center and near the die-ingot interface under the same level reduction. The cymbal-shaped die provided the most effective void closure, while the concave-shaped die resulted in less void closure, particularly near the ingot-die interface, compared to other geometries. Therefore, applying the same amount of reduction

with different die geometries creates different levels of strain and stress throughout the ingot's thickness, aiding in the removal of voids and porosity.

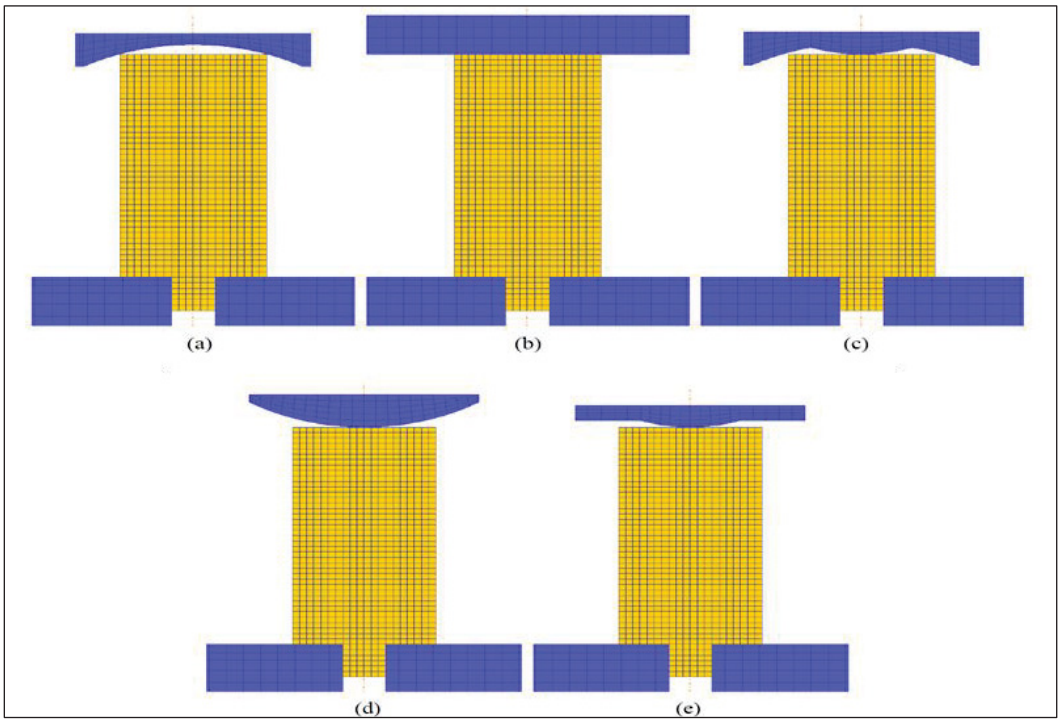

Figure 1.29 FEM models for upsetting with different die geometries (a) concave die (b) flat die (c) M shape die (d) convex die and (e) cymbal shape die
Taken from X. Zhang et al. (2012)

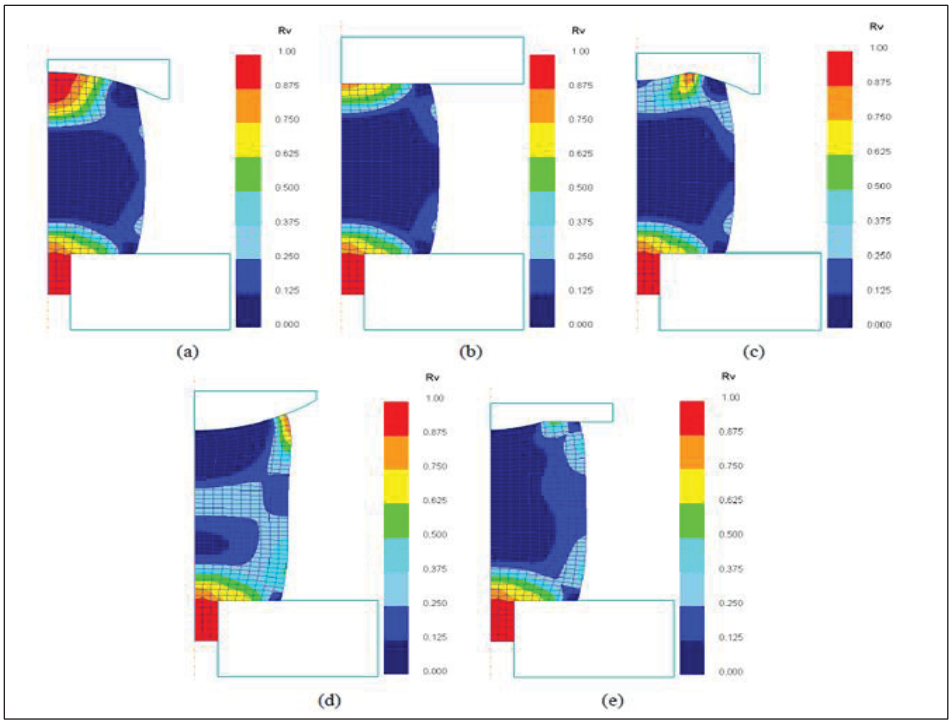

Figure 1.30 Relative void volume variation after upsetting with 36% deformation for (a) concave die (b) flat die (c) M shape die (d) convex die (e) cymbal shape die
Taken from X. Zhang et al. (2012)

Zhang et al. (X. Zhang et al., 2012) further investigated the impact of varying die geometries on the relative void volume closure during the blocking process, specifically at 24% deformation. Figure 1.31a-b illustrate the FE models employed for the blocking process, utilizing double V dies and flat dies, respectively. Figure 1.32 presented demonstrates the relative void closure volume achieved after 24% deformation during the blocking process. The analysis revealed that the relative void closure volume is significantly higher for double V dies compared to double flat dies. The authors concluded that, under equivalent deformation conditions, double V dies offer a greater void closure volume than both flat and FML dies.

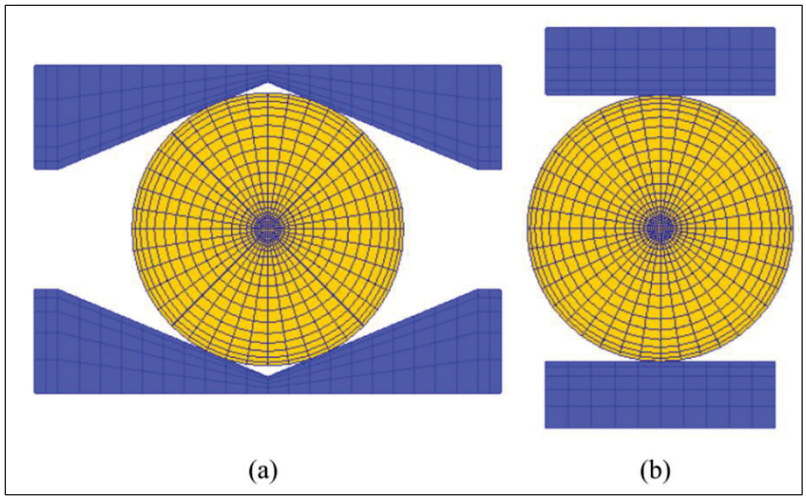

Figure 1.31 Meshed FE model for blocking process using
(a)135° V dies and, (b) flat dies
Taken from X. Zhang et al. (2012)

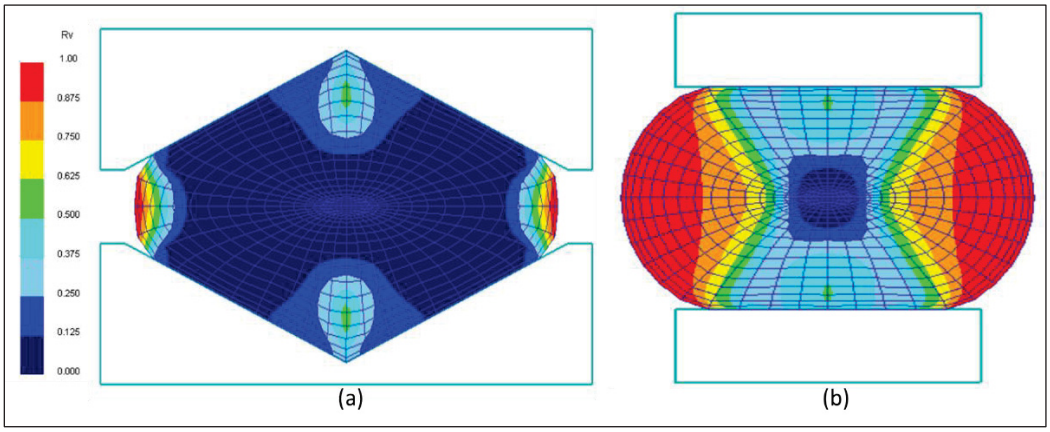

Figure 1.32 Relative void volume closure at end of blocking process with
24% reduction using (a) V 135° dies and, (b) flat die
Taken from X. Zhang et al. (2012)

The following section examines the influence of deformation level and deformation route on microstructure evolution and mechanical properties variation during hot deformation.

1.6.2 Influence of deformation path on microstructure evolution

Few studies in the open literature address the influence of deformation paths on deformation, microstructure evolution, and the variation of mechanical properties during the rolling process. One study examined the effects of simple shear, compressive, and combined deformation paths on microstructure and mechanical properties. To assess the mechanical properties, hardness measurements were taken, and comparisons were made between the different deformation paths. Based on the comparative analysis, the optimal deformation path was identified, which resulted in a homogeneous hardness distribution and the finest grain size.

Hamad et al. (Hamad et al., 2014) investigated the effect of deformation path on microstructure evolution and microhardness in interstitial-free (IF) steel using the differential speed rolling (DSR) process. In this process, different height reductions of 50% and 75% were applied. Figure 1.33 illustrates the variation in mean grain size and the density of high-angle grain boundaries (HAGBs) with respect to different deformation levels. The study found that an increase in the deformation level led to a higher fraction of HAGBs, while the mean grain size decreased.

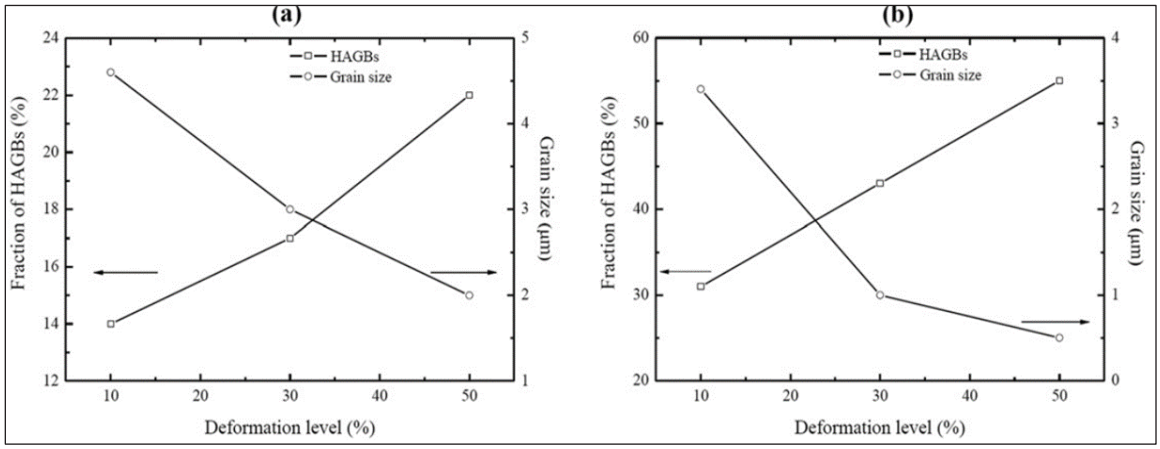

Figure 1.33 Shows the variation of mean grain size and high angle grain boundaries with different deformation levels after total height reduction (a) 50% and (b) 75% Taken from Hamad et al. (2014)

Figure 1.34 demonstrates the variation in average microhardness as a function of different deformation levels. It can be observed that as the deformation level increases from 50% to 75%, the average microhardness increases correspondingly. The authors also reported that increasing the deformation level from 50% to 75% leads to greater homogeneity in the distribution of microhardness values across the sample thickness, specifically from the top to the bottom surface.

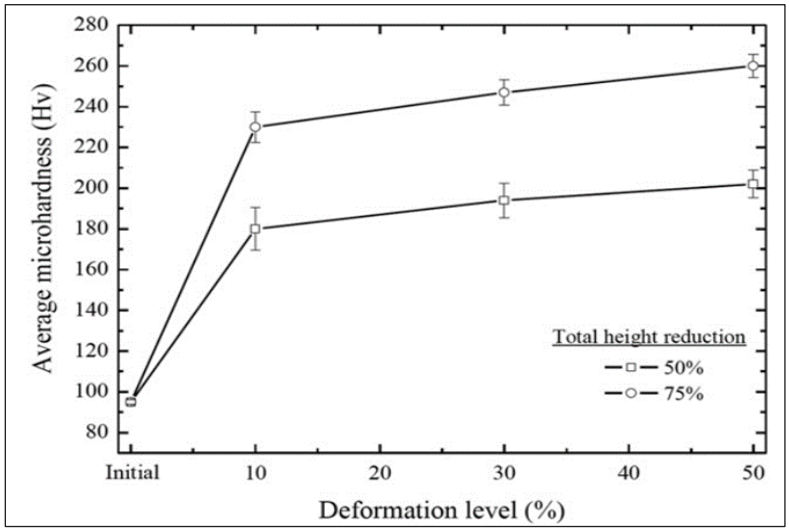

Figure 1.34 Represents the variation of microhardness values
IF steel samples with different level of deformation
Taken from Hamad et al. (2014)

Sakai et al. (Sakai, Mori, & Utsunomiya, 2007) examined the effect of three different deformation routes in plane strain on microstructure evolution during the rolling of 1100 aluminum sheets. The three deformation routes employed in plane strain were: simple shear (s1), compressive (s0), and a combination of compressive and simple shear (s0.8, s0.6, and s0.3). The investigation reported that specimens subjected to simple shear and compressive deformation exhibited larger grain sizes compared to those deformed via the combined deformation path. The strain path change promoted a higher level of grain refinement. Figure 1.35 illustrates the microstructure evolution during different deformation routes on as-received samples.

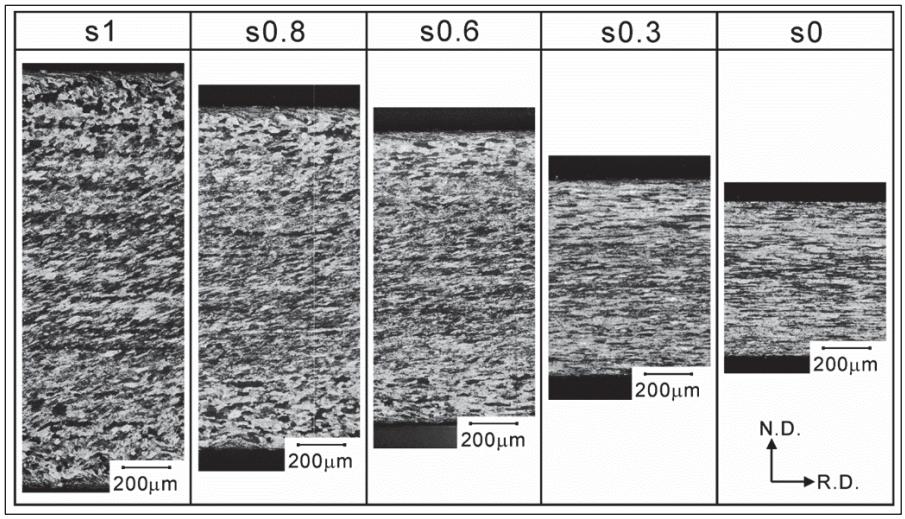

Figure 1.35 Represents the effect of different deformation routes on microstructure of as-received samples
Taken from Sakai, Mori, & Utsunomiya, (2007)

Figure 1.36 shows the number of high angle grain boundaries (HAGBs) for different samples subjected to various deformation paths. The authors reported the effect of deformation routes on the density of HAGBs (misorientation). In the s0.6 samples, the HAGBs density was highest compared to the other five samples, and these samples exhibited the finest grain size. The formation of these HAGBs is likely attributed to grain subdivision (Hughes & Hansen, 1997), a process influenced by changes in stable end orientations resulting from variations in the deformation path. Recrystallization nucleation sites were more prevalent in specimens subjected to the combined deformation path, particularly in the s0.6 specimen. It is possible that the change in deformation route increases stored energy, promoting the formation of finer recrystallized grains.

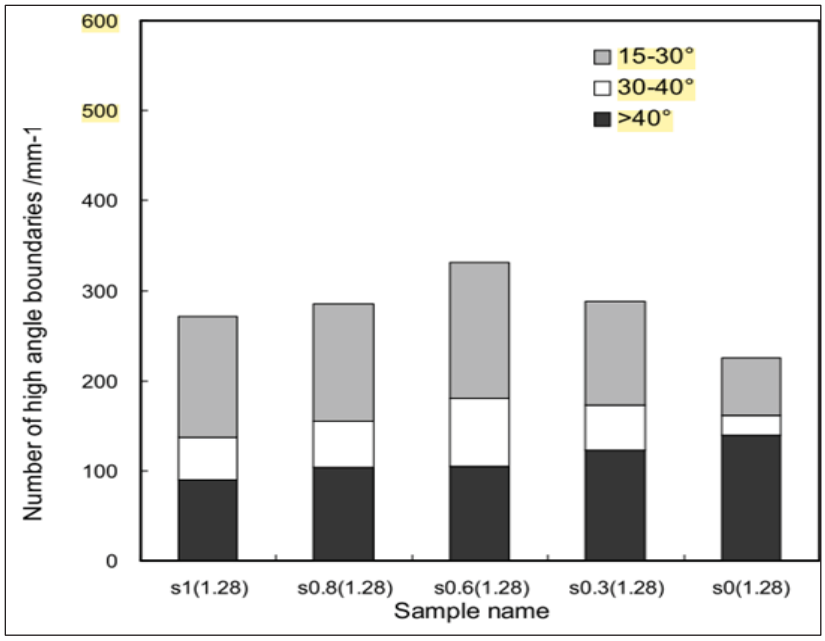

Figure 1.36 Influence of deformation routes on high angle grain boundaries
Taken from Sakai, Mori, & Utsunomiya, (2007)

1.6.3 Heterogeneity study

To compare FE analysis and experimental results under varying deformation conditions, the Coefficient of Variation (CoV) index is commonly used in the literature. The CoV value ranges from 0 to 1, where a value close to zero indicates a homogeneous distribution of parameters, and a value close to one indicates a heterogeneous or non-uniform distribution. The CoV provides a single numerical value for analyzing the output parameter results, enabling the assessment of homogeneity or heterogeneity. The CoV value is calculated using the mean and standard deviation (Johnson, Richard A., Irwin Miller, 2018). For simulation results, the heterogeneity index is computed for each element, thus encompassing the entire workpiece. Previous studies have used CoV, standard deviation, and mean to analyze heterogeneity during ring rolling processes (Anjami & Basti, 2010; Nayak, Kumar Singh, et al., 2023; Zhu, Yang, Guo, & Gu, 2012a). The CoV values enable the comparison of results and assist in determining the optimal combination of parameters that yields a homogeneous distribution of output results.

1.7 Gaps in literature, objectives and scope of the present work

1.7.1 Gaps in literature

A detailed review of the existing literature has indicated that there is a limited amount of data available on the effect of deformation path on damage and microstructure evolution during the open die forging process. Furthermore, the available literature does not address the influence of deformation path using combination of FE analysis and physical simulation of large size ingot forging. Additionally, the impact of deformation path on microstructure evolution and its effect on mechanical properties distribution during multi-step deformation has not been investigated.

Based on this comprehensive literature review, the following research gaps and opportunities for original contributions have been identified:

1. Limited data is reported on the influence of deformation path on microstructure evolution during open die forging large size ingot.
2. Very few articles reported on the influence of deformation path on damage evolution during open die forging.
3. Inadequate studies have been reported on the influence of the deformation path on the kinetics of recrystallization during open die forging.
4. No data is available on the effect deformation path on microstructure evolution and mechanical properties during the multi-step deformation of high strength tool steel.

1.7.2 Objective of the thesis

Considering the literature gaps reported above, the objectives of this thesis are proposed to address these gaps. The main objective and sub-objectives of this study are outlined as follows:

Main objective: Influence of deformation path on microstructure and damage evolution during open die forging of high strength steels.

To accomplish the main objective, the study is divided into the following three sub-objectives:

1. Examine the influence of deformation path on microstructure evolution during the open die forging of large size ingot of high strength steel during upsetting process.
2. Investigate the influence of deformation path on the stress state and damage evolution along the central axis of a large size ingot of high strength steel during the cogging process.
3. Examine the influence of deformation path on microstructure evolution and mechanical properties variation during multi-step deformation process of high strength steel.

This study is mainly divided into two parts: experimental work and finite element (FE) analysis. The scope of the study is discussed in detail in the following section.

1.8 Scope of the thesis

1.8.1 Physical simulations

Hot compression and tensile tests will be conducted using a Gleeble 3800 thermomechanical simulator. To develop a comprehensive material and microstructure model, hot compression tests will be performed on medium carbon low alloy high strength steel. The flow curves obtained from the hot compression tests will be utilized to develop the material and microstructure model for modified AISI P20 steel. Hot tensile tests will be carried out on AISI H13 steel to determine damage values within the relevant forging temperature range. And, the specimen dimensions before and after the deformation will be used to calculate damage values for AISI H13 steel.

To achieve the final sub-objective, physical simulations of a multi-step deformation process will be performed using the Gleeble 3800, with a special attachment, the MaxStrain unit. Multi-step deformation experiments will be conducted using two deformation paths, illustrated by

combining two die geometries: Flat-Flat and Concave-Concave. At the end of the experiments, the specimens will be analyzed for microstructure changes and mechanical property measurements.

1.8.2 Characterization

Hot compressed and multi-step deformed specimens will be sectioned parallel to the compression axis to facilitate a detailed study of microstructure evolution and mechanical property measurements. The heterogeneity in grain size distribution along the central cross-section of the compressed samples will be examined. Additionally, the average grain size will be calculated as a function of various process parameters. Furthermore, multi-step deformed samples will be used to investigate the influence of deformation path on both microstructure and mechanical properties. By comparing the results obtained from the two die geometries, the impact of deformation path on the final microstructure and mechanical properties will be evaluated.

1.8.3 FE analysis

The developed material and microstructure model will be integrated into FE software for the numerical simulation of the hot deformation and forging process. An FE model was created to simulate the hot compression test using Forge® NxT3.2. This model was then validated against measured flow stress and average grain size data obtained at different deformation conditions. The validated FE model will be scaled up to simulate large industrial ingots during open die forging processes, such as upsetting and cogging, using four deformation paths. The results from the FE analysis will be used to predict key parameters, including equivalent strain distribution, temperature distribution, DRX volume fraction, grain size distribution, and damage evolution under different deformation paths. By comparing these results, the optimal deformation path or die geometry for open die forging of steel can be identified. Additionally, an FE model was developed to simulate the multi-step deformation process and validated with measured grain size and hardness data. The validated FE model will be used to predict material

flow, DRX volume fraction, and grain size evolution after multi-step deformation employing two deformation paths.

CHAPTER 2

EXPERIMENTAL AND FE ANALYSIS METHODOLOGY

2.1 Introduction

This chapter provides a comprehensive overview of the experimental and simulation methodologies, tools and techniques utilized in the thesis work. The chapter is divided into two sections. The first section delves into the experimental techniques, covering the selection of materials, the preparation of specimens for the experiments, conduct of hot compression, hot tensile and multi-step deformation tests, mechanical and microstructure characterization of material. The second section focuses on the tools employed for the development and analysis of finite element (FE) models.

2.2 Industrial Forging Process

This research project was undertaken in collaboration with Finkl Steel, a steel forging company based in Sorel, Quebec, Canada. The material used in this investigation was supplied by Finkl Steel, Sorel. The steel manufacturing process began with the melting of scrap metal in an electric arc furnace, followed by refining and degassing steps to control the alloy composition. The molten metal was then poured into a casting mold to solidify into an ingot. Subsequently, the solidified ingot was transferred to a forging furnace, where it was heated to 1260 °C and soaked before the forging operation. The ingot was then subjected to open die forging using 5000 and 2000 metric-ton hydraulic presses, and the forging loads were compared with the FE predictions. Before the forging dies were preheated to 250 to 300℃. A Figure 2.1 illustrates the forging press at the industrial partner's facility.

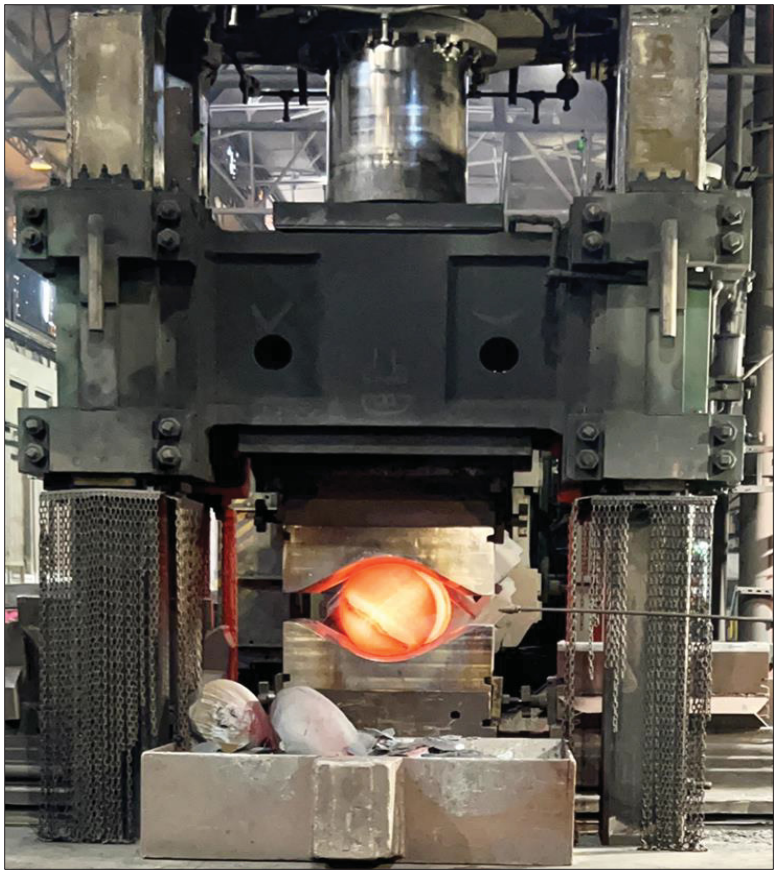

Figure 2.1 Hydraulic forging press at Finkl Steel, Sorel, Canada

2.3 Specimen preparation

To conduct hot deformation studies, samples were obtained from the central and quarter regions of the forged slab. The as-received material was in a double-tempered heat-treated condition, and its initial microstructure consisted of a bainitic phase. A schematic diagram provides a visual representation of the forged slab and Figure 2.2 shows the locations from where the samples were extracted. Compression and MaxStrain (multi-step deformation) specimens were machined by Finkl Steel in accordance with our specific requirements. Compression samples, each measuring 15 mm in height and 10 mm in diameter, and multi-step deformation samples, each measuring 196 mm x 15 mm x 15 mm, were prepared for the experiments. Hot tensile specimens were prepared from the center of AISI H13 forged bar of diameter 572 mm.

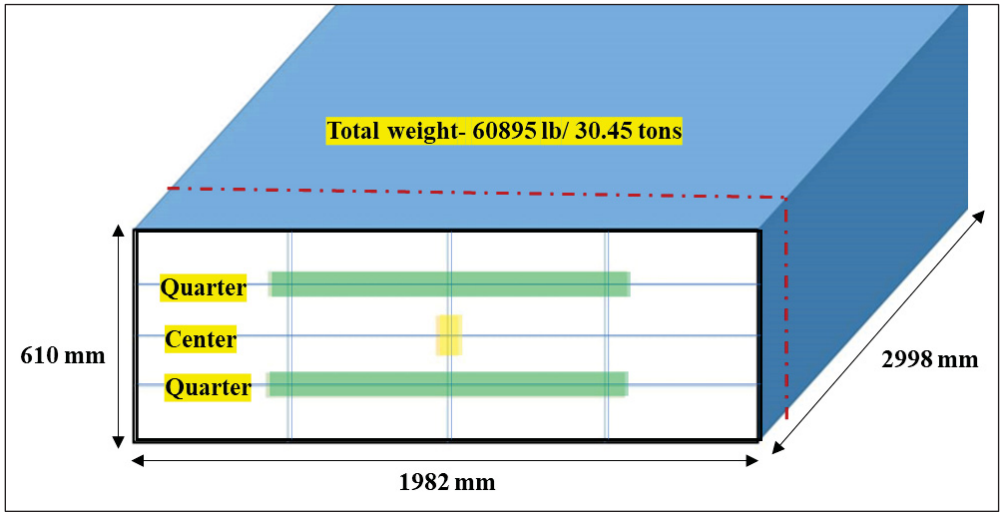

Figure 2.2 Schematic of the forged slab of modified AISI P20 steel and material location used for sample preparation

2.4 Hot deformation experiments

Hot deformation experiments were performed using the Gleeble 3800 thermo-mechanical simulator. Thermomechanical parameters used for these experiments were selected based on industrial condition such as, deformation rates, amount of deformation and temperatures. The following sections will deal with details of the experiments.

2.4.1 Compression tests

Three key parameters were considered for hot deformation testing: temperature, strain rate and strain. Ingot temperature was measured using a high-performance thermal camera to monitor the furnace and the entire open die forging process (Dourandish, 2022). Based on these measurements, a hot deformation temperature range of 1050°C to 1200°C was selected. Strain and strain rate data were extracted from press charts generated by a hydraulic press during actual open die forging operations. These charts provide a graphical representation of press position, load, and time. By analyzing the press position and time data, strain and strain rate were calculated for both single step and multi-step forging processes. The analysis of the actual

forging process revealed strain rates ranging from 0.001 s^{-1} to 0.01 s^{-1} and deformations between 35% and 45%. The experimental conditions were designed to encompass a broader range of strain rates, from 0.001 s^{-1} to 1 s^{-1}, and a deformation level of approximately 60% to comprehensively address the requirements of industry, academia, and scientific research. Figure 2.3 provides a detailed overview of the experimental setup, experimental plan and testing cycle.

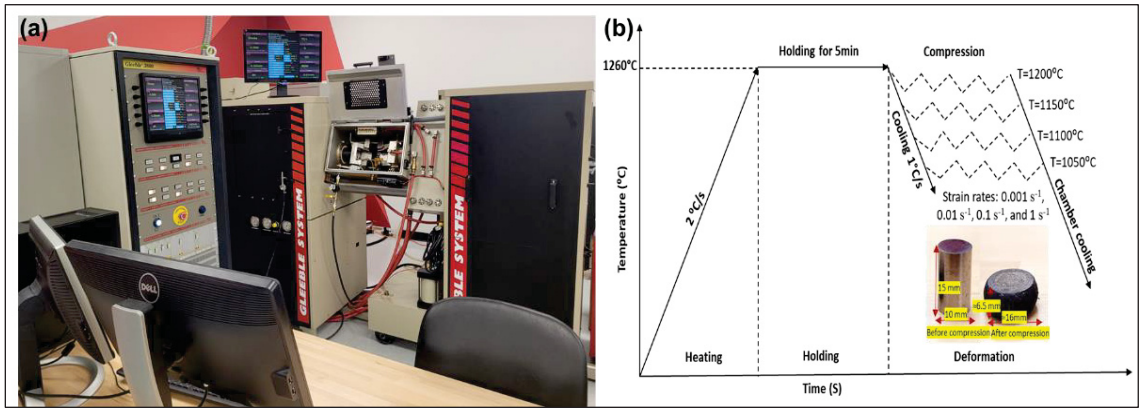

Figure 2.3 (a) Gleeble-3800 thermo-mechanical simulator (b) Shows the schematic of heating, holding and hot compression test cycle

Gleeble thermo-mechanical simulator heating is based on Joule effect. Passing the electric current through the material with resistance leads to generation of heat. Gleeble thermo-mechanical simulator is provided with feedback loop which can maintain temperature or increase/decrease the temperature by altering the current. So, to optimize the temperature gradient for given steel grade, trial test was needed. In total 18 heating and holding cycle tests were performed initially in order to optimize temperature gradient between center to end of specimens. Figure 2.4 shows the results for the 1st and 18th trial. The average temperature gradient between center and two end of specimens was reduced from 24°C to 6°C during these trials. During the trial tests, graphite sheet on the anvil assembly and the cooling rates of left and right jaw were optimized to reduce the temperature gradient for modified AISI P20 steel specimens. In the beginning, graphite sheet thickness was (0.254mm and 0.508mm), and it was optimized to (0.508mm and 1.016mm). Graphite sheet thickness is proportional to the heating resistance, as the thickness increases resistance in anvil assembly increases. Cooling rate for

the left and right Jaw was 0.7 Gallons per Minutes (gpm) and was optimized to 1gpm. Initially, in the trial tests, the soaking time of 10 minutes was applied, but later it was reduced to 5 minutes based on temperature gradient results obtained via the thermocouple attached to the center and end of the specimens. Material's thermal conductivity is the major reason behind such temperature difference. Hence, for the actual experiments 5 minutes soaking time was used as shown in Figure 2.4b.

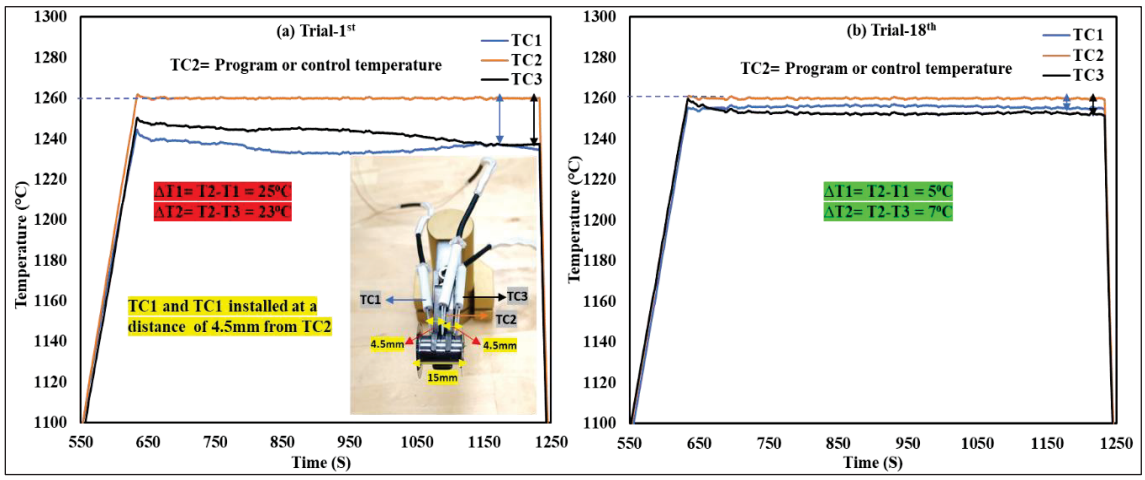

Figure 2.4 Temperature gradient optimization using three thermocouples (a) Temperature gradient during the 1st trail (b) Temperature gradient during the 18th trial

2.4.2 Tensile tests

The main objective of performing hot tensile experiments for AISI H13 steel specimens was to calculate the critical damage value for the forging temperature range for this steel. Tensile tests were performed at temperatures and strain rate range of 800-1200°C and $0.05s^{-1}$ respectively, as shown Figure 2.5a. For the precise measurement of the change in gauge length extensometer was used as shown in Figure 2.5b. Two tensile tests were performed at each temperature for repeatability. Specimen diameter were measured before and after the experiments (near to the fracture cross-section), as shown in Figure 2.5c. These experiments results and process of damage calculation are explained in the following chapter.

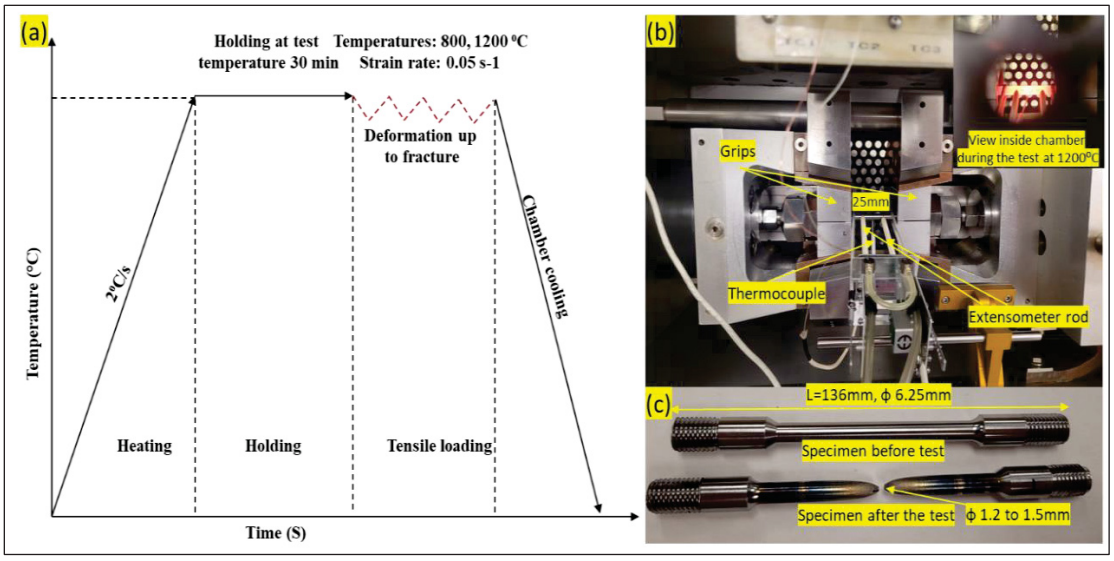

Figure 2.5 (a) Hot tensile testing cycle for AISI H13 steel (b) Tensile setup inside the Gleeble-3800 (c) Specimen before and after the test

2.4.3 Multi-step deformation tests

Multi-step deformation process was performed using the Maxstrain unit of Gleeble 3800 thermomechanical simulator. Figure 2.6a shows the experimental setup used for the multi-step deformation experiments. Figure 2.6b shows the schematic of the heating and multi-step deformation testing cycle with four deformation steps. Temperature and strain rate of 1150°C and 0.01 s^{-1} respectively were selected for multi-step deformation tests, based on the analysis of the hot compression test results. In order to investigate the effects of deformation paths, two die geometries: flat and concave were used in the experiments, based on our recent research findings (Dhondapure et al., 2024, 2023).

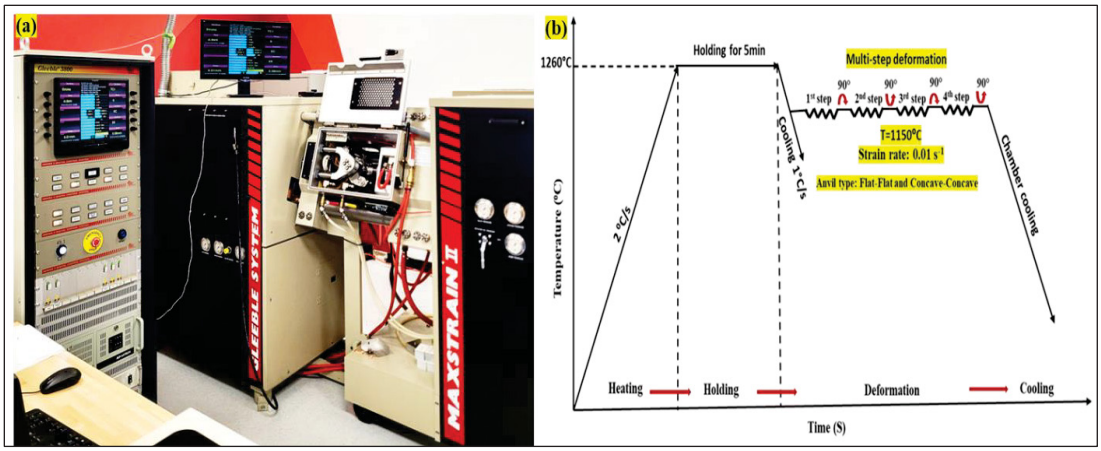

Figure 2.6 (a) Gleeble 3800 with MaxStrain module attachment (b) Multi-step deformation experimental plan and heating, testing cycle

For MaxStrain experiments, a type K thermocouple was attached with the specimen inside the hole using glue and cement. Prior to conducting the multi-step deformation tests, numerous trials were carried out to establish a reliable thermocouple installation procedure for stable temperature readings. Super glue and high temperature with cement were used in this process, as illustrated in Figure 2.7a-b. The installation process involved inserting them into a 3mm diameter hole. One to two drops of super glue were applied inside the hole to secure the ceramic tube against the wall of hole, and the glue was allowed to cure for ten seconds. Subsequently, high temperature cement was applied around the wires and over the specimen surface to seal the hole. The specimens were then left to air dry overnight for best results. Figure 2.7c shows the specimens before and after thermocouple installation. Once stable temperature was achieved via the thermocouple and the process was robust, the actual tests were conducted. By implementing the optimized thermocouple installation method and appropriate PID parameters, the temperature gradient between the programmed and measured temperatures was reduced from 23°C to 1°C.

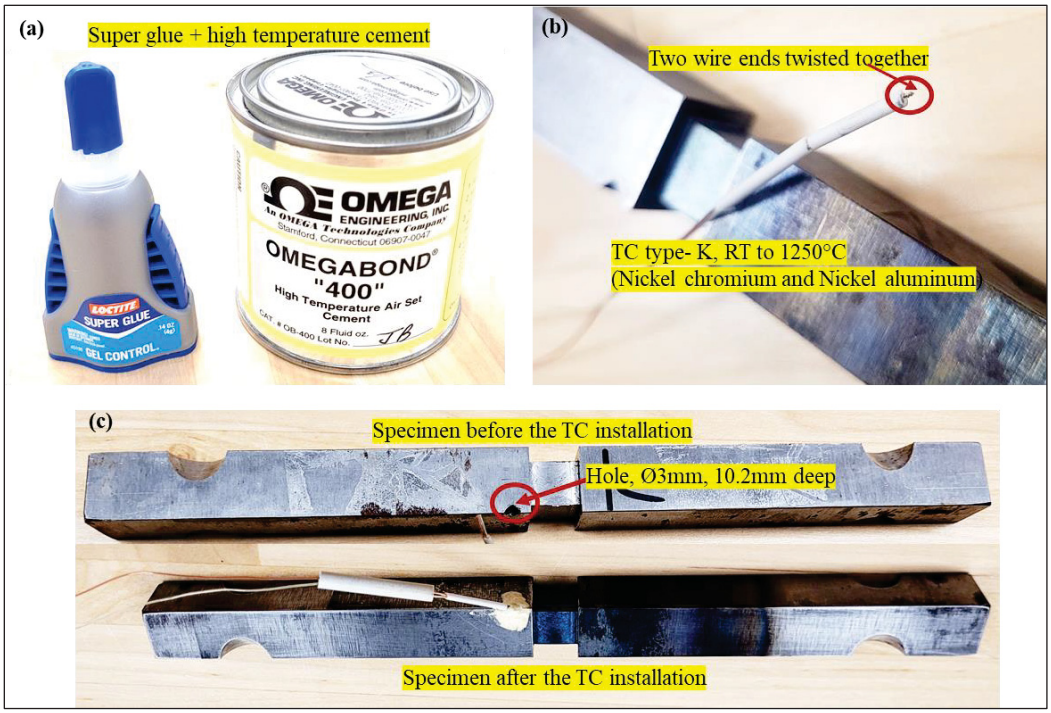

Figure 2.7 Thermocouple (TC) installation procedure for Maxstrain specimen (a) Super glue and high temperature cement (b) Twisted wire for installation (c) Specimen before and after TC installation

2.4.4 Samples preparation and Material characterization

After the completion of compression and multi-step deformation testing, specimens were sectioned parallel to the deformation axis using a precision cutting tool as shown in Figure 2.8a. During the cutting process, water-based coolant was employed to prevent the specimens from overheating. The sectioned specimens were then hot mounted using a Struers LaboPress as shown Figure 2.8b. Subsequently, the specimens were polished to a 1 µm finish using manual polishing machine, as shown in Figure 2.8c, following standard polishing procedures. After polishing, the specimens were thoroughly cleaned using an ultrasonic cleaner. Then the specimens were chemically etched with suitable etchant to reveal the grain boundaries and microstructure. Microstructural characterization was conducted using two primary techniques. Olympus LEXT OLS4100 laser confocal microscope was employed for optical microscopy, as shown in Figure 2.8d, while a Hitachi TM3000 scanning electron microscope was used for electron microscopy, as shown in Figure 2.8e.

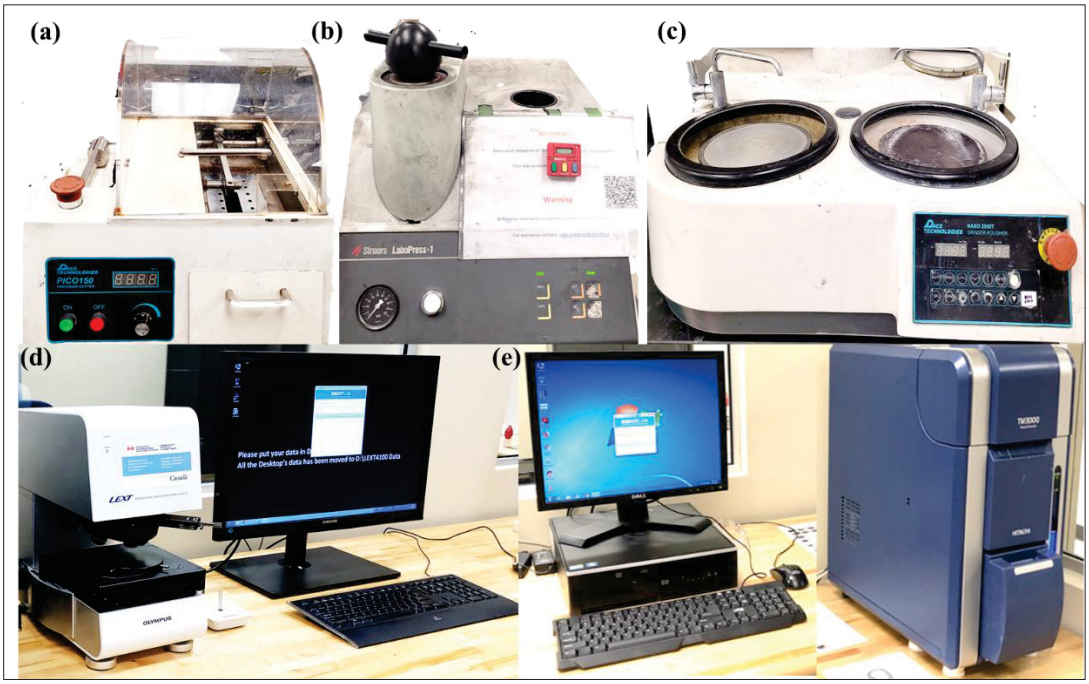

Figure 2.8 Equipment's used for sample preparation and imaging (a) Precision cutter (b) Hot mounting machine (c) Manual polishing machine (d) LEXT OLS4100 Optical microscope (e) TM300 Scanning electron microscope

2.4.5 Flow stress analysis and Material modelling

Gleeble thermomechanical simulator stores the flow stress data as origin file. These flow curves were plotted to visually analyze the influence of temperature and strain rate on flow stress. It is important to note that the raw flow stress data obtained directly from the Gleeble tests is influenced by factors such as friction and adiabatic heating. To accurately model the material and microstructure, it is necessary to eliminate these effects. Therefore, friction and temperature corrections were applied to the flow stress data. The detailed procedures for these corrections, as well as the subsequent material and microstructure modeling, are presented in Chapter 3.

2.5 Finite element modelling

In this investigation, Forge NxT software was selected over DEFORM-3D for the FE analysis of hot deformation and forging processes. Forge NxT offers several advantages, including a more user-friendly model setup, superior capabilities for predicting microstructural evolution and dynamic recrystallized grain size, and dedicated design features tailored specifically for the numerical simulation of bulk metal forming processes. A 3D FE model for the isothermal hot compression test, multi-step deformation and industrial open die forging were developed using the Forge NxT 3.2 software. Figure 2.9 shows the graphical user interface of the FE software with FE model setup for upsetting process with tetrahedron mesh. For remeshing criteria based on deformation was used and which value varies between 1.3 to 1.8. The proposed material and microstructure were implemented into the software using a user subroutine developed by Transvalor. This subroutine allows users to customize the material model and also provides the option to incorporate alternative material models in the numerical simulation.

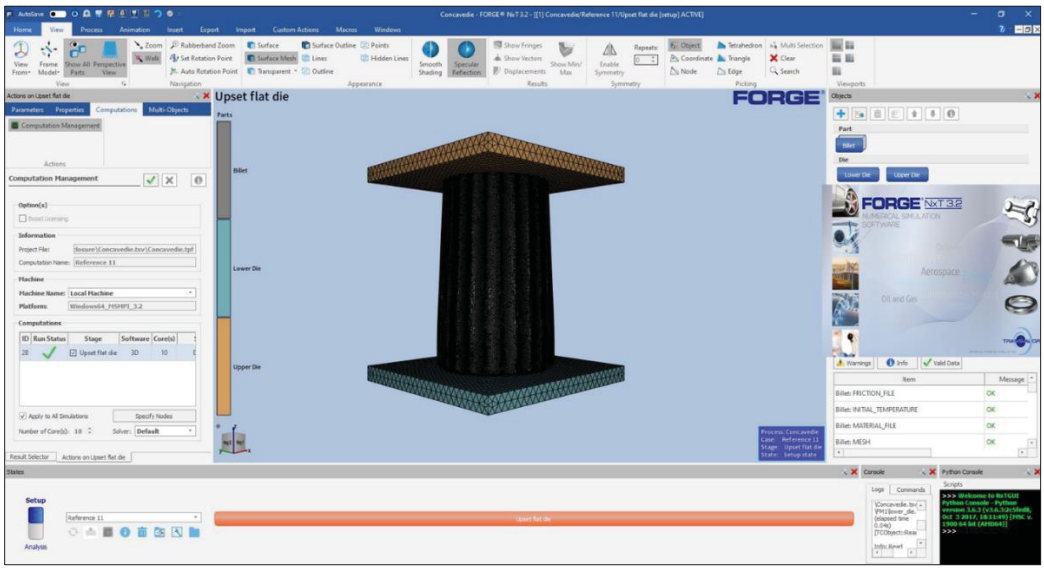

Figure 2.9 Graphical user interface of Forge NxT 3.2 FE analysis software

All required dies, workpieces and ingots 3D CAD models were developed using CATIA V5-6R2020 software and saved as Standard for the Exchange of Product (STP) file which is

supported by Forge NxT 3.2 software. Initially, several trial simulations were conducted to optimize the die curvature for concave and convex dies, as well as the V-die angle. The optimized die curvature was found to provide more homogeneous and higher level of deformation compared to the conventional flat die geometry, particularly in the Dead Metal Zone (DMZ). For further finite element (FE) analysis, the optimized die curvature and angles were utilized. A 3D FE model incorporating various deformation paths, represented by different die geometries, was developed to analyze industrial open die forging processes, such as upsetting and cogging. At the conclusion of the FE analysis, the results for all deformation paths were recorded and used for detailed analysis and interpretation. The specific inputs and boundary conditions applied for the FE analysis of both the hot deformation of lab scale samples and the open die forging of industrial scale processes are discussed in detail in the following chapters. For the numerical simulation of the lab scale hot compression test, an isothermal model was considered, with the die and workpiece maintained at the same constant temperature. In contrast, for the industrial upsetting and cogging simulations, different temperatures were assigned to the die and workpiece to replicate actual industrial conditions. Heat transfer between the die, workpiece, and the surrounding environment (air) was also modeled. However, in the FE model, the effects of thermal gradients on friction, deformation, microstructure, and damage evolution were not considered.

Following chapters present the results, outcomes, and conclusions for sub-objectives 1, 2, and 3, discussed in Chapters 3, 4, and 5, respectively. Chapter 3 focuses on the development of the material and microstructure model for modified AISI P20 steel and integration of developed models into the finite element (FE) software Forge NxT 3.2. The developed FE model is validated and scaled up for industrial upsetting process simulations to investigate the influence of the deformation path on microstructure evolution.

CHAPTER 3

INFLUENCE OF DEFORMATION PATH ON MICROSTRUCTURE EVOLUTION DURING THE OPEN DIE FORGING OF LARGE SIZE INGOT OF HIGH STRENGTH STEEL: EXPERIMENTS AND FE ANALYSIS

Prashant Dhondapure[a], Navneeth Rajakrishnan[a], Soumyarajan Nayak[b], Henri Champliaud[a], Jean-Benoit Morin[c], Mohammad Jahazi[a]

[a]Department of Mechanical Engineering, École de Technologie Supérieure, 1100 Notre Dame West, Montreal, Quebec H3C 1K3, Canada.
[b]Advanced Forming Research Centre (AFRC), University of Strathclyde, 85 Inchinnan Drive, Inchinnan, Renfrewshire, PA4 9LJ, UK.
[c]Finkl Steel-Sorel Inc., 100 McCarthy, Saint-Joseph-de-Sorel, Quebec J3R 3M8, Canada.

Paper published in *International Journal Advanced Manufacturing Technology,* September 2024

Summary

The inhomogeneity present in the deformation and microstructure during the open die forging of large size ingot significantly influences the mechanical properties of the final part. This study aims to develop a microstructure based finite element (FE) model and investigate the influence of deformation path on microstructure evolution during the upsetting process of large size ingot of a high strength steel. The difference in deformation path is achieved by modification in anvil shape such as flat, v shape, convex and concave die. To achieve this goal, hot compression tests were carried out on AISI modified P20 steel using the Gleeble 3800® Thermomechanical Simulator. Utilizing the acquired and corrected flow stress data, a material model and a microstructure model were established, and both formulated models were then integrated into the Forge NxT 3.2® finite element simulation software through the inclusion of a dedicated user subroutine. The predictions from the FE analysis were validated with

experimental results on standard size hot compression specimens, which allowed for the accurate prediction of the dynamic recrystallized average grain size at the end of hot deformation. Afterwards, the validated FE model was scaled up to simulate the industrial upsetting process, making it possible to investigate the effect of deformation path on inhomogeneity of strain and microstructure evolution at the end of upsetting process for large sized forged ingots. An evaluative analysis of four die geometries, aimed at identifying the optimal die shape for minimizing inhomogeneity in strain and grain size across a large size forged ingot, was conducted. It was found that the convex die provokes the lowest deformation, while the concave die induces the highest deformation values at the center of the ingot. Utilizing the Coefficient of Variation (CoV) as an indicator of heterogeneity, it was determined that the v-die and concave die resulted in a more consistent grain size distribution compared to the flat and convex dies.

3.1 Literature review

Large size forged blocks, of final dimensions 900 x 2050 x 3850 mm^3 and weighting over 40 metric tons, are manufactured from medium carbon high strength steels. These blocks are widely utilized in the automotive industry for manufacturing molding dies, particularly for bumper and dashboard production using the plastic injection process. The production process for large ingots typically involves steelmaking, succeeded by ingot casting, open die forging, and final heat treatment (K. Chadha, Ahmed, Aranas, Shahriari, & Jahazi, 2018; K. Chadha et al., 2017; Mha et al., 2023; Murugesan & Jung, 2019). The slow solidification of large size ingots often results in casting defects such as an uneven microstructure, macro segregation, cavities, voids, inclusions etc. These defects exert a substantial impact on the mechanical properties of the final products (Ghodrati et al., 2022).

Forging plays a pivotal role in mitigating casting defects (Dhondapure et al., 2023; Dourandish et al., 2022). The primary objective of forging is to achieve the desired shape while obtaining specific microstructural attributes. Essential thermomechanical parameters, including the heating rate to the forging temperature, holding time in the furnace, percent deformation, and

deformation rate, must be carefully controlled to attain a favorable microstructure and optimal mechanical properties throughout the thickness of the large forged component (Dasari et al., 2023). The open die forging process primarily consists of hot compression, where work strengthening effects such as hardening (WH) and precipitation occur concurrently with softening phenomena like recovery and recrystallization under dynamic thermomechanical loads (Ebrahimi et al., 2017; Tavakoli, Mirzadeh, & Zamani, 2019). The formation of finer grains during the forging is primarily attributed to static recrystallization (SRX) and dynamic recrystallization (DRX). The magnitude and intensity of these phenomena are significantly influenced by three macroscopic factors: strain, strain rate and temperature (Rudra et al., 2019; Tian, Chadha, & Aranas, 2023; Zeng, Hu, Peng, Hu, & Xiao, 2022). Certainly, achieving a homogenous distribution of strain and grain sizes in hot deformation regions is feasible in small to medium sized bars and slabs (Geisler, Sadeghifar, Morin, Loucif, & Jahazi, 2023). However, in the case of ingots with larger diameter and thickness exceeding 800 mm, it is common to encounter inhomogeneity in grain size distribution. These variations frequently give rise to irregularities in mechanical properties, which may lead to rejection of parts (Bontcheva & Petzov, 2003).

In addition to the aforementioned parameters, the deformation path is also a crucial factor. It is dependent upon equipment specifications, such as ingot and die geometries (Dudra & Im, 1990; Marcin Kukuryk, 2024). The deformation path significantly impacts the distribution of strain, and therefore microstructure evolution, and ultimately the final mechanical properties of the material (Dasari et al., 2023; Dourandish et al., 2022). A crucial aspect of designing optimal open die forging processes for industry involves a thorough understanding of the interaction between process and geometrical parameters and their impact on microstructure evolution, which ultimately affect the final mechanical properties. Therefore, it is important to consider deformation path illustrated by different die geometries for a comprehensive analysis of microstructure evolution during open die forging, utilizing both finite element analysis and experimental approaches (Markov, Perig, Zlygoriev, Markova, & Grin, 2017).

Kukuryk et al. (Marcin Kukuryk, 2020, 2024) investigated the impact of different die geometries, including flat, convex, and angle shaped anvils, on void closure and the evolution of stress-strain states during the cogging process of a X5CrNi18-10 stainless steel and a X32CrMoV12-28 die steel. He reported that altering the die geometry enhanced the equivalent strain level and overall homogeneity in strain distribution and absence of tensile stresses at the center, contributing to improved forging outcomes. Christiansen et al. (Christiansen, Hattel, et al., 2014; Christiansen, Martins, Bay, & Hattel, 2014) examined the impact of varying lower anvil v-die angles (ranging from 60º to 180º) on porosity and void closure through laboratory scale experiments. Their findings indicated that utilizing a v-die angles of 120° and 150° led to the closure of centerline porosity and high amount deformation compared to other die angles. Zhang et al. (X. Zhang et al., 2012) studied the effects of different die geometries on void closure through a multiscale finite element analysis of a large size ingot. Their findings indicated that the cymbal shape and v-die configurations successfully closed voids at the center and near the die surface during the upsetting and cogging processes, respectively. Dudra et al. (Dudra & Im, 1990) investigated the impact of v-die and flat dies on void closure, focusing on the levels of equivalent strain and hydrostatic stress at the center of the ingot during open die forging. The study concluded that the criteria based on equivalent strain provided a more effective indicator of void closure, and the use of a v-die contributed to enhanced strain in the deformation region, specially at the center. Tamura et al. (Tamura & Tajima, 2003) examined the influence of anvil surface curvature on the Dead Metal Zone (DMZ) using a 3D rigid plastic finite element (FE) analysis during open die forging. They found that a smaller radius of curvature on the anvil surface significantly improved the DMZ near the die surface. The authors concluded that varying the anvil surface curvature contributes to the elimination or reduction in the size of the DMZ. In a recent research article Kukuryk (Marcin Kukuryk, 2024) studied the effects of three anvil shapes–flat, angled (v-die) and three radius die–on void closure and deformation distribution during the cogging process of a 55NiMoV7. The author concluded that angled anvils were more effective for void closure and three radius anvil produced high uniformity in the strain distribution in the deformation region. In their research Chen et al. (F. Chen, Ren, Chen, Cui, & Ou, 2016) studied the effect of inhomogeneity on final microstructure and defects, and employed numerical simulation to analyze the upsetting

process of a X20Cr13 steel with laboratory scale specimens. Their findings highlighted the impact of inhomogeneity in strain distribution on the dynamic recrystallization (DRX) volume fraction and grain size distribution after the forming process, and confirmed that with higher inhomogeneity, defects rise in the formed part.

The above analysis of the scientific literature illustrates the existence of direct and robust correlations between the deformation, deformation path, and void closure in the forged workpiece and the successful application of FEM to the analysis of the deformation process. However, few studies are available on the impact of the deformation path on inhomogeneity of the strain distribution and microstructure evolution during open die forging of large size ingots.

The present research aims to address this gap and investigates the influence of deformation path on strain distribution, DRX volume fraction and DRX grain size evolution during the upsetting stage of open die forging of an industrial scale ingot. A precise constitutive and microstructure model was developed for a high strength steel, characterizing the flow stress with respect to hot working variables such as strain, strain rate, and deformation temperature. The adjustment of the actual stress from the measured stress, accounting for deformation heating and friction effects, was incorporated. An evaluation was conducted, contrasting the experimental flow stress data with those calculated using the formulated constitutive equations. A constitutive and microstructure model was integrated into the Forge NxT 3.2® finite element analysis code using an adapted user subroutine. The finite element model was created and validated for the examination of hot compression tests, and the validated model was then scaled up to analyze the upsetting process for an industrial size ingot for various deformation paths. Predictions were made regarding the distribution and variation of equivalent plastic strain, temperature, DRX volume fraction, and DRX grain size.

3.2 Material and experimental procedure

3.2.1 Material

AISI modified P20 steel utilized in this study was sourced from Finkl Steel, located in Sorel, Quebec, Canada. The chemical configuration of the investigated steel is outlined in Table 3.1. The steel manufacturing process commenced with the melting of scrap metal in an electric arc furnace, followed by refining and degassing to control the alloy composition. The molten metal was then poured into a casting mold and allowed to solidify. Subsequently, the solidified ingot was transferred to the forging furnace, where it was heated to 1260 °C and soaked prior to the forging operation. After forging, the ingot was subjected to post forging heat treatment processes to achieve the desired mechanical properties. Compression test samples were machined from both the center and quarter locations of a 610 mm (24 inch) thick rectangular slab of width 1981 mm (78 inch).

Table 3.1 Constituent elements of AISI modified P20 steel (%wt.)

Elements	C	Mo	Mn	Ni	Si	Cr	Cu	Balance
Weight%	0.31	0.51	0.90	0.70	0.35	1.85	0.15	Fe

3.2.2 Isothermal hot compression tests

The selection of hot compression test parameters aimed at replicating real world industrial forging practices. Ingot temperature was monitored using a thermal camera throughout the forging process. To ascertain strain and strain rate, hydraulic press data capturing press pressure and position during forging were analyzed. This data enabled determination of applied strain and strain rate for each time segment, which guided the design of laboratory scale trials. Cylindrical specimens measuring 10 mm in diameter and 15 mm in height were fabricated from the industrial sized forged bar. These specimens were then utilized in high temperature hot compression tests using the Thermomechanical Simulator, Gleeble 3800®, given in Figure

3.1. The experiments were conducted over a temperature range of 1050 °C to 1200 °C and at strain rates ranging from 0.001 s^{-1} to 1 s^{-1}. The empirical data obtained from the experiments were employed in developing a constitutive material and microstructure model for predicting flow stress, strain distribution and DRX grain size evolution, subsequently applied to model the upsetting process.

As depicted in Figure 3.2, the cylindrical specimens underwent heating to the desired temperature at a rate of 2 °C/s under vacuum conditions. Following this, they were held at the target temperature for 5 minutes to ensure uniform temperature distribution. Subsequently, the specimens were gradually cooled at a rate of 1 °C/s until they reached the testing temperature prior to initiating the deformation process. Succeeding the 60% compression deformation, the specimens underwent chamber cooling to room temperature. Figure 3.2 shows the photograph of the specimen before and after deformation.

Figure 3.1 The thermomechanical simulator, Gleeble 3800®, used for the high temperature isothermal compression tests

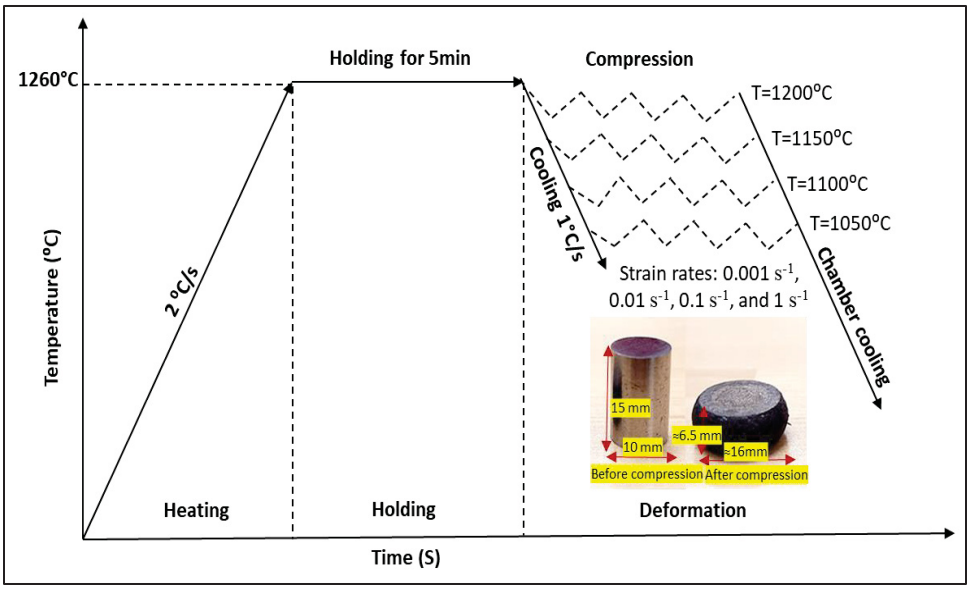

Figure 3.2 The diagram shows the heating, holding and hot compression testing cycle

3.3 Flow stress analysis and corrections

The flow curves resulting from hot compression experiments conducted at various strain rates and deformation temperatures are displayed in Figure 3.3. Notably, the stress-strain curves exhibited significant sensitivity to changes in strain rate and temperature. The flow curves demonstrated a pronounced decrease with rising temperature, while, at a constant temperature, an increase in the strain rate resulted in an increase of the flow stress. Examining the stress-strain curves in Figure 3.3 revealed the existence of three distinct stages of stress changes with increasing strain. In the initial phase of deformation, there was a notable stress increase primarily because of work hardening up to the peak. Subsequently, after the work hardening, the flow stress consistently decreased after a peak point. This indicated a growing prevalence of thermal softening, attributed to dynamic recovery (DRV) and dynamic recrystallization (DRX). The softening stage displayed three distinct stress patterns as strain increased: a) A gradual decline leading to a stable state, accompanied by DRV/DRX softening, was noticeable. This trend was evident across all deformation strain rates and temperatures ranging from 0.001 s^{-1} to 0.1 s^{-1}, excluding 1050 °C and 1100 °C; b) At 1050°C, 1100 °C, and at strain rate of 0.1 s^{-1}, elevated stress levels were observed with minimal softening and observable work

hardening; and c) A continual rise with notable work hardening occurs at all temperatures and highest strain rate 1 s^{-1}, which specifies softening resulting from DRX, identified by a flow curve exhibiting a single crest succeeded by stable flow stress (example: black and red curves in Figure 3.3, transpires at elevated temperatures and reduced strain rates (Tize Mha et al., 2023). Conversely, for deformations performed under higher strain rates and decreased temperatures, the heightened rate of work hardening hinders the softening influence of DRX. As a results, both the peak stress and the onset of stable flow stress shift to higher strain levels. The decrease in stress, as illustrated in Figure 3.3, is attributed to the manifestation of DRX across all temperatures and strain rates within the range of 0.001 s^{-1} to 0.1 s^{-1}.

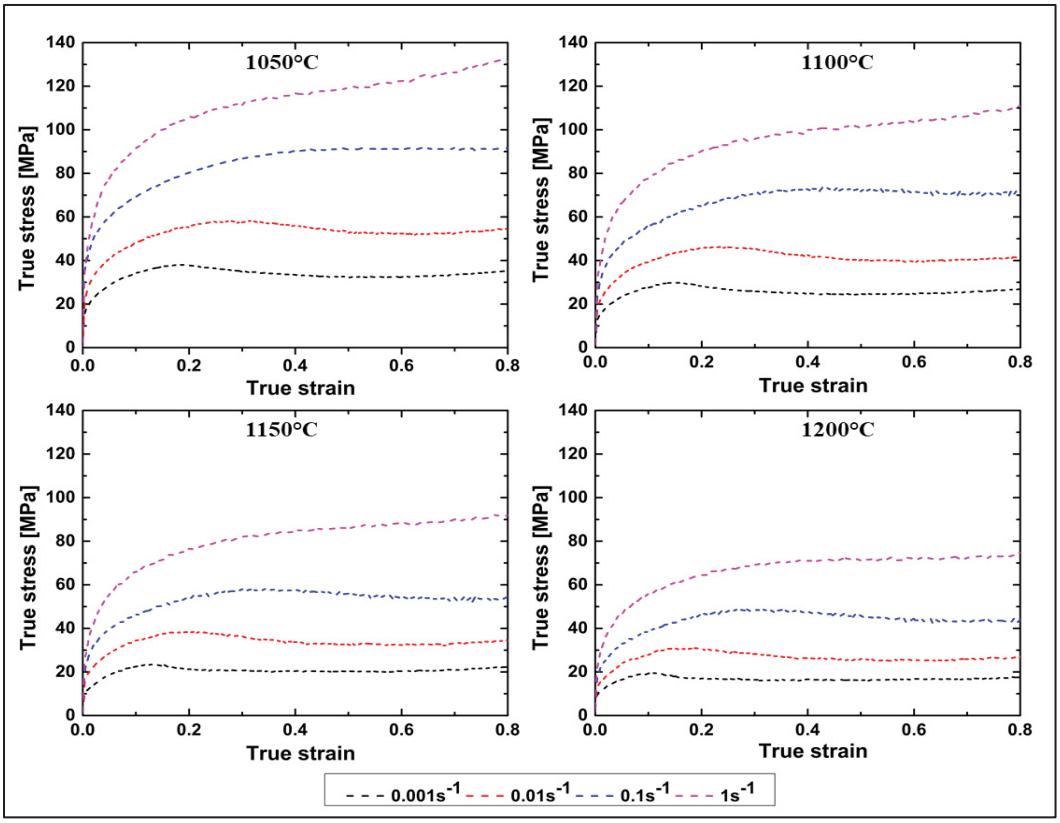

Figure 3.3 Flow stress curves of medium carbon high strength steel obtained from hot compression test

3.3.1 Flow stress correction for the adiabatic heating

In the course of a hot compression test, a fraction of the accumulated deformation energy converts into heat, leading to temperatures surpassing the nominal value (Saksala, 2019). This temperature differential, intricately connected to the applied strain rate, could introduce inaccuracies in stress measurements conducted by the apparatus, demanding correction. When dealing with lower strain rates, the extended deformation duration provides ample time for the dissipation of the generated heat into the environment, classifying the flow behavior as occurring under isothermal conditions (F. Chen et al., 2016; Dourandish et al., 2024). Contrastingly, at higher strain rates, the heat produced during deformation cannot completely dissipate from the sample, gets trapped and results in rise in temperature. In such instances, the process is considered adiabatic. To rectify the adiabatic heating effect, the following expression Equation 3.1, proposed in (S. Li, Li, He, & Wang, 2019) was used:

$$\Delta T = \frac{0.95\,\eta}{\rho C_p}\int_0^{\varepsilon}\sigma d\varepsilon \tag{3.1}$$

Where, C_p denotes the specific heat, ρ represents the material density, σ stands for the flow stress, ε represents the strain, and η signifies the thermal efficiency. The density (ρ) and specific heat (C_p) of the studied steel were determined for different temperatures using JMatPro® simulation software (Castellanos, Rieiro, Cars, Muoz, & Ruano, 2007). Temperature increments were computed utilizing Equation 3.1 over a range of strain values from 0 to 0.8.

$$\Delta\sigma = \frac{Q}{\alpha\, n_1 R}\left(\frac{1}{T_n + \Delta T} - \frac{1}{T_n}\right) \tag{3.2}$$

Where, $\Delta\sigma$ represents the change in flow stress due to the adiabatic heating, Q denotes the activation energy of hot deformation, α and n_1 are the material constants, R represents universal gas constant, T_n, test or measured temperature and ΔT, change temperature due to the adiabatic heating. The change in flow stress is calculated using the expression in Equation

3.2. At the lowest strain rates of 0.01 s^{-1} and 0.001 s^{-1}, and across all temperatures, adiabatic heating was observed to be less than 1 °C. Consequently, it was not taken into consideration for the calculation. The variations in ΔT and Δσ with respect to ε̇ are depicted in Figure 3.4 for specimens deformed at different deformation rates and temperatures. It is observed that as the temperature decreases and the strain rate increases, adiabatic heating and changes in flow stress value also increase. At the lowest temperature of 1050 °C and the highest strain rate of 1 s^{-1}, the maximum adiabatic heating was observed, with a temperature increase of approximately 14 °C and a change in flow stress of about 12 MPa. Given the hot compression temperature range of 1050 °C to 1200 °C, a 14 °C increase in temperature will not significantly affect grain size evolution. Therefore, this temperature rise was not considered in the microstructure evolution study.

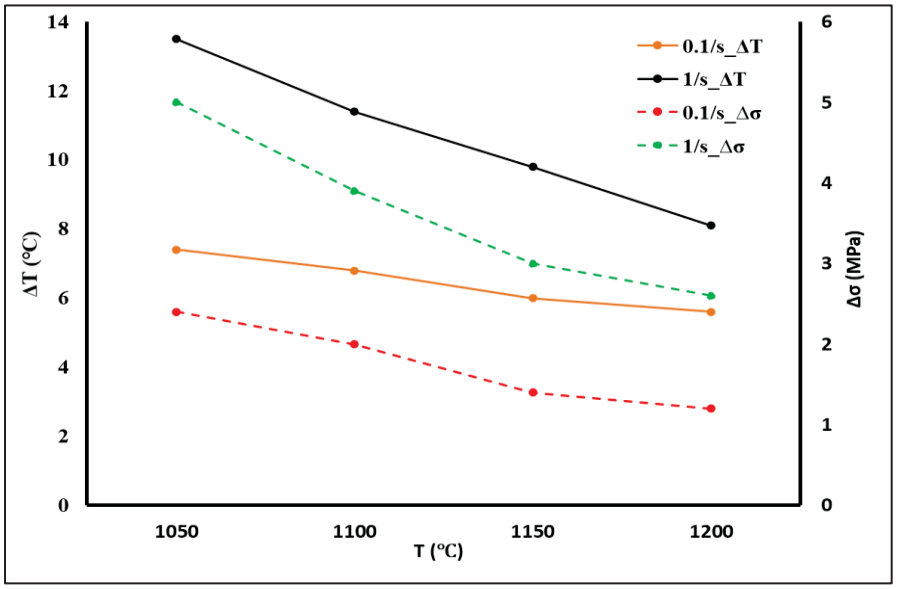

Figure 3.4 Increase in temperature and reduced stress values due to the adiabatic heating during hot compression testing

3.3.2 Flow stress correction for the friction

The friction between the anvil and specimen at their interface results in the formation of a stagnant region, inducing uneven deformation and, subsequently, introducing errors in the assessment of flow stress during hot compression tests. Despite the integration of tantalum

sheets to mitigate friction, the influence of friction between the anvil and specimen becomes increasingly prominent as the strain increases (Nasraoui, Forquin, Siad, & Rusinek, 2012; Saksala, 2019). Figure 3.5 illustrates a schematic representation of the compression test specimen geometry before and after the test with the geometrical parameters. Table 3.2 provides important geometrical parameters used in the friction correction calculation. In order to calculate the difference in flow stress, we initially calculated the friction coefficient using the relevant expression used for the calculation of friction and corrected the flow stress using the expressions given below Equations 3.3 to 3.6 (Y. P. Li, Onodera, Matsumoto, & Chiba, 2009).

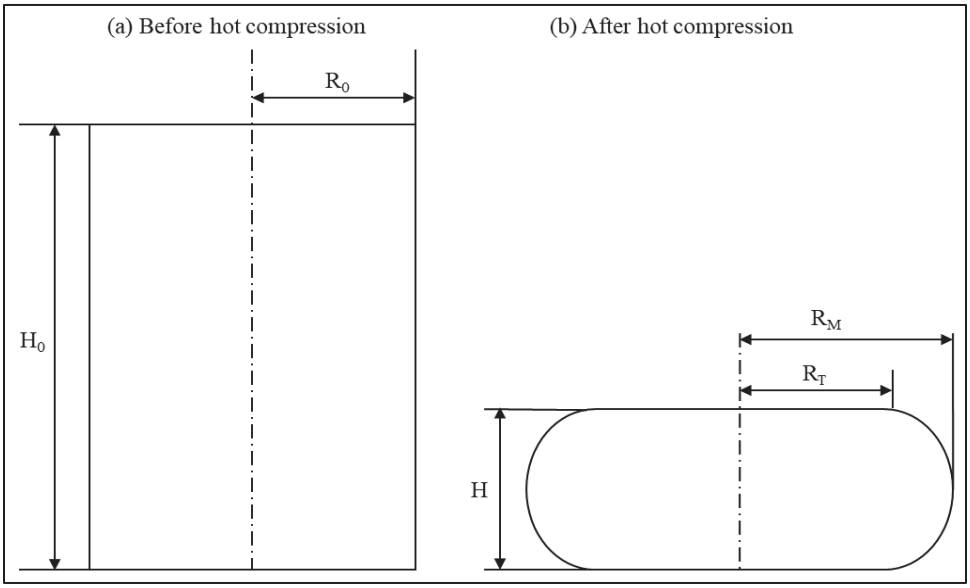

Figure 3.5 The schematic of specimen geometry: **a** before hot compression and, **b** after hot compression test

Barreling factor:

$$B = 4\,\frac{\Delta R}{R}\,\frac{\mathrm{H}}{\Delta H} \tag{3.3}$$

Radius (mm) :

$$R = R_0 \times \sqrt{\left(\frac{H_0}{H}\right)} \tag{3.4}$$

Friction coefficient:

$$\mu = \frac{\left(\frac{R}{H}\right) B}{\left(\frac{4}{\sqrt{3}}\right) - \left(\frac{2b}{3\sqrt{3}}\right)} \tag{3.5}$$

Corrected stress (MPa):

$$\sigma_f = \frac{\sigma}{\{1 + \left(\frac{2}{3\sqrt{3}}\right) \times \mu \times \left(\frac{R_0}{H_0}\right) \times e^{\left(\frac{3\varepsilon}{2}\right)}\}} \tag{3.6}$$

Table 3.2 Important parameters used for the friction correction

Notations	Signifies
R_0	Initial radius of the cylinder
H_0	Initial height of the cylinder
H	Height after the deformation
R_M	Maximum radius after the deformation
R_T	Top radius after the deformation
μ	Friction coefficient
B	Barreling factor
ΔH	Difference between initial and final height
ΔR	Difference between maximum and top radius
ε	Amount of deformation
σ	Measured flow stress
σ_f	Friction corrected flow stress

The modified flow curve diagrams, accounting for both adiabatic heating and the impact of friction, are depicted in Figure 3.6. It was observed that experimental flow stress curves surpass the adjusted ones, signifying that friction has a more prominent influence on flow stress compared to adiabatic heating. Consequently, the adjusted flow stress curves were utilized in formulation of the constitutive and microstructure model in the following section.

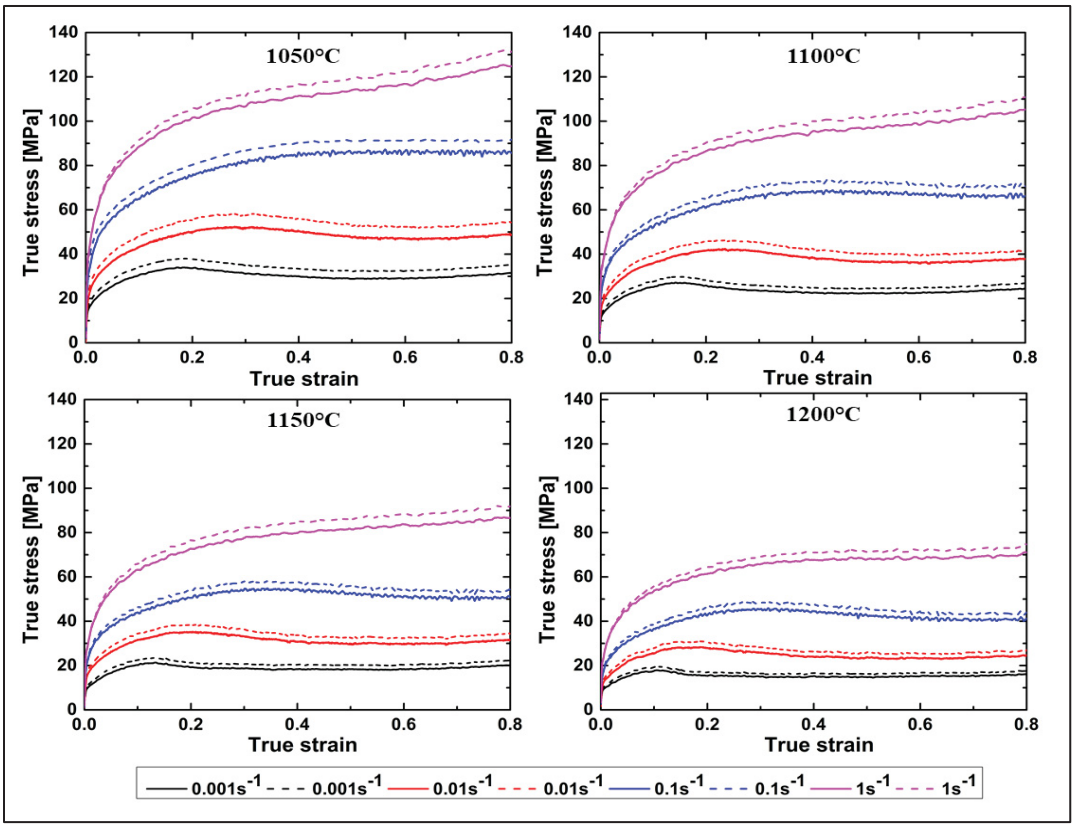

Figure 3.6 Flow stress curves measured (dashed) and corrected (solid) for both adiabatic heating and friction

3.4 Identification of constitutive law parameters

3.4.1 The Arrhenius model

The constitutive model by C.M. Sellars and W.J. McTegart in 1966 established a relation between essential parameters governing hot deformation, such as temperature, strain rate and activation energy, while maintaining a constant deformation value (C.M. Sellars & W.J. McTegart, 1966). This correlation is expressed in Equation 3.7, wherein the Zener-Hollomon parameter is denoted as Z.

$$Z = \dot{\varepsilon}\, exp\left(\frac{Q}{RT}\right) \tag{3.7}$$

Within the provided formula, Q denotes the activation energy (in $kJ.mol^{-1}$), R represents the universal gas constant (in $kJ.mol^{-1}.K^{-1}$), and α, n and A denote material constants.

The Arrhenius constitutive model established the relationship among deformation temperature, strain rate, and flow stress, as described by Equation 3.8:

$$\dot{\varepsilon} = AF(\sigma)\exp\left(-\frac{Q}{RT}\right) \tag{3.8}$$

Here, F(σ) denotes either a power function or an exponential function or a hyperbolic sine function, as explained below by Equation 9:

$$F(\sigma) = \begin{cases} \sigma^{n_1} & (\alpha\sigma < 0.8), \\ \exp(\beta\sigma) & (\alpha\sigma > 1.2), \\ [\sinh(\alpha\sigma)]^n & (For\ all\ \sigma). \end{cases} \tag{3.9}$$

Where, A, n, β, n_1, α = material constants, $\alpha = \frac{\beta}{n_1}$

Integration of the aforementioned equations yielded the formulation for the ultimate flow stress, predominantly depending on the values of α, Z, A, and n. These particular material constants were determined through regression analysis using flow stress curves acquired from hot compression experiments conducted at different rates of strain and temperatures. Table 3.3 provides the material parameters for the Arrhenius model, and the expression in Equation 10 delineates the resultant flow stress.

Table 3.3 P20 steel material constants for the Arrhenius constitutive model

$\beta(MPa^{-1})$	n_1	$\alpha(MPa^{-1})$	n	$Q(K\ J\ mol^{-1})$	$lnA\ (s^{-1})$
0.0985	4.5923	0.02146	3.3898	334.5	24.76

$$\sigma = \frac{1}{\alpha} ln \left\{ \left(\frac{Z}{A}\right)^{\frac{1}{n}} + \left[\left(\frac{Z}{A}\right)^{\frac{2}{n}} + 1 \right]^{1/2} \right\} \tag{3.10}$$

The material constants listed in Table 3.3 were established without considering the impact of strain. As depicted in Figure 3.3, as the strain increases from 0.01 to 0.8, the material's flow stress exhibits both hardening and softening behaviors. Consequently, the impact of strain on flow stress and material behavior becomes substantial, underscoring the necessity to consider the effect of strain. To address this, a modified Arrhenius or strain compensated model was introduced (Yin & Wu, 2022). The material constants α, n, Q, and A were expressed as functions of strain, utilizing polynomial functions of strain with degrees ranging from 1 to 4, as shown in expressions Equations 3.11 to 3.14. Table 3.4 provides the material coefficients for the strain compensated model, in addition to the constants of the polynomial function.

$$\alpha = B_0 + B_1\varepsilon + B_2\varepsilon^2 + B_3\varepsilon^3 + B_4\varepsilon^4 \tag{3.11}$$

$$n = C_0 + C_1\varepsilon + C_2\varepsilon^2 + C_3\varepsilon^3 + C_4\varepsilon^4 \tag{3.12}$$

$$Q = D_0 + D_1\varepsilon + D_2\varepsilon^2 + D_3\varepsilon^3 + D_4\varepsilon^4 \tag{3.13}$$

$$lnA = E_0 + E_1\varepsilon + E_2\varepsilon^2 + E_3\varepsilon^3 + E_4\varepsilon^4 \tag{3.14}$$

Table 3.4 Constant of polynomial equation for modified Arrhenius model

α	n	Q($\times 10^3$)	lnA
$B_0 = 0.0253$	$C_0 = 5.9623$	$D_0 = 0.2600$	$E_0 = 0.0192$
$B_1 = -0.0178$	$C_1 = -18.4751$	$D_1 = 2.2695$	$E_1 = 0.1790$
$B_2 = -0.0066$	$C_2 = 68.9920$	$D_2 = -13.2845$	$E_2 = -1.0654$
$B_3 = 0.1406$	$C_3 = -142.0610$	$D_3 = 28.9781$	$E_3 = 2.3443$
$B_4 = -0.1731$	$C_4 = 114.7900$	$D_4 = -21.7864$	$E_4 = -1.7682$

3.4.2 Hansel-Spittel model

The Hansel-Spittel model is a phenomenological material model employed to foresee material responses under conditions of elevated temperature deformation. This model is dependent on temperature, strain and strain rate variations (Nalawade, Puranik, Balachandran, Mahadik, & Balasubramanian, 2013). It takes into account both material strengthening and softening phenomena that occur during the hot deformation process (Niu et al., 2022). Equation 3.15 provides the mathematical expression for the Hansel Spittel model, that highlights the relation between flow stress and the inherent material parameters.

$$\sigma = A_o e^{m_1 T} \varepsilon^{m_2} \dot{\varepsilon}^{m_3} e^{\frac{m_4}{\varepsilon}} (1+\varepsilon)^{m_5 T} e^{m_6 \varepsilon} \dot{\varepsilon}^{m_7} T^{m_8} \tag{3.15}$$

Where, σ = stress (MPa), $\dot{\varepsilon}$ = strain rate (s^{-1}), ε = strain, T= hot deformation temperature (°C) and A, m_1 to m_8 are the material parameters. Table 3.5 shows the material parameter values for Hansel-Spittel constitutive model.

Table 3.5 Material parameters for Hansel-Spittel model

A	m_1	m_2	m_3	m_4	m_5	m_6	m_7	m_8
137.95	-0.0359	0.337	0.0108	-0.001	-0.002	-0.659	-2.538	0.625

3.4.3 Assessment of the developed constitutive model

Figure 3.7 illustrates a comparison of the precision and correlation between experimentally obtained and predicted flow stress values using two distinct constitutive models. Figure 3.7a-b specifically showcase predictions made by the Arrhenius and Hansel-Spittel models, respectively. The assessment involves the examination of the average absolute relative error (AARE) and R-square values. AARE values, calculated through Equation 3.16, served as a

metric to evaluate the efficacy of flow stress predictions made by both models (Nayak et al., 2020). The AARE values for the Arrhenius and Hansel-Spittel models were determined to be 3.4% and 6.5%, respectively. Furthermore, R-square values, calculated using the linear fit method to assess the correlation between experimental and predicted flow stress, were found to be 0.9940 and 0.9750 for the Arrhenius and Hansel-Spittel models, respectively.

$$AARE = \frac{1}{N}\sum_{i=1}^{i=N}\left|\frac{\sigma_x^i-\sigma_y^i}{\sigma_x^i}\right|\times 100 \tag{3.16}$$

Where, σ_x and σ_y represents the experimental and predicted flow stress value respectively. Hence, considering the AARE and R-square values, the predictions of the Arrhenius model demonstrated a higher level of accuracy, closely aligning with the measured flow stress values compared to the Hansel-Spittel model. Therefore, the Arrhenius model was incorporated into the Forge NxT 3.2® software to model the forging process and predict the flow stress, strain, and temperature distribution map upon completion of the forging.

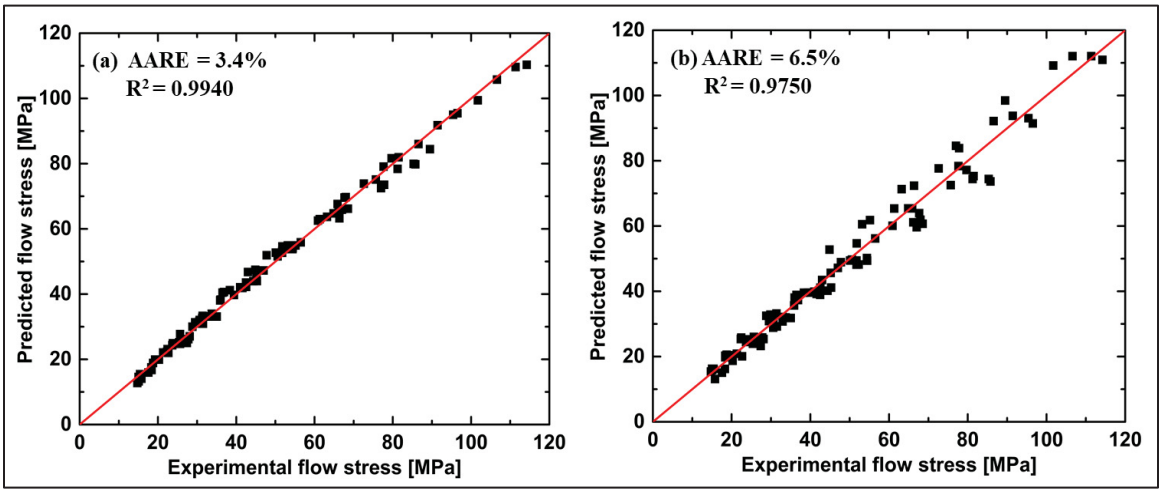

Figure 3.7 Comparison of precision and correspondence between experimentally determined and predicted flow stress values using: a Arrhenius model and, b Hansel-Spittel model

3.5 Microstructure modeling and FE modeling

3.5.1 Identification of microstructure model parameters

In materials characterized by low stacking fault energy (SFE) such as steel, DRX is the primary softening mechanism during hot deformation. It is initiated upon reaching a critical deformation level known as critical strain ε_c which varies with temperature and strain rate (Babu, Mandal, Athreya, Shakthipriya, & Sarma, 2017). The DRX fraction occurring during deformation can be computed by establishing a relationship among different strains, such as total strain, strain for the 50% DRX, and critical strain (Peng et al., 2022). Similarly, the DRX grain size, Zener-Holloman parameter, and DRX fraction could be calculated using the expressions given in Table 3.6. The equations governing this phenomenon are rooted in the Johnson–Mehl–Avrami–Kolmogorov (JMAK) model (Melvin Avrami, 1940; Mélvin Avrami, 1939; Johnsson & Mehl, 1940):

$$X_{drx} = 1 - e^{(-b.t^n)} \tag{3.17}$$

Where, the constants 'b' and 'n' represent the Avrami coefficients. The coefficients of the formula outlined in Table 3.6 were derived from the flow curve data using the regression analysis and subsequent metallographic analysis of hot compressed cylindrical samples (Johnsson & Mehl, 1940; Peng et al., 2022).

The material parameters essential for FE analysis and their incorporation into the Finite Element Method model (FEM) included deformation temperature T (°C), critical strain ε_c, strain rate $\dot{\varepsilon}$ (s^{-1}), initial grain size d_0 (µm), DRX volume fraction (X_{drx}), and DRX grain size D_{drx} (µm). The procedures used to determine these parameters were elaborated in a recent publication (Ivaniski, Epp, Zoch, & Da Silva Rocha, 2019). These parameters and expressions, outlined in Table 3.6, were integrated with the microstructural model and subsequently implemented into the FORGE NxT 3.2® software.

Table 3.6 Equations describing the microstructure evolution
Adapted from Xiaoqin Zhou, Ma, Feng, & Zhang, (2020)

Parameters	Equations
Zener-Hollomon	$z = \dot{\varepsilon} \exp\left(\frac{334500}{R.T}\right)$
Critical strain	$\varepsilon_c = 4.4 \times 10^{-5} \dot{\varepsilon}^{-0.1262} Z^{0.2903}$
50% recrystallization	$\varepsilon_{0.5} = 6.3 \times 10^{-2} Z^{0.117} \dot{\varepsilon}^{0.012} \exp\left(\frac{26128}{R.T}\right)$
Dynamic recrystallization fraction	$X_{drx} = 1 - \exp\left(-0.318\left(\frac{\varepsilon - \varepsilon_c}{\varepsilon_{0.5}}\right)^3\right)$
Recrystallized Grain size	$D_{drx} = 14\, \dot{\varepsilon}^{0.07} Z^{-0.205} \exp\left(\frac{-42327}{R.T}\right). X_{drx}^{0.21}$

3.5.2 Finite element modeling and analysis

A user subroutine was used to integrate the constitutive and microstructure models into the finite element software Forge NxT 3.2®. The hot compression process was simulated using a 3D FE model. The input boundary conditions used for the FE analysis mimicked those of the experimental tests, including amount of deformation, deformation rate, and thermal exchange between the workpiece and anvil. The friction factor was calculated using initial and final geometrical dimensions at the end of hot compression using Equation 3.5. Mesh convergence analysis was conducted by varying the element size to ensure accuracy of FE analysis. Numerical simulations were performed on a FE model using tetrahedral elements with four nodes. The meshed FE models, illustrated in Figure 3.8a-b, showcase the model configuration before and after deformation, respectively. Input boundary conditions for the FE model, such as the test temperature, die velocity (deformation rate), and degree of deformation, were calculated and assessed according to the actual industrial forging schedule. Specially, amount of deformation and die velocity were calculated using press chart provided by industrial partner which represents entire open die forging of the large ingot. The boundary conditions for heat

transfer with the ambient air and between the die and workpiece were modeled in the FE analysis using convective and conductive heat transfer coefficients. The coefficient values are provided in the table below. Table 3.7 provides the input boundary conditions to FE model.

Table 3.7 Input boundary conditions to hot compression FE model

Parameters	Input boundary conditions
Initial dimensions of specimen (mm)	10 (D) x 15 (H)
Type of anvil (upper and lower)	Flat
Specimen initial temperature (ºC)	1200 and 1050
Die temperature (ºC)	1200 and 1050
Deformation rate (s^{-1})	0.001 to 1
Ingot material	Modified AISI P20 steel
Material model	Arrhenius
Amount of deformation (%)	≈60
Mesh size (mm)	0.7 (tetrahedron)
Count of mesh elements	15709 (workpiece)
Convective heat transfer coefficient ($W.m^{-2}.K^{-1}$)	10
Conductive heat transfer coefficient ($W.m^{-2}.K^{-1}$)	10^4
Friction coefficient	0.4

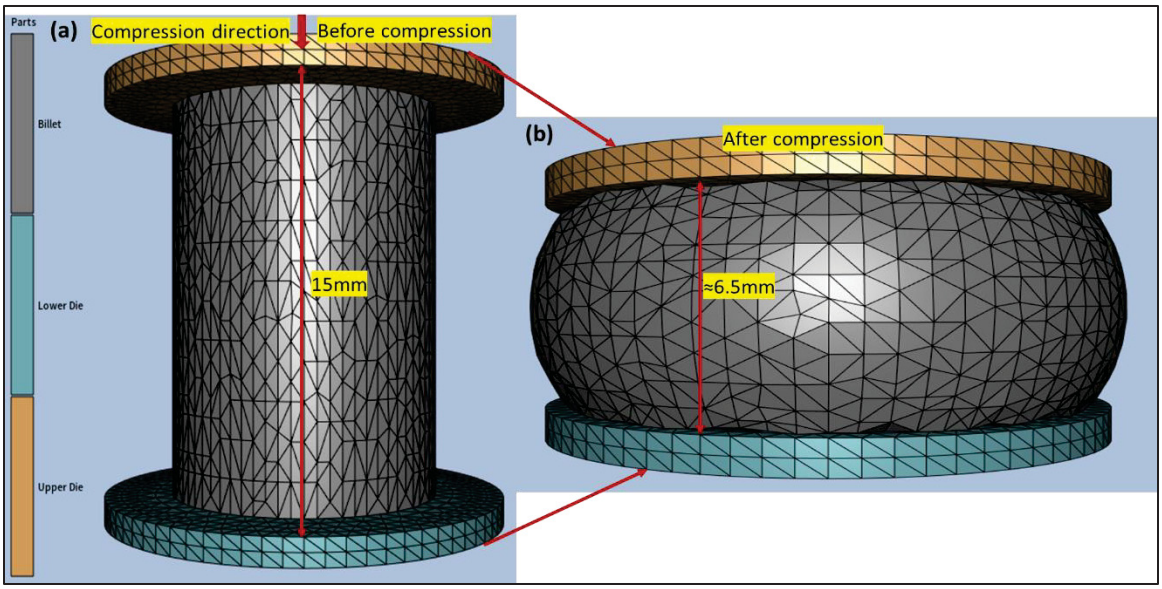

Figure 3.8 Finite element model for the simulation of hot compression test
a) Before the deformation, b) After the deformation (zoom image)

Figure 3.9 illustrates the results of the FE analysis for critical parameters equivalent plastic strain and temperature evolution after the isothermal hot compression test simulation at 1200°C and $0.1s^{-1}$. In Figure 3.9a, the equivalent plastic strain distribution map at the end of compression reveals inhomogeneity in deformation, with higher deformation at the center of value 1.2 and lower deformation at value 0.3 at the die and specimen interface, referred to as the dead metal zone (DMZ) or lower deformation zone. Figure 3.9b displays the temperature distribution, indicating a temperature rise of around 6°C at center of specimen due to adiabatic heating, closely aligning with results shown in Figure 3.9. Therefore, the predictions from the developed FE model were accurate and very close to the experimental and analytical values.

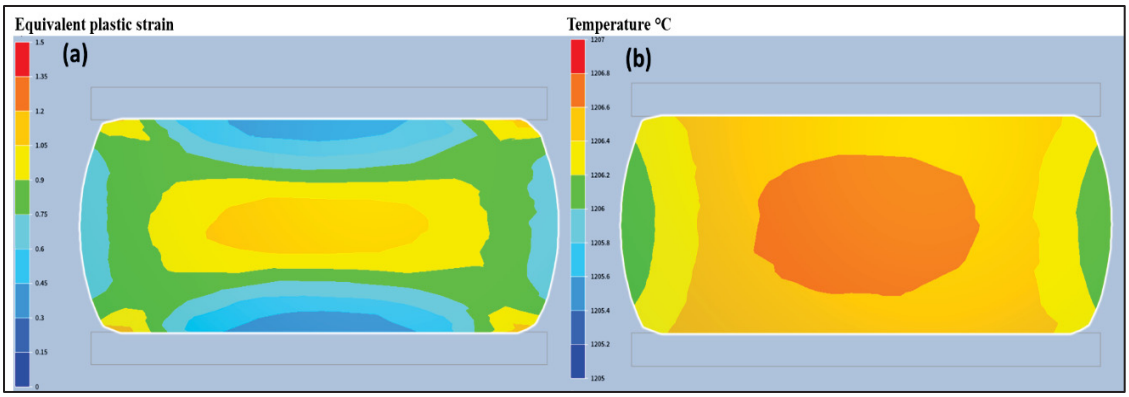

Figure 3.9 FE analysis of deformation at 1200 °C and $0.1s^{-1}$ after 60% deformation: a) equivalent plastic strain and, b) temperature distribution

3.5.3 Validation of FE model

Figure 3.10 illustrates a comparison between the measured and predicted stress versus strain plots, showcasing the FE model's commendable and acceptable predictability. The percentage error between the measured and predicted flow stress was found to be around 5%. The average grain size distribution map at the end of the isothermal hot compression test at 1200°C and $0.01s^{-1}$ is shown in Figure 3.11. Specifically, Figure 3.11a represents the predicted grain size distribution map, while Figure 3.11b illustrates stitched image and distribution of grain size at end of deformation. To determine the average grain size after the hot compression tests, specimens were cut parallel to the compression axis using a precision cutter machine, enabling microscopic examination. Subsequently, the specimens underwent the standard procedure for sample surface cleaning. After cleaning, the specimen faces were etched using various etchant and methods outlined in existing literature. However, these approaches proved ineffective, or achieved only limited success, in revealing Prior Austenite Grain Boundaries (PAGBs) in the investigated steel. A different approach using swab etching utilizing a solution consisting of 100 ml saturated aqueous picric acid and 0.5 g sodium dodecyl benzene sulfonate, demonstrated remarkable effectiveness in delineating the PAGBs in this steel (Sinha, Payton, Gonzales, Abrahams, & Song, 2017).

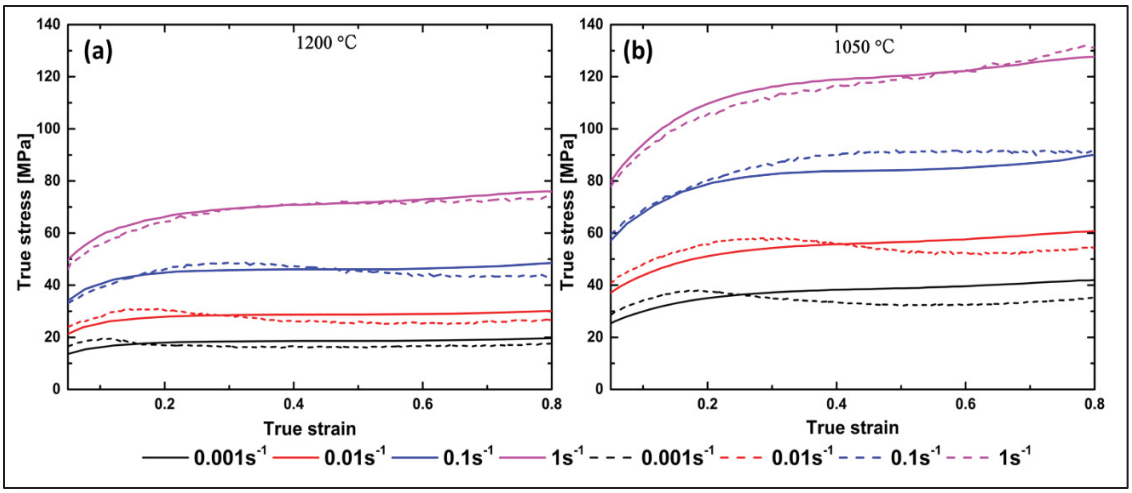

Figure 3.10 Stress versus strain plots for measured (dashed) and predicted (solid) flow stress at strain rates $0.001s^{-1}$ to $1s^{-1}$ and at two temperatures: a) 1200 ºC, b) 1050 ºC (higher and lower temperature)

The etching duration varied between 3 to 5 minutes based on the deformation and heat treatment conditions of the material. Micrographs were captured using an Olympus LEXT OLS4100 laser confocal microscope. The measured average grain size was calculated using the standard ASTM E112. For measuring the average grain size before and after deformation, the ImageJ software was employed. Figure 3.11 show predicted and measured grain sizes using optical microscopy at 1200°C and $0.01s^{-1}$, with average grain sizes of 221µm and 215µm, respectively. Figure 3.12 summarizes the comparison between the average measured and FE predicted grain sizes for different forging conditions. It can be seen that the prediction accuracy fluctuates within the range of approximately 3 to 7%, thereby, indicating a very good predictability of the microstructural model.

As discussed in the preceding section, inhomogeneity was observed in the distribution of grain size from the center to DMZ on both sides upper and lower of the specimen. The measured grain size in the DMZ varied between 370 µm and 600 µm, with an average grain size in the DMZ of approximately 450 µm. Hence, it is crucial to eliminate or minimize inhomogeneity to the greatest extent possible by adjusting machine characteristics, such as die geometry and process parameters. For further investigation, four die geometries: flat, convex, v-die, and concave were considered to examine the influence of the deformation path on the

inhomogeneity distribution of strain and grain size evolution. The validated FE model was scaled up to simulate the actual industrial upsetting process with a large size ingot, as detailed in the subsequent section of results and discussion.

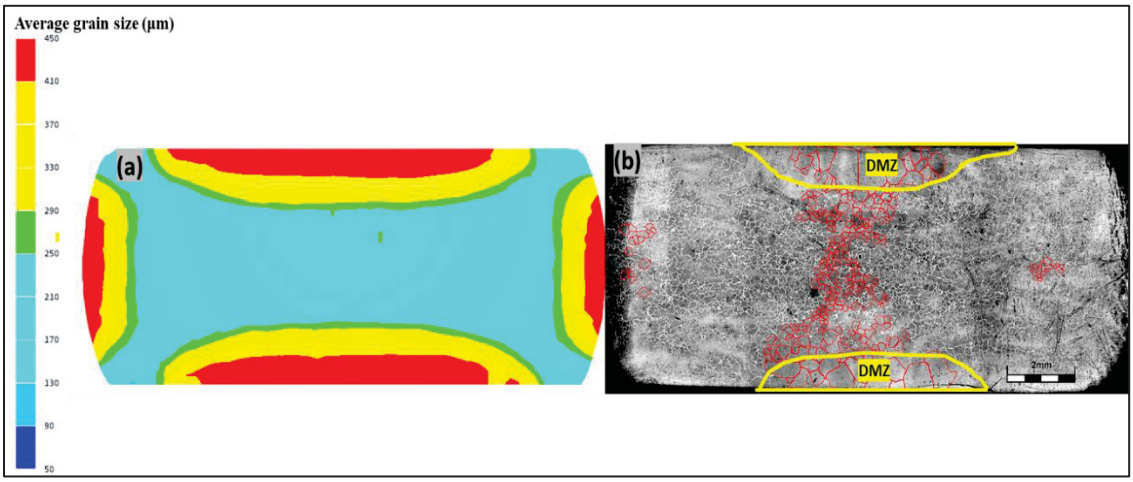

Figure 3.11 Average grain size distribution map at 1200 ºC, 0.01s^{-1}: a) predicted, b) Stitched optical micrograph shows grain size distribution (grain boundary highlighted with red color from center to DMZ)

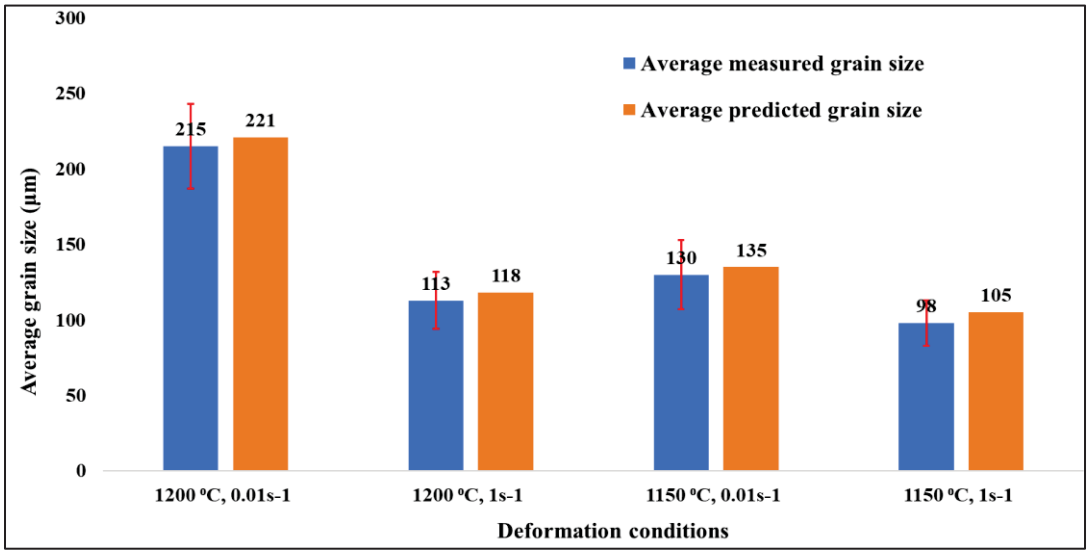

Figure 3.12 Comparison between measured and predicted grain size

3.6 Results and discussion

3.6.1 Influence of deformation path during the industrial upsetting process

Figure 3.13 illustrates the FE model, showcasing the mesh geometry employed in simulating the industrial scale upsetting process. The four die geometries used in the simulation are shown in Figure 3.13a-d. The boundary conditions for the finite element analysis mirrored those of the industrial process, encompassing factors such as initial billet temperature, deformation rate, amount of deformation, and heat transfer considerations involving the environment and the die workpiece interface. Detailed input boundary conditions for the finite element analysis are provided in Table 3.8.

Table 3.8 Input boundary conditions for upsetting process simulation

Parameters	Input boundary conditions
Ingot initial dimensions (mm)	1600 (D) x 2550 (H)
Upper die	Flat, convex, v-die and concave
Lower die	Flat
Ingot initial temperature (°C)	1200
Die temperature (°C)	300
Die velocity (mm/sec)	≈13
Ingot material	Modified AISI P20 steel
Material model	Arrhenius
Amount of deformation (%)	≈50
Mesh size (mm)	15 (tetrahedron)
Count of mesh elements	1788942 (workpiece)
Convective heat transfer coefficient ($W.m^{-2}.K^{-1}$)	10
Conductive heat transfer coefficient ($W.m^{-2}.K^{-1}$)	10^4
Friction coefficient	0.8

The flat and curved dies were square shaped and had a side length of 2500 mm, the convex and concave dies had a radius of curvature of 1400 mm, and the v-die had an angle of 140 degrees. The initial billet used for upsetting had a cylindrical shape, diameter of 1600 mm (D) and height of 2550 mm (H). The billet was positioned between the upper and lower dies and 50% deformation was achieved in the upsetting process. The final dimensions of the billet upon upsetting were 1250 mm (H) x 3200 mm (D). The finite element model at the end of the upsetting process is shown in Figure 3.14a-d displays the equivalent plastic strain distribution at end of the upset using the flat, v-die, convex, and concave dies, respectively.

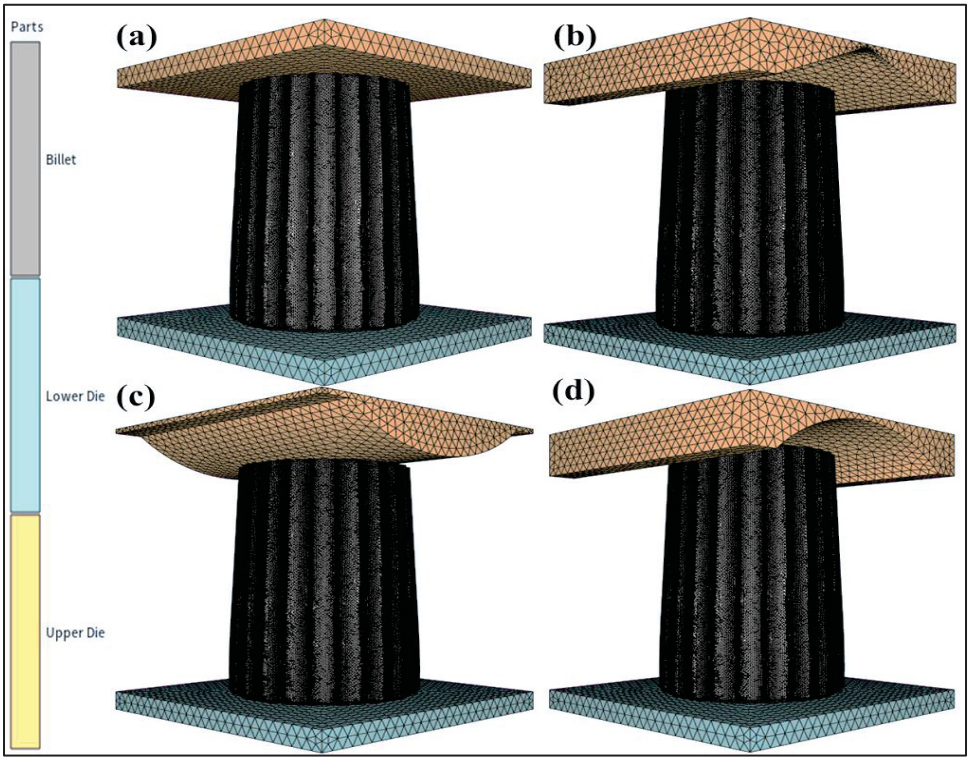

Figure 3.13 Finite element model used for the upsetting process simulation prior to the deformation with: a flat, b v-die, c convex and, d concave die

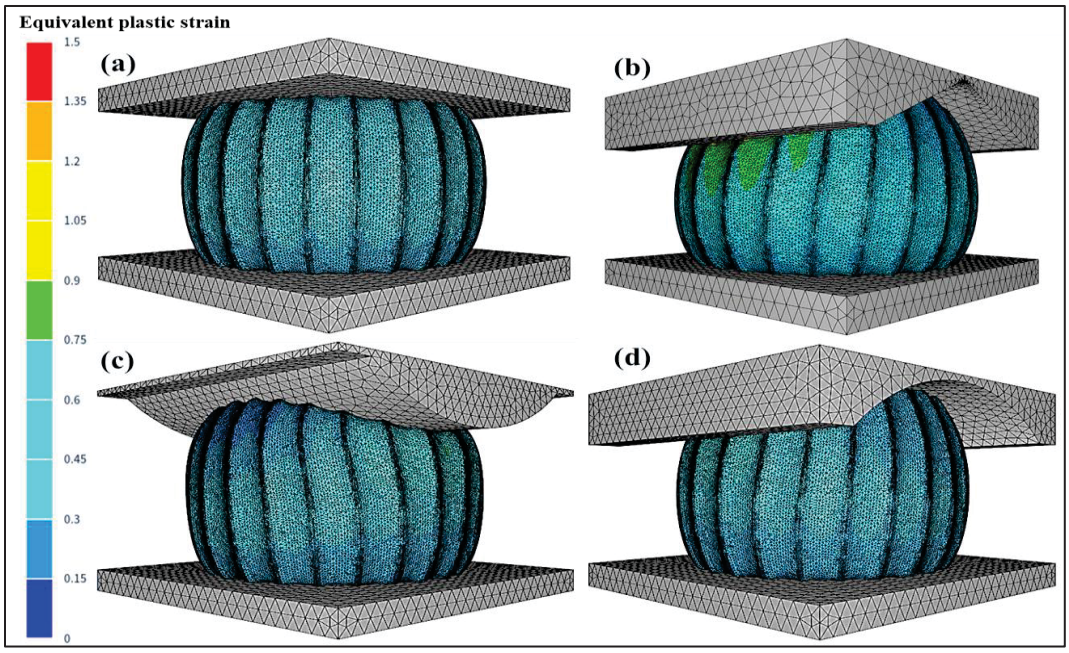

Figure 3.14 Finite element model showing the equivalent plastic strain distribution in upset of ingot after 50% deformation, for: a flat, b v-die, c convex and, d concave die

3.7 Identification of important parameters

To examine the impact of the deformation path on the industrial upsetting process, critical parameters such as equivalent plastic strain, temperature, DRX volume fraction, and microstructure evolution (DRX grain size) were identified. At the conclusion of the upsetting process, a comparison was conducted among the mentioned parameters for various deformation paths. The results are discussed in the following section.

3.7.1 Equivalent plastic strain distribution

Figure 3.15a-d shows the distribution of equivalent plastic strain at the end of the upsetting process for a large size industrial ingot utilizing flat, v-die, convex, and concave die, respectively. The results indicate that altering the die surface curvature did lead to variation in the strain distribution in the ingot cross section. The equivalent plastic strain values at the center of the forged ingot varied between 0.9 and 1.2 for the flat die, 1.2 and 1.3 for the v-die,

0.9 and 1 for the convex die, and 1.3 to 1.5 for the concave die. Notably, the results indicate that, at the center of the ingot, the concave die induced higher equivalent plastic strain compared to flat, convex, and v-die curvatures for the same amount of input deformation. Similar observations were reported by the present authors in a recent publication discussing the cogging process of AISI H13 steel (Dhondapure et al., 2023). Du et al. (Du S, Li Y, 2015) reported findings in the forging process of a railway axle, the equivalent plastic strain at the center of the workpiece registered as 1.35 with flat anvils and 1.57 with concave anvils. Xu et al. (Xu et al., 2021) in a comparable study, found that the curvature of the concave die resulted in improved compressive deformation. Hence, by changing the die curvature, both deformation path and amount of deformation were modified because this change modifies both amount and distribution of the strain throughout the volume of the material.

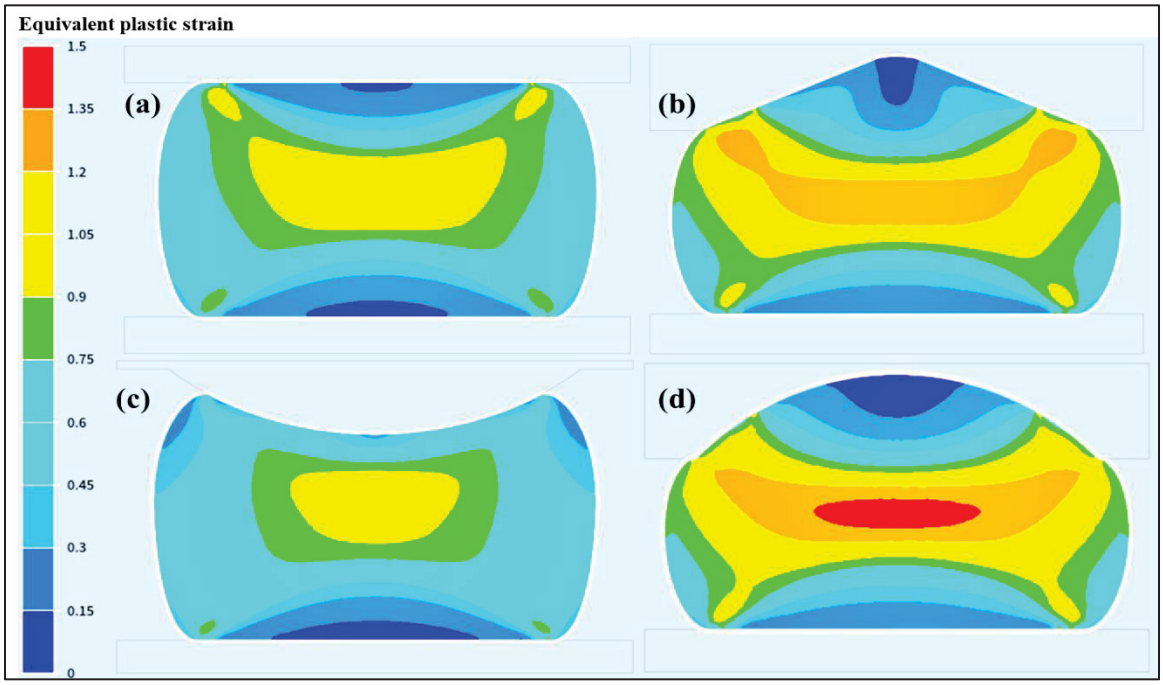

Figure 3.15 Distribution of equivalent plastic strain after the upsetting process with: a flat, b v-die, c convex and, d concave die

3.7.2 Temperature distribution

Figure 3.16a-d illustrates the temperature distribution at the end of the upsetting process. Examining the temperature distribution map reveals that the temperature drop at the die and workpiece interface was more pronounced for the curved dies compared to the flat die. The temperature at the die and workpiece interface decreases from 1200 °C to 420 °C for a thickness of 86mm, and on the external surface of the ingot, it decreases to 1046 °C for a thickness of 56mm. This indicates that a larger contacted area results in a higher heat transfer at the die and workpiece interface. Specifically, for the v-die and concave die, the temperature drop was greater compared to the flat and convex die.

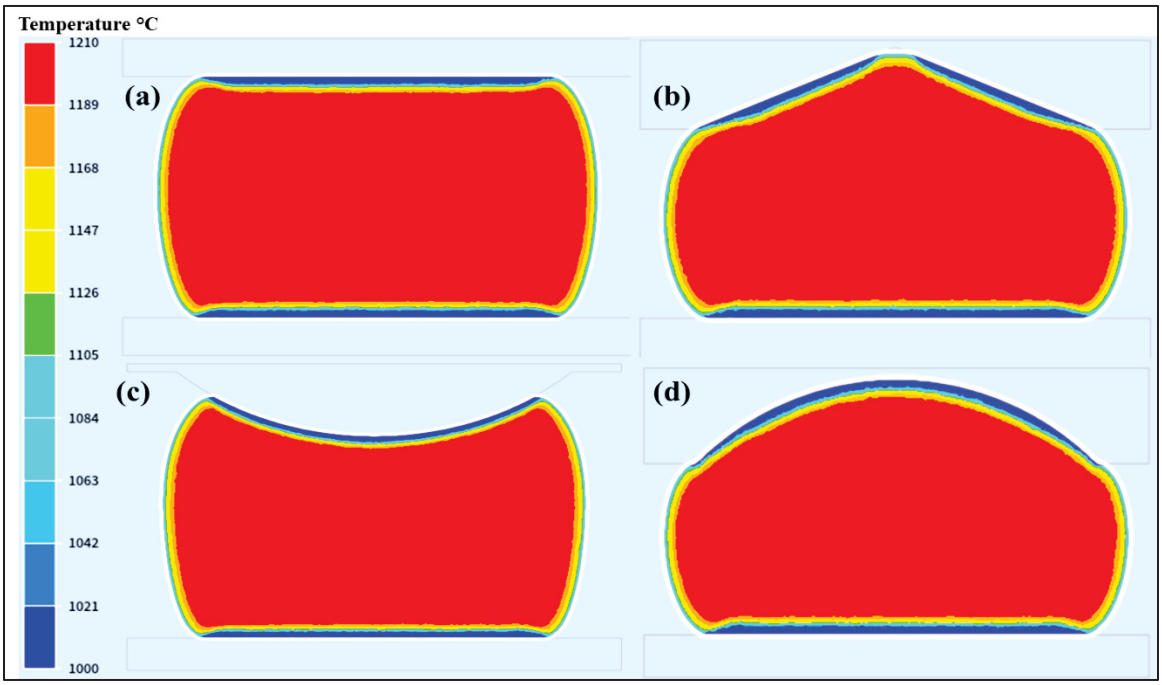

Figure 3.16 Distribution of temperature after the upsetting process using: a flat, b v-die, c convex and, d concave die

3.7.3 Dynamic recrystallization volume fraction (X_{drx})

Figure 3.17a-d illustrates the distribution of dynamic recrystallization volume fraction at the end of the upsetting process. The results indicate that the distribution of X_{drx} closely mirrors the variation in equivalent plastic strain discussed in the previous section. Using a flat die during upsetting, a large DMZ forms near the die and workpiece interface. In contrast, the use of curved dies, such as convex, v-die, and concave die, results in a smaller DMZ compared to the flat die. This indicates that the application of curved dies increases the amount of strain from 0.15 to 0.6 in the DMZ; hence, reducing the heterogeneity in the distribution of strain and DRX volume fraction was significantly improved in about half of the DMZ volume, as shown in Figure 3.17b&d. Results also show that using v-die and concave die, increased the DRX volume fraction at the center, and significantly enhanced it in the DMZ, compared to the flat die as well as the convex die. The above findings are in agreement with those reported by Chen et al. (F. Chen et al., 2016) who indicated that homogenous distribution and higher amount of deformation result in a higher amount of DRX volume fraction. Muszka et al. (Muszka, Madej, & Majta, 2013) examined the impact of various deformation paths on deformation and microstructure inhomogeneity during the angular drawing of low carbon and microalloyed steels. Their findings indicated that a complex deformation path results in homogeneous deformation and microstructure evolution, which align with the findings of the present study.

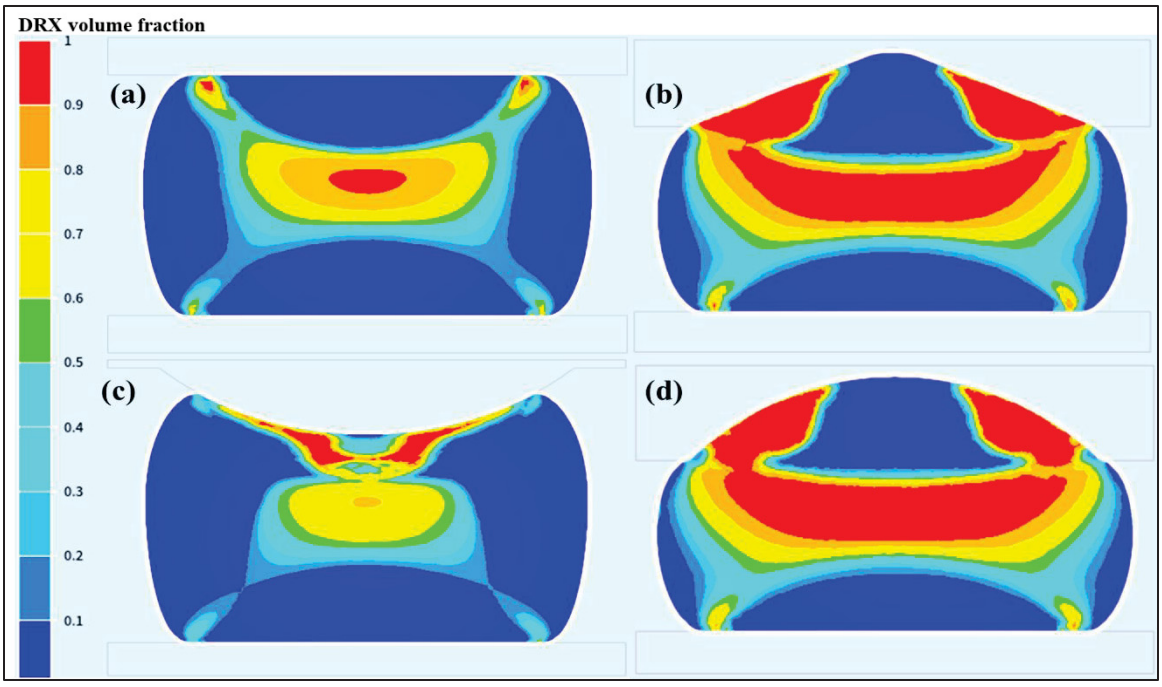

Figure 3.17 Distribution of dynamic recrystallization volume fraction after the upsetting process using: a flat, b v-die, c convex and, d concave die

3.7.4 DRX grain size distribution

Figure 3.18a-d shows the distribution of DRX grain size at the end of upsetting process. Grain size distribution map shows a similar trend to that of equivalent plastic strain and DRX volume fraction. The initial average grain size was determined following a 5 minute holding of the sample at 1260 °C, revealing a value of around 450 μm. Upon 50% deformation by upsetting, grain size variation in the FE models was found to be between 90 μm (recrystallized) to 450 μm (non-recrystallized). As shown in Figure 3.18a using flat dies, size of DMZ region was larger compared to the curve dies. Specially, the v-die and concave die showed higher amounts of recrystallized grain fraction compared to the flat and convex dies. Therefore, application of curve dies led to reduction of DMZ size and increased the homogenous distribution of strain, so that higher recrystallized grains fraction was obtained.

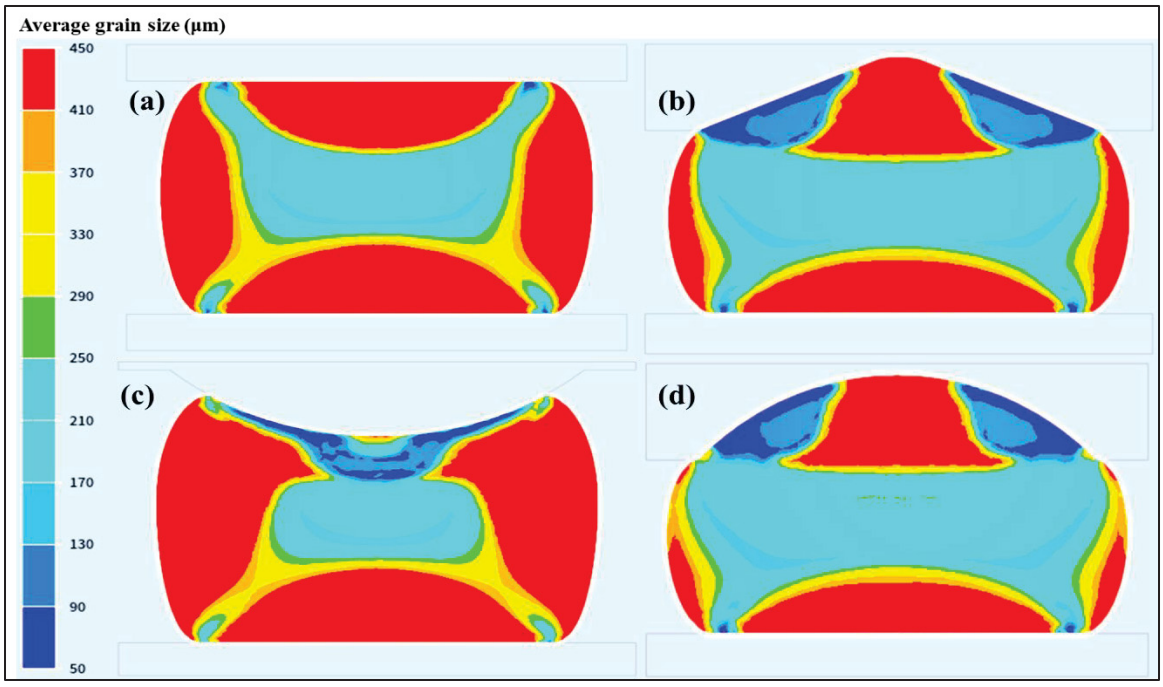

Figure 3.18 Distribution of DRX grain size (in µm) after the upsetting process using: a flat, b v-die, c convex and, d concave die

At the contact points of the curved surfaces of the v-die, convex, and concave dies with the ingot face, a higher level of strain around 0.6 was observed compared to the flat die strain of around 0.15, as illustrated in Figure 3.15. Similar observation have been reported regarding the hot cogging of tool steel (Marcin Kukuryk, 2019). This increased deformation amount leads to a higher amount of DRX volume fraction, as depicted in Figure 3.17, as well as higher recrystallized grain fraction compared to the flat die in the DMZ, as shown in Fig. 18.

3.7.5 Heterogeneity study

A study on heterogeneity was performed with the objective of comparing and determining the optimum die geometry. The coefficient of variation (CoV), defined as the ratio of standard deviation to the mean value, was used as the heterogeneity index in the present work (Zhu, Yang, Guo, & Gu, 2012b). A CoV value close to 0 indicates a homogenous distribution of the parameter and 1 signifies the highest heterogeneity (Nayak, Kumar Singh, et al., 2023). The heterogeneity index was computed by evaluating equivalent plastic strain and average grain

size for each of the 1,788,942 elements covering the entire forged ingot. Figure 3.19 shows the change in CoV for equivalent plastic strain and average grain size with different deformation paths illustrated, using the four selected die geometries. As is quite evident, there is a significant and steady decrease in the CoV value as we move from the flat die to convex die, v-die, and finally concave die, with concomitant improvements in homogeneity in the distribution of strain and average grain size. The analysis of the heterogeneity index reveals that the highest and lowest CoV values were 0.65 and 0.18 for the flat and concave dies, respectively. Notably, upsetting with a v-die and concave die yields more consistent deformation in comparison to the flat and convex dies. Figure 3.15 and Figure 3.18 highlighted that the upsetting process with v-die and concave die contributed to achieving higher strain levels, more homogenous strain and average grain size distribution compared to the flat and convex dies. Similar observations were reported by the present authors in a recent publication concerning the cogging process of AISI H13 steel (Dhondapure et al., 2023).

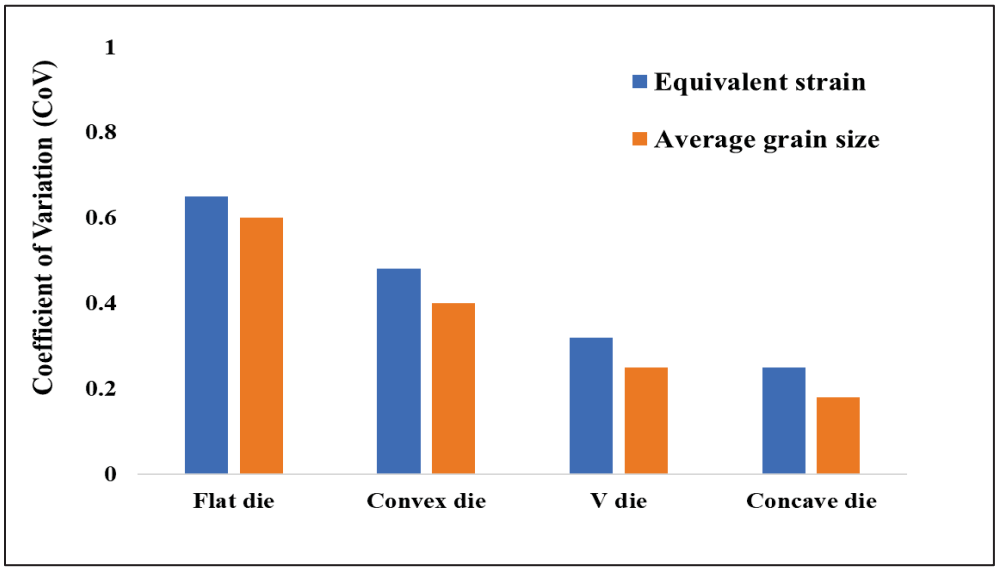

Figure 3.19 The coefficient of variation (CoV) of equivalent plastic strain and average grain size with different deformation paths at end of upsetting process

3.8 Summary and conclusions

In this research, constitutive and microstructure models were tailored for a high strength steel. Both models were incorporated into Forge NxT 3.2® through a dedicated user subroutine to establish a FE model to analyze both the hot compression test and the industrial upsetting processes. The accuracy of the developed FE model was affirmed through experimental validation of flow stress and average grain size evolutions. The validated FE model was then applied to simulate the industrial upsetting process with the goal of evaluating the grain size inhomogeneity in the forged ingot at the end of the upsetting process. The study provided comprehensive insights into the optimal deformation path, identifying the most suitable die geometry for the upsetting process. The significant findings and conclusions derived from this investigation are outlined below:

1. The flow stress curves in the range of 1050 °C to 1200 °C temperature and from 0.001 s^{-1} to 1 s^{-1} strain rates, exhibited a notable difference. A precise constitutive model, adjusted for adiabatic temperature and friction corrections, was established.
2. The comprehensive constitutive and microstructure model integrated into the Forge NxT 3.2® software demonstrated strong correlation with experimental data.
3. The simulation results indicated that use of dies with v or concave geometries reduced strain and grain size heterogeneity by 30 to 40% through the entire volume of the forged product.

3.9 Data availability

The raw or processed data required to replicate these findings cannot be disclosed at this time due to privacy and ethical considerations, as this data is currently being utilized for an ongoing investigation.

3.10 Acknowledgments

The research described in this paper was financially supported by Mitacs and Finkl Steel-Sorel under project number [IT164670]. We extend our gratitude to Mr. Radu Romanica for his precise execution of the Gleeble experiment. Additionally, we acknowledge the assistance and support provided by Mr. Patrice Lasne from Transvalor in implementing a novel material model into the Forge NxT® 3.2 software.

3.11 Conflict of interest

The authors state that they do not have any conflicts of interest.

The findings of Chapter 3 demonstrated that modifying the deformation path or die geometry significantly affected material flow and microstructure evolution during the upsetting of industrial-scale ingots. These insights were implemented at the industrial level. In the following chapter, optimum material model for AISI H13 was developed. Critical damage value for the forging temperature rang was calculated. Using validated FE model, the influence of the deformation path on damage development and stress state evolution during the cogging of AISI H13 steel was investigated.

CHAPTER 4

INFLUENCE OF DEFORMATION PATH ON THE STRESS STATE AND DAMAGE EVOLUTION ALONG THE CENTRAL AXIS OF A LARGE SIZE FORGED INGOT OF AISI H13 STEEL

Prashant Dhondapure[a], Pierre Tiza Mha[a], Soumyarajan Nayak[b], Lea Ebacher[a], Simin Dourandish[a], Henri Champliaud[a], Jean-Benoit Morin[c], Mohammad Jahazi[a,]

[a]Department of Mechanical Engineering, École de Technologie Supérieure, 1100 Notre Dame West, Montreal, Quebec H3C 1K3, Canada.
[b]Department of Metallurgical Engineering and Materials Science, Indian Institute of Technology Bombay, Mumbai 400076, India.
[c]Finkl Steel-Sorel Inc., 100 McCarthy, Saint-Joseph-de-Sorel, Quebec J3R 3M8, Canada.

Paper published in *Journal of Materials Research and Technology,* November 2023

Summary

Development of cracks along the center axis of large high strength steel bars commonly occurs during the forging and leads to excessive part rejections. The present investigation aims to develop a better understanding of the evolution of stress-strain states during the forging operation and in particular the effect of deformation path illustrated by die geometry, on the evolution of damage during the cogging of an AISI H13 steel. Hot compression and tensile tests were performed using Gleeble-3800 thermo-mechanical simulator to develop the optimum material model which was then implemented in the finite element (FE) code Forge NxT 3.2® using a developed user subroutine. Normalized Cockcroft and Latham damage criterion and maximum shear stress (Tresca's) theory of failure were used to predict the damage and failure in the center axis of the shaft through FE analysis with three different die shapes: concave, flat, and convex. A comparative study between the three die geometries was conducted to quantify the effects of each of them on the sensitivity to central burst damage. FE

model was validated using industrial data. The lowest and highest damage values were found to occur in the case of cogging with concave and flat die, respectively. The coefficient of variation (CoV) is employed as a measure of heterogeneity and it was found that the concave die provides more uniform deformation and most favorable results for the cogging compared to the flat and convex dies. The novel approach, application of concave die successfully implemented at the industrial scale cogging.

4.1 Literature Review

Cogging is a forging process to manufacture different types of straight and stepped shafts from rectangular or square blocks by application of compressive force. Large industrial size forged shafts made of AISI H13 tool steels are widely used in the energy and transportation industries (B. Li, Zhang, Zhang, Chen, & Zhang, 2018; Marashi et al., 2017). The manufacturing of large ingots especially high strength steels consists of melting in an electric arc furnace, followed by degassing, ingot casting, open die forging, and finally quench and temper operations before machining. Open die forging of large size ingots consists of upsetting, Free from Mannesmann effect(FM), and cogging process (Dourandish et al., 2022). The formation and propagation of a defect, known as center burst, along the center axis during hot deformation (rolling, forging, etc.) of high strength steels is often observed in the industry and reported in the literature (Bulzak, Pater, Tomczak, & Majerski, 2020). The occurrence of this defect brings unrecoverable damage to the part and results in total or partial rejection (B. V. Krishna & Sidhu, 2002; Zhenwei et al., 2022). Therefore, to address the issue it is very important to identify and quantify the role of each of the manufacturing process parameters that lead to center burst defect formation.

AISI H13 is a high strength highly alloyed steel characterized by high molybdenum and vanadium contents that significantly increase the resistance to hot deformation (Genel, 2006; Mahlami & Pan, 2017). Therefore, forging of AISI H13 alloy is challenging due to the high sensitiveness to high temperature deformation and high resistance to deformation at lower forging temperatures. Han et al. (Yuan, Wei, Han, Shan, & Guo, 2021) reported that the

application of higher forging loads is not a viable solution as it could lead to even more center burst defects during the cogging process. Figure 4.1a shows the center burst formation at extreme end of the workpiece indicated with an arrow. Figure 4.1b shows the propagation of the center burst defect along the center axis of the workpiece found during the quality check. Yang et al. (C. Yang, Dong, & Hu, 2018) it have been reported that the center burst defect will propagate through the central axis of a workpiece (as shown in Figure 4.1) with increase in number of passes under the radial compression.

In the literature, the available data on the formation of center crack and burst is mostly related to Cross Wedge Rolling (CWR) process and very little or no data is reported on cogging. Although, fundamentally cogging and CWR are similar as radial compression is the most important loading in both the cases. Hence, an analysis of the published literature on center burst cracking during the CWR process is provided hereafter. Lee et al. (Lee et al., 2008) found that center cracks formed during the CWR process in the middle of the shaft in both radial and axial directions.

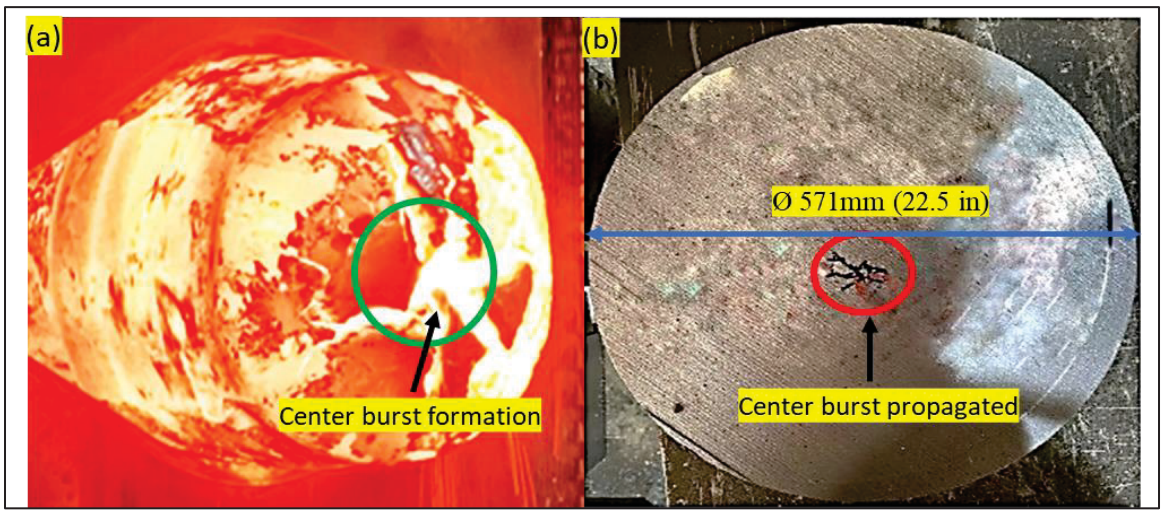

Figure 4.1 Center burst occurred during the cogging of AISI H13 steel (a) center burst formation at extreme end of the workpiece (b) center burst propagated along the center axis of the workpiece

Zhou et al. (Xianyan Zhou, Shao, Pruncu, et al., 2020; Xianyan Zhou, Shao, Zhang, et al., 2020; Xianyan Zhou, Sun, Wang, & Jiang, 2022) studied the central crack formation during the cross wedge rolling of pure aluminum using FE analysis and lab scale experiments and proposed damage criteria to predict the risk of center crack formation. They reported that the maximum tensile and shear stresses were the key parameters for damage occurrence along the center axis of the workpiece. Li et al. (Q. Li et al., 2002) studied experimentally the center crack formation in a 1100 H16 aluminum alloy and investigated on the mechanisms responsible for ductile fracture at the center of the workpiece. They reported that significant void formation and propagation occurred along the center axis of the workpiece, induced by shear and tensile stresses, respectively. Kukuryk (Marcin Kukuryk, 2019) used normalized Cockcroft and Latham damage criteria for the prediction of damage during multi pass cogging of lab scale specimens made of 30CrMoV1211 steel and reported that tensile stresses were the primary factor influencing the initiation of discontinuities along the center axis of the workpiece. In a recent study, the same authors Kukuryk et al. (Marcin Kukuryk, 2021) studied a two-stage cogging process of a X5CrNi18-10 stainless steel, using flat and shaped anvils, and calculated the distribution of effective strain and stress, mean stress, and stress triaxiality in the radial direction. They identified the damage criteria that best represented the center burst cracking during the cogging of the investigated alloy.

Very little data is available in the open literature on the formation of center burst during the cogging of high strength steel bars and even less in relation to AISI H13 steel, despite the important industrial applications of this steel (S. Chen, Qin, Chen, & Choy, 2018; Yahui Han, Li, Ren, Qiu, Li, et al., 2021a; Park et al., 2023). The reported studies have focused on relating material tearing and center burst formation to the evolution of the flow curve on laboratory scale compression samples and not assessing the risk of center burst formation as a function of deformation conditions representing the cogging process. The data is even more scarce when it comes to the influence of *die geometry* on stress-strain states and damage evolution at the center of the workpiece during the cogging process of large size round bars (Connolly, Sivaswamy, Rahimi, & Vorontsov, 2023; Markov et al., 2017). Most of the existing data on the influence of die geometry is on void closure. Kukuryk et al. (Marcin Kukuryk, 2019)

studied the effect of flat, v-shaped die and assembly of three radial dies on void closure on a X40CrMoV511 steel. The authors found that v-shaped die was the most efficient in closing axial voids of various sizes, as compared to the other types of dies. Dudra et al. (Dudra & Im, 1990) analyzed the influence of flat, v-shape, and Mannesmann effect-Free dies on void closure during open die forging. This analysis was based on effective strain and hydrostatic stresses at the center of the billet. The authors reported that effective strain was a better indicator for void closure. Zhang et al. (X. Zhang et al., 2012) studied the effect of die geometry on void closure during the forging of a heavy ingot using multi scale FE analysis. They reported that cymbal shape and v-shape die provided the best results for voids closing around the axis and near to the die surface during upsetting and cogging operations, respectively. Tamura et al. (Tamura & Tajima, 2003) employing rigid plastic finite element analysis for open die forging, optimized die curvature radius to ensure void closure in a stainless steel bar using the criterion based on equivalent plastic strain value. Kukuryk (Marcin Kukuryk, 2020) studied the effect of convex die, assembly of three radial anvils and skew anvils die surface on stress-strain states during the cogging of a X32CrMoV12-28 die steel. The authors concluded that by variation of die curvature, stress-strain states can be varied in the absence of tensile stresses along the center axis of the workpiece and proposed a criterion to predict the damage. Ghiotti et al. (Ghiotti et al., 2009) reported the formation of the Mannesmann defect during rolling, cogging and cross wedge rolling along the longitudinal axis of a steel bar. They proposed a model to predict the Mannesmann effect at the center of the bar using a damage law that considered the impact of flaws already present in the metal during the fabrication process. Recently, Lin et al. (Lin et al., 2022) studied the effect of flexible rollers on the defects present at center of a C45 steel bar during skew rolling. The authors determined deformation conditions that would minimize the tensile and shear stresses in order to avoid the formation of central defects along the center axis of the workpiece. Successfully produced rolled bar free from the center defect in absence of Mannesmann effect.

Based on the above literature review it can be said that the crucial factors affecting the occurrence of center cracks and bursts during radial compression include maximum tensile stress, maximum shear stress, and stress-strain states at the center of the workpiece. This study

aims to identify the key deformation parameters that increase the sensitivity to center burst defect formation and propagation during the cogging process of an AISI H13 steel and in particular determine the effect of die geometry on stress-strain states and the center burst damage evolution. A secondary objective is then to develop a predictive model and of apply it to an industrial size workpiece. To this end, the optimum constitutive model, which provided the most accurate flow stress prediction, was determined and integrated into the Forge NxT 3.2® FEM code using a specially developed subroutine. The FE simulation of cogging process using concave, flat and convex die were performed. The critical damage value in the range of examined forging temperatures was calculated for the AISI H13 steel and used for the prediction of risky zones for burst formation. The validated FE model used for the prediction of center burst formation during the cogging of AISI H13 steel on an industrial scale.

4.2 Material

The AISI H13 steel material used in this study was manufactured and provided by Finkl Steel-Sorel, Quebec, Canada. The production process commenced by melting of scrap metal through electric arc furnace, followed by refining and degassing to control the alloy composition. The melting process was followed by ingot casting and solidification. The solidified ingot was transferred to the forging furnace and heated up to 1260 °C before forging and post forging heat treatment processes. Tensile and compression test specimens were machined from the quarter location of the 571 mm diameter shaft. Table 4.1 shows the chemical composition of the AISI H13 steel in weight percentage.

Table 4.1 Composition of chemical elements in AISI H13 steel

Elements	C	Mn	Si	Cr	Mo	V	Fe
Weight %	0.4	0.4	1.05	5.15	1.35	1	Balance

4.3 Experimental procedure

4.3.1 Hot compression test

Hot compression tests were conducted using Gleeble-3800® thermo-mechanical simulator to obtain flow curves for AISI H13 steel and develop the material model for the finite element analysis of the cogging process. The samples with diameter of 10 mm and height of 15 mm were produced in accordance with the ASTM E209 standard. A preliminary analysis of the industrial conditions (press charts, temperature measurements, die velocity, etc.) allowed for the determination of deformation temperatures, reduction per pass, strain rates and strain. Figure 4.2 illustrates the laboratory test conditions, encompassing three temperatures 1260 °C, 1200 °C and 1150 °C, coupled with four strain rates 0.001 s^{-1}, 0.01 s^{-1}, 0.1 s^{-1} and 1 s^{-1} that are representative of the industrial forging process. The specimen was heated up to a temperature of 1260 °C at a heating rate of 2 °C /s and maintained for 15 mins to guarantee consistent temperature across the entire volume. It was then cooled at a rate of 1 °C/s to the test temperature. After reaching the test temperature, it was held for 1 minute before deformation was applied. Nickel based paste and 0.1 mm tantalum sheet were placed between the anvil and the specimen's surface to minimize the friction during deformation. The sampling rate was adjusted to ensure an equal number of data points were recorded at all strain rates. After the hot compression test, the flow stress data was automatically exported from the Gleeble 3800 in OriginLab® software on the computer connected with the controller. Figure 4.3 presents the measured true stress-strain curve subsequent to the hot compression test, considering all possible combinations of process parameters (3 temperatures and 4 strain rates). Flow curves in Figure 4.3, demonstrate both the occurrence of hardening and softening phenomena at lower strain rates of 0.001 s^{-1} and 0.01 s^{-1}, while only hardening is noticeable at strain rates of 0.1 s^{-1} and 1 s^{-1}.

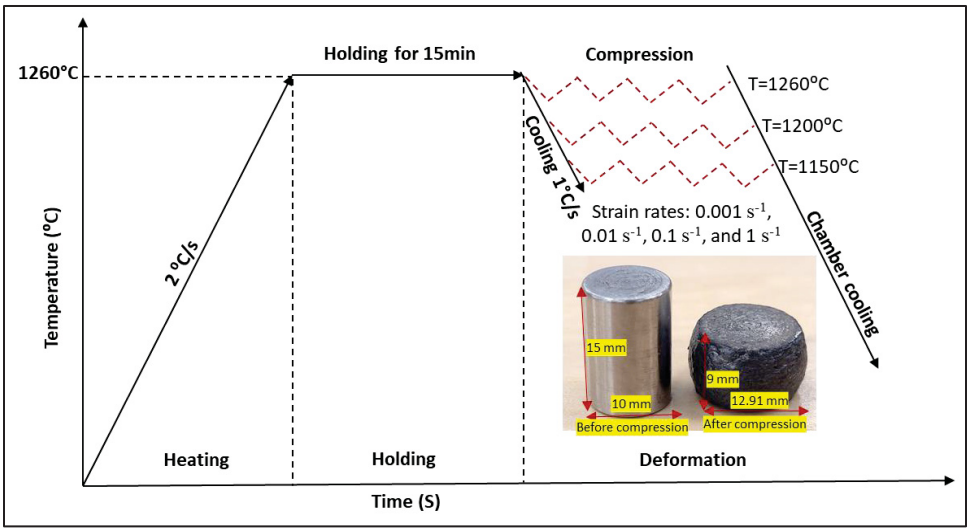

Figure 4.2 Heating and thermomechanical testing cycle

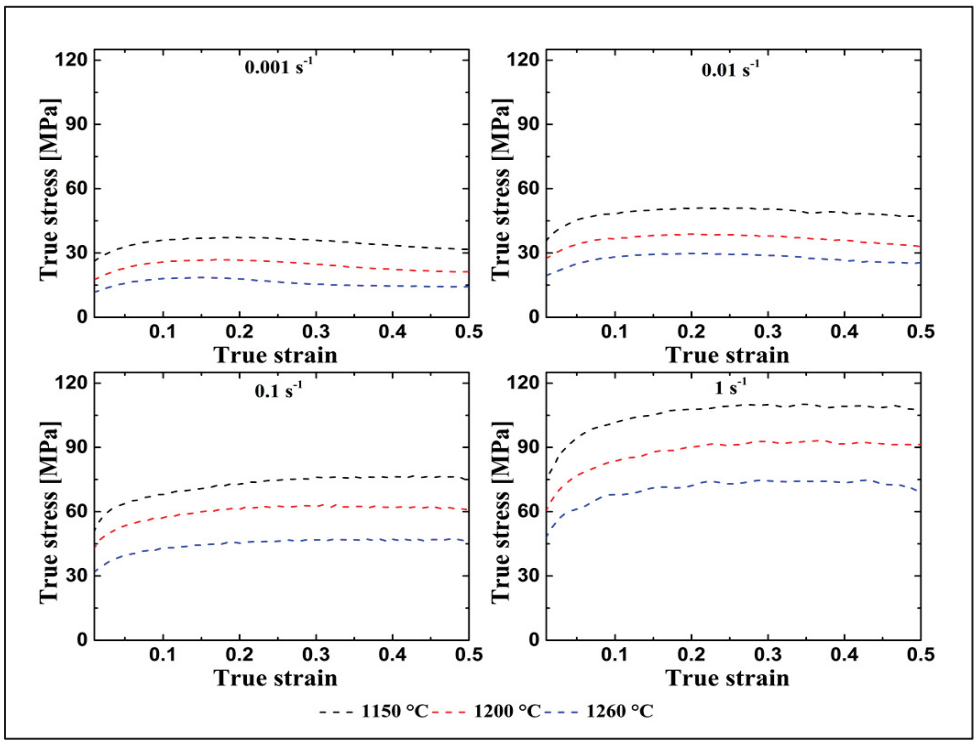

Figure 4.3 Flow stress behavior of AISI H13 steel after the hot isothermal compression

4.3.2 Hot tensile test experiments

The main objective out of the hot tensile testing was to calculate the critical damage value in the range of forging temperature and deformation rate for AISI H13 using normalized Cockcroft and Latham criterion. The hot tensile test specimens (gauge length = 66 mm and diameter = 6.25 mm.) were prepared according to ASTM E8 standard (ASTM E8, 2010). Figure 4.4a shows the tensile setup inside the Gleeble 3800 thermo-mechanical simulator chamber with installed extensometer to measure the elongation in the gauge length of the specimen. Figure 4.4b illustrates tensile test setup with thermocouple and extensometer inside the Gleeble chamber. Figure 4.4c shows the tensile specimen before and after test with dimensions. Figure 4.5a shows the heating and tensile testing sequence at two distinct temperatures, 800 °C and 1200 °C, employing a strain rate of 0.05 s^{-1}. Test specimen diameter and length, both before and after test, were recorded to calculate the percentage reduction in cross-sectional area and the elongation. Like the compression test data, tensile test data were also recorded and automatically exported in OriginLab® software. Figure 4.5b shows the true stress-strain curves after the hot tensile test.

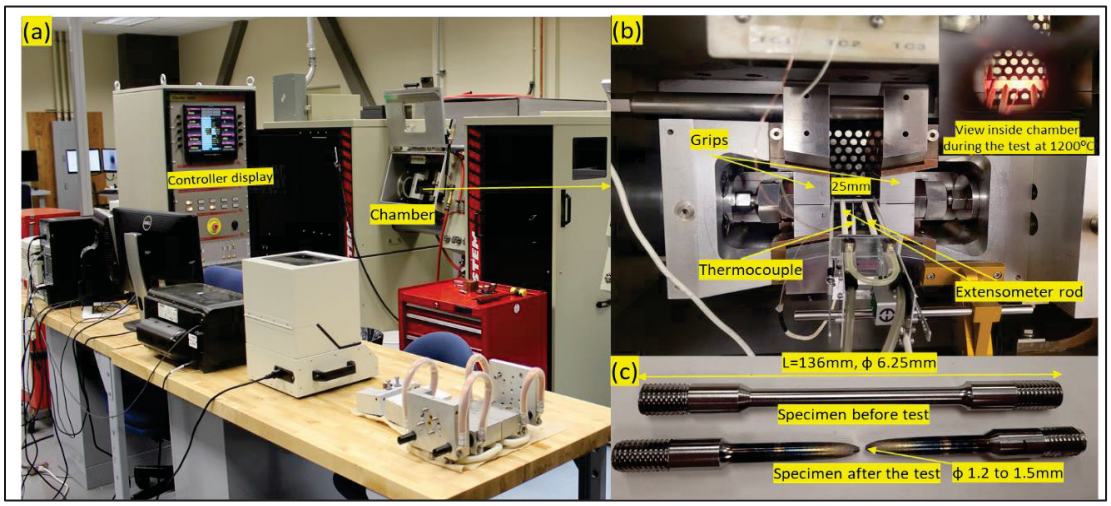

Figure 4.4 Experimental setup (a) Gleeble 3800 thermo-mechanical simulator (b) tensile test setup inside the Gleeble chamber (c) tensile specimen before and after the test

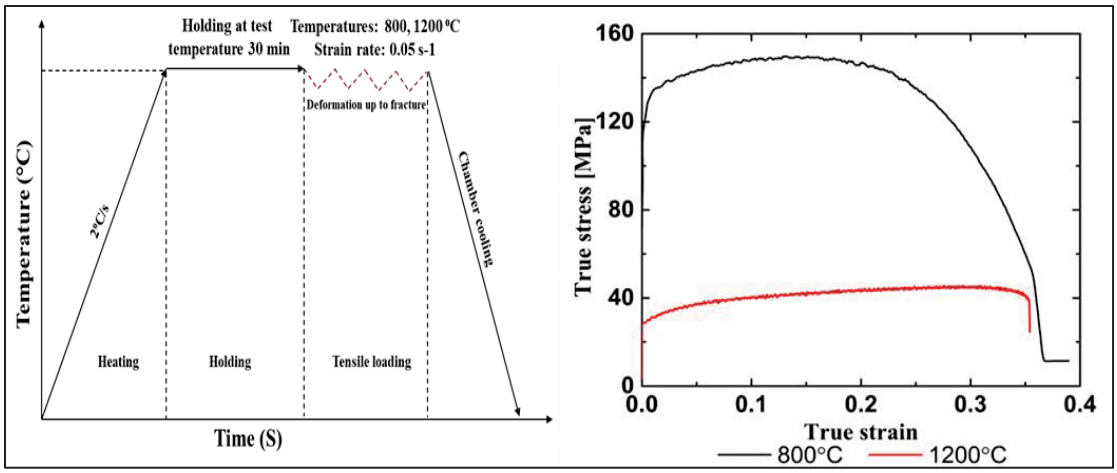

Figure 4.5 (a) The heating and deformation process (b) true stress-strain plot for AISI H13 steel following a hot tensile test at strain rate 0.05 s^{-1}

4.4 Identification of Constitutive law parameters and calculation of damage value

4.4.1 Arrhenius Model

The established model (C.M. Sellars & W.J. McTegart, 1966) provides the relation between critical factors for hot deformation, such as strain rate, temperature and activation energy, while maintaining a constant deformation value. The relationship is presented in Equation 4.1 where Z is known as the Zener-Hollomon parameter:

$$Z = \dot{\varepsilon}\, e^{(\frac{Q}{RT})} \tag{4.1}$$

In the above equation, Q represent the activation energy (kJ.mol^{-1}), R stands for the universal gas constant (kJ.mol^{-1}.K^{-1}) and A, α and n are constants specifics to the material.
Arrhenius model also provides the relation between strain rate, flow stress, and deformation temperature, given by Equation 4.2.

$$\dot{\varepsilon} = \mathrm{AF}(\sigma)\, e^{(-\frac{Q}{RT})} \tag{4.2}$$

Here, F(σ) takes the form of a power function, exponential function, or Hyperbolic sine function as presented below:

$$F(\sigma) = \sigma^{n_1} \ (\alpha\sigma < 0.8) \tag{4.3}$$

$$F(\sigma) = e^{(\beta\sigma)} \ (\alpha\sigma > 1.2) \tag{4.4}$$

$$F(\sigma) = [\sinh(\alpha\sigma)]^n \ (For\ all\ \sigma) \tag{4.5}$$

$$\alpha = \frac{\beta}{n_1} \tag{4.6}$$

In this context, A, n, n_1, β and α represent material constants, with the additional relationship in Equation 4.6. Combining the equations above, provides the expression for the flow stress, which primarily depends on the values of α, Z, A and n. The corresponding values for these material constants were determined through regression analysis and the results are reported in Table 4.2 for a strain of 0.5.

Table 4.2 Material parameters for the Arrhenius Model at strain 0.5

$\beta(MPa^{-1})$	n_1	$\alpha(MPa^{-1})$	n	$Q(K\ J\ mol^{-1})$	$lnA\ (s^{-1})$
0.1230	5.9313	0.0207	4.36	503.079	16.067

On the basis of the above equations, the flow stress could be expressed as Equation 4.7:

$$\sigma = \frac{1}{\alpha} ln \left\{ \left(\frac{Z}{A}\right)^{\frac{1}{n}} + \left[\left(\frac{Z}{A}\right)^{\frac{2}{n}} + 1 \right]^{1/2} \right\} \tag{4.7}$$

The material constants mentioned above in Table 4.2 were determined for a fixed value of strain (0.5). As shown in Figure 4.3, when the strain increases from 0.01 to 0.5, the flow stress exhibits both hardening and softening behaviors in the material and therefore, it must be

considered in the analysis (Jeong, Park, Kim, Shin, & Kim, 2023; Nayak et al., 2020). To address the impact of strain on flow stress, a modified Arrhenius model, known as the strain-compensated model (Yin & Wu, 2022), was used in the present study. The material parameters α, n, Q, and A were formulated as functions of strain by employing polynomial functions of degree six. These functions are detailed and provided in Equations 4.8-4.11. Table 4.3 provides the material parameters for the strain-compensated model, along with the coefficients of the polynomial function. Figure 4.6 shows a comparison of flow stress between experimental and Arrhenius model predicted values is presented

$$\alpha = B_0 + B_1\varepsilon + B_2\varepsilon^2 + \cdots\cdots\cdots\cdots + B_m\varepsilon^m \tag{4.8}$$

$$n = C_0 + C_1\varepsilon + C_2\varepsilon^2 + \cdots\cdots\cdots\cdots + C_m\varepsilon^m \tag{4.9}$$

$$Q = D_0 + D_1\varepsilon + D_2\varepsilon^2 + \cdots\cdots\cdots\cdots + D_m\varepsilon^m \tag{4.10}$$

$$lnA = E_0 + E_1\varepsilon + E_2\varepsilon^2 + \cdots\cdots\cdots\cdots + E_m\varepsilon^m \tag{4.11}$$

Table 4.3 Coefficient of polynomial function for modified Arrhenius model for the AISI H13

α	n	Q($\times 10^{-6}$)	lnA
B_0 =0.0324	C_0 =4.435	D_0 = 0.556	E_0 = 40.9638
B_1 =-0.294	C_1 =-7.379	D_1 =-0.353	E_1 =-23.1777
B_2 =2.9275	C_2 =144.102	D_2 =-4.033	E_2 =-391.262
B_3 =-15.482	C_3 =-1106.84	D_3 =42.129	E_3 =3803.6
B_4 =44.606	C_4 =3735.17	D_4 =-144.929	E_4 =-12996.1
B_5 =-65.421	C_5 =-5896.13	D_5 =206.846	E_5 =18786.2
B_6 =38.146	C_6 =3577.77	D_6 =-101.488	E_6 =-9517.32

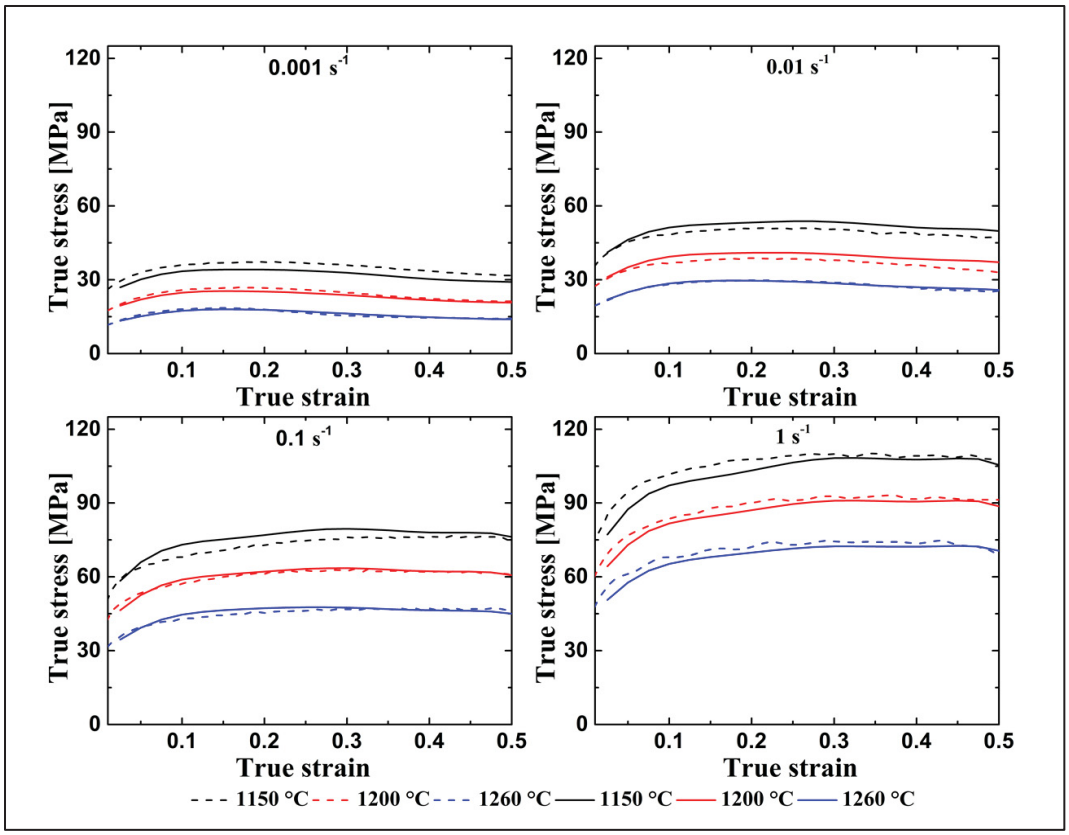

Figure 4.6 Contrasting between experimental (dashed) and predicted (solid) flow stress using the Arrhenius model

4.4.2 Hansel-Spittel and Johnson-Cook Models

The Hansel-Spittel (Nalawade et al., 2013) and Johnson-Cook models (Johnson & Cook, 1985) are phenomenological material models widely used for the prediction of material response during high temperature deformation. Both models have been implemented as default in many materials FE modeling software (Mha et al., 2023). They take into consideration temperature and strain rate dependencies and consider the occurrence of both hardening and softening phenomena during the material's hot deformation process (Niu et al., 2022). Equation 4.12, depicts the mathematical formulation of the Hansel-Spittel model, establishing the relationship between flow stress and the material parameters.

$$\sigma = A_o e^{m_1 T} \varepsilon^{m_2} \dot{\varepsilon}^{m_3} e^{\frac{m_4}{\varepsilon}} (1+\varepsilon)^{m_5 T} e^{m_6 \varepsilon} \dot{\varepsilon}^{m_7} T^{m_8} \tag{4.12}$$

Where, σ represents stress (MPa), $\dot{\varepsilon}$ stands for strain rate (s^{-1}), ε indicates strain, T represents the deformation temperature (°C) and A, m_1 through m_8 are specific material constants reported in Table 4.4.

Table 4.4 Material parameters for Hansel-Spittel model

A	m_1	m_2	m_3	m_4	m_5	m_6	m_7	m_8
3×10^{11}	-0.0027	0.2380	0.1888	-0.0001	-0.0010	-0.0457	-2.5382	0

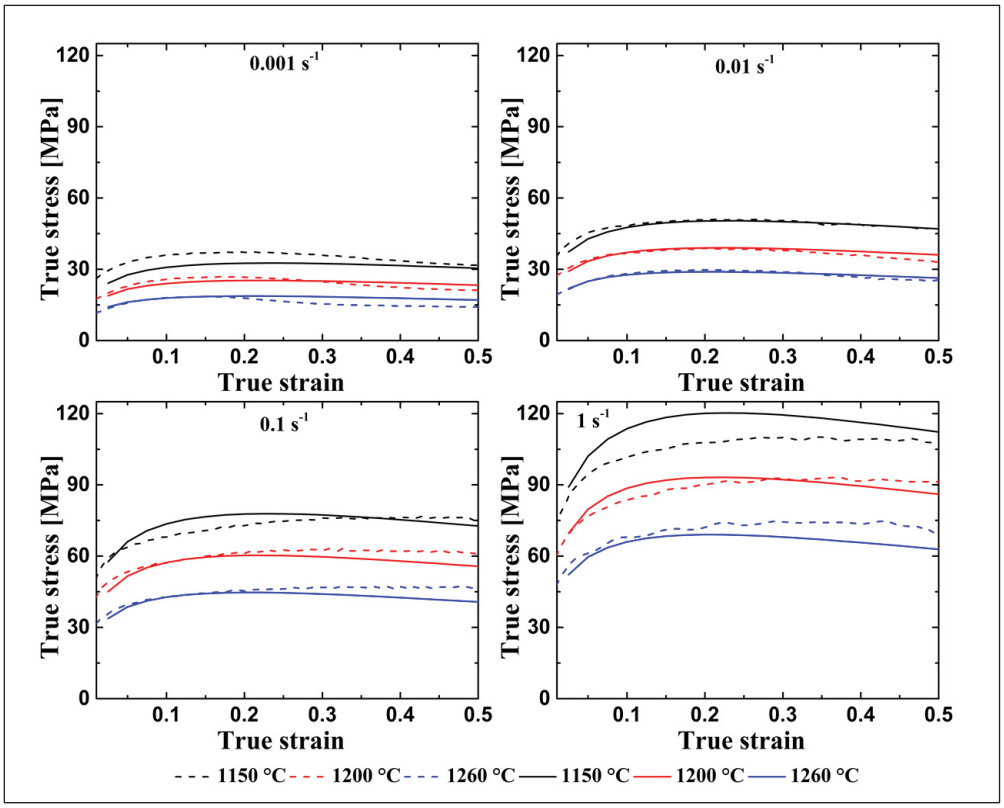

Figure 4.7 Contrasting between experimental (dashed) and predicted (solid) flow stress using the Hansel-Spittel

Figure 4.6 shows a comparison of flow stresses between experimental and Arrhenius model predicted values. Dashed lines represent the experimental data, while solid lines represent the predicted values. The difference between the measured and predicted values is small. However, this difference becomes more pronounced as strain rate increases and temperature decreases. In Figure 4.7 a comparison of flow stress between experimental and Hansel-Spittel model

predicted values is presented. The difference between measured and predicted values are clearly higher compared to the Arrhenius model, especially at higher strain rates $0.1s^{-1}$ and $1s^{-1}$. Notably, for the lowest temperature of 1150 °C and highest strain rates, the Hansel-Spittel model is unable to predict the softening behavior of the AISI H13 material. The quantification of error and R-square values for the predicted flow stresses by the Arrhenius and Hansel-Spittel models is addressed in the subsequent section.

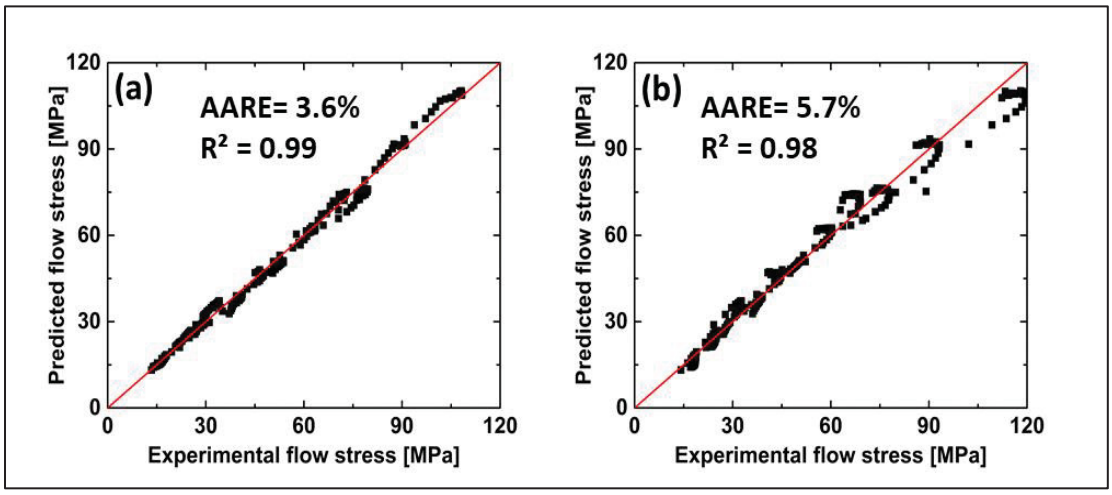

Figure 4.8 Comparison of accuracy and correlation between experimentally measured and predicted flow stress values by employing (a) Arrhenius model and (b) Hansel - Spittel model

Figure 4.8a-b provide a comparison between experimental and predicted flow stress values using both constitutive models. The evaluations conducted using the average absolute relative error (AARE) and R-square values. AARE values, computed using Equation 4.13, were employed to assess the efficiency of flow stress prediction by the two models. AARE values for Arrhenius and Hansel- Spittel model were found to be 3.6% and 5.7%, respectively. R-square values were calculated for Arrhenius and Hansel-Spittel model were found to be 0.9936 and 0.9802, respectively. A similar analysis, which will not be detailed here, was conducted for the Johnson-Cook model and led to similar results. Specifically, for the same data-set, AARE and R-square value were found to be 13.5% and 0.89, respectively. Finally, it must be noted that comparable findings for both models were reported by (Pasco et al., 2022). for modified-H13 steel.

$$AARE = \frac{1}{N}\sum_{1}^{N}\left|\frac{\sigma_e^i - \sigma_p^i}{\sigma_e^i}\right| \times 100 \quad (4.13)$$

Where, σ_e represents the experimental flow stress value, and σ_p denotes the predicted flow stress value.

The above analysis showed that predictions from the Arrhenius model demonstrated higher accuracy and closer alignment with the experimental flow stress values compared to Hansel-Spittel and Johnson and Cook models. As a result, the Arrhenius model was integrated into Forge NxT 3.2® software to simulate the cogging process and predict the stress, strain, and damage evolution map at the end of cogging.

4.5 Normalized Cockcroft and Latham Criterion

This criterion relies on the evolution of the maximum tensile principal stress, effective stress-strain, and strain at the point of fracture. Oh and Kobayashi (S. I. Oh, Chen, & Kobayashi, 1979) proposed a ductile damage criterion to identify the regions prone to ductile damage and crack initiation. During the forging process, ductile failure occurs due to the accumulation of plastic tensile strain and tensile stresses. The damage value reflects the accumulation of damage during the metal forming process (Gontarz & Piesiak, 2015; X. Yang et al., 2022). The critical damage value varies with temperature and strain rate. Stefanik et al. (Stefanik, Dyja, & Mróz, 2011) examined the impact of these parameters on a BSt500S steel and observed that as temperature and strain rate rise, the limiting damage value also increases. Equation 4.14 and Equation 4.15 provide the relationship between the critical damage value and material properties at a given temperature and strain rate. Both equations are available in the Forge NxT 3.2® (G., 1968) . Equation 4.15 is a simplified form of Equation 4.14, and by using it, we can easily obtain an approximate estimate of the critical damage value. Employing this simplified equation to calculate the critical damage value of the material does not require running numerical simulations or validating the tensile test FE model. Therefore, within the scope of this work, the simplified equation was considered for damage value calculations in the forging temperature range. In the present study, the damage values were calculated based on the

percentage reduction in cross-sectional area using Equation 4.15 at constant temperature and strain rate. For this calculation, specimen diameters were measured before deformation and after fracture. Table 4.5 provides the hot tensile properties, percentage reduction in area and the damage values at 800 °C and 1200 °C, for a strain rate of 0.05 s^{-1} determined from the hot tensile tests. Interpretation of cogging results were based on the yield strength and damage values to predict the risky zones for the center burst defect formation and propagation.

$$C_{CR} = \int_0^{\bar{\varepsilon}_f} \left(\frac{\sigma_1}{\bar{\sigma}}\right) d\bar{\varepsilon} \tag{4.14}$$

$$C_{CR} = 1.5 \times \ln\left(1 + \frac{A\%}{100}\right) \tag{4.15}$$

Where, $\bar{\varepsilon}$ is the equivalent strain, $\bar{\varepsilon}_f$ is the strain at fracture, σ_1 is the maximum principal stress, $\bar{\sigma}$ is the effective stress, A% is the reduction of cross section near to fracture.

Table 4.5 AISI H13 steel hot tensile properties and corresponding damage value

Temperature (ºC)	Yield strength (MPa)	Final diameter at necking c/s (mm)	% Reduction in cross section area	Critical damage value (C_{CR})
800	125	~1.5	94	0.99
1200	29	~1.2	96.5	1.01

4.6 Finite element modeling and analysis

The industrial cogging process was simulated using commercial finite element software Forge NxT 3.2®. A three-dimensional finite element model was employed for this analysis. Figure 4.9 shows the finite element model along with the mesh geometry that was used for simulating the cogging process. The three die geometries concave, flat and convex, that were used for the simulation are shown in Figure 4.9a-c. The discretized FE model was used for the numerical simulation with four node tetrahedron elements and mesh sensitivity analysis was performed

to ensure the accuracy of output results. The boundary conditions used in the finite element analysis were similar to the industrial process. This encompassed factors such as the initial billet temperature, deformation rate, amount of deformation applied per blow, and the heat transfer aspects with the environment and the die-workpiece interface. Table 4.6 provides the details of the input boundary conditions used for the FE analysis.

Table 4.6 Input boundary conditions for FE analysis

Parameters	Input to FE model
Ingot initial dimensions	711 mm x 711 mm x 2540 mm
Upper and lower die	Concave, flat and convex
Ingot initial temperature	1260 ºC
Die temperature	35 ºC
Die velocity	15 mm/sec
Material	AISI H13 steel
Material model	Arrhenius
Displacement per blow	165 mm
Mesh size	26 mm (tetrahedron)
Number of mesh elements	126121 (workpiece)
Heat Transfer coefficient with air	10 $W.m^{-2}.K^{-1}$
Heat Transfer coefficient with die	10000 $W.m^{-2}.K^{-1}$
Friction coefficient	0.8

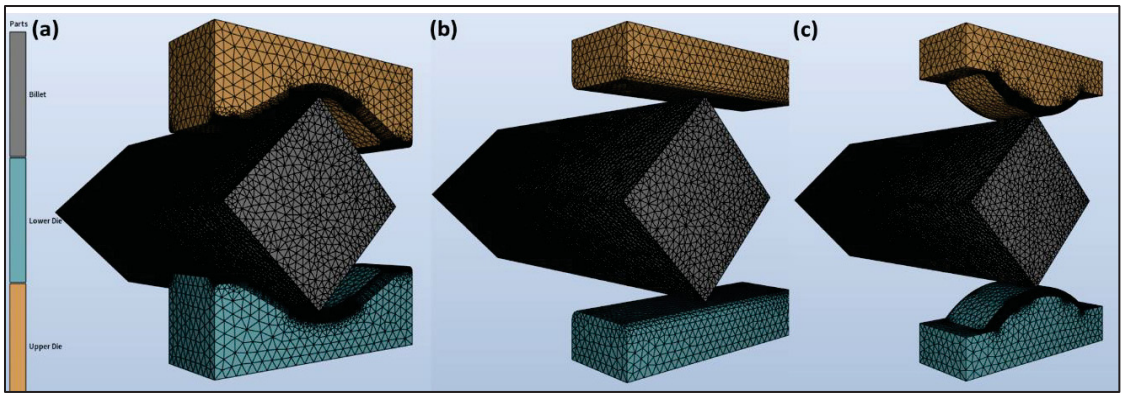

Figure 4.9 Finite element model for cogging simulation before deformation with (a) concave (b) flat and (c) convex die

The dimensions of the flat and curve dies were 304 mm x 406 mm x 1016 mm and the radius of curvature for the curve dies was 203 mm. During the cogging process, the initial billet with a square cross section of 711 mm x 711 mm x 2540 mm was positioned between the upper and lower dies along their edges. At end of every pass, the billet was rotated by 90, 45, and 22.5 degrees to begin the next pass. This process is repeated until a target round shaft with a diameter of approximately 571 mm was obtained.

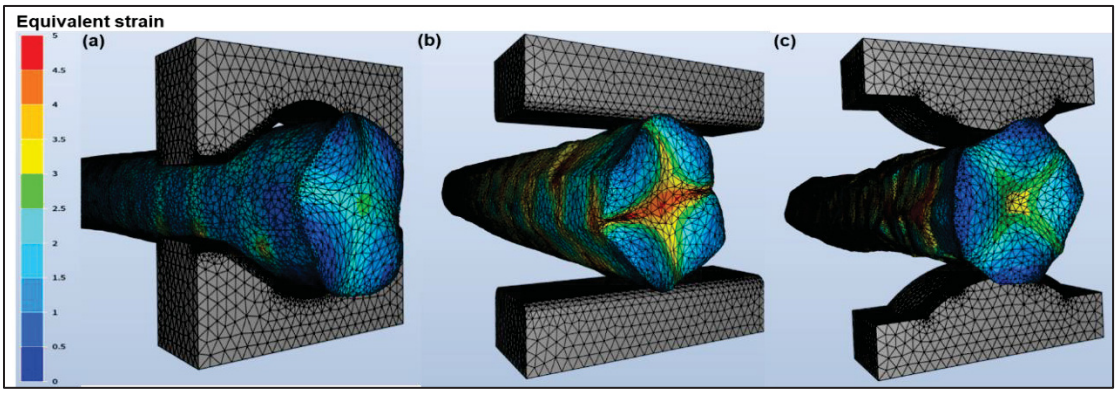

Figure 4.10 Finite element model for cogging simulation after deformation at the end of cogging showing the effective strain distribution with (a) concave (b) flat and (c) convex die

Figure 4.10 shows the finite element model at the end of the cogging process. Figure 4.10a-c shows equivalent strain distribution with concave, flat and convex dies, respectively. The results show that the flat die created higher equivalent strain values compared to the concave

and convex dies curvature. It is interesting to note that to reach the same final dimensions concave, flat and convex dies required number of passes were 12, 19, and 16, respectively.

Moreover, it can be seen that for the same amount of deformation, concave die produces more deformation compared to flat and convex die. Therefore, the concave die requires a smaller number of passes to achieve the final dimensions of the shaft and complete the cogging process.

4.6.1 Industrial setup and validation of FE model

Figure 4.11 shows the forging setup at partner industry, Finkl steel, Sorel, Quebec, Canada. Figure 4.11a shows the 2000 metric tons forging press. Figure 4.11b-c show concave and flat die setup for the cogging of AISI H13 steel, respectively. Press pressure and position data was collected during the cogging operation. Using press pressures, forging loads were calculated in metric tons and with press position data, strain rate and percent deformation were calculated. Figure 4.12 shows the comparison of predicted and measured maximum force for each blow during cogging for the first two passes. It must be noted that, 8 blows were considered in each pass. Figure 4.12a-b shows the comparison between predicted and measured maximum force versus number of blows for concave and flat dies, respectively. Specifically, it can be seen that as contact area between the die and the workpiece surface for the concave die is higher compared to the flat die; as a result, the concave die shows a higher value of maximum force. The average absolute relative error between measured and predicted maximum force were calculated for concave and flat dies, and were found to be ≈ 7% and ≈ 5.3%, respectively. Comparative analysis shows good agreement between predicted and measured maximum forces. Measured force gives slightly higher value compared to the predicted due to the differences in friction conditions. Figure 4.1b and Figure 4.13 shows that final diameter of the shaft at end of cogging process in the industry and at end of FE analysis were very close to each other. AARE value found to be less than 2%; thereby, confirming the validity of the findings.

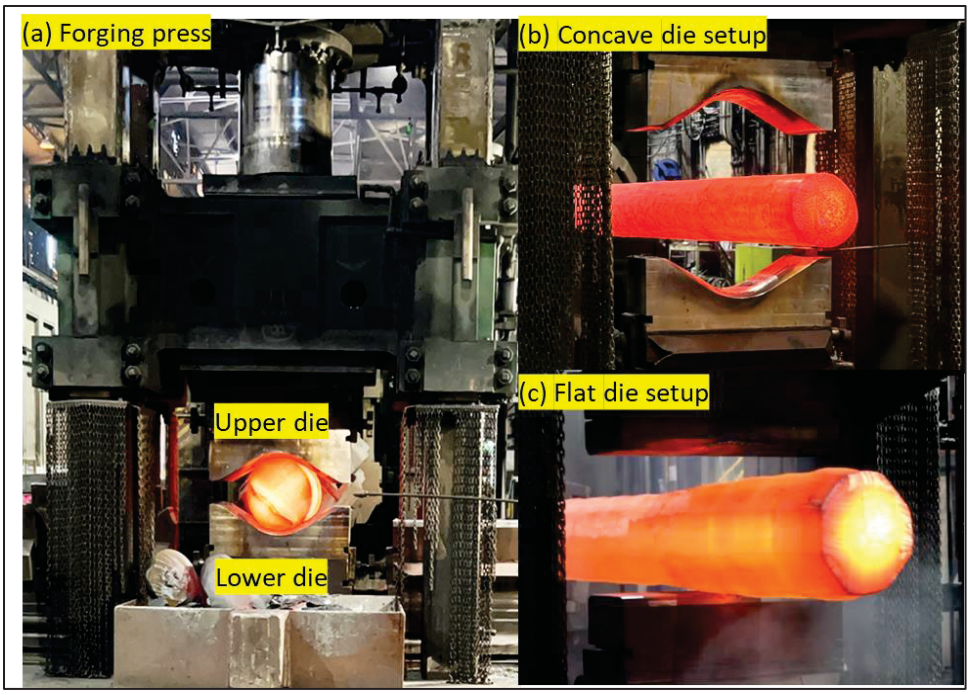

Figure 4.11 Cogging setup at partner industry Finkl steel, Sorel, Canada
(a) 2000 metric tons forging press (b) Concave and (c) Flat die setup

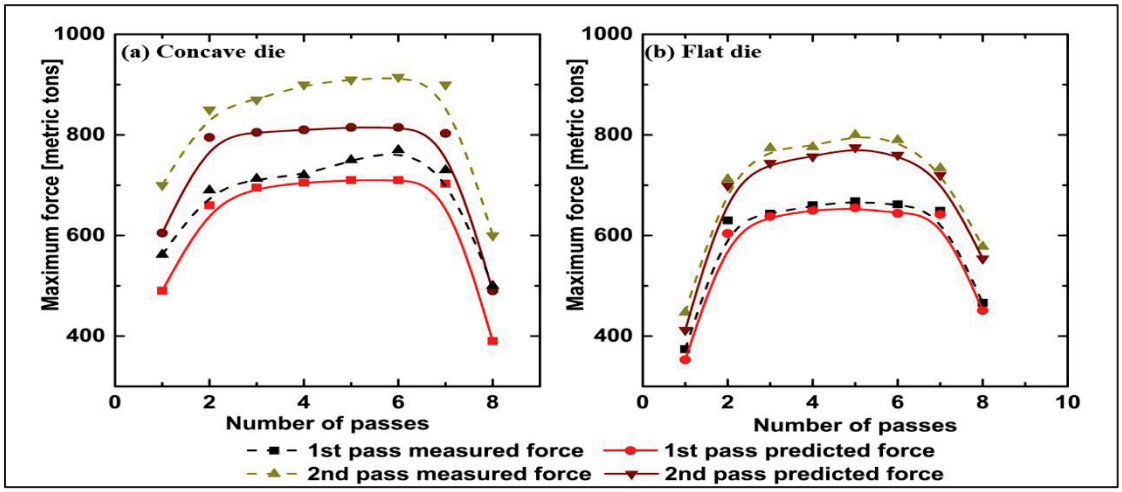

Figure 4.12 Comparison of the measured and predicted maximum force for the initial 2 passes during the cogging process of an industrial size ingot of AISI H13 steel, as shown in (a) for the concave and (b) for the flat die

Figure 4.13 shows the distribution map of equivalent strain along the longitudinal and transverse cross sections of the shaft at the end of the cogging process. The left and right

transverse cross sections were captured at the extreme end and center of the shaft, respectively. The figures in the right cross section display the resulting diameter of the shaft after the simulation using the corresponding die geometries. Following the completion of the cogging process, there is a greater accumulation of equivalent strain at the center of the shaft on the cross section located at the extreme end, in contrast to the cross section at the center. The concave die exhibits a more uniform distribution of equivalent strain across all regions of the shaft, including the surface, center, and extreme edges, in comparison to the convex and flat dies. The outcomes indicate localized deformation along the center axis and extreme edges with the flat die. Conversely, the convex die induces localized deformation at the surface and just below the surface because of its sharper curvature, differing from the concave and flat dies.

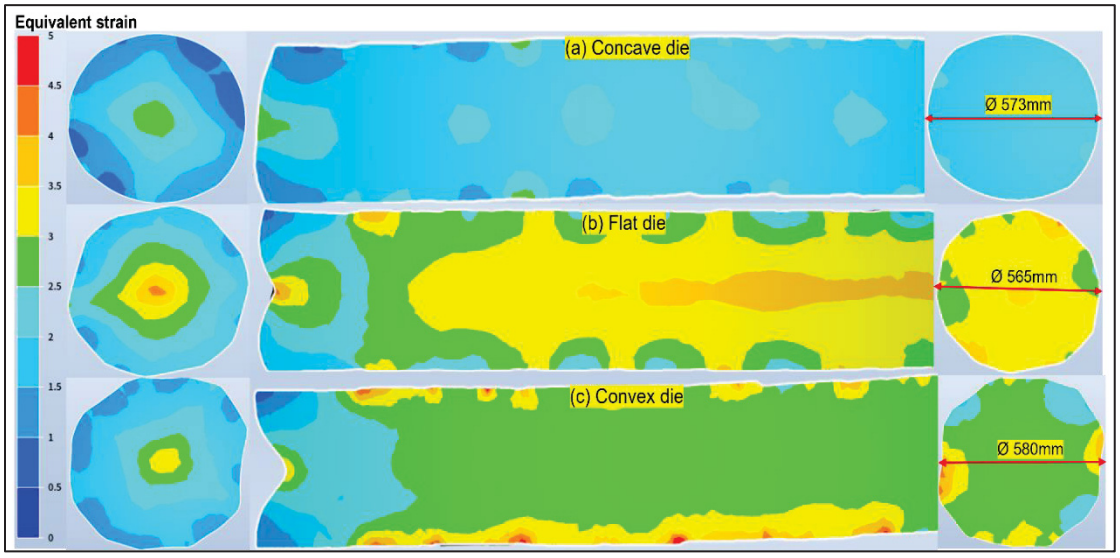

Figure 4.13 The distribution of equivalent strain is shown along the longitudinal and transverse cross sections of the shaft after the cogging process using (a) concave, (b) flat, and (c) convex die

Figure 4.14 presents the distribution of damage values on both the longitudinal and transverse cross sections of the shaft upon completion of the cogging process. The pattern of damage value distribution aligns with that of the equivalent strain distribution. Left and right transverse cross sections were taken at the extreme end and at the center of the shaft, respectively. Upon completing the cogging process, it was observed that damage accumulation at the center of the shaft's extreme end cross section was more pronounced compared to the center cross section.

This disparity can be attributed to varying stress-strain conditions. When employing the concave die, damage distribution exhibited uniformity across the surface, central region, and extreme edges of the shaft. In contrast, the flat and convex dies displayed non-uniform damage distribution. The most substantial damage was identified at the extremities and along the central axis of the shaft. These outcomes align closely with experimental observations, indicating that the shaft's extremities were more susceptible to damage, which in turn could initiate cracks and lead to burst formation. Yang et al. (C. Yang et al., 2018) reported that after burst formation with an increase in the number of passes, crack propagation took place along the longitudinal axis through the center of the shaft.

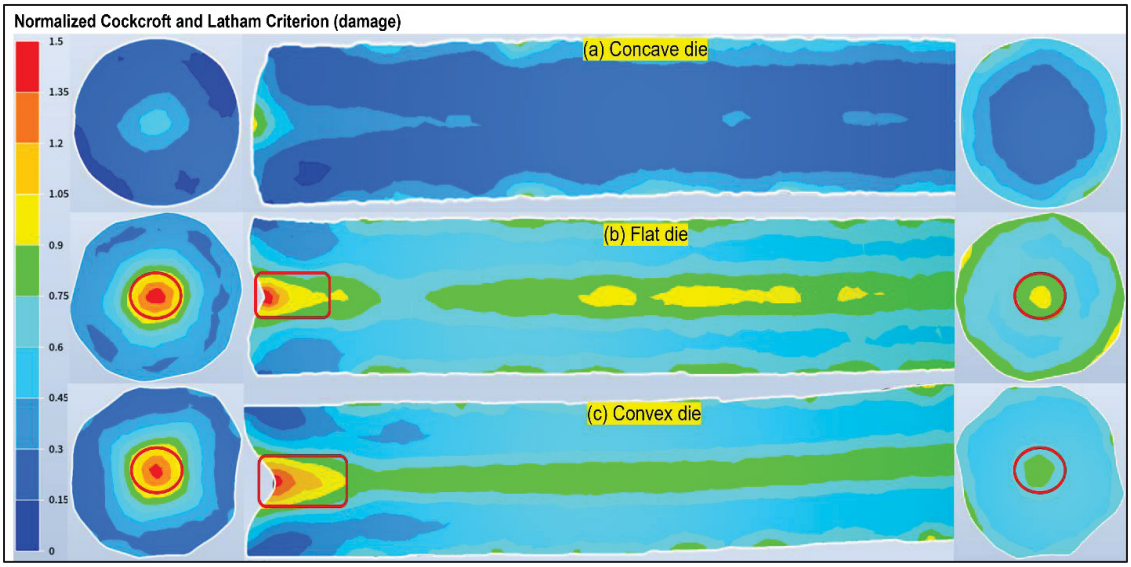

Figure 4.14 Damage value distribution along longitudinal and transverse cross section of shaft at the end of cogging with (a) concave (b) flat and (c) convex die

4.7 Results and Discussion

4.7.1 Identification of the key parameters

To analyze the cogging process, data was collected at the end of each pass. For data recording, two distinct regions were selected: the two ends and the central area of the shaft. This selection was prompted by the non-uniform distribution of deformation and damage along the

longitudinal axis. Figure 4.15 shows the placement of sensors in simulation used for data acquisition. Sensors 1 to 5 were positioned along the longitudinal cross section, aligned with the center axis of the shaft. Sensors 1 and 5 were located at the two extreme ends, while sensors 2, 3, and 4 were positioned within the central regions of the shaft. Equivalent strain, damage value, maximum shear stress and stress triaxiality variations were plotted to show how the average values from the two extreme ends (1 and 5) compare to the average values from the central region (2, 3, and 4) in relation to the number of passes. This analysis is presented in the following:

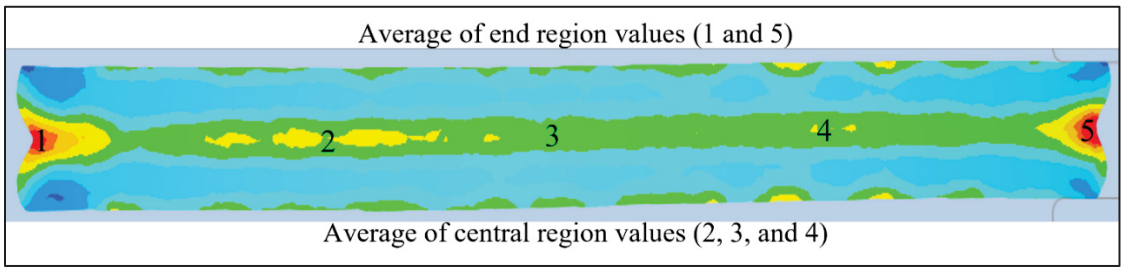

Figure 4.15 Sensor location for data recording at the end of each pass

4.7.2 Equivalent strain distribution

Figure 4.16 depicts the change in equivalent strain as the number of passes increases throughout the cogging process. The results show a linear increase with the increasing number of passes. Notably, the average equivalent strain value at the two ends surpassed the average value within the central region of the shaft at the end of each pass. The average equivalent strain values at the end of cogging varied between 2.4 and 2.9 for the concave die, 3.3 and 4.5 for the flat die, and 2.9 and 3.4 for the convex die, encompassing both ends and the central region.

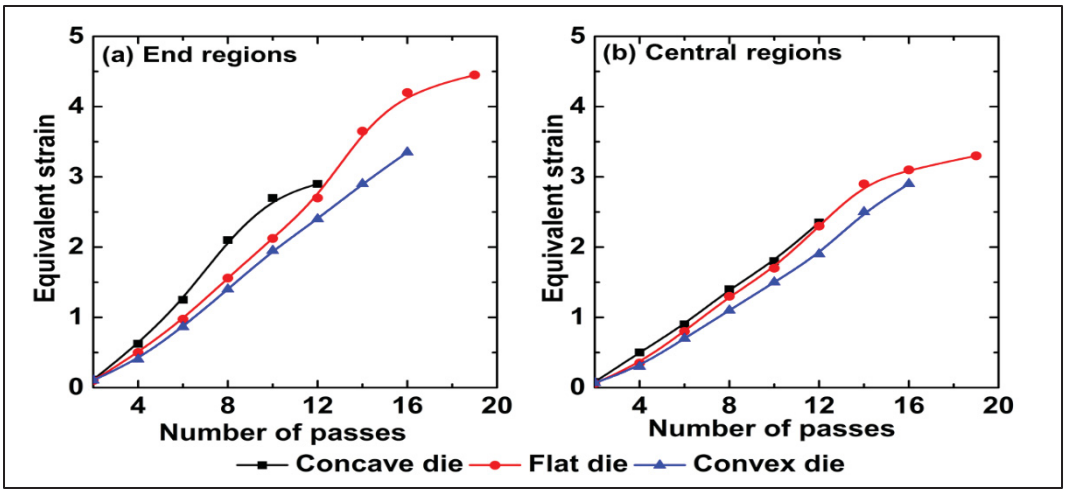

Figure 4.16 Change in equivalent strain with the number of passes during the cogging of H13 steel, depicted as: (a) the average of two end values and (b) the average of values in the central region of the shaft

The results show that, employing the concave die led to higher equivalent strain values at both locations when compared to the flat and convex dies. Du et al. (Du S, Li Y, 2015) reported that during the forging of a railway axle, the equivalent strain at the workpiece center during forging with flat and concave anvils were 1.35 and 1.57, respectively. Xu et al. (Xu et al., 2021) in a similar study stated that the curvature of the concave die induced higher compressive deformation. Thus, by altering the die curvature, the deformation path and intensity of deformation were modified, leading to a more uniform deformation of the material.

4.7.3 Damage value

Based on the outcomes of the hot tensile tests, critical damage values were computed, revealing a variation ranging from 0.9 to 1 at temperatures of 800 °C and 1200 °C, respectively. Figure 4.17 shows that with an increment in the number of passes, the damage value exhibited a linear rise both at the two ends and within the central region along the center axis of the shaft. The average damage values at the two ends were noted to be greater compared to the average value in the central region of the shaft. Initially, up to the 8th pass, the damage values for all die geometries were quite similar. However, after the 8th pass, there was a swift increase to 1.5 and 1.8 for the flat and convex dies, respectively. In contrast, for the concave die, the damage

value increased at a comparatively slower rate, reaching 0.7 at the end of the cogging. Hence, minimizing the number of passes to attain the desired shaft dimensions is of utmost significance. This investigation revealed that utilizing the concave die allowed reaching the required final dimensions in as few as 12 passes, compared to 19 passes with the flat die and 16 passes with the convex die.

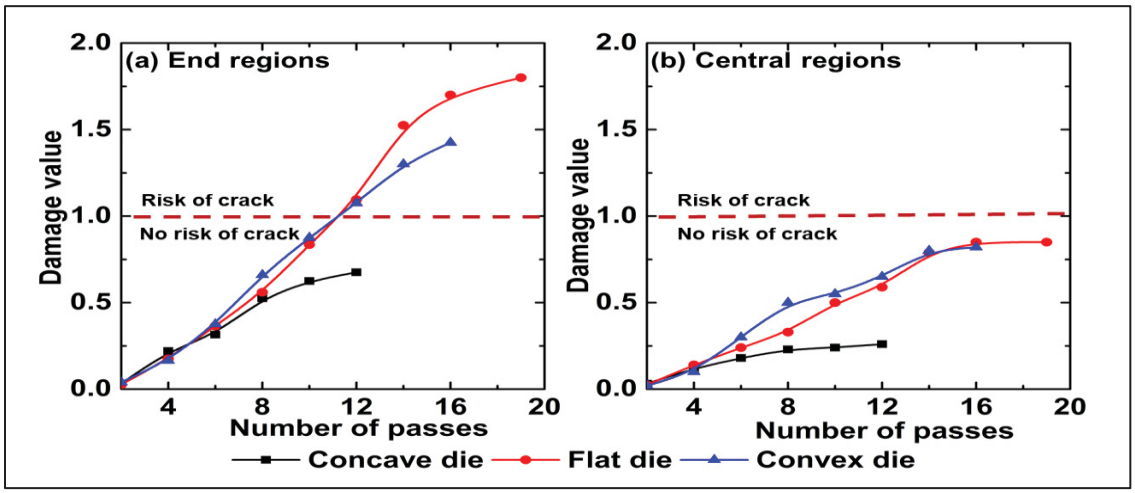

Figure 4.17 Change in damage value with the increase in the number of passes during H13 steel cogging, shown as: (a) the average of two end values and (b) the average of values in the central region of the shaft

4.7.4 Maximum shear stress

The critical threshold for the maximum shear stress was determined as 62.5 MPa through the hot tensile tests. Figure 4.18 demonstrates the change in the maximum shear stress as the number of passes increases during the cogging process. The findings indicate a linear increase in the maximum shear stress value as the number of passes is increasing, both at the two ends and within the central region along the center axis of the shaft. The average maximum shear stress values at the two ends were noted to be higher than the average values in the central region. At the end of cogging, the average maximum shear stress in the central region and at the two ends of the shaft ranged from 26 to 60 MPa for the concave die, 36 to 84 MPa for the flat die, and 29 to 66 MPa for the convex die. Figure 4.18a shows the average value of the maximum shear stress at the end of the cogging for the two ends of the shaft for flat and convex

dies. Notably, this value surpasses the critical threshold for crack initiation, indicating a definite potential for center burst and crack formation. Figure 4.18b shows the average values within the central region of the shaft for the three die geometries. These values remain below the critical stress threshold (62.2 MPa), implying a minimal risk of crack occurrence. Using the concave die geometry, the maximum shear stress value was below the critical threshold in all regions, in contrast to the flat and convex dies. Therefore, with concave die curvature, it was possible to reduce the maximum shear stress value to approximately 60 MPa.

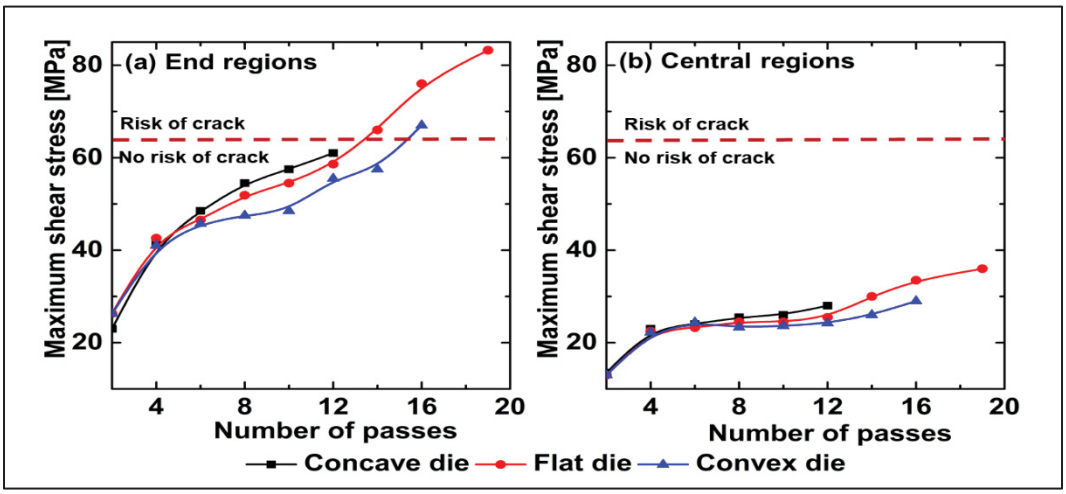

Figure 4.18 Change in maximum shear stress with the increase in the number of passes during the cogging of H13 steel, depicted as: (a) the average of two end values and (b) the average values in the central region of the shaft

4.7.5 Stress triaxiality

The critical stress triaxiality value, necessary to prevent the initiation and formation of cracks in the material, should be equal to or lower than dotted line in Figure 4.19 (-0.3) (Geisler et al., 2023). High negative value reduces the risk of central burst formation (Bao & Wierzbicki, 2005). Figure 4.19 shows the variation of stress triaxiality with the number of passes during cogging. Unlike equivalent strain, damage value and maximum shear stress value, the stress triaxiality value in the central region demonstrates a decrease (more negative value) with the rising number of passes, in contrast to the average value at the two ends of the shaft. Throughout the cogging process, the stress triaxiality variation curve exhibited a sinusoidal

waveform. This phenomenon arises from the alternating compressive and tensile stress states that the material undergoes along the center axis of the shaft with each pass; as the number of passes increases, and as the average stress triaxiality in the central region decreases.

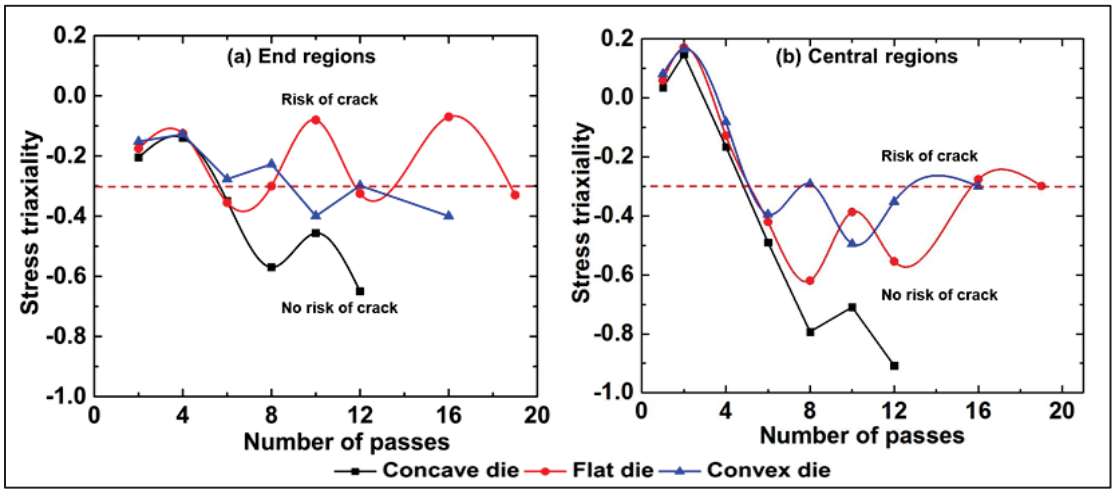

Figure 4.19 Variation of stress triaxiality with the increase in the number of passes during the cogging of H13 steel, represented as: (a) the average of two end values and (b) the average values in the central region of the shaft

The average stress triaxiality values at the extreme ends for all three dies are illustrated in Figure 4.19a. The results show that the stress triaxiality values for the concave die range between -0.2 and -0.7, with the majority of values situated in the region of no crack risk. Similar results were obtained for the central region, as presented in Figure 4.19b. It can be seen that the smallest triaxiality stress values are for the concave die; although, in this case, the two other dies also fall within the safe zone; however, the values are still significantly higher than the ones for the concave die. The large negative value indicates the presence of dominant compressive deformation and stress states along the center axis of the workpiece.

A comparison between the three die geometries that summarizes the above results is provided in Table 4.7, all the parameter values were reported from the extreme end to the central region at the end of cogging. Where it can be seen that the concave die configuration yields to more uniform deformation distribution, maximum shear stress, and lower damage values featuring a notably negative stress triaxiality value of -0.9 (indicative of compressive stress states), in

contrast to the flat die. Furthermore, the comparison demonstrates that all the parameter values for the convex die fall within the range between concave and flat dies.

Table 4.7 Comparison and summary of above results

Parameters	Concave die	Flat die	Convex die
Number of passes requires to achieve final diameter (571mm)	12	19	16
Equivalent strain	2.4 to 2.9	3.3 to 4.5	2.9 to 3.4
Damage value	0.3 to 0.7	0.8 to 1.8	0.8 to 1.4
Maximum shear stress (MPa)	28 to 60	36 to 84	29 to 66
Stress triaxiality	-0.7 to -0.9	-0.32 to -0.3	-0.4 to -0.3

The above results are in agreement with those of Yang et al. (C. Yang et al., 2018) who emphasized the significance of maximum shear stress and maximum tensile stress (first principal stress) as crucial factors influencing the formation and propagation of center burst formation. The results reported by Zhou et al. (Xianyan Zhou, Shao, Zhang, et al., 2020)on the role of tensile and maximum shear stresses on central crack formation during cross wedge rolling are confirmed by our study for cogging of AISI H13. Specifically, our analysis showed that the maximum shear stress initiated void formation, while principal stress expedited crack propagation. Kukuryk et al. (Marcin Kukuryk, 2021) study involved the examination and comparison of three ductile damage criteria. The analysis also revealed that the normalized Cockcroft and Latham damage criterion was an efficient measure for the ductile damage prediction during the cogging process.

Figure 4.16 shows that equivalent strain variation with the same amount of deformation per blow, the concave die induces a greater level of compressive deformation at the center of the shaft than the flat and convex dies. This observation might be attributed to the larger contact area achieved with the concave die in contrast to the other two die geometries. The increased

contact area with the workpiece surface, coupled with the inward shape of the die, results in greater constraining of the lateral material flow (Dyja, Banaszek, Mróz, & Berski, 2004). For flat and convex dies, the contact area was smaller, and there was less control over the lateral material flow. The obtained results are in agreement with those of (Marcin Kukuryk, 2021) who studied the effect of the convex anvils on the stress state and fracture prediction in two stage cogging of a stainless steel bar.

Figure 4.17 and Figure 4.18 shows that the accumulation of damage and maximum shear stress value primarily occurs along the center axis of the shaft, with the highest values concentrated at the two ends of the shaft. This pattern amplifies the risk of crack initiation. Cogging using flat or convex dies surpasses the upper limit of the critical damage value (i.e., 1) and the maximum shear stress value of 62.5 MPa at the end of the cogging process. In such circumstances, the material becomes susceptible to cracking. Figure 4.19 presents the stress triaxiality variation in relation to the number of passes. It must be noted that cogging with flat or convex dies resulted in slightly negative stress triaxiality values (ranging from -0.1 to -0.3 at the two ends of the shaft). In contrast, the use of the concave die yielded stress triaxiality values ranging between -0.2 to -0.7 at the end of cogging. Therefore, the concave die generates more pronounced compressive stresses and deformation at the center, accompanied by smaller damage values (0.3 to 0.7) and uniform deformation. Therefore, concave die curvature provides the more compressive stress-strain states compared to flat and convex die.

4.7.6 Heterogeneity in equivalent strain distribution

Study of heterogeneous distribution of equivalent strain holds importance for the forging process. In case of bulk forming process, inhomogeneities in distribution of plastic strain impact the deformation behavior, microstructure and mechanical properties (B. Li, Zhang, Hu, & Zhang, 2020; Nayak, Singh, Prasad, & Narasimhan, 2023). The heterogeneity index was calculated by measuring the equivalent strain in each of the 126121 elements, in the entire forged bar at the end of 12 passes. In this study, the coefficient of variation (CoV) is introduced as a heterogeneity index for cogging process studies. The coefficient of variation is computed

by dividing the standard deviation by the mean value (Zhu et al., 2012b). In the recent studies available in the literature, heterogeneity in the ring rolling process was expressed using the CoV (Nayak, Kumar Singh, et al., 2023). The dimensionless value CoV, offers insight into the level of variability in relation to the mean within a population. A larger value of CoV indicates higher level of non-uniformity in distribution. The mean (μ) and standard deviation (σ) were computed using the formulae provided in Equation 4.16 and Equation 4.17 respectively. Equation 18 is employed to determine the coefficient of variation, as demonstrated below.

$$\mu = \Sigma_{i=1}^{N} \bar{\varepsilon}_i / N \tag{4.16}$$

$$\sigma = \sqrt{\frac{\Sigma_{i=1}^{N} (\bar{\varepsilon}_i - \mu)^2}{N - 1}} \tag{4.17}$$

$$CoV = \frac{\sigma}{\mu} \tag{4.18}$$

Where, N is the number of elements in the entire ingot. $\bar{\varepsilon}_i$ equivalent strain corresponding to a single element.

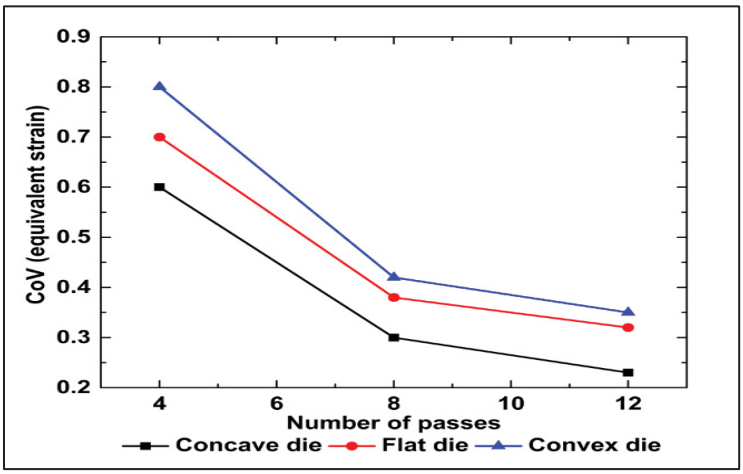

Figure 4.20 Shows the CoV variation of equivalent strain with an increase number of passes

Figure 4.20 show the variation of CoV as a function of the number of passes during the cogging process with concave, flat and convex die. It is observed that as the number of passes increase, the CoV value decreases which results in better homogeneity in strain distribution. This indicates decrease in heterogeneity in equivalent strain distribution as the number of passes increases. Cogging with concave die provides more uniform deformation compared to the flat and convex die. Figure 4.16 and Figure 4.20 show that cogging process with concave die helps in obtaining higher strain levels and uniform deformation compared to flat and convex die and staying below the cracking threshold.

The new approach of using concave die during the cogging of AISI H13 steel has been implemented in the industry as shown in Figure 4.11c. Resulting in the elimination of the center burst defects while the number of passes were reduced from 19 to 12; thereby, reducing energy consumption and increasing the production output.

4.8 Conclusions

This study comprises of development of constitutive model for AISI H13 steel. This model was then implemented via user subroutine to develop a 3D thermo-mechanically coupled FE model of industrial cogging process. The developed FE model was validated using industrial data. Cogging process was optimized using a series of FE simulations run to ascertain the effect of deformation path defined by die geometry (concave, flat and convex) on the stress-strain states and damage evolution along the central axis of the shaft. The objective was to anticipate critical regions prone to center burst formation during the cogging of AISI H13 steel. Complete information on risky zone for the center burst formation was obtained and the best die geometry for the cogging process has been identified. The key finding and conclusions drawn from this study could be summarized as:

1. An optimum material model was developed based on the Arrhenius constitutive model and validated with experimental flow stress data. It shows more accurate prediction compared to the Hansel - Spittel and Johnson - Cook model. Additionally, the critical damage value for the forging temperature range was determined.

2. The developed material and damage model were integrated into the Forge NxT 3.2® and cogging process was simulated for industrial size ingot. The validated FE model offers the capability to forecast the risky area prone to center burst formation during cogging.
3. The concave die provided more uniform and higher compressive deformation, along with lower damage values compared to the flat and convex die during the cogging of highly sensitive material AISI H13 steel.
4. A novel approach and application of concave die in cogging were implemented in the industry and resulted in an elimination of center burst in the shaft and increased production output.

4.9 CRediT authorship contribution statement

Prashant Dhondapure: Conceptualization, Methodology, Visualization, Formal analysis, Validation, Writing – original draft. Pierre Tiza Mha: Methodology, Writing – review & editing. Soumyarajan Nayak: Methodology, Data Curation, Writing – review & editing. Lea Ebacher: Data Curation, Investigation. Simin Dourandish: Methodology, Resources. Henri Champliaud: Supervision, Writing – review & editing. Jean-Benoit Morin: Resources, Writing – review & editing. Mohammad Jahazi: Supervision, Conceptualization, Resources, Writing – review & editing, Project administration, Funding acquisition.

4.10 Declaration of Competing Interest

The authors state that they have no known financial conflicts of interest or personal relationships that could have been seen as potentially influencing the work presented in this paper.

4.11 Data availability

The raw or processed data needed to replicate these results cannot be disclosed presently due to privacy and ethical considerations, as this data is being employed for an ongoing investigation.

4.12 Acknowledgments

This work was funded by Finkl Steel-Sorel and MITACS through a grant number [IT164670]. We would like to thanks Mr. Radu Romanica for conducting the Gleeble experiment precisely. We also appreciate help and support Mr. Patrice Lasne and Mr. John Swanson from Transvalor for helping us to implement a new material model into the Forge NxT® 3.2 software.

Using the material and microstructure model developed in Chapter 3, the final sub-objective was achieved. In Chapter 5, both physical and numerical simulations of the multi-step deformation process were conducted. Through experimental methods and finite element (FE) analysis, the influence of the deformation path on microstructure evolution and the distribution of mechanical properties during the multi-step deformation process was investigated.

CHAPTER 5

INFLUENCE OF DEFORMATION PATH ON MICROSTRUCTURE EVOLUTION DURING MULTI-STEP DEFORMATION OF A HIGH STRENGTH STEEL: EXPERIMENTS AND FE ANALYSIS

Prashant Dhondapure[a], Soumyaranjan Nayak[b], Simin Dourandish[c], Mohammad Jahazi[a,]

[a]Department of Mechanical Engineering, École de Technologie Supérieure,
1100 Notre Dame West, Montreal, Quebec H3C 1K3, Canada.
[b]Advanced Forming Research Centre (AFRC), University of Strathclyde,
85 Inchinnan Drive, Inchinnan, Renfrewshire, PA4 9LJ, UK.
[c]Finkl Steel-Sorel Inc., 100 McCarthy, Saint-Joseph-de-Sorel, Quebec J3R 3M8, Canada.

Paper submitted for publication in J*ournal of Manufacturing Processes*, March 2025

Summary

This study aims to investigate the effect of deformation path on deformation and microstructure evolution during the multi-step deformation of a high strength steel. The deformation paths were illustrated by flat and concave surface curvatures. Multi-step deformation experiments were conducted on high strength steel specimens using thermo-mechanical simulator, Gleeble 3800 equipped with a special purpose attachment, MaxStrain®. All tests were performed at a strain rate of 0.01 s^{-1} and a temperature of 1150°C considering two deformation paths. A total true strain of 0.84 was achieved over four steps, with approximately 0.21 strain applied per step. The results were used to analyze the influence of varying deformation paths on microstructure evolution and hardness distribution. A finite element (FE) model was developed using Forge® NxT 3.2 FE code to simulate the multi-step deformation process. The FE model was validated against measured average grain size and hardness distribution after the multi-step deformation experiments. This validated FE model was capable of predicting strain

distribution, dynamic recrystallization (DRX) volume fraction, and grain size evolution during the multi-step deformation process. A comparative study of the results obtained from two deformation paths was conducted to determine the optimal deformation path, to achieve uniform strain and grain size distribution. The Coefficient of Variation (CoV) was used to assess the heterogeneity of the hardness distribution. The results suggest that concave anvils promote a higher and more uniform strain distribution, leading to a homogeneous distribution of grain size and hardness. A higher and more uniform strain distribution facilitates complete dynamic recrystallization (DRX) with a finer grain size, resulting in a higher and more homogeneous hardness distribution.

5.1 Literature Review

In recent years, demand for large size components has increased in automobile and transport industry. This has resulted in an increased demand for large size dies and plastic injection molds that would allow fabrication of very large size bumpers and dash boards. High strength forged steels are used for the fabrication of large size molds and dies for extrusion or plastic injection technologies. The manufacturing of preform for mold and die starts with casting, open die forging, heat treatment and final machining to the desired shapes (Kanwal Chadha, 2018; Harris et al., 2017; Mha et al., 2023; Murugesan & Jung, 2019). During the casting and forging, *single* and *multi-step*, process inhomogeneities arise due to temperature gradient and non-uniform deformation leading to variations in microstructure and mechanical properties distribution throughout the thickness of the final products (Ahmadi et al., 2025; M. Kukuryk, 2015; Marcin Kukuryk, 2024). Large forged ingots are often characterized by undesirably large grains at their center. One objective of this work is to develop a method for reducing grain size in this central region. Nevertheless, for larger ingots, particularly those exceeding 800 mm in diameter and thickness, grain size distribution is often non-uniform. This inhomogeneity can result in inconsistent mechanical properties, potentially leading to part rejection (Bontcheva & Petzov, 2003). These imperfections become more prominent during manufacturing of large size molds and dies which could lead to part rejection during the quality check (Dhondapure et al., 2023; Dourandish et al., 2022; Ghodrati et al., 2022; Niu & Zhang, 2022). The present

authors investigated the effect of different deformation paths on microstructure evolution during *single step* upsetting process of a high strength steel (Dhondapure et al., 2024). In the present work, multi-step deformation process was considered, as it allows producing more complex geometries and more importantly, it has been reported that it is a crucial process for reducing casting defects (Dhondapure et al., 2023; Dourandish et al., 2022). Precise control of key thermomechanical parameters, including heating rate, holding time, deformation severity, deformation rate, and machine characteristics, is essential during multi-step deformation to ensure a favorable microstructure and optimal mechanical properties through the thickness of large forgings (Dasari et al., 2023).

In addition to above discussed parameters, the deformation path plays a critical role during the hot metalworking of metals. It has a substantial effect on material flow (i.e., strain distribution) and consequently on metallurgical phenomena, particularly dynamic recovery (DRV) and dynamic recrystallization (DRX), that influence the final grain size of the forged material (Chegini, Aboutalebi, Seyedein, Ebrahimi, & Jahazi, 2020; Dudra & Im, 1990; Marcin Kukuryk, 2024). Therefore, designing optimal multi-step forging processes necessitates a deep understanding of how process and geometric parameters interact and affect microstructural development, which ultimately governs final mechanical properties (Dudra & Im, 1990; J. J. Jonas, Sellars, & Tegart, 1969; Mandal, Jayalakshmi, Bhaduri, & Subramanya Sarma, 2014; Markov et al., 2017; McQueen, 2002).

The effect of thermomechanical parameters such as deformation temperature, strain rate has been extensively studied, resulting in vast literature detailing the behavior of various materials under the different deformation conditions (J. J. Jonas et al., 1969; J. Li et al., 2021; Mandal et al., 2014; McQueen, 2002; Nayak et al., 2020; Tize Mha et al., 2023; Ye, Zhai, Zhou, Wang, & Jiang, 2020; Yi Zhang et al., 2016). However, other factors which equally affect the material response to deformation are machine characteristics and die geometry (Ahmadi et al., 2025; Christiansen, Hattel, et al., 2014; Dudra & Im, 1990). In this study die geometry was consider to provide different deformation paths.

Despite extensive research on the influence of thermomechanical parameters on single step deformation using flat dies, the available studies in the literature on the effect of deformation path on microstructure evolution during multi-step deformation are limited. In particular, publications in open literature on microstructure based FE simulation of multi-step deformation process considering different deformation paths are very limited (Christiansen, Hattel, et al., 2014; Christiansen, Martins, et al., 2014; Gruber et al., 2021). The present work addresses the above gap in the literature. Employing a combination of physical simulation of multi-step deformation process and numerical simulation to carry out. Further, a comparative analysis of the impact of dies geometry on microstructure homogeneity of a multi-step deformed specimen and propose the optimal die geometry for the industrial scale forgings.

5.2 Material and method

Medium carbon low alloy high strength steel provided by Finkl Steel (Sorel, Quebec, Canada) was used for the present investigation. The elemental composition of the alloy is provided in Table 5.1.

Table 5.1 Chemical configuration of medium carbon low alloy high strength steel Taken form (Dhondapure et al., 2024)

Elements	C	Mo	Mn	Ni	Si	Cr	Cu	Balance
Weight%	0.31	0.51	0.90	0.70	0.35	1.85	0.15	Fe

Specimens for the MaxStrain tests were prepared from a rectangular forged slab of high strength steel of dimension 635mm x 1986mm x 2997mm. As shown in the Figure 5.1a square bars measuring 15mm x 15mm x 195.58mm were machined from the center of the slab and received from the Finkl Steel to perform final machining at ETS, Montreal. These square bars were then further machined to prepare the final MaxStrain specimens. As shown in the Figure 5.1b, square bar machined at middle to convert a 15mm x 15mm x 12mm cross-section into a 10mm x 10mm x 12mm reduced size square cross-section. It must be mentioned that the multi-step deformation is applied in the reduced section, as shown in Figure 5.1b.

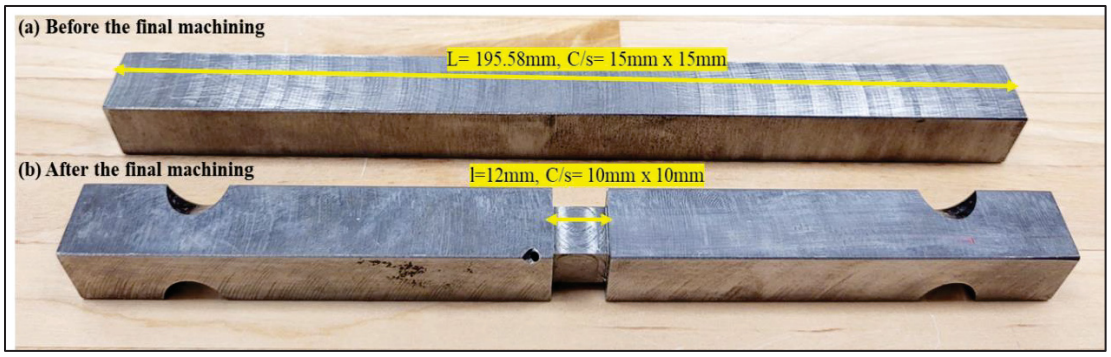

Figure 5.1 Specimen before (a); and after (b) the final machining of the square cross-section bar received from Finkl Steel

5.3 Multi-step deformation experiments

In this study, flat, and concave surface curvature anvils, shown in Figure 5.2, were used for the multi-step deformation experiments. Figure 5.2a-b show schematic of the anvil geometries with dimensions and final machined anvils from the tungsten carbide rectangular blocks of size 10mm x 20mm x 25mm respectively. Two pair of each anvil was prepared for testing, to simulate the condition of Flat-Flat and Concave-Concave anvils combination during multi-step deformation process. The surface curvature of concave anvils was optimized with the help of FE analysis to ascertain higher and uniform deformation. Higher and uniform deformation helps to produce better mechanical properties after the deformation.

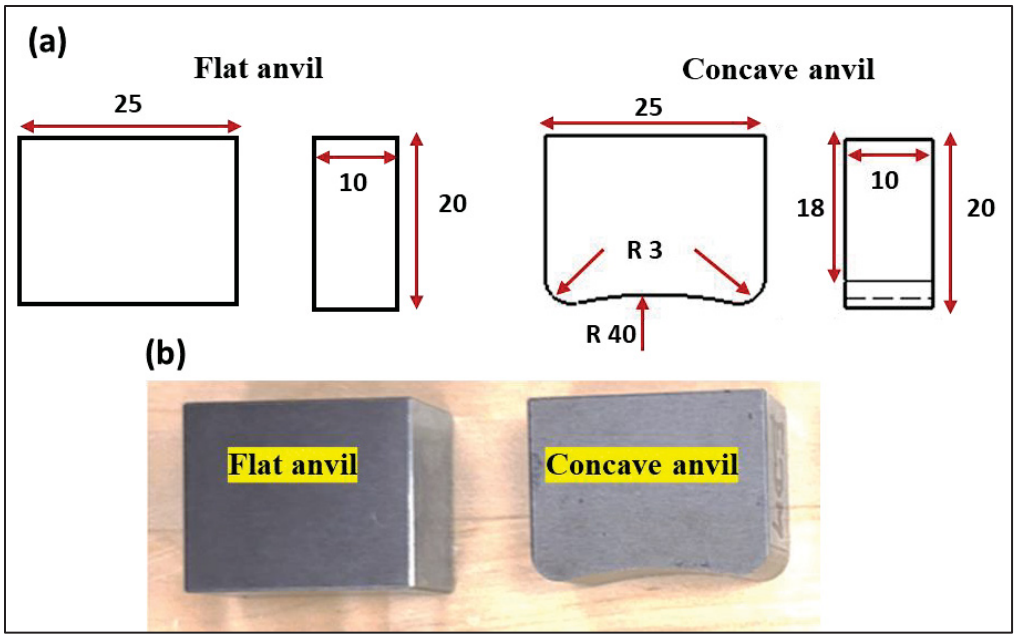

Figure 5.2 (a) schematic of anvil geometries with their dimensions (all dimensions are in mm); (b) final machined anvils of tungsten carbide

The multi-step deformation experiments employing different deformation paths were performed on Gleeble 3800 with MaxStrain® system, experimental setup in the laboratory at École de Technologie Supérieure (ETS), Montreal, Canada as shown in Figure 5.3. This system is developed by Dynamic Systems Inc. (DSI), United States. In the Gleeble system all test parameters can be controlled with as per the input program parameters with high precision during the deformation process. Figure 5.3b-c gives view inside the Maxstrain chamber with concave anvils setup and specimen installed inside during the heating to the test temperature respectively.

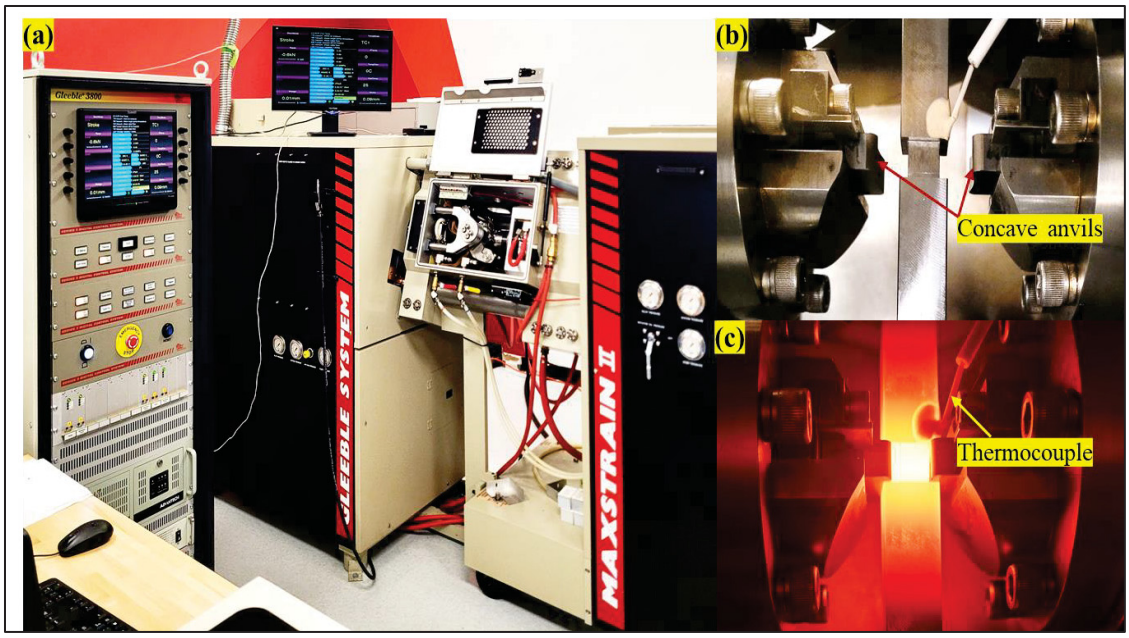

Figure 5.3 Experimental setup for multi-step deformation, (a) gleeble 3800 with MaxStrain® module; (b) experimental setup with concave anvils, specimen with installed thermocouple; (c) View inside the vacuum chamber during testing

The multi-step deformation test parameters, including temperature, applied deformation, and strain rate for each step, were selected to reflect actual industrial forging conditions. During the heating and holding phases, prior to deformation, the anvils were positioned approximately 0.5mm from the specimen to preheat them close to the test temperature, thus minimizing the temperature gradient during the multi-step deformation. Before conducting the actual experiments, numerous trials were performed to establish a reliable thermocouple installation procedure. Super glue and high-temperature white cement were used to secure the thermocouples within the 3mm diameter holes. This optimized installation method ensured temperature stability with a temperature gradient of less than 2°C. Figure 5.4a illustrates the heating, holding, and multi-step deformation cycle used in the experiments. Before the deformation specimens were heated to 1260°C, at a rate of 2°C/s under vacuum to avoid high temperature oxidation. A holding time of 5 minutes was applied to ensure uniform temperature distribution in the 12mm long square cross-section. Afterward, the specimens were cooled to the test temperature of 1150°C at a cooling rate of 1°C/s, followed by different hits at a strain rate of 0.01 s^{-1}. After the first step of deformation, the specimen was rotated clockwise by 90°

around its longitudinal axis and compressed again in a direction perpendicular to the original compression axis. Again, after the second step deformation, it was rotated counterclockwise by 90° to its previous orientation and deformed once more. This cycle was repeated to complete four steps to achieve the required level of deformation, total true strain of 0.84 in four steps, around 0.21 strain per step. At the end of the 4th step, the specimens underwent chamber cooling under the vacuum. Figure 5.4b presents the MaxStrain specimen before and after the multi-step deformation process. Further, multi-step deformed specimens were used for the detail characterization and comparison of results was done for two deformation paths.

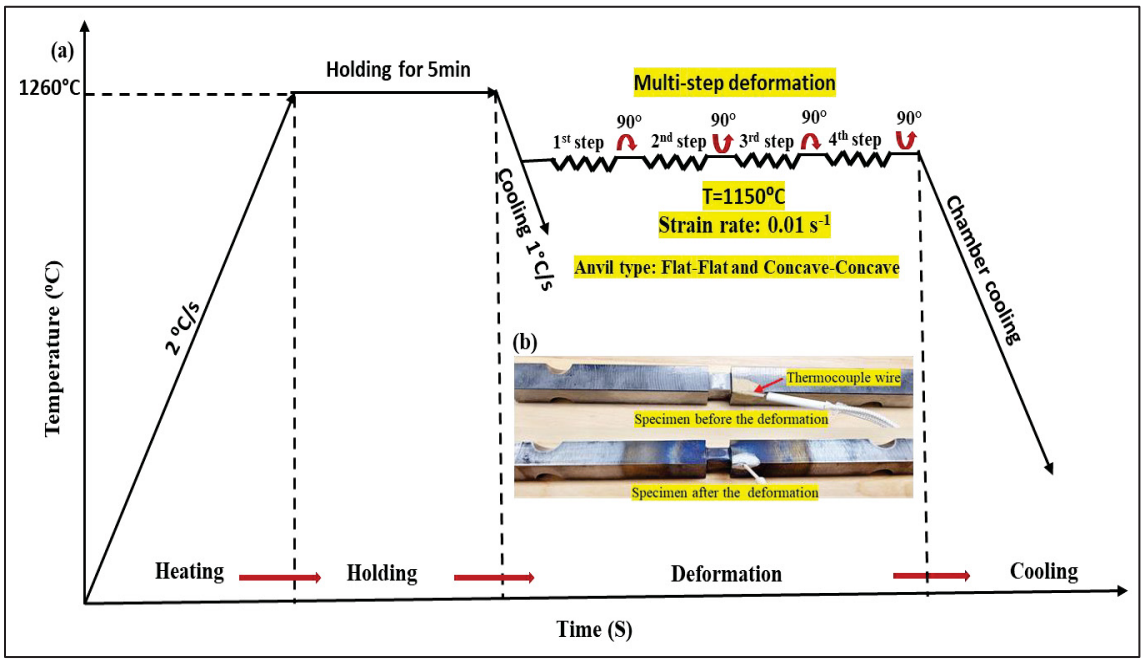

Figure 5.4 (a) schematic of multi-step deformation testing cycle using MaxStrain® module; (b) represents, specimen before and after the deformation

Following the multi-step deformation testing, specimens were sectioned parallel to the deformation axis for microstructure analysis and grain size measurement. The cut specimens were then hot mounted for polishing. Standard polishing techniques were employed for surface preparation prior to chemical etching. To reveal the grain boundaries in the multi-step deformed specimens, an etchant consisting of saturated picric acid and sodium dodecyl benzene sulfonate was used: 100ml of saturated picric acid, 0.5g of sodium dodecyl benzene

sulfonate, and 3-4 drops of HCl (GEORGE F. VANDER VOORT, 2010; S. Bechet and L. Beaujard, 1995). This etchant was applied at room temperature for 3 to 5 minutes to reveal the prior austenite grain boundaries. Using the laser confocal microscope, optical micrographs were taken for microstructure comparison and grain size measurement. The average grain size was determined according to standard ASTM E112 ("Standard Test Methods for Determining Average Grain Size," 2010). In addition, detailed explanation of the metallographic procedures and techniques used can be found in recent research published by the authors (Dhondapure et al., 2024).

5.4 Material and microstructure model

A precise material model was developed for the steel under investigation to accurately predict flow stress across varying temperatures and strain rates. Several constitutive models were evaluated, and their predictive accuracy compared. The results of this comparison indicated that the Arrhenius model offered superior predictions for the investigated steel compared to the Hansel-Spittel and Johnson-Cook models (Dhondapure et al., 2024). The strain dependent Arrhenius model describes the relationship between temperature, strain rate, and activation energy using the following equation (Koval, Das, Paramatmuni, Pickering, & Cogswell, 2025; Mha et al., 2023).

$$\sigma(y) = \frac{1}{\alpha(\varepsilon)} ln\left\{\left(\frac{Z(\varepsilon)}{A(\varepsilon)}\right)^{\frac{1}{n(\varepsilon)}} + \sqrt{\left(\frac{Z(\varepsilon)}{A(\varepsilon)}\right)^{\frac{2}{n(\varepsilon)}} + 1}\right\} \tag{5.1}$$

$$Z = \dot{\varepsilon}\, exp\left(\frac{Q}{RT}\right) = A[sinh(\alpha\sigma)]^n \tag{5.2}$$

In this equation, Z represents the Zener-Hollomon parameter, and Q signifies the activation energy necessary to overcome resistance to deformation. The material specific constants are denoted by A, α, and n, while R represents the universal gas constant. Temperature is represented by T, strain rate by $\dot{\varepsilon}$, and applied stress by σ.

It is widely accepted that during the hot metal working process microstructure evolution is mainly governed by three phenomena: work hardening, dynamic recovery (DRV) and dynamic recrystallization (DRX). In materials with low stacking fault energy (SFE), DRX is the primary softening mechanism, typically occurring after a critical deformation threshold was reached (S. Bechet and L. Beaujard, 1995). The DRX volume fraction is a function of strain, strain rate, deformation temperature, and initial grain size. Its evolution is commonly modeled using the Johnson-Mehl-Avrami-Kolmogoro (JMAK) equation, where the Avrami coefficient (b) and Avrami exponent describes the nucleation and growth kinetics of recrystallized grains (GEORGE F. VANDER VOORT, 2010):

$$X(t) = 1 - e^{-b.t^n} \tag{5.3}$$

Here, *b* and *n* represent the Avrami coefficients. These developed material and microstructure models were integrated into the Forge® NxT 3.2 finite element software to effectively replicate microstructure evolution of the large size bloc during multi-step forging. Further details regarding the determination of model constants and the model integration process can be found in a recent publication by the authors (Dhondapure et al., 2024; Dourandish et al., 2024).

5.5 FE modeling of multi-step deformation process

The multi-step deformation process was simulated using Finite Element (FE) code Forge® NxT 3.2. A 3D FE model was used for this analysis. Figure 5.5 shows the FE model with mesh geometry used for the simulation of the multi-step deformation process. Two different anvil surface curvatures were used in the present investigations, as shown Figure 5.2. FE model with two anvil geometries, flat and concave were used for simulation as shown in Figure 5.5a-b respectively. Tetrahedron four node mesh type was used for the meshing and mesh sensitivity analysis was done to optimize the mesh size. Table 5.2 provides detail input boundary conditions and specimen dimensions used for this analysis. Boundary conditions used for the FE analysis were determined based on the industrial data and previous study done by the

present authors (Dhondapure et al., 2024). This includes the total amount of deformation, temperature, strain rate, heat transfer coefficient, material and microstructure model.

Table 5.2 Input boundary conditions used for numerical simulation of multi-step deformation.

Parameters	Input boundary conditions
Size of deformation region (mm)	10 x 10 x 12
Type of anvils (upper and lower)	Flat-Flat and Concave-Concave
Specimen initial temperature (ºC)	1150
Die temperature (ºC)	1150
Deformation rate (s^{-1})	0.01
Ingot material	Modified AISI P20 steel
Material model	Arrhenius
Microstructure model	JAMK
Total number of steps	4
Deformation in each step	≈0.21
Total deformation	≈0.84
Mesh size (mm)	0.7 (tetrahedron)
Convective heat transfer coefficient ($W.m^{-2}.K^{-1}$)	10
Conductive heat transfer coefficient ($W.m^{-2}.K^{-1}$)	10^4
Friction coefficient	0.8

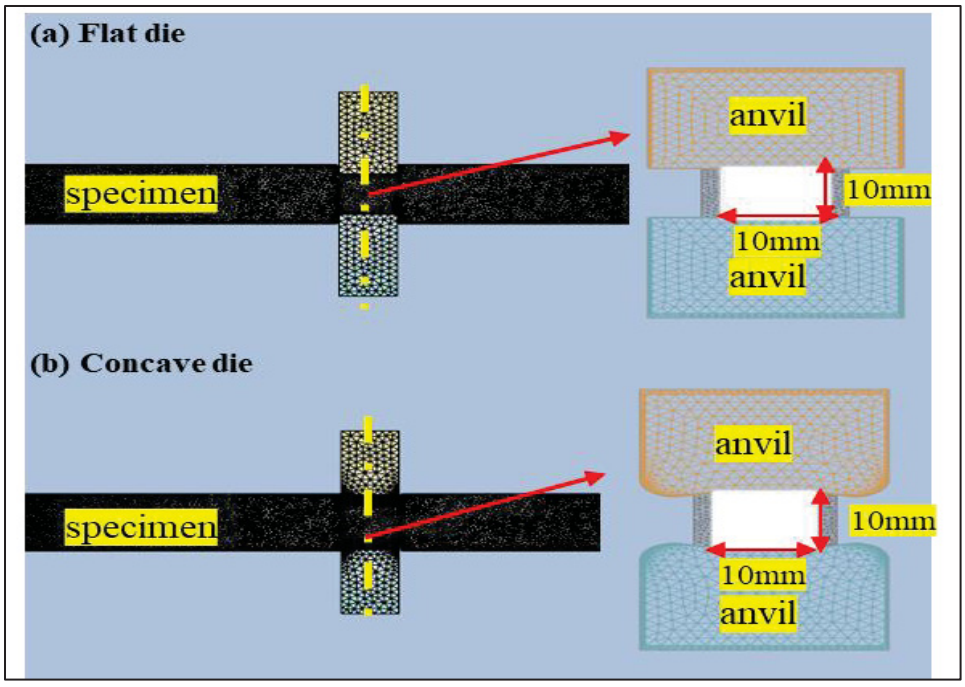

Figure 5.5 Shows the FE model with: (a) flat anvils and;
(b) concave anvils

5.6 Results and discussion

5.6.1 Equivalent plastic strain distribution

Figure 5.6 shows the FE analysis results for equivalent plastic strain distribution at end of multi-step deformation process with flat and concave anvils. This study found that modifying the die surface curvature directly affected strain distributed within the hot deformed specimens. Specifically, at the center of the specimen different levels of equivalent plastic strain were experienced depending on the die shape. Flat anvils resulted in strain values ranging from 1.5 to 2.2, and concave anvils exhibited the higher strain level, ranging from 1.75 to 2.4. These findings demonstrate a clear link between die curvature and the resulting material flow within the workpiece.

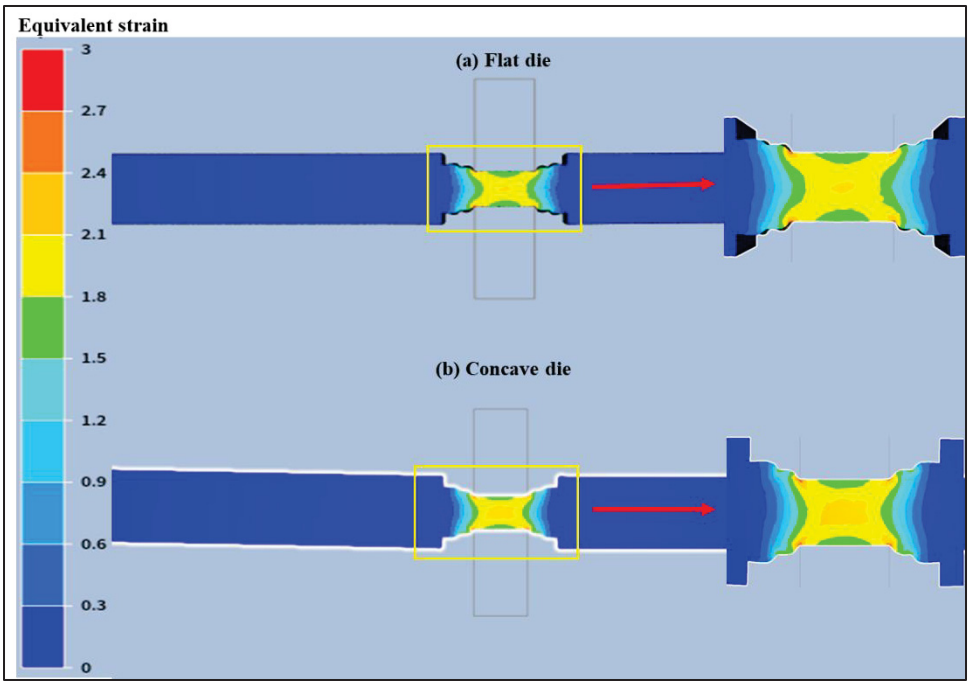

Figure 5.6 Distribution of equivalent plastic strain after the multi-step deformation with: (a) flat anvil and; (b) concave anvil

This observation aligns with previous research on the cogging process of AISI H13 steel, where similar trends were identified (Dhondapure et al., 2023). Furthermore, Du et al. (Du S, Li Y, 2015) found that in forging a railway axle, concave anvils led to higher central strain (1.57) than flat anvils (1.35). Similarly, Xu et al. (Xu et al., 2021) demonstrated that a concave die profile enhanced compressive deformation. These results collectively demonstrate that die curvature influences not only the deformation path but also the magnitude and distribution of strain within the workpiece. Modifying the die curvature allows for effective control over both the pattern and extent of deformation. While existing literature primarily focuses on the effect of deformation path only on the strain distribution and research on the impact of deformation path on microstructure evolution and mechanical properties after multi-step deformation remains limited.

5.6.2 DRX volume fraction distribution

The FE analysis results reported in Figure 5.7, show the distribution of DRX volume fraction where it can be seen that the concave anvils provide higher DRX volume fraction compared to the flat anvils. Specifically, Concave anvils give 85 to 100% of DRX volume fraction across cross section, while most of the cross section with flat anvil give between 60 to 80% DRX volume fraction. Therefore, concave anvils provide complete and homogenous distribution of DRX volume fraction.

This study findings corroborate previous research by Chen et al. (F. Chen et al., 2016), who demonstrated a link between homogenous deformation, higher deformation levels, and increased DRX volume fractions. Similarly, Muszka et al. (Muszka et al., 2013) investigated the influence of different deformation paths on deformation and microstructural inhomogeneity in low carbon microalloyed steels during angular drawing. Their research, which revealed that complex deformation paths promote homogenous deformation and microstructural evolution, aligns with the observations of this study. Both studies highlight the importance of deformation path complexity in achieving desirable microstructural characteristics. Nevertheless, existing research primarily focuses on the influence of deformation paths on the distribution of dynamically recrystallized (DRX) fraction during single stage and uniaxial compression.

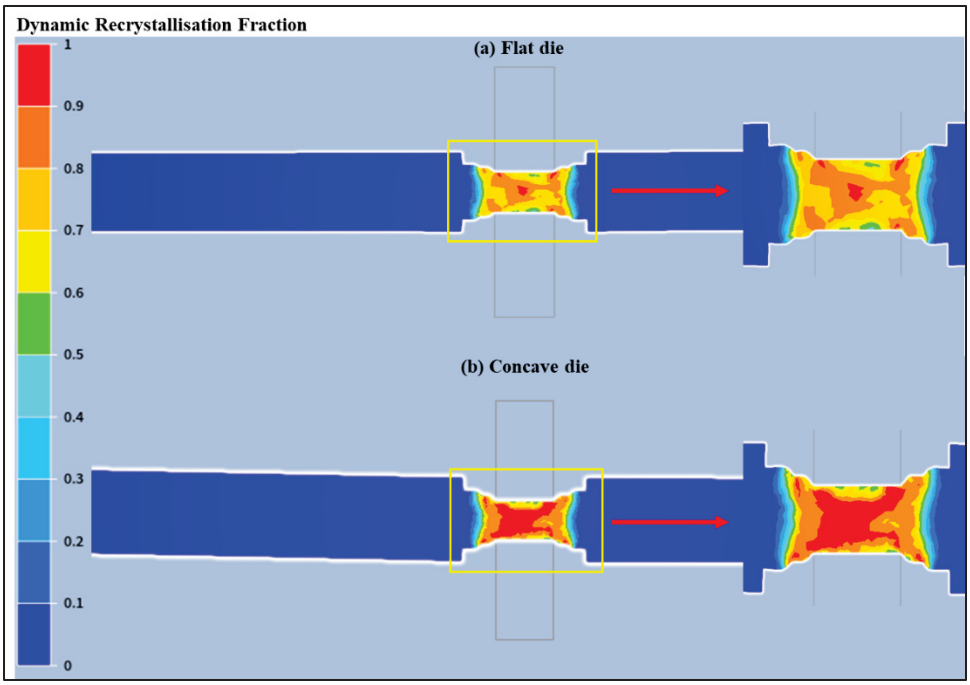

Figure 5.7 Distribution of DRX volume fraction after the multi-step deformation with: (a) flat anvil and; (b) concave anvil

5.6.3 Average DRX grain size distribution

Figure 5.8 illustrate FE analysis results of the average grain size distribution. Before deformation, the initial average grain size was 450μm, as measured after holding the sample at 1260°C for 5 minutes. This value is representative of the grain size observed at the center of a large size forging which is not desirable. After the multi-step deformation, the average DRX grain size predicted for flat and concave anvils 190.5μm and 143.7μm, respectively. From Figure 5.8a-b, it is observed that concave anvils provide not only smaller grain sizes, but also, a more homogenous grain size distribution compared to the flat anvils, due to the complete DRX. The more uniform and finer size grains endorse homogenous, higher, and more consistent mechanical properties.

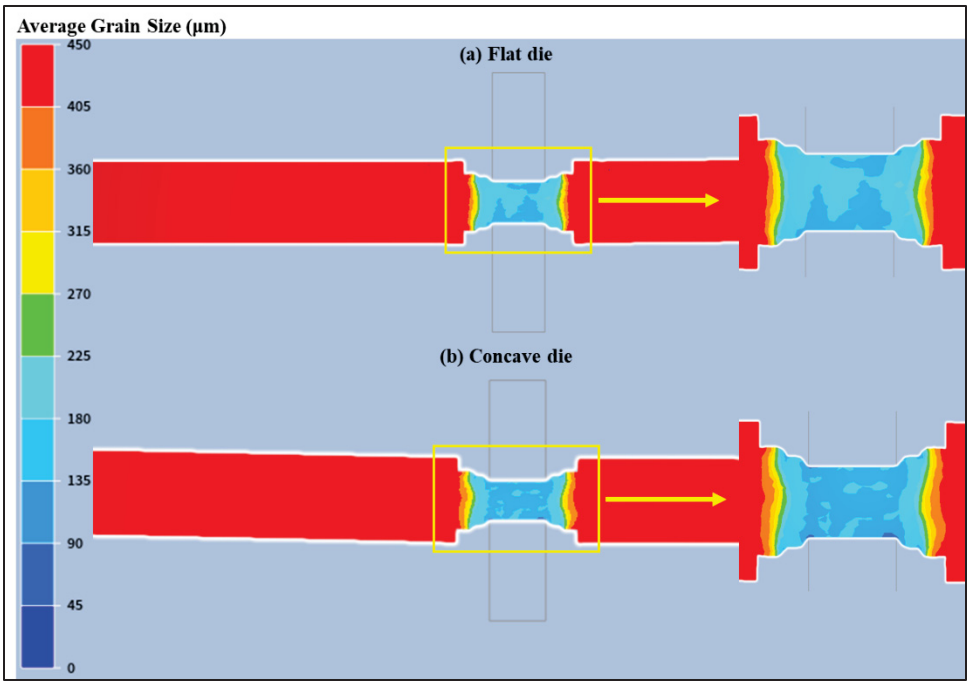

Figure 5.8 Distribution of average grain size after the multi-step deformation with: (a) flat anvil and; (b) concave anvil

5.7 Microstructure investigation and validation of FE model

Figure 5.9 presents optical micrographs taken at the top, center, and bottom along the central axis of each specimen. The micrographs reveal that the grain size in the dead zones, near the top and bottom surfaces, are coarser compared to the grain size at the center for both deformation paths. At the specimen surface, friction with the anvil generates shear stresses that reduce effective plastic strain in that region. As a result, the surface undergoes lower levels of deformation, which inhibits dynamic recrystallization (DRX) and leads to coarser grains compared to the interior. The limited deformation is because of friction between the anvil and specimen. In contrast, the central region experiences higher effective plastic strain and therefore undergoes more complete DRX, resulting in finer and more equiaxed grains. Within the rest of the material, the grain size distributions appear similar for both anvils types. The average grain size for the specimens deformed with the flat and concave anvils was 178.5μm and 135.3μm respectively. As reported in Figure 5.6, the equivalent strain varies from 1.5 to 2.4 from the surface to the center of specimen. The higher deformation level achieved with the

concave anvils resulted in complete DRX and results in the finer DRX grains compared to the specimen deformed with the flat anvils.

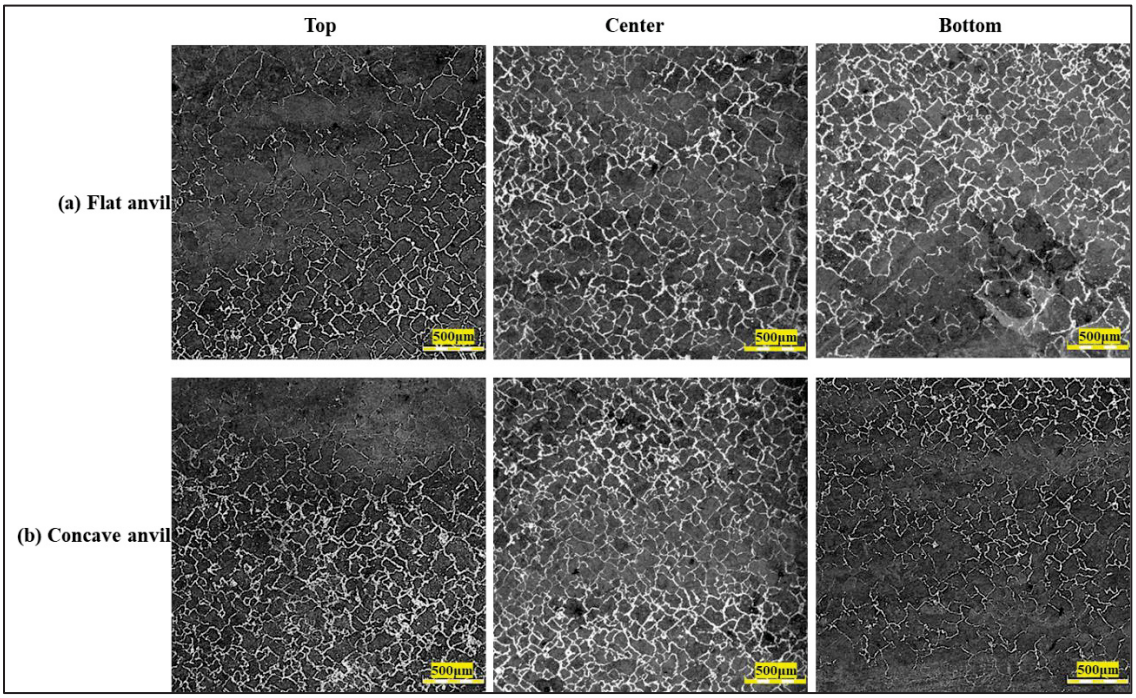

Figure 5.9 Optical micrographs of specimens after multi-step deformation with:
(a) flat anvil and; (b) concave anvil

Figure 5.10 presents a comparison between the average predicted grain size and the measured grain size after multi-step deformation. The prediction accuracy for flat and concave anvils varies between 5.8% and 6.3% respectively, indicating good agreement between the predicted and measured values. Therefore, the developed FE model can effectively predict grain size evolution during the multi-step deformation process. Similar finding were reported in literature during the single stage deformation of steel, validation of measured and predicted data (Dhondapure et al., 2024; Dourandish et al., 2024).

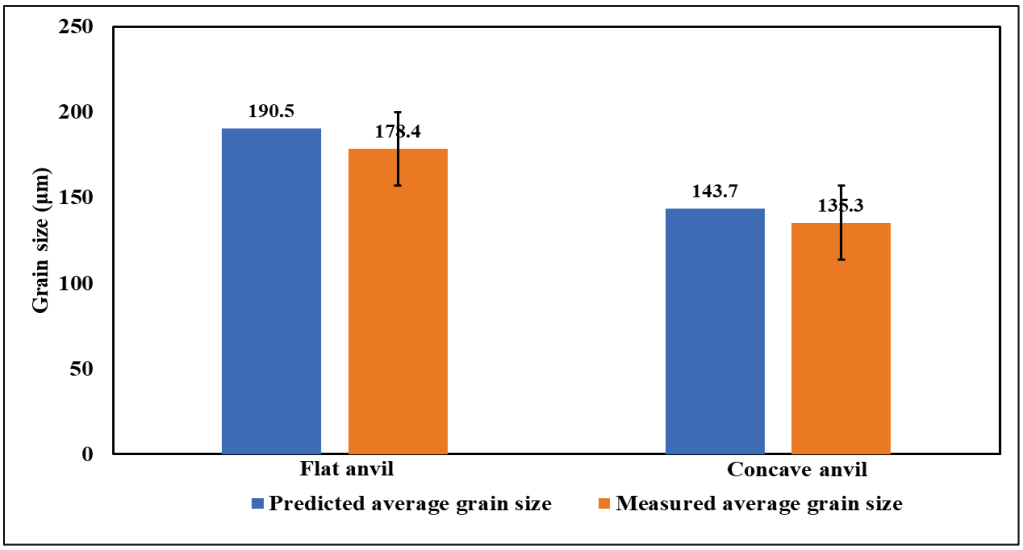

Figure 5.10 Shows the accuracy between predicted and measured average grain size after the multi-step deformation with flat and concave anvil

5.7.1 Hardness measurement and heterogeneity study

Figure 5.11 presents the hardness measurements for specimens subjected to multi-step deformation using flat and concave anvils. Hardness was measured at 0.5 mm intervals along the vertical and horizontal axes, as well as along two diagonals (labeled 1st and 2nd) as indicated in the schematic. For the flat anvil, the average hardness was 643.6 HV with a standard deviation of 68.3 HV, while the concave anvil produced an average hardness of 659.3 HV with a standard deviation of 41.6 HV. As discussed above, concave anvils produce a finer grain size compared to flat anvils. According to the Hall-Petch relationship, this smaller grain size translates to higher mechanical strength in metallic materials (Hall, 1951; Petch Norman J., 1953). The figure clearly demonstrates that the concave anvil resulted in more consistent hardness values, exhibiting less spread in hardness compared to the flat anvil.

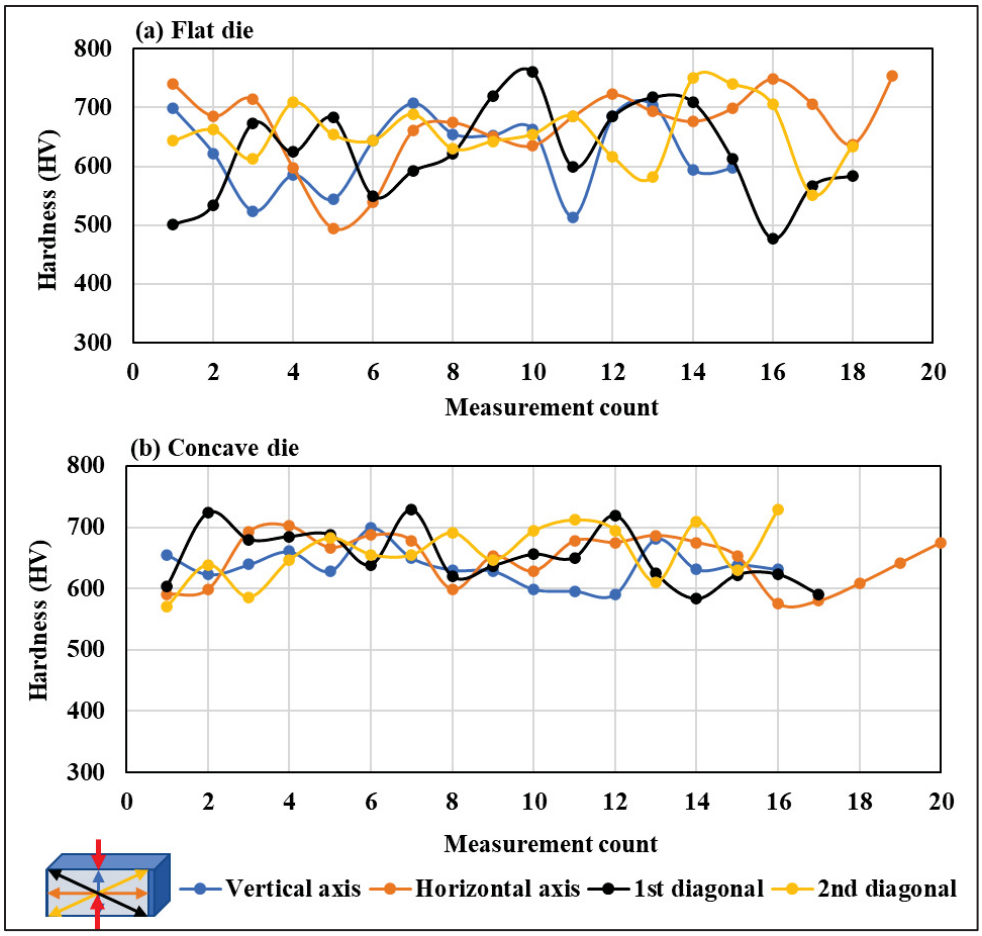

Figure 5.11 Hardness measurement for multi-step deformed specimens with: (a) flat anvils and; (b) concave anvils

A heterogeneity study, using the Coefficient of Variation (CoV) as heterogeneity index, was conducted on hardness values to identify an optimal deformation path used. The CoV, has been defined as the ratio of the standard deviation to the mean (Zhu et al., 2012b). A CoV near zero indicates a homogeneous distribution, while a value of one represents maximum heterogeneity (Nayak, Kumar Singh, et al., 2023). Figure 5.12 shows a clear trend of decreasing CoV values when progressing from flat to concave anvils, indicating improved homogeneity in hardness values distribution. The highest CoV (0.15) was associated with the flat anvil, while the lowest (0.06) corresponded to the concave anvil. As shown in Figure 5.6 and Figure 5.9, the concave anvils facilitated higher strain levels and more homogeneous distributions of both strain and average grain size. These findings were consistent with studies reported in open literature

(Hamad et al., 2014; M. Kukuryk, 2015; Marcin Kukuryk & Winczek, 2018). The findings demonstrate that multi-step deformation using concave anvils results in more uniform hardness values compared to using flat anvils, due to the homogenous distribution of DXR grain size and microstructure. Therefore, this study recommends the use of concave surface curvature dies for the multi-step forging of large industrial components in place of conventional flat surface dies.

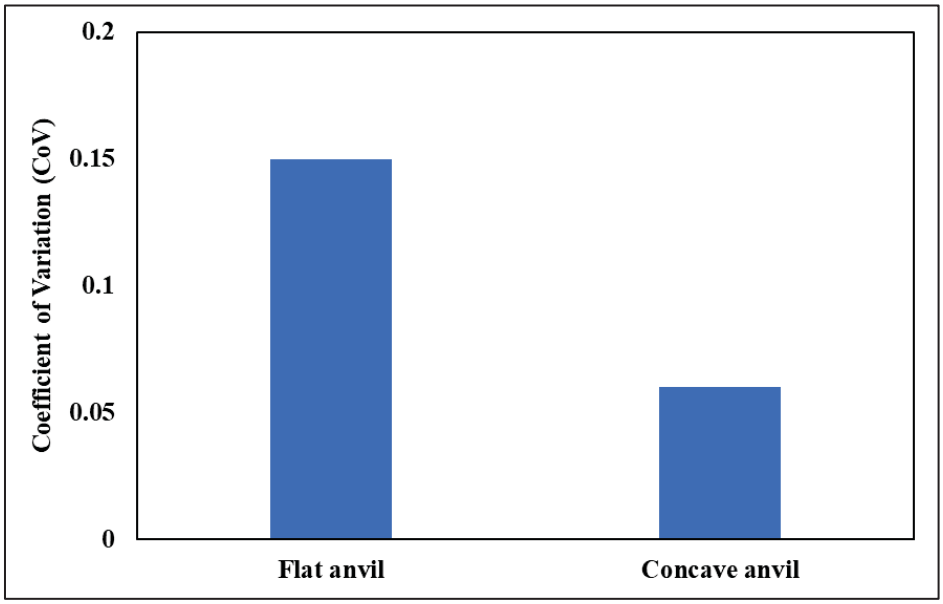

Figure 5.12 The coefficient of variation for hardness values after the multi-step deformation process

5.8 Conclusions

This investigation combines experiments and FE analysis to study the influence of deformation paths on deformation. Microstructure and mechanical property evolution studied during the multi-step deformation of a high strength steel at 1150 °C and a strain rate of 0.01 s^{-1}. Two distinct deformation paths, defined by flat and concave anvils, were analyzed. The key findings and conclusions are summarized below:

1. Both experimental and FE analysis results demonstrate that the deformation path significantly influences the level of deformation and microstructural evolution during multi-step deformation.

2. Concave anvils promote higher and more uniform deformation, higher volume fraction of DRX and more uniform distribution of DRX grain size compared to flat anvil.
3. More uniform hardness distribution was found on specimens deformed with the concave anvil.
4. Concave anvils provide an optimal deformation path for the multi-step deformation process of large size forgings made of high strength steel, leading to improved forge quality.

5.9 CRediT authorship contribution statement

Prashant Dhondapure: Conceptualization, Methodology, Visualization, Formal analysis, Validation, Writing – original draft. Soumyarajan Nayak: Methodology, Data Curation, Writing – review & editing. Simin Dourandish: Resources, Writing – review & editing. Mohammad Jahazi: Supervision, Conceptualization, Resources, Writing – review & editing, Project administration, Funding acquisition.

5.10 Declaration of Competing Interest

The authors state that they have no known financial conflicts of interest or personal relationships that could have been seen as potentially influencing the work presented in this paper.

5.11 Data availability

The raw or processed data needed to replicate these results cannot be disclosed presently due to privacy and ethical considerations, as this data is being employed for an ongoing investigation.

5.12 Acknowledgments

This work was funded by Finkl Steel-Sorel, Canada and MITACS through a grant number [IT164670]. We would like to thanks Mr. Radu Romanica for helping with conducting the MaxStrain experiment precisely.

CONCLUSIONS

During the large-scale forging of high strength tool steels, achieving uniform mechanical properties without any central defects is challenging. It is crucial to understand the relationship between thermomechanical conditions and hot forging variables to address this issue effectively. Additionally, material flow plays a critical role in ensuring uniform deformation and minimizing tensile stress along the central axis of the ingot during the forging process. In this research, material flow was intentionally modified by altering the die geometry (deformation path) to investigate how these changes interact with microstructure development and damage evolution during the hot deformation of high strength tool steels. The conclusions drawn from the investigation related to the three articles are:

Influence of deformation path on microstructure evolution during the open die forging of large size ingot of high strength steel during upsetting process:

This research involved the development of material and microstructure models for a high strength steel, which were integrated into Forge NxT 3.2 using a user subroutine to develop a microstructure based finite element model. The accuracy of the FE model was confirmed through experimental validation of flow stress and average grain size evolution. The validated FE model was then applied to simulate the industrial upsetting process, focusing on assessing the grain size inhomogeneity in the forged ingot at the end of the process. The study offered valuable insights into the optimal deformation path, identifying the best die geometry for the upsetting process.

Influence of deformation path on the stress state and damage evolution along the central axis of a large size ingot of high strength steel during the cogging process:

In this sub-objective, an optimum constitutive model for AISI H13 steel was developed, which was implemented through a user subroutine to develop a finite element model for the industrial

cogging process, which is characterized by large number of deformations passes. A series of FE simulations were conducted to optimize the cogging process, specifically examining the effect of deformation path, defined by die geometry (concave, flat, and convex), on the stress-strain states and damage evolution along the central axis of the shaft. Detailed information about the risky zones for center burst formation was obtained, and the optimal die geometry for the cogging process was determined. An optimal material model was developed based on the Arrhenius constitutive model and validated with experimental flow stress data, offering more accurate predictions compared to the Hansel-Spittel and Johnson-Cook models. Additionally, the critical damage value for the forging temperature range was established. The validated FE model allows for the prediction of areas at risk for center burst formation during cogging. The concave die was found to provide more uniform and higher compressive deformation, along with lower damage values compared to the flat and convex dies during the cogging of highly sensitive AISI H13 steel.

Influence of deformation path on microstructure evolution and mechanical properties variation during multi-step deformation process of high strength steel:

This study combined experimental methods and finite element analysis to investigate the impact of deformation paths on microstructure evolution. The evolution of microstructure and mechanical properties was examined using two different deformation paths. Both experimental results and FE simulations showed that the deformation path plays a crucial role in determining microstructural changes during multi-step deformation. Concave anvils resulted in higher and more uniform deformation, a greater volume fraction of dynamic recrystallization (DRX), and a more consistent distribution of DRX grain sizes compared to flat anvils. Additionally, specimens deformed with the concave anvil exhibited a more uniform hardness distribution. The use of concave anvils provides an optimal deformation path for the multi-step deformation of large high strength steel forgings, resulting in improved forge quality.

LIST OF REFERENCES

Abud, A. P. R., Coletto, E. L. O., Oliveira, S. M. De, & Kuczera, D. (2010). Revealing Prior Austenite Grain Boundaries. *Microscopy and Microanalysis*, *16*(Suppl 2), 6–7. https://doi.org/10.1017/S14319276100

Ahmadi, H., Dehghan, S., & Ranjbar, H. (2025). Enhancement of upsetting technology for minimizing internal defects in heavy ingot casting : simulation , optimization , and experimental validation. *International Journal of Material Forming*, *18(1)*, 21. https://doi.org/https://doi.org/10.1007/s12289-025-01883-x

Ahmed, M. Z., Chadha, K., Reddy, S. R., Shahriari, D., Bhattacharjee, P. P., & Jahazi, M. (2020). Influence of Process Parameters on Microstructure Evolution During Hot Deformation of a Eutectic High-Entropy Alloy (EHEA). *Metallurgical and Materials Transactions A: Physical Metallurgy and Materials Science*, *51*(12), 6406–6420. https://doi.org/10.1007/s11661-020-05991-y

Altan, T., & Ngaile, G. (2005). Cold and Hot Forging. In *Cold and Hot Forging*. https://doi.org/10.31399/asm.tb.chffa.9781627083003

Anjami, N., & Basti, A. (2010). Investigation of rolls size effects on hot ring rolling process by coupled thermo-mechanical 3D-FEA. *Journal of Materials Processing Technology*, *210*(10), 1364–1377. https://doi.org/10.1016/j.jmatprotec.2010.03.026

Arikawa, T., Yamabe, D., & Kakimoto, H. (2014). Influence of anvil shape of surface crack generation in large hot forging process. *Procedia Engineering*, *81*(October), 480–485. https://doi.org/10.1016/j.proeng.2014.10.026

ASTM E8. (2010). ASTM E8/E8M standard test methods for tension testing of metallic materials 1. *Annual Book of ASTM Standards 4*, (C), 1–27. https://doi.org/10.1520/E0008

Avrami, Melvin. (1940). Kinetics of phase change. II Transformation-time relations for random distribution of nuclei. *The Journal of Chemical Physics*, *8*(2), 212–224. https://doi.org/10.1063/1.1750631

Avrami, Mélvin. (1939). Kinetics of phase change. I: General theory. *The Journal of Chemical Physics*, *7*(12), 1103–1112. https://doi.org/10.1063/1.1750380

Babu, K. A., Mandal, S., Athreya, C. N., Shakthipriya, B., & Sarma, V. S. (2017). Hot deformation characteristics and processing map of a phosphorous modified super austenitic stainless steel. *Materials and Design*, *115*, 262–275. https://doi.org/10.1016/j.matdes.2016.11.054

Banaszek, G., Ozhmegov, K., Kawałek, A., Sawicki, S., Arbuz, A., & Naizabekov, A. (2023). Modeling of Closure of Metallurgical Discontinuities in the Process of Forging Zirconium Alloy. *Materials*, *16*(15). https://doi.org/10.3390/ma16155431

Bao, Y., & Wierzbicki, T. (2005). On the cut-off value of negative triaxiality for fracture. *Engineering Fracture Mechanics*, *72*(7), 1049–1069. https://doi.org/10.1016/j.engfracmech.2004.07.011

Bitterlin, M., Loucif, A., Charbonnier, N., Jahazi, M., Lapierre-Boire, L. P., & Morin, J. B. (2016). Cracking mechanisms in large size ingots of high nickel content low alloyed steel. *Engineering Failure Analysis*, *68*, 122–131. https://doi.org/10.1016/j.engfailanal.2016.05.027

Bontcheva, N., & Petzov, G. (2003). Microstructure evolution during metal forming processes. *Computational Materials Science*, *28*(3-4 SPEC. ISS.), 563–573. https://doi.org/10.1016/j.commatsci.2003.08.014

Bulzak, T., Pater, Z., Tomczak, J., & Majerski, K. (2020). Hot and warm cross-wedge rolling of ball pins - comparative analysis. *Journal of Manufacturing Processes*, *50*(August 2019), 90–101. https://doi.org/10.1016/j.jmapro.2019.12.001

C.M. Sellars, & W.J. McTegart. (1966). On the mechanism of hot deformation. *On the Mechanism of Hot Deformation, Acta Metallurgica*, *14*(9), 1136–1138. https://doi.org/https://doi.org/10.1016/0001-6160(66)90207-0

Castellanos, J., Rieiro, I., Cars, M., Muoz, J., & Ruano, O. A. (2007). Analysis of adiabatic heating in high strain rate torsion tests by an iterative method: Application to an ultrahigh carbon steel. *WIT Transactions on Engineering Sciences*, *57*(1), 219–228. https://doi.org/10.2495/MC070221

Chadha, K., Ahmed, Z., Aranas, C., Shahriari, D., & Jahazi, M. (2018). Influence of strain rate on dynamic transformation of austenite in an as-cast medium-carbon low-alloy steel. *Materialia*, *1*(May), 155–167. https://doi.org/10.1016/j.mtla.2018.04.006

Chadha, K., Shahriari, D., Tremblay, R., Bhattacharjee, P. P., & Jahazi, M. (2017). Deformation and Recrystallization Behavior of the Cast Structure in Large Size, High Strength Steel Ingots: Experimentation and Modeling. *Metallurgical and Materials Transactions A: Physical Metallurgy and Materials Science*, *48*(9), 4297–4313. https://doi.org/10.1007/s11661-017-4177-8

Chadha, Kanwal. (2018). Microstructure Evolution Of Medium Carbon Low Alloy Steel During Ingot Breakdown Process by MANUSCRIPT-BASED THESIS PRESENTED TO ÉCOLE DE. *Doctoral Thesis in Electronics, Montreal, École de Technologie Supérieure*. https://doi.org/https://espace.etsmtl.ca/id/eprint/2310

Chamanfar, A., Chentouf, S. M., Jahazi, M., & Lapierre-Boire, L. P. (2020a). Austenite grain growth and hot deformation behavior in a medium carbon low alloy steel. *Journal of Materials Research and Technology*, *9*(6), 12102–12114. https://doi.org/10.1016/j.jmrt.2020.08.114

Chamanfar, A., Chentouf, S. M., Jahazi, M., & Lapierre-Boire, L. P. (2020b). Austenite grain growth and hot deformation behavior in a medium carbon low alloy steel. *Journal of Materials Research and Technology*, *9*(6), 12102–12114. https://doi.org/10.1016/j.jmrt.2020.08.114

Chegini, M., Aboutalebi, M. R., Seyedein, S. H., Ebrahimi, G. R., & Jahazi, M. (2020). Study on hot deformation behavior of AISI 414 martensitic stainless steel using 3D processing map. *Journal of Manufacturing Processes*, *56*(May), 916–927. https://doi.org/10.1016/j.jmapro.2020.05.008

Chen, F., Ren, F., Chen, J., Cui, Z., & Ou, H. (2016). Microstructural modeling and numerical simulation of multi-physical fields for martensitic stainless steel during hot forging process of turbine blade. *International Journal of Advanced Manufacturing Technology*, *82*(1–4), 85–98. https://doi.org/10.1007/s00170-015-7368-8

Chen, M. S., Lin, Y. C., & Ma, X. S. (2012). The kinetics of dynamic recrystallization of 42CrMo steel. *Materials Science and Engineering: A*, *556*, 260–266. https://doi.org/10.1016/j.msea.2012.06.084

Chen, S., Qin, Y., Chen, J. G., & Choy, C. M. (2018). A forging method for reducing process steps in the forming of automotive fasteners. *International Journal of Mechanical Sciences*, *137*(December 2017), 1–14. https://doi.org/10.1016/j.ijmecsci.2017.12.045

Christiansen, P., Hattel, J. H., Bay, N., & Martins, P. A. F. (2013). Modelling of Damage During Hot Forging of Ingots. *STEELSIM 2013 - The 5th International Conference*.

Christiansen, P., Hattel, J. H., Bay, N., & Martins, P. A. F. (2014). Physical modeling and numerical simulation of V-die forging ingot with central void. *Proceedings of the Institution of Mechanical Engineers, Part C: Journal of Mechanical Engineering Science*, *228*(13), 2347–2356. https://doi.org/10.1177/0954406213517878

Christiansen, P., Martins, P. A. F., Bay, N., & Hattel, J. H. (2014). Multi-objective optimization of die geometry in ingot forging. *Procedia Engineering*, *81*(October), 2457–2462. https://doi.org/10.1016/j.proeng.2014.10.350

Cojocaru, E. M., Nocivin, A., Răducanu, D., Angelescu, M. L., Cinca, I., Balkan, I. V., … Cojocaru, V. D. (2021). Microstructure evolution during hot deformation of uns s32750 super-duplex stainless steel alloy. *Materials*, *14*(14), 1–12. https://doi.org/10.3390/ma14143916

Connolly, D., Sivaswamy, G., Rahimi, S., & Vorontsov, V. (2023). Miniaturised experimental simulation of open-die forging. *Journal of Materials Research and Technology*, *26*, 3146–3161. https://doi.org/10.1016/j.jmrt.2023.08.073

Dasari, S. K., Ganguly, S., Abutunis, A., Chandrashekhara, K., Buchely, M. F., Lekakh, S. N., … Natarajan, T. (2023). Implementation of Experimental Static Recrystallization of High Strength Steel into Computational Simulation of Multi-pass Slab Hot Rolling. *Metals and Materials International*, (0123456789). https://doi.org/10.1007/s12540-023-01442-6

Dhondapure, P., Rajakrishnan, N., Nayak, S., & Champliaud, H. (2024). Influence of deformation path on microstructure evolution during the open die forging of large size ingot of high strength steel : experiments and FE analysis. *The International Journal of Advanced Manufacturing Technology*, *134(7)*(0123456789), 3733–3750. https://doi.org/10.1007/s00170-024-14360-7

Dhondapure, P., Tize Mha, P., Nayak, S., Ebacher, L., Dourandish, S., Champliaud, H., … Jahazi, M. (2023). Influence of deformation path on the stress state and damage evolution along the central axis of a large size forged ingot of AISI H13 steel. *Journal of Materials Research and Technology*, *27*(November), 8244–8257. https://doi.org/10.1016/j.jmrt.2023.11.206

Dieter, G. E., Kuhn, H. a., & Semiatin, S. L. (2003). Handbook of Workability and Process Design. *Handbook of Workability and Process Design*, 278–290.

Dourandish, S. (2022). *Microstructure-Based Process Modeling of Open Die Forging of a High Strength Martensitic Stainless Steel by MANUSCRIPT-BASED THESIS PRESENTED TO ÉCOLE DE*.

Dourandish, S., Champliaud, H., Morin, J. B., & Jahazi, M. (2022). Microstructure-based finite element modeling of a martensitic stainless steel during hot forging. *International Journal of Advanced Manufacturing Technology*, *123*(7–8), 2833–2851. https://doi.org/10.1007/s00170-022-10306-z

Dourandish, S., Champliaud, H., Morin, J. B., & Jahazi, M. (2024). Numerical simulation and experimental validation of microstructure evolution during the upsetting process of a large size martensitic stainless steel forging. *International Journal of Material Forming*, *17*(4). https://doi.org/10.1007/s12289-024-01840-0

Du S, Li Y, S. J. (2015). Optimization of Forging Process Parameters and Anvil Design for Railway Axle During High-Speed Forging. *ASME International Mechanical Engineering Congress and Exposition*, *57366*, 1–6. https://doi.org/https://doi.org/10.1115/IMECE2015-50695

Du, S., Chen, S., Song, J., & Li, Y. (2017). Hot Deformation Behavior and Dynamic Recrystallization of Medium Carbon LZ50 Steel. *Metallurgical and Materials*

Transactions A: Physical Metallurgy and Materials Science, *48*(3), 1310–1320. https://doi.org/10.1007/s11661-016-3938-0

Dudra, S. P., & Im, Y. T. (1990). Analysis of void closure in open-die forging. *International Journal of Machine Tools and Manufacture*, *30*(1), 65–75. https://doi.org/10.1016/0890-6955(90)90042-H

Dyja, H., Banaszek, G., Mróz, S., & Berski, S. (2004). Modelling of shape anvils in free hot forging of long products. *Journal of Materials Processing Technology*, *157–158*(SPEC. ISS.), 131–137. https://doi.org/10.1016/j.jmatprotec.2004.09.022

Ebacher, L., Jahazi, M., Morin, J. B., & Ritchey, B. (2022). Thermomechanical Study of H13 Hot Forged Bars. *4th International Ingot Casting Rolling Forging, ICRF 2022 - Conference Proceedings*, (June), 26–37. https://doi.org/10.33313/530/003

Ebrahimi, G. R., Momeni, A., Kazemi, S., & Alinejad, H. (2017). Flow curves, dynamic recrystallization and precipitation in a medium carbon low alloy steel. *Vacuum*, *142*, 135–145. https://doi.org/10.1016/j.vacuum.2017.05.010

El-Danaf, E., Kalidindi, S. R., & Doherty, R. D. (2001). Influence of deformation path on the strain hardening behavior and microstructure evolution in low SFE FCC metals. *International Journal of Plasticity*, *17*(9), 1245–1265. https://doi.org/10.1016/S0749-6419(00)00090-5

El Wahabi, M., Gavard, L., Montheillet, F., Cabrera, J. M., & Prado, J. M. (2005). Effect of initial grain size on dynamic recrystallization in high purity austenitic stainless steels. *Acta Materialia*, *53*(17), 4605–4612. https://doi.org/10.1016/j.actamat.2005.06.020

Fanfoni, M., & Tomellini, M. (1998). The Johnson-Mehl-Avrami-Kolmogorov model: A brief review. *Nuovo Cimento Della Societa Italiana Di Fisica D - Condensed Matter, Atomic, Molecular and Chemical Physics, Biophysics*, *20*(7), 1171–1182. https://doi.org/10.1007/BF03185527

G., C. M. (1968). Ductility and workability of metals. *J. of Metals*, *96*, 2444. Retrieved from https://cir.nii.ac.jp/crid/1572824499676083456

Gao, S., Sang, Y., Li, Q., Sun, Y., Wu, Y., & Wang, H. (2022). Constitutive modeling and microstructure research on the deformation mechanism of Ti-6Al-4V alloy under hot forming condition. *Journal of Alloys and Compounds*, *892*, 162128. https://doi.org/10.1016/j.jallcom.2021.162128

Geisler, A., Sadeghifar, M., Morin, J. B., Loucif, A., & Jahazi, M. (2023). Void closure during open die forging of large size martensitic stainless-steel ingots: an experimental-analytical-numerical study. *International Journal of Material Forming*, *16*(1), 1–11. https://doi.org/10.1007/s12289-022-01735-y

Genel, K. (2006). Boriding kinetics of H13 steel. *Vacuum*, 1–7.

GEORGE F. VANDER VOORT. (2010). Revealing Prior Austenite Grain Boundaries. *Microscopy and Microanalysis*, *16*(Suppl 2), 6–7. https://doi.org/10.1017/S14319276100

Ghazani, M. S., & Eghbali, B. (2018). A Ductile Damage Criterion for AISI 321 Austenitic Stainless Steel at Different Temperatures and Strain Rates. *Arabian Journal for Science and Engineering*, *43*(9), 4855–4861. https://doi.org/10.1007/s13369-018-3191-5

Ghiotti, A., Fanini, S., Bruschi, S., & Bariani, P. F. (2009). Modelling of the Mannesmann effect. *CIRP Annals - Manufacturing Technology*, *58*(1), 255–258. https://doi.org/10.1016/j.cirp.2009.03.099

Ghodrati, N., Baiteche, M., Loucif, A., Gallego, P. I., Jean-Benoit, M., & Jahazi, M. (2022). Influence of Hot Top Height on Macrosegregation and Material Yield in a Large-Size Cast Steel Ingot Using Modeling and Experimental Validation. *Metals*, *12*(11). https://doi.org/10.3390/met12111906

Gontarz, A., & Piesiak, J. (2015). Determining the Normalized Cockroft-Latham Criterion for Titanium Alloy Ti6Al4V in Tensile Testing At Room Temperature. *Proceedings of the World Congress on Mechanical, Chemical, and Material Engineering*, (248), 4–7.

Gruber, C., Raninger, P., Stanojevic, A., Godor, F., Rath, M., Kozeschnik, E., & Stockinger, M. (2021). Simulation of dynamic and meta-dynamic recrystallization behavior of forged Alloy 718 parts using a multi-class grain size model. *Materials*, *14*(1), 1–15. https://doi.org/10.3390/ma14010111

Hall, E. O. (1951). The deformation and ageing of mild steel: III Discussion of results. *Proceedings of the Physical Society. Section B*, *64*(9), 747–753. https://doi.org/10.1088/0370-1301/64/9/303

Hamad, K., Chung, B. K., & Ko, Y. G. (2014). Effect of deformation path on microstructure, microhardness and texture evolution of interstitial free steel fabricated by differential speed rolling. *Materials Characterization*, *94*, 203–214. https://doi.org/10.1016/j.matchar.2014.05.019

Han, Yahui, Li, C., Ren, J., Qiu, C., Chen, S., & Li, E. (2021). Dynamic recrystallization behavior during hot deformation of as-cast 4Cr5MoSiV1 steel. *Journal of Materials Science*, *56*(14), 8762–8777. https://doi.org/10.1007/s10853-021-05792-7

Han, Yahui, Li, C., Ren, J., Qiu, C., Li, E., & Chen, S. (2021a). Characterization of Hot Deformation Behavior and Processing Map of As-Cast H13 Hot Work Die Steel. *Metals and Materials International*, *27*(9), 3574–3589. https://doi.org/10.1007/s12540-020-00863-x

Han, Yahui, Li, C., Ren, J., Qiu, C., Li, E., & Chen, S. (2021b). Microstructural Evolution during Homogenization and Hot Deformation for As-Cast H13 Steel. *Steel Research International*, *92*(3), 1–10. https://doi.org/10.1002/srin.202000439

Han, Ying, Liu, G., Zou, D., Liu, R., & Qiao, G. (2013). Deformation behavior and microstructural evolution of as-cast 904L austenitic stainless steel during hot compression. *Materials Science and Engineering: A*, *565*, 342–350. https://doi.org/10.1016/j.msea.2012.12.043

Han, Ying, Wu, H., Zhang, W., Zou, D., Liu, G., & Qiao, G. (2015). Constitutive equation and dynamic recrystallization behavior of as-cast 254SMO super-austenitic stainless steel. *Materials and Design*, *69*, 230–240. https://doi.org/10.1016/j.matdes.2014.12.049

Harris, N. (2016). *Determination of Optimal Forging Conditions for Void Elimination in Large Steel Ingots*.

Harris, N., Shahriari, D., & Jahazi, M. (2017). Development of a fast converging material specific void closure model during ingot forging. *Journal of Manufacturing Processes*, *26*, 131–141. https://doi.org/10.1016/j.jmapro.2017.02.021

Hughes, D. A., & Hansen, N. (1997). High angle boundaries formed by grain subdivision mechanisms. *Acta Materialia*, *45*(9), 3871–3886. https://doi.org/10.1016/S1359-6454(97)00027-X

Humphreys, Frederick John, and M. H. (2012). Recrystallization and related annealing phenomena. *Elsevier*.

Humphreys, F. J., & Hatherly, M. (2004). Hot Deformation and Dynamic Restoration. *Recrystallization and Related Annealing Phenomena*, (1981), 415–V. https://doi.org/10.1016/b978-008044164-1/50017-7

Humphreys, F. J., & Matherly, M. (2004). 6.1.1 The occurrence of recovery. *Recrystallization and Related Annelaling Phenomena*, 437–444.

Ivaniski, T. M., Epp, J., Zoch, H. W., & Da Silva Rocha, A. (2019). Austenitic grain size prediction in hot forging of a 20mncr5 steel by numerical simulation using the JMAK model for industrial applications. *Materials Research*, *22*(5). https://doi.org/10.1590/1980-5373-MR-2019-0230

Jang, Y. S., Ko, D. C., & Kim, B. M. (2000). Application of the finite element method to predict microstructure evolution in the hot forging of steel. *Journal of Materials Processing Technology*, *101*(1), 85–94. https://doi.org/10.1016/S0924-0136(99)00460-4

Jeong, H. Y., Park, J., Kim, Y., Shin, S. Y., & Kim, N. (2023). Processing parameters optimization in hot forging of AISI 4340 steel using instability map and reinforcement

learning. *Journal of Materials Research and Technology*, *23*, 1995–2009. https://doi.org/10.1016/j.jmrt.2023.01.106

Ji, H., Duan, H., Li, Y., Li, W., Huang, X., Pei, W., & Lu, Y. (2020). Optimization the working parameters of as-forged 42CrMo steel by constitutive equation-dynamic recrystallization equation and processing maps. *Journal of Materials Research and Technology*, *9*(4), 7210–7224. https://doi.org/10.1016/j.jmrt.2020.04.078

Jin, Z., Li, K., Wu, X., & Dong, H. (2015). Modelling of Microstructure Evolution during Thermoplastic Deformation of Steel by a Finite Element Method. *Materials Today: Proceedings*, *2*, S460–S465. https://doi.org/10.1016/j.matpr.2015.05.062

Johnson, Richard A., Irwin Miller, and J. E. F. (2018). Probability and Statistics for Engineers. In *The American Statistician* (9th ed., Vol. 49). Pearson education limited. https://doi.org/10.2307/2684651

Johnson, G. R., & Cook, W. H. (1983). A Computational Constitutive Model and Data for Metals Subjected to Large Strain, High Strain Rates and High Pressures. *Proceedings 7th International Symposium on Ballistics*, 541–547.

Johnson, G. R., & Cook, W. H. (1985). Fracture characteristics of three metals subjected to various strains, strain rates, temperatures and pressures. *Engineering Fracture Mechanics*, *21*(1), 31–48. https://doi.org/10.1016/0013-7944(85)90052-9

Johnsson, W. A., & Mehl, R. F. (1940). Reaction kinetics in processes of nucleation and growth. *Trans. Am. Inst. Min. Metall. Eng.*, *135*(1089), 416–442.

Jonas, J. J., Sellars, C. M., & Tegart, W. J. M. G. (1969). Strength and structure under hot-working conditions. *Metallurgical Reviews*, *14*(1), 1–24. https://doi.org/10.1179/mtlr.1969.14.1.1

Jonas, John J., Quelennec, X., Jiang, L., & Martin, É. (2009). The Avrami kinetics of dynamic recrystallization. *Acta Materialia*, *57*(9), 2748–2756. https://doi.org/10.1016/j.actamat.2009.02.033

Jonšta, P., Kurka, V., Vindyš, M., & Kander, L. (2021). The effect of forging conditions on final macrostructure of slab ingot from the 55nicrmov7 tool steel. *Metals*, *11*(3), 1–16. https://doi.org/10.3390/met11030435

Kakimoto, H., & Arikawa, T. (2014). Prediction of surface crack in hot forging by numerical simulation. *Procedia Engineering*, *81*(October), 474–479. https://doi.org/10.1016/j.proeng.2014.10.025

Koval, O., Das, A., Paramatmuni, C., Pickering, E., & Cogswell, D. (2025). Evaluation of uncertainty in material flow predictions in hammer forging of steel through constitutive

modelling. *Journal of Manufacturing Processes*, *133*(December 2024), 1207–1221. https://doi.org/10.1016/j.jmapro.2024.11.048

Krishna, B. V., & Sidhu, R. K. (2002). Analysis of center burst during hot forging. *Journal of Failure Analysis and Prevention*, *2*(5), 61–66. https://doi.org/10.1007/bf02715471

Krishna, R. H., & Jena, D. P. (2019). Analytical and numerical modelling of open-die forging process for elliptical cross-section of billet. *Measurement: Journal of the International Measurement Confederation*, *134*, 855–865. https://doi.org/10.1016/j.measurement.2018.12.023

Kukuryk, M. (2015). Analysis of deformation and microstructural evolution in the hot forging of the Ti-6Al-4V alloy. *Archives of Metallurgy and Materials*, *60*(2A), 597–604. https://doi.org/10.1515/amm-2015-0179

Kukuryk, Marcin. (2019). Experimental and FEM Analysis of Void Closure in the Hot Cogging Process of Tool Steel. *Metals*, *9*(538). https://doi.org/doi:10.3390/met9050538

Kukuryk, Marcin. (2020). Analysis of deformation and prediction of cracks in the cogging process for die steel at elevated temperatures. *Materials*, *13*(24), 1–17. https://doi.org/10.3390/ma13245589

Kukuryk, Marcin. (2021). Analysis of deformation, the stressed state and fracture predictions for cogging shafts with convex anvils. *Materials*, *14*(11). https://doi.org/10.3390/ma14113113

Kukuryk, Marcin. (2024). Experimental and numerical study of the closure of voids with different size and various locations in the three-dimensional cogging process. *International Journal of Material Forming*, *17*(1), 1–15. https://doi.org/10.1007/s12289-023-01798-5

Kukuryk, Marcin, & Winczek, J. (2018). Analysis of deformation and microstructure evolution during the cogging process of Waspaloy alloy. *MATEC Web of Conferences*, *157*. https://doi.org/10.1051/matecconf/201815702022

Kvačkaj, T., Tiža, J., Bacsó, J., Kováčová, A., Kočiško, R., Pernis, R., … Purcz, P. (2014). Cockcroft-Latham ductile fracture criteria for non ferrous materials. *Materials Science Forum*, *782*(March 2021), 373–378. https://doi.org/10.4028/www.scientific.net/MSF.782.373

Lee, H. W., Lee, G. A., Yoon, D. J., Choi, S., Na, K. H., & Hwang, M. Y. (2008). Optimization of design parameters using a response surface method in a cold cross-wedge rolling. *Journal of Materials Processing Technology*, *201*(1–3), 112–117. https://doi.org/10.1016/j.jmatprotec.2007.11.287

Li, B., Zhang, S., Hu, R., & Zhang, X. (2020). Dislocation density and grain size evolution in hard machining of H13 steel: Numerical and experimental investigation. *Journal of Materials Research and Technology*, *9*(3), 4241–4254. https://doi.org/10.1016/j.jmrt.2020.02.051

Li, B., Zhang, S., Zhang, Q., Chen, J., & Zhang, J. (2018). Modelling of phase transformations induced by thermo-mechanical loads considering stress-strain effects in hard milling of AISI H13 steel. *International Journal of Mechanical Sciences*, *149*(June), 241–253. https://doi.org/10.1016/j.ijmecsci.2018.10.010

Li, J., Wu, X., Cao, L., Liao, B., Wang, Y., & Liu, Q. (2021). Hot deformation and dynamic recrystallization in Al-Mg-Si alloy. *Materials Characterization*, *173*(November 2020), 110976. https://doi.org/10.1016/j.matchar.2021.110976

Li, Q., Lovell, M. R., Slaughter, W., & Tagavi, K. (2002). Investigation of the morphology of internal defects in cross wedge rolling. *Journal of Materials Processing Technology*, *125–126*, 248–257. https://doi.org/10.1016/S0924-0136(02)00303-5

Li, S., Li, L., He, H., & Wang, G. (2019). Influence of the deformation heating on the flow behavior of 6063 alloy during compression at medium strain rates. *Journal of Materials Research*, *34*(2), 309–320. https://doi.org/10.1557/jmr.2018.367

Li, W., Liang, C., & Zhang, X. (2022). Numerical simulation of microstructure evolution of high-purity tantalum during rolling and annealing. *Modelling and Simulation in Materials Science and Engineering*, *30*(3). https://doi.org/10.1088/1361-651X/ac4d78

Li, Y. P., Onodera, E., Matsumoto, H., & Chiba, A. (2009). Correcting the stress-strain curve in hot compression process to high strain level. *Metallurgical and Materials Transactions A: Physical Metallurgy and Materials Science*, *40*(4), 982–990. https://doi.org/10.1007/s11661-009-9783-7

Liang, Q., Liu, X., Li, P., Ding, P., & Zhang, X. (2020). Development and application of high-temperature constitutive model of hni55-7-4-2 alloy. *Metals*, *10*(9), 1–19. https://doi.org/10.3390/met10091250

Lin, L., Wang, B., Zhou, J., & Shen, J. (2022). Manufacturing large shafts by a novel flexible skew rolling process. *International Journal of Advanced Manufacturing Technology*, *118*(9–10), 2833–2851. https://doi.org/10.1007/s00170-021-08079-y

Lou, Y. (2013). EVALUATION OF DUCTILE FRACTURE CRITERIA IN A GENERAL THREE-DIMENSIONAL STRESS STATE CONSIDERING THE STRESS TRIAXIALITY AND THE. *Acta Mechanica Solida Sinica*, *26*(6), 642–658. https://doi.org/10.1016/S0894-9166(14)60008-2

Mahlami, C. S., & Pan, X. (2017). Mechanical properties and microstructure evaluation of

high manganese steel alloyed with vanadium. *AIP Conference Proceedings*, *1859*. https://doi.org/10.1063/1.4990236

Mandal, S., Jayalakshmi, M., Bhaduri, A. K., & Subramanya Sarma, V. (2014). Effect of Strain Rate on the Dynamic Recrystallization Behavior in a Nitrogen-Enhanced 316L(N). *Metallurgical and Materials Transactions A: Physical Metallurgy and Materials Science*, *45*(12), 5645–5656. https://doi.org/10.1007/s11661-014-2480-1

Marashi, J., Yakushina, E., Xirouchakis, P., Zante, R., & Foster, J. (2017). An evaluation of H13 tool steel deformation in hot forging conditions. *Journal of Materials Processing Technology*, *246*, 276–284. https://doi.org/10.1016/j.jmatprotec.2017.03.026

Markov, O. E., Perig, A. V., Zlygoriev, V. N., Markova, M. A., & Grin, A. G. (2017). A new process for forging shafts with convex dies. Research into the stressed state. *International Journal of Advanced Manufacturing Technology*, *90*(1–4), 801–818. https://doi.org/10.1007/s00170-016-9378-6

McQueen, H. J. (2002). Elevated-temperature deformation at forming rates of 10-2 to 102 s-1. *Metallurgical and Materials Transactions A: Physical Metallurgy and Materials Science*, *33*(2), 345–362. https://doi.org/10.1007/s11661-002-0096-3

Mha, P. T., Dhondapure, P., Jahazi, M., & Tongne, A. (2023). Interpolation and Extrapolation Performance Measurement of Analytical and ANN-Based Flow Laws for Hot Deformation Behavior of Medium Carbon Steel. *Metals*, *13*. https://doi.org/https://doi.org/10.3390/met13030633

Mirzadeh, H., & Najafizadeh, A. (2013). Hot deformation and dynamic recrystallization of 17-4 PH stainless steel. *ISIJ International*, *53*(4), 680–689. https://doi.org/10.2355/isijinternational.53.680

Mirzadeh, H., Najafizadeh, A., & Moazeny, M. (2009). Flow curve analysis of 17-4 PH stainless steel under hot compression test. *Metallurgical and Materials Transactions A: Physical Metallurgy and Materials Science*, *40*(12), 2950–2958. https://doi.org/10.1007/s11661-009-0029-5

Mochugovskiy, A. G., Kaplanskaya, L. Y., Mosleh, A. O., Palacheva, V. V., & Mikhaylovskaya, A. V. (2023). Microstructure Evolution and Constitutive Modelling of Deformation Behavior for Al-Mg-Si-Cu-Sc-Zr Alloy Processed with Isothermal Multidirectional Forging. *Applied Sciences*, *13*(24), 13054. https://doi.org/10.3390/app132413054

Murugesan, M., & Jung, D. W. (2019). Two flow stress models for describing hot deformation behavior of AISI-1045 medium carbon steel at elevated temperatures. *Heliyon*, *5*(4), e01347. https://doi.org/https://doi.org/10.1016/j.heliyon.2019.e01347

Muszka, K., Madej, L., & Majta, J. (2013). The effects of deformation and microstructure inhomogeneities in the Accumulative Angular Drawing (AAD). *Materials Science and Engineering: A*, *574*, 68–74. https://doi.org/10.1016/j.msea.2013.03.024

Myint, P. W., Hagihara, S., Tanaka, T., Taketomi, S., & Tadano, Y. (2017). Determination of the values of critical ductile fracture criteria to predict fracture initiation in punching processes. *Journal of Manufacturing and Materials Processing*, *1*(2). https://doi.org/10.3390/jmmp1020012

Nalawade, R. S., Puranik, A. J., Balachandran, G., Mahadik, K. N., & Balasubramanian, V. (2013). Simulation of hot rolling deformation at intermediate passes and its industrial validity. *International Journal of Mechanical Sciences*, *77*, 8–16. https://doi.org/10.1016/j.ijmecsci.2013.09.017

Nasraoui, M., Forquin, P., Siad, L., & Rusinek, A. (2012). Influence of strain rate, temperature and adiabatic heating on the mechanical behaviour of poly-methyl-methacrylate: Experimental and modelling analyses. *Materials and Design*, *37*, 500–509. https://doi.org/10.1016/j.matdes.2011.11.032

Nayak, S., Dhondapure, P., Singh, A. K., Prasad, M. J. N. V., & Narasimhan, K. (2020). Assessment of constitutive models to predict high temperature flow behaviour of Ti-6Al-4V preform. *Advances in Materials and Processing Technologies*, *6*(2), 296–310. https://doi.org/10.1080/2374068X.2020.1731233

Nayak, S., Kumar Singh, A., Gokhale, H., Prasad, M. J. N. V., & Narasimhan, K. (2023). Optimization of Ti-6Al-4V ring rolling process by FE simulation using RSM. *International Journal of Solids and Structures*, *262–263*(July 2022), 112064. https://doi.org/10.1016/j.ijsolstr.2022.112064

Nayak, S., Singh, A. K., Prasad, M. J. N. V., & Narasimhan, K. (2023). Development of microstructural heterogeneities and dynamic restoration activity during ring rolling of Ti-6Al-4V alloy and its tensile response. *Journal of Alloys and Compounds*, *963*(June), 171241. https://doi.org/10.1016/j.jallcom.2023.171241

Niu, L., & Zhang, Q. (2022). A void closure model based on hydrostatic integration and the Lode parameter for additive manufacturing AlSi10Mg. *Journal of Manufacturing Processes*, *73*(November 2021), 235–247. https://doi.org/10.1016/j.jmapro.2021.10.056

Niu, L., Zhang, Q., Wang, B., Han, B., Li, H., & Mei, T. (2022). A modified Hansel-Spittel constitutive equation of Ti-6Al-4V during cogging process. *Journal of Alloys and Compounds*, *894*, 162387. https://doi.org/10.1016/j.jallcom.2021.162387

Oh, S.-I., Walters, J., & Wu, W.-T. (2018). Finite Element Method Applications in Bulk Forming. *Metals Process Simulation*, *22*, 267–289. https://doi.org/10.31399/asm.hb.v22b.a0005539

Oh, S. I., Chen, C. C., & Kobayashi, S. (1979). Ductile fracture in axisymmetric extrusion and drawing: Part 2 workability in extrusion and drawing. *Journal of Manufacturing Science and Engineering, Transactions of the ASME*, *101*(1), 36–44. https://doi.org/10.1115/1.3439471

Park, J., Kim, Y., Jeong, H., Kwon, H., Kwon, Y., & Kim, N. (2023). Cogging process design of M50 bearing steel for billet quality. *Journal of Materials Research and Technology*, *26*, 5576–5593. https://doi.org/10.1016/j.jmrt.2023.08.275

Pasco, J., McCarthy, T., Parlee, J., Nazri, N. A., Padmajan, S., Rodrigues, S., & Aranas, C. (2022). Constitutive modeling of modified-H13 steel. *MRS Communications*, *12*(3), 343–351. https://doi.org/10.1557/s43579-022-00182-9

Peng, Y., Guo, S., Liu, C., Barella, S., Liang, S., Gruttadauria, A., & Mapelli, C. (2022). Dynamic recrystallization behavior of low-carbon steel during hot rolling process: modeling and simulation. *Journal of Materials Research and Technology*, *20*, 1266–1290. https://doi.org/10.1016/j.jmrt.2022.07.039

Petch Norman J. (1953). The Cleavage Strength Of Polycrystals. *J. Iron Steel Inst.*, *174*, 25–28.

Petryk, H., Stupkiewicz, S., & Kuziak, R. (2008). Grain refinement and strain hardening in IF steel during multi-axis compression: Experiment and modelling. *Journal of Materials Processing Technology*, *204*(1–3), 255–263. https://doi.org/10.1016/j.jmatprotec.2007.11.068

Pinheiro, P., Monteiro, W. A., Barbosa, R., & Cetlin, P. R. (2004). The effect of strain path on the mechanical behavior and dislocation arrangements in the hot working of copper. *Materials Science and Engineering: A*, *368*(1–2), 280–285. https://doi.org/10.1016/j.msea.2003.11.008

Ren, F. C., Chen, J., & Chen, F. (2014). Constitutive modeling of hot deformation behavior of X20Cr13 martensitic stainless steel with strain effect. *Transactions of Nonferrous Metals Society of China (English Edition)*, *24*(5), 1407–1413. https://doi.org/10.1016/S1003-6326(14)63206-4

Rudra, A., Das, S., & Dasgupta, R. (2019). Constitutive Modeling for Hot Deformation Behavior of Al-5083 + SiC Composite. *Journal of Materials Engineering and Performance*, *28*(1), 87–99. https://doi.org/10.1007/s11665-018-3813-9

S. Bechet and L. Beaujard. (1995). New reagent for the micrographical demonstration of the austenite grain of hardened or hardened-tempered steels. *Rev. Metall.*, *52*(10), 830–836.

Saadatkia, S., Mirzadeh, H., & Cabrera, J. M. (2015). Hot deformation behavior, dynamic recrystallization, and physically-based constitutive modeling of plain carbon steels.

Materials Science and Engineering: A, *636*, 196–202. https://doi.org/10.1016/j.msea.2015.03.104

Sakai, T., Mori, K., & Utsunomiya, H. (2007). Effect of Deformation Route on Recrystallization Behaviour of 1100 Aluminum Sheet. *Materials Science Forum*, *550*(1), 315–320. https://doi.org/10.4028/www.scientific.net/msf.550.315

Saksala, T. (2019). Numerical modeling of adiabatic heat generation during rock fracture under dynamic loading. *International Journal for Numerical and Analytical Methods in Geomechanics*, *43*(9), 1770–1783. https://doi.org/10.1002/nag.2935

Samantaray, D., Mandal, S., & Bhaduri, A. K. (2009). A comparative study on Johnson Cook, modified Zerilli-Armstrong and Arrhenius-type constitutive models to predict elevated temperature flow behaviour in modified 9Cr-1Mo steel. *Computational Materials Science*, *47*(2), 568–576. https://doi.org/10.1016/j.commatsci.2009.09.025

Samantaray, D., Mandal, S., Bhaduri, A. K., Venugopal, S., & Sivaprasad, P. V. (2011). Analysis and mathematical modelling of elevated temperature flow behaviour of austenitic stainless steels. *Materials Science and Engineering: A*, *528*(4–5), 1937–1943. https://doi.org/10.1016/j.msea.2010.11.011

Samantaray, D., Mandal, S., Borah, U., Bhaduri, A. K., & Sivaprasad, P. V. (2009). A thermo-viscoplastic constitutive model to predict elevated-temperature flow behaviour in a titanium-modified austenitic stainless steel. *Materials Science and Engineering: A*, *526*(1–2), 1–6. https://doi.org/10.1016/j.msea.2009.08.009

Shang, X., Cui, Z., & Fu, M. W. (2018). A ductile fracture model considering stress state and Zener–Hollomon parameter for hot deformation of metallic materials. *International Journal of Mechanical Sciences*, *144*(June), 800–812. https://doi.org/10.1016/j.ijmecsci.2018.06.030

Shokry, A., Gowid, S., Kharmanda, G., & Mahdi, E. (2019). Constitutive models for the prediction of the hot deformation behavior of the 10%Cr steel alloy. *Materials*, *12*(18), 1–18. https://doi.org/10.3390/ma12182873

Sinha, V., Payton, E. J., Gonzales, M., Abrahams, R. A., & Song, B. S. (2017). Delineation of Prior Austenite Grain Boundaries in a Low-Alloy High-Performance Steel. *Metallography, Microstructure, and Analysis*, *6*(6), 610–618. https://doi.org/10.1007/s13632-017-0403-4

Standard Test Methods for Determining Average Grain Size. (2010). *Astm E112-10*, *13*(Reapproved), 1–27. https://doi.org/10.1520/E0112-13R21.1.4

Stebunov, S., Vlasov, A., & Biba, N. (2018). Prediction of fracture in cold forging with modified Cockcroft-Latham criterion. *Procedia Manufacturing*, *15*(September), 519–

526. https://doi.org/10.1016/j.promfg.2018.07.264

Stefanik, A., Dyja, H., & Mróz, S. (2011). Determination of the critical value of normalized Cocroft - Latham criterion during multi slight rolling based on tensile test. *Archives of Metallurgy and Materials*, *56*(2), 543–550. https://doi.org/10.2478/v10172-011-0058-0

STEVE P. DUDRA and YONG-TAEK IM. (1990). I n v e s t i g a t i o n of m e t a l f l o w in o p e n - d i e f o r g i n g w i t h d i f f e r e n t die a n d b i l l e t g e o m e t r i e s. *Journal of Materials Processing Technology*, *21*, 143–154.

Tamura, K., & Tajima, J. (2003). Optimisation of open die forging condition and tool design for ensuring both internal quality and dimensional precision by three-dimensional rigid-plastic finite element analysis. *Ironmaking and Steelmaking*, *30*(5), 405–411. https://doi.org/10.1179/030192303225001801

Tang, B., Cheng, L., Kou, H., & Li, J. (2015). Hot forging design and microstructure evolution of a high Nb containing TiAl alloy. *Intermetallics*, *58*, 7–14. https://doi.org/10.1016/j.intermet.2014.11.002

Tang, L., Jiang, F., Teng, J., Fu, D., & Zhang, H. (2019). Strain path dependent evolutions of microstructure and texture in AZ80 magnesium alloy during hot deformation. *Journal of Alloys and Compounds*, *806*, 292–301. https://doi.org/10.1016/j.jallcom.2019.07.262

Tavakoli, M., Mirzadeh, H., & Zamani, M. (2019). Ferrite recrystallisation and intercritical annealing of cold-rolled low alloy medium carbon steel. *Materials Science and Technology (United Kingdom)*, *35*(16), 1932–1941. https://doi.org/10.1080/02670836.2019.1655862

Terhorst, M., Feuerhack, A., Trauth, D., & Klocke, F. (2016). Extension of the normalized Cockcroft and Latham criterion with temperature-dependent critical damage values for predicting chevron cracks in solid forward extrusion. *International Journal of Material Forming*, *9*(4), 449–456. https://doi.org/10.1007/s12289-015-1231-1

Tian, Y., Chadha, K., & Aranas, C. (2023). Deformation-Induced Strengthening Mechanism in a Newly Designed L-40 Tool Steel Manufactured by Laser Powder Bed Fusion. *Acta Metallurgica Sinica (English Letters)*, *36*(1), 21–34. https://doi.org/10.1007/s40195-022-01461-z

Tize Mha, P., Dhondapure, P., Jahazi, M., Tongne, A., & Pantalé, O. (2023). Artificial Neural Network-Based Critical Conditions for the Dynamic Recrystallization of Medium Carbon Steel and Application. *Metals*, *13*(10). https://doi.org/10.3390/met13101746

Wang, Z., Xue, H., & Zhao, D. (2018a). Microstructure evolution and surface cracking behavior of superheavy forgings during hot forging. *Advances in Materials Science and Engineering*, *2018*, 1–10. https://doi.org/10.1155/2018/4780638

Wang, Z., Xue, H., & Zhao, D. (2018b). Microstructure evolution and surface cracking behavior of superheavy forgings during hot forging. *Advances in Materials Science and Engineering*, *2018*, 1–9. https://doi.org/10.1155/2018/4780638

Wei, H. lian, Liu, G. quan, Xiao, X., & Zhang, M. he. (2013). Dynamic recrystallization behavior of a medium carbon vanadium microalloyed steel. *Materials Science and Engineering: A*, *573*, 215–221. https://doi.org/10.1016/j.msea.2013.03.009

Xu, Y., Zhang, Y., Zhuang, X., Cao, Z., Lu, Y., & Zhao, Z. (2021). Numerical modeling and anvil design of high-speed forging process for railway axles. *International Journal of Material Forming*, *14*(5), 813–832. https://doi.org/10.1007/s12289-020-01590-9

Yan, T., Yu, E., & Zhao, Y. (2013). Constitutive modeling for flow stress of 55SiMnMo bainite steel at hot working conditions. *Materials and Design*, *50*, 574–580. https://doi.org/10.1016/j.matdes.2013.03.082

Yang, C., Dong, H., & Hu, Z. (2018). Micro-mechanism of central damage formation during cross wedge rolling. *Journal of Materials Processing Technology*, *252*(March 2017), 322–332. https://doi.org/10.1016/j.jmatprotec.2017.09.041

Yang, X., Zhang, Z., Meng, M., Jia, J., Zhang, H., Lei, G., & Yu, J. (2022). Hot tensile deformation behaviors and a fracture damage model of the Mg-Gd-Y-Zn-Zr alloy. *Journal of Materials Research and Technology*, *18*, 255–267. https://doi.org/10.1016/j.jmrt.2022.02.104

Ye, L., Zhai, Y., Zhou, L., Wang, H., & Jiang, P. (2020). The hot deformation behavior and 3D processing maps of 25Cr2Ni4MoV steel for a super-large nuclear-power rotor. *Journal of Manufacturing Processes*, *59*(September), 535–544. https://doi.org/10.1016/j.jmapro.2020.09.062

Yin, L., & Wu, Y. (2022). Comparison of Constitutive Models and Microstructure Evolution of GW103K Magnesium Alloy during Hot Deformation. *Materials*, *15*(12). https://doi.org/10.3390/ma15124116

Yuan, L., Wei, Q., Han, L., Shan, D., & Guo, B. (2021). A new hot forging method for the die temperature higher than the billet temperature. *International Journal of Advanced Manufacturing Technology*, *116*(9–10), 3063–3074. https://doi.org/10.1007/s00170-021-07656-5

Zeng, S., Hu, S., Peng, B., Hu, K., & Xiao, M. (2022). The constitutive relations and thermal deformation mechanism of nickel aluminum bronze. *Materials and Design*, *220*. https://doi.org/10.1016/j.matdes.2022.110853

Zhang, C., Shahriari, D., Loucif, A., Melkonyan, H., & Jahazi, M. (2018). Influence of

thermomechanical shrinkage on macrosegregation during solidification of a large-sized high-strength steel ingot. *International Journal of Advanced Manufacturing Technology*, *99*(9–12), 3035–3048. https://doi.org/10.1007/s00170-018-2695-1

Zhang, Chunping, Loucif, A., Tremblay, R., & Jahazi, M. (2019). Influence of non-uniform temperature distribution of the mold on solidification behavior in large-size steel ingots. *Proceedings for the 8th International Conference on Modeling and Simulation of Metallurgical Processes in Steelmaking, STEELSIM 2019*, (August), 573–581. https://doi.org/10.33313/503/060

Zhang, R., Wang, D. J., & Yuan, S. J. (2017). Effect of multi-directional forging on the microstructure and mechanical properties of TiBw/TA15 composite with network architecture. *Materials and Design*, *134*, 250–258. https://doi.org/10.1016/j.matdes.2017.08.055

Zhang, X., Ma, F., Ma, K., & Li, X. (2012). Multi-scale analysis of void closure for heavy ingot hot forging. *Modern Applied Science*, *6*(10), 15–25. https://doi.org/10.5539/mas.v6n10p15

Zhang, X. X., Cui, Z. S., Chen, W., & Li, Y. (2009). A criterion for void closure in large ingots during hot forging. *Journal of Materials Processing Technology*, *209*(4), 1950–1959. https://doi.org/10.1016/j.jmatprotec.2008.04.051

Zhang, Yi, Chai, Z., Volinsky, A. A., Tian, B., Sun, H., Liu, P., & Liu, Y. (2016). Processing maps for the Cu-Cr-Zr-Y alloy hot deformation behavior. *Materials Science and Engineering: A*, *662*, 320–329. https://doi.org/10.1016/j.msea.2016.03.033

Zhang, Yu, Guo, B., Li, Q., Li, X., Jian, J., Jin, Y., & Ao, J. (2021). Damage and Cracking Prediction of AISI 410 Martensitic Stainless Steel at Elevated Temperatures. *Steel Research International*, *92*(9), 1–12. https://doi.org/10.1002/srin.202100030

Zhenwei, W., Jianping, W., Changwen, H., Jiabing, S., Baoguo, X., & Xingquan, Z. (2022). Cracking failure analysis of steel piston forging die. *Engineering Failure Analysis*, *138*(November 2021), 106291. https://doi.org/10.1016/j.engfailanal.2022.106291

Zhou, Xianyan, Shao, Z., Pruncu, C. I., Hua, L., Balint, D., Lin, J., & Jiang, J. (2020). A study on central crack formation in cross wedge rolling. *Journal of Materials Processing Technology*, *279*(August 2019). https://doi.org/10.1016/j.jmatprotec.2019.116549

Zhou, Xianyan, Shao, Z., Zhang, C., Sun, F., Zhou, W., Hua, L., … Wang, L. (2020). The study of central cracking mechanism and criterion in cross wedge rolling. *International Journal of Machine Tools and Manufacture*, *159*(August). https://doi.org/10.1016/j.ijmachtools.2020.103647

Zhou, Xianyan, Sun, C., Wang, B., & Jiang, J. (2022). Investigation and prediction of central

cracking in cross wedge rolling. *International Journal of Advanced Manufacturing Technology*, *123*(1–2), 145–159. https://doi.org/10.1007/s00170-022-10126-1

Zhou, Xiaoqin, Ma, W., Feng, C., & Zhang, L. (2020). Flow stress modeling, processing maps and microstructure evolution of 05Cr17Ni4Cu4Nb Martensitic stainless steel during hot plastic deformation. *Materials Research Express*, *7*(4). https://doi.org/10.1088/2053-1591/ab89d8

Zhu, S., Yang, H., Guo, L. G., & Gu, R. J. (2012a). Investigation of deformation degree and initial forming temperature dependences of microstructure in hot ring rolling of TA15 titanium alloy by multi-scale simulations. *Computational Materials Science*, *65*, 221–229. https://doi.org/10.1016/j.commatsci.2012.07.014

Zhu, S., Yang, H., Guo, L. G., & Gu, R. J. (2012b). Investigation of deformation degree and initial forming temperature dependences of microstructure in hot ring rolling of TA15 titanium alloy by multi-scale simulations. *Computational Materials Science*, *65*, 221–229. https://doi.org/10.1016/j.commatsci.2012.07.014